Design strategies using transition metal-based oxides for water electrolysis

A Dissertation Submitted to the

Indian Institute of Technology Guwahati

in Partial Fulfilment for the Degree of

DOCTOR of PHILOSOPHY

by

Sourav Bhowmick

DEPARTMENT OF CHEMISTRY

INDIAN INSTITUTE OF TECHNOLOGY GUWAHATI

GUWAHATI, ASSAM, INDIA

FEBRUARY 2023

Design strategies using transition metal-based oxides for water electrolysis

A Dissertation Submitted to the

Indian Institute of Technology Guwahati

in Partial Fulfilment for the Degree of

DOCTOR of PHILOSOPHY

by

Sourav Bhowmick

Roll No.: 176122028

DEPARTMENT OF CHEMISTRY

INDIAN INSTITUTE OF TECHNOLOGY GUWAHATI

GUWAHATI, ASSAM, INDIA

FEBRUARY 2023

STATEMENT

I hereby declare that the scientific findings included in this thesis entitled, "**Design strategies using transition metal-based oxides for water electrolysis**" is the outcome of research work carried out by me under the supervision of Prof. Mohammad Qureshi, at the Department of Chemistry, Indian Institute of Technology Guwahati, Assam, India, for the award of the degree of Doctor of Philosophy.

The work embodied in this thesis is the result of original research done by me except where otherwise stated in this thesis with proper citations. I confirm that the investigations were conducted in accord with the ethics policies and integrity standards of the Indian Institute of Technology Guwahati and that the research data are presented honestly and without prejudice. The thesis work has not been submitted for a degree or professional qualification to any other university or institution.

IIT Guwahati
February 2023

Sourav Bhowmick
Candidate
Department of Chemistry
IIT Guwahati
Guwahati-781039, Assam
India

Dr. Mohammad Qureshi
Professor, FRSC
Department of Chemistry
Indian Institute of Technology Guwahati
Guwahati – 781039, India
Tel: +91 – 361 – 2582320;
Email: mq@iitg.ac.in

CERTIFICATE

Certified that the work described in this thesis entitled "**Design strategies using transition metal-based oxides for water electrolysis**" by Mr. Sourav Bhowmick, Department of Chemistry, Indian Institute of Technology Guwahati has been carried out his thesis work under my supervision and has not been submitted elsewhere for a degree.

Guwahati
February 2023

Mohammad Qureshi
Thesis supervisor
Department of Chemistry
Indian Institute of Technology Guwahati
Guwahati – 781039, Assam, India

ACKNOWLEDGEMENT

This thesis signifies not only my work at IITG and in MSL (CHEL-109) but the wonderful journey that I have experienced throughout my tenure. The half a decade has been nothing short of amazing. Since my first day here I have been accompanied by the most amazing people who have always been by my cradle in achieving the milestone. I have been given enough unique opportunities and have been fortunate enough to make the most out of them. Throughout these years I have learned that there are some who are strong-willed, some who always find alternatives and also some who are a bit of both. This thesis is the result of work by several people, who I wish to thank but also the result of many experiences I have encountered at IITG from dozens of remarkable individuals who I also wish to acknowledge.

Foremost, I would like to express my sincere gratitude to my thesis supervisor, Prof. Mohammad Qureshi, for giving me the opportunity to work under his expert supervision. I am thankful to him for introducing me to the unique area of specialization "Electrochemical Water Splitting". His constant encouragement and judicious suggestions have provided me with the zeal to carry out my research work. His constant faith in me while providing alternate research works has uplifted my scientific grasp. I am also pleased for providing the freedom and space to express my thoughts and explore the science in my own way.

I would also like to appreciate my thesis committee members for guiding me through all these years. Thank you, Prof. Chivukula Vasudeva Sastri, Prof. Parameswar Krishnan Iyer and Dr. Nageswara Rao Peela for your constant support, valuable suggestions and periodic evaluation of my thesis work. Additionally, I would like to recognize C. V. Sastri for providing the CH instrument to carry out the electrochemical experiments during the initial phase of my thesis work. I would also acknowledge Prof. Aditya Narayan Panda for providing help and support whenever needed.

A special thanks to Indian Institute of Technology Guwahati and Ministry of Health and Research Development for providing all the necessities and financial support to carry out my research work. I would also extend my gratitude for all the faculty members and staff members of department of chemistry for their help regarding various aspects. My sincere thanks to the staff of Central Instruments Facility for their help and guidance for utilization of the various instrumental facilities.

From layman to being professional, dozens of people are to be credited for. My lab seniors have been a source of support and energy, and their indispensable input and guidance are worth mentioning. Dr. Anindya Sundar Patra, Dr. Mohammad Shaad Ansari, Dr. Avishek Banik and Dr. Gaurangi Gogoi, thank you for being the tutors and motivation in lab. Dr. Tushar Kanta Sahu, Dr. Suhaib Alam and Dr. Adit Kumar Shah, thank you being my mentor and not less than friend who have made my stay in the lab more comfortable. Ching Thian Moi, thank you for your help in the work. Manoj Kumar Mohanta, a lab mate cum friend, thanks a lot for all the help. From lab to tea stalls to badminton court, you have been my best companion. And my lab juniors, Nitul Kalita, Alpana Sahu, Peeyush Pandey and N Anjana Singha, I really appreciate your timely assistance, support and for creating an enjoyable atmosphere in the lab. Nevertheless, I am also thankful to the M.Sc. project students, Ankit Dhankar, Rohan Jena, Shipra Suman, Sandeep Yadav, Kamlesh Mewara Amit Kumar and Aswathi K S, for helping me to gain more insights of the research topic. Thank you everyone at the lab for many years of tea, snacks, parties, movies, outings and fun while working on the thesis!

Friends have always been my moral support and special strength throughout my life. Words are way less to express my gratefulness to them but yet I would like to mention some close ones without whom this journey would have been more of a suffering. Sarbani Roy, you have always been there for me since the Cotton days. Your indefinable support through thick and thin have really encouraged me to continue my hustle at IITG and life. Sujit Kumar Deb, I am really grateful for your constant care and support during tough times and also providing me with all the help required to carry out my research work. Deboshree Choudhury, Anirban Nandy, Chiranjit Chakraborty, Manoj Chakraborty, Snehasish Sharma and Bijoy Majumdar, your friendship is truly appreciated for your unconditional support and encouragement all these years. Karanika Sonowal, your help regarding the analyses of my samples is really appreciated. Sucharita Shil and Aparna Saha, your respective contributions and support are also acknowledged.

My friends at IITG have been my pillars of strength and motivation to carry out my PhD work. Debojit Paul and Subhamoy Biswas, you two were not less than a family at IITG. From small instants to huge moments, you people always stood beside me and encouraged me carry forward. Monikha Chetia, Arpita Shome, Shilpa Bhuyan, Angana Borbora and Rakesh Mazumdar, thank you so much for creating all the cherishable moments and intended funs, foremost needed for the uplifted mood during this rough journey of PhD. And Angana,

you are also thanked for being my badminton partner since my masters till date. A special mention to the person, Aviti Katare, for your love, care and enthusiastic support towards the completion of my thesis. Also special thanks to Pronoy Dutta, Umesh Kumar Bagha, Manmath Mishra, Jagnyesh Satpathy, Pragya Gupta and Saptarshi Gupta for being integral part of this journey. The trivial helps from Abhay Pratap Singh, Subhrajyoti Ghosh, Abhijeet Rana, Sagnik De, Bishwanath Mahato and Araghni Bhattacharya are also been acknowledged.

I would also like to extend my gratitude to my all teachers/faculties and friends from my school, Bachelor's and Master's. Although they were far apart during this tenure, their direct or indirect support and motivation has guided me to reach this far. Among all, special thanks to my M.Sc. dissertation guide, Dr. Ranjit Thakuria, for mounting the passion of research and aspiring me to begin this journey. Also, I would acknowledge my PhD batch mates whose trivial supports are worth mentioning.

Lastly, I would like to finish with my pillars of strength, where the most basic source of my life energy resides: "*My Family*". Their unconditional love and support throughout the years have brought me to such an upright position where I am right now. The most dedicated person for this thesis is my *mother* (Kalpana Bhowmick) whose eternal love and faith in me has provided with all the positive vibes that I needed to move forward in my life. My *father* (Subodh Bhowmick) whose support, knowledge and sacrifices have moulded me with all the enthusiasms and confidence that provided the energy to drive towards my goal. This thesis also belongs to my elder brother (Sanjay Bhowmick), uncles, aunties and my lovely cousins. They have cherished every great achievement and supported me whenever I needed it.

It is difficult to weave all the names in a single piece of writing. So, any omission in this brief acknowledgement does not mean lack of gratitude.

Sourav

Dedicated To

“ মা ও বাবা ”

Family & Friends

TABLE OF CONTENTS

Thesis Title:	**Design strategies using transition metal-based oxides for water electrolysis**
Name of the Candidate:	Sourav Bhowmick
Registration Number:	176122028
Thesis Supervisor:	Prof. Mohammad Qureshi
Department:	Chemistry
Institute:	Indian Institute of Technology Guwahati, Assam – 781039, India.

Thesis Overview

- ✓ **Chapter 1:** The current scenario of the on-going research and challenges related to the development of efficient, cost-effective, and stable electrocatalysts are been briefly illustrated in this chapter. This chapter also explains the different strategies and methodologies to be employed for the development of an efficient electrocatalyst for enhanced water splitting and dissociation performance. The chapter concludes with the objectives and motivation that led to the design and fabrication of several metal oxide-based catalysts for water electrolysis.
- ✓ **Chapter 2:** This chapter illustrates the synthetic protocols of the electrocatalysts and the instrumentation techniques used for their characterizations. It also discusses the methods for fabrication of the working electrodes and bipolar membrane utilized for electrochemical applications and the performance parameters for determination of their catalytic activities.
- ✓ **Chapter 3: Doping and overlayer strategy: Strontium doped Lanthanum manganite overlayered with Cobalt Phosphate for oxygen evolution reaction**

(*ACS Applied Energy Materials*, **2020**, *3*, 1279)

In this chapter, we have utilized the doping strategy to enhance the electrochemical performance by virtue of its increased bulk conductivity. $LaMnO_3$, a 3D perovskite was chosen due to its high flexibility of elemental composition, tunable electronic/defect structure and high stability. Here, Sr^{2+} was doped into the La^{3+} (A-site) resulting in conversion of some Mn^{3+} to Mn^{4+} state which tends the Mn–O–Mn bond to ~180°, thereby enhancing the conductivity due to facile charge mobility within the bulk. $La_{0.7}Sr_{0.3}MnO_3$ was found to be best performing electrocatalyst and in turn was further modified with an overlayer of cobalt phosphate (Co-Pi). The faster reaction kinetics of cobalt phosphate ($Co^{2+} \leftrightarrow Co^{3+} \leftrightarrow Co^{4+}$) at the electrolyte interface led to ~4-fold enhanced turnover frequency of the composite due to the ~12-fold

reduced charge transfer resistance (R_{ct}) value. The $La_{0.7}Sr_{0.3}MnO_3$/Co-Pi also delivered lower overpotential of 220 mV with Tafel slope of 62 mV/decade. Further, the ~98% Faradaic Yield and 16 hours long-run stability proved the high efficiency of the composite electrocatalyst.

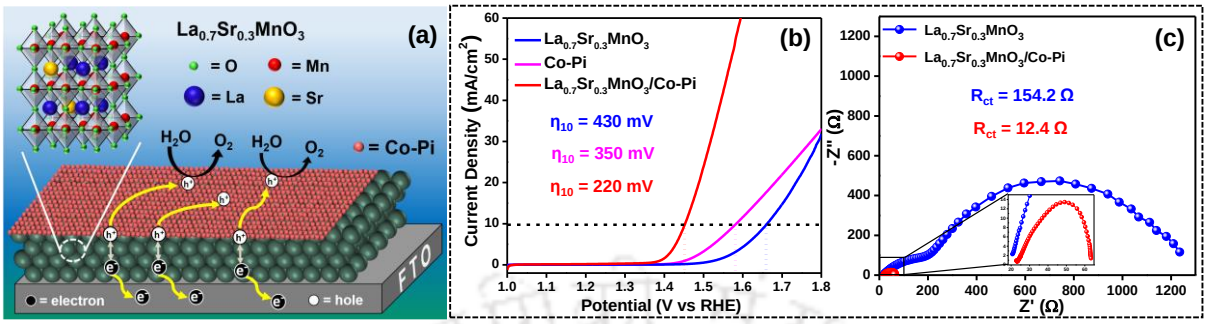

Figure 2.1: (a) Schematic representation of the $La_{0.7}Sr_{0.3}MnO_3$/Co-Pi composite electrode over FTO substrate undergoing the OER process, (b) Polarization curve depicting the over potential values, and (c) Nyquist-plots with the obtained R_{ct} values

✓ **Chapter 4: Transcription strategy: Morphological transformation of Strontium doped lanthanum manganite for oxygen evolution reactions**

(*Sustainable Energy Fuels*, **2021**, *5*, 6392)

In this chapter, we have utilized the morphological strategy to increase the electroactive sites and the bulk conductivity of 3D perovskites thereby enhancing their electrochemical performance.

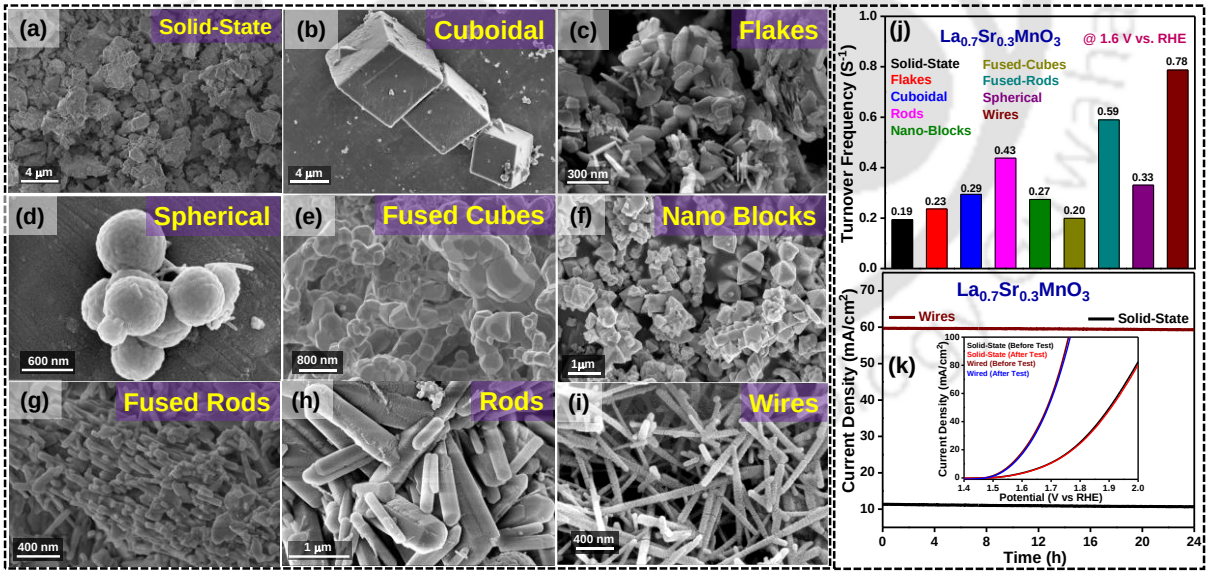

Figure 4.1: FESEM images of (a) general solid-state, (b-i) synthesized morphological LSMO, (j) Turnover frequencies of all LSMO, and (k) long-term stability test of general solid-state LSMO and wire-shaped LSMO with their corresponding LSV as inset

$La_{0.7}Sr_{0.3}MnO_3$ (LSMO) was found to be better electrocatalyst but its high temperature solid-state synthesis restricted tuning of desired morphology. The diffusion mediated solid-state reaction process led to the idea of utilization of transcription methodology. Here one of

the precursors, MnO_x, was tuned into desired morphology and latter utilized as template during solid-state reaction to transcript the pre-defined morphology onto LSMO. On application of this transcription methodology, a library of desired morphological LSMOs were synthesized with increased electroactive sites and charge conductivity than the general solid-state LSMO. The electrochemical performances showed that the 1D wire-shaped LSMO attained ~4-fold enhanced electrochemical active surface area and ~2-fold reduced charge transfer resistance than the general solid-state LSMO resulting in overpotential of 330 mV with Tafel slope of 76 mV/decade. The high stability of the electrocatalyst was confirmed from its 24 hours continuous OER performance with ~98% average Faradaic yield while the high activity was confirmed from the ~4-fold enhanced turnover frequency.

✓ **Chapter 5: Morphology and overlayer strategy: Oxygen evolution reaction performance of di-manganese copper oxide coupled with nickel borate**

(*Sustainable Energy Fuels*, **2021**, *5*, 2517)

In this chapter, we have synthesized a complex metal oxide, di-manganese copper oxide having high stability and electrochemical activity by virtue of its mixed valence states of Mn (III/IV) and Cu (II/I).

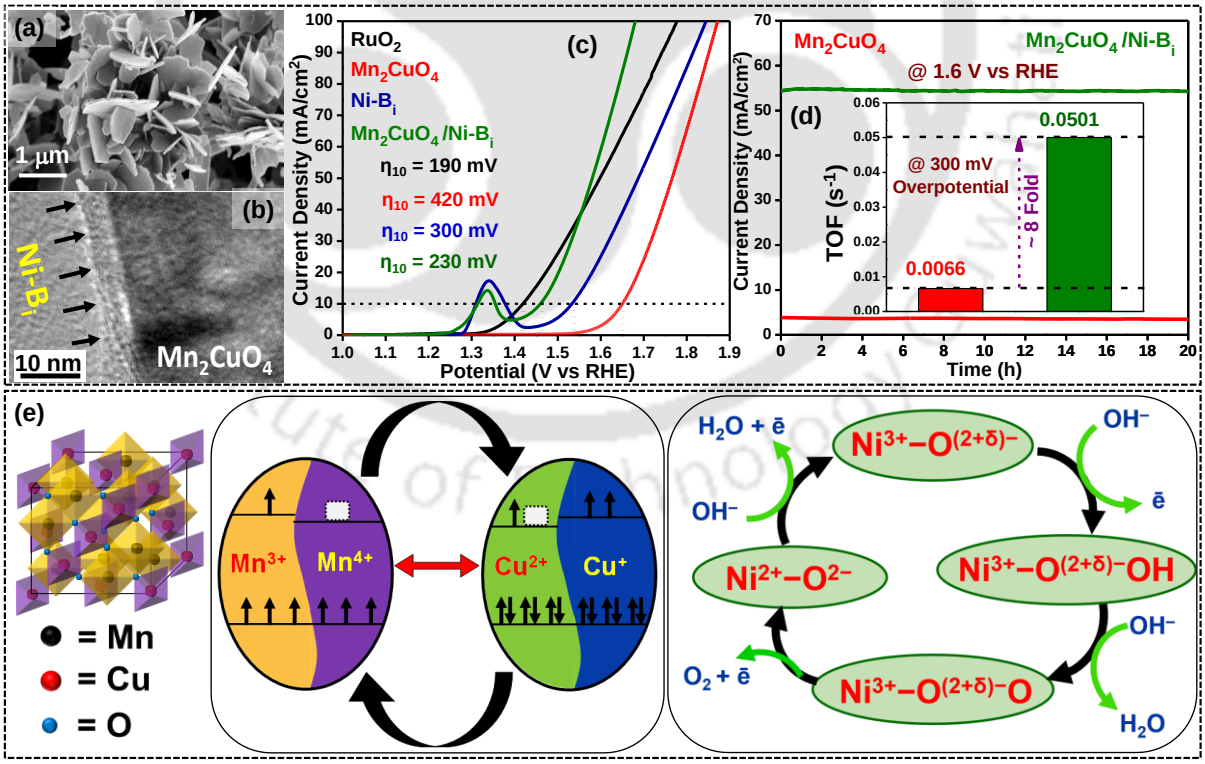

Figure 5.1: (a) FESEM image of 2D flake-like structures of Mn_2CuO_4, (b) FETEM image of composite showing the Ni-B_i overlayer over Mn_2CuO_4 particle, (c) Polarization curve showing the overpotential values, (d) stability curves with turnover frequencies as inset, and (e) schematic representation of the multi-metal redox cycles undergoing the OER process

The 2D flake-like structures of as-synthesized Mn_2CuO_4 provides better exposed surface for the incoming electrolyte molecules to interact with the electroactive sites and the redox couple ($Mn^{3+} + Cu^{2+} \leftrightarrow Mn^{4+} + Cu^{+}$) within the bulk stabilizes the molecule during the OER, thus providing the high electrochemical performance. The OER kinetics is further boosted by depositing nickel borate (Ni-B_i) over its surface via electrodeposition. The redox cycle of Ni atom ($Ni^{2+} \leftrightarrow Ni^{3+}$) facilitates the charge transfer process at the electrolyte interface thereby accelerating the overall water oxidation process. The composite electrocatalyst, Mn_2CuO_4/Ni-B_i, showed a lower overpotential of 230 mV at current density of 10 mA/cm^2 with Tafel slope of 56 mV/decade. The Ni-B_i overlayer also increased the overall electrochemical active surface area with corresponding double-layer capacitance value of 55 mF/cm^2 and reduced the charge transfer resistance at the electrolyte interface to 13.15 Ω. The self-redox property of Mn_2CuO_4 provides the high stability as confirmed from 20 hours of continuous OER with average Faradaic yield of ~98%. The redox cycle Ni-B_i additionally resulted in ~8-fold enhanced turnover frequency of the composite electrocatalyst.

✓ **Chapter 6: Morphology, overlayer and hetero-junction strategy: Bifunctional Mn_2O_3/CuO-$(VO)_3(PO_4)_2.6H_2O$ for electrochemical water splitting**

(*ACS Applied Materials & Interfaces*, **2022**, *14*, 52204)

In this chapter, we have synthesized a *n-p* type heterojunction comprising Mn_2O_3 and CuO to fabricate a bi-functional electrocatalyst undergoing both HER and OER. Also, the difference in rate of diffusion coefficients of the respective metal ions ($D_{Mn} > D_{Cu}$) led to transformation of Mn_2O_3 solid spheres into hollow spherical structures of Mn_2O_3/CuO due to the ion-exchange Kirkendall effect. The hollow spheres led to the increase in number of electroactive sites owing to more exposed surface area, while the *n-p* heterojunction led to more charge separation and accumulation at the semiconductor interface thereby increasing the electrocatalytic activity of the semiconductor towards overall water splitting. The ~3-fold enhanced double-layer capacitance (C_{dl}) and ~2-fold reduced charge transfer resistance (R_{ct}) for Mn_2O_3/CuO compared to bare Mn_2O_3 results in improved OER (η_{10} = 280 mV) and HER (η_{10} = 310 mV) performances. The bi-functional property of the semiconductor was further boosted by the addition of vanadyl phosphate (VOP), owing to its high charge transfer coefficient value (α), as overlayer over the Mn_2O_3/CuO particles. The composite, Mn_2O_3/CuO-VOP, resulted in much enhanced OER (η_{10} = 190 mV) and HER (η_{10} = 220 mV) performances with overall cell voltage of 1.64 V @ current density of 10 mA/cm^2. The durability of the composite electrocatalyst was also examined with 36 hours of long-run stability test for both OER and

HER while its electrochemical activity towards water splitting was confirmed from the obtained average Faradaic yield of ~98%.

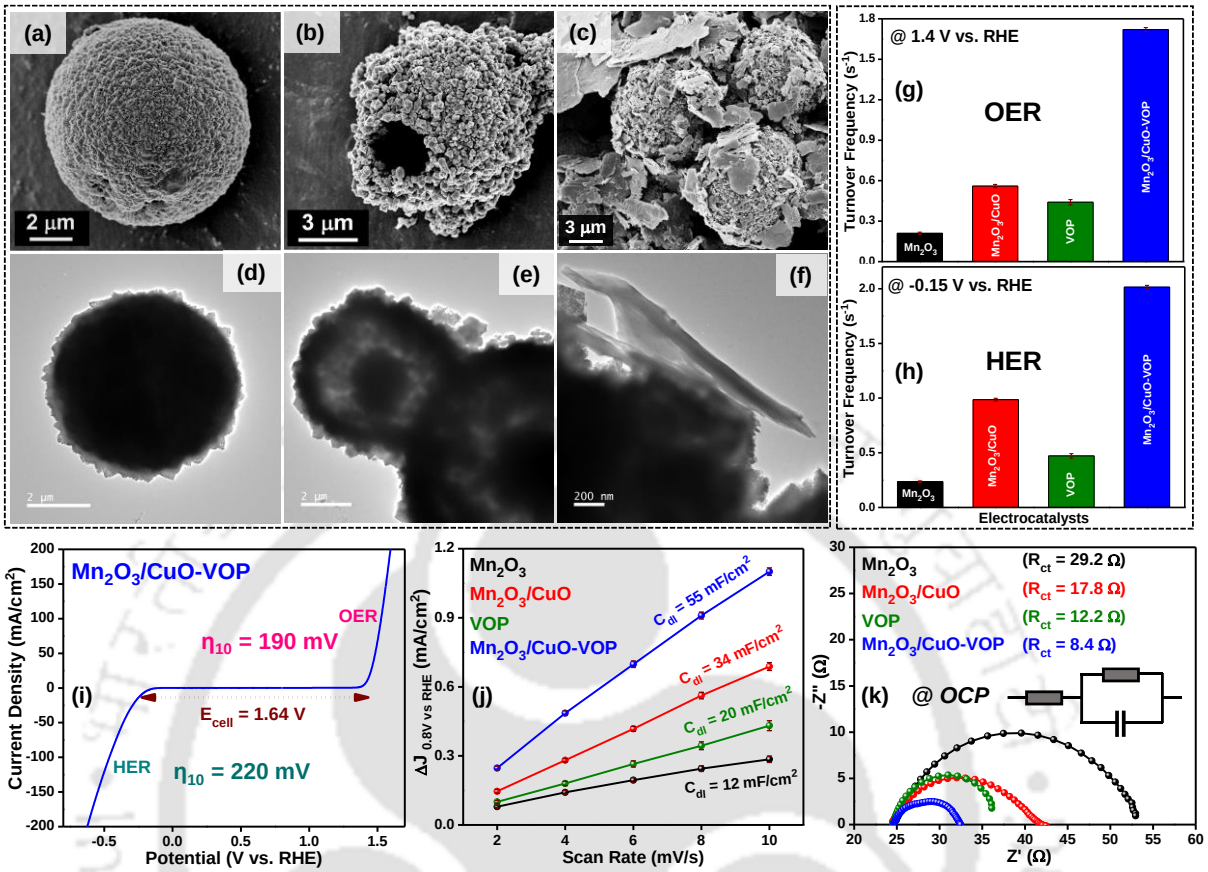

Figure 6.1: FESEM images of (a) Mn_2O_3, (b) Mn_2O_3/CuO, (c) Mn_2O_3/CuO-VOP, and (d-f) their corresponding FETEM images showing the morphological transformation from solid sphere to hollow spherical structure and the overlying 2D sheets, respectively, turnover frequencies of the electrocatalysts for (g) OER and (h) HER, (i) overall water splitting depicting the cell voltage, (j) Current vs scan rate depicting the C_{dl} values, and (k) Nyquist plot @ OCP depicting the R_{ct} values

✓ **Chapter 7: Membrane Strategy: Vanadium oxide nanosheets infused functionalized polysulphone bipolar membrane for water dissociation**

(*Applied Materials & Interfaces*, **2023**, DOI: 10.1021/acsami.2c20090)

In this chapter, we have utilized the water dissociation process occurring at the interfacial layer (IL) of a bipolar membrane (BPM) generating H^+ and OH^- ions which are then converted to H_2 and O_2 at cathode and anode, respectively. Polysulphone (PSp) polymer has been functionalized with anionic, $–SO_3^-$ (SPSp), and cationic, $–R_4N^+$ (QPSp), groups to synthesize the cation exchange layer (CEL) and anion exchange layer (AEL). To boost the water dissociation at the IL region, 2D V_2O_5 nanosheets were synthesized owing to its high affinity towards water adsorption. The V_2O_5 nanosheet was blended with polyvinyl alcohol (PVA) and incorporated at the IL region between the SPSp and QPSp to fabricate the composite BPM

(BPM_VO-ns). The PVA provided the adhesion of the two IEL and V_2O_5 acted as the catalyst. The H-bond formation between the V_2O_5 and H_2O weakened the H–OH bond thereby easy dissociation as supported by the lower water dissociation voltage (V_{diss}) of 1.11 V and low pseudo-limiting current density ($I_{p\text{-}lim}$) of 0.98 mA/cm^2 at 1 V. The reduced dissociation resistance (R_{diss}) of 0.027 Ω.cm^2 and transmembrane voltage (V_{trans}) of 3.6 V @ current density of 100 mA/cm^2 also supports the high activity of the composite BPM towards water dissociation process.

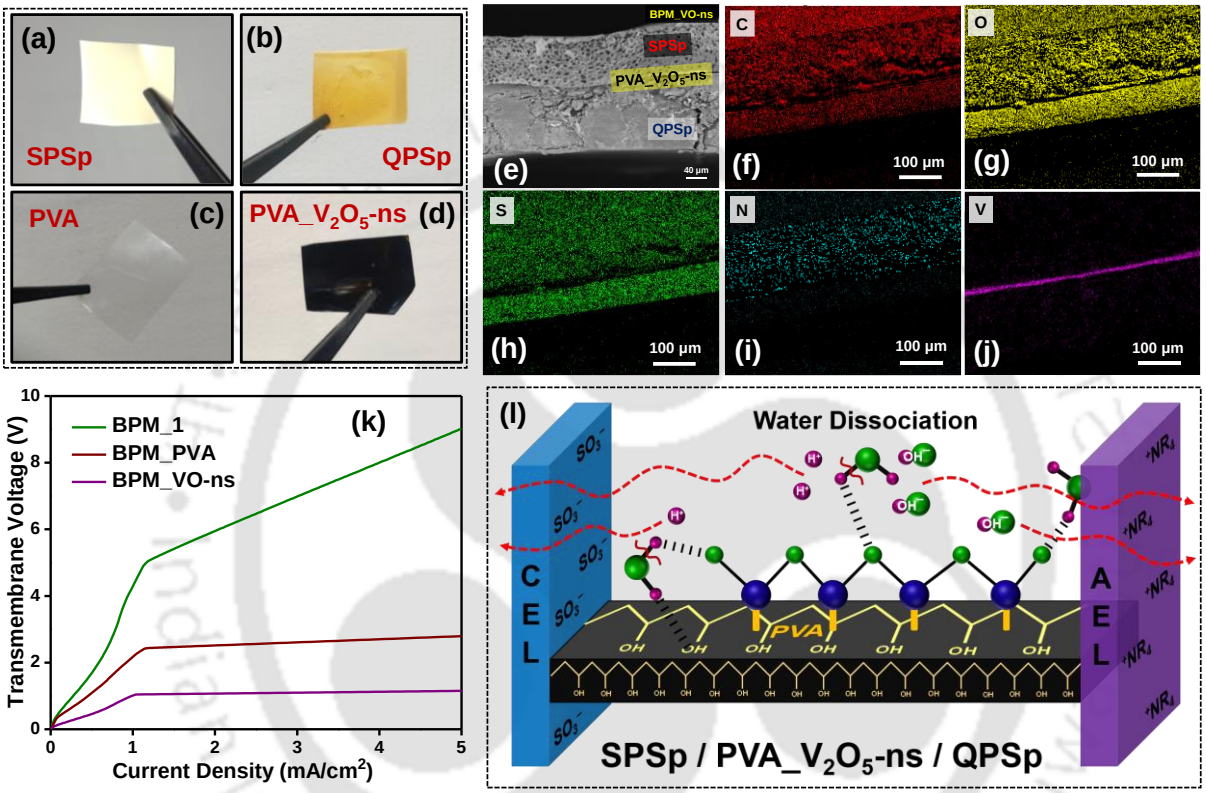

Figure 7.1: Digital images of (a) SPSp, (b) QPSp, (c) PVA, (d) PVA_V_2O_5-ns, (e) FESEM image of composite BPM, EDS mapping showing the presence of (f) carbon, (g) oxygen, (h) sulphur, (i) nitrogen, (j) vanadium, (k) current-voltage curve showing the WD performance, and (l) schematic of the plausible mechanism undergoing in the IL region for enhanced water dissociation process

✓ Chapter 8: Thesis overview and future perspectives

The current chapter, in short, summarizes the conclusions and the overview of the present thesis. It also discusses the possible modifications that can be done in the near future towards the practicality of the electrochemical water splitting.

CHAPTER 1

Introduction and Literature Survey

This chapter comprises a comprehensive overview of electrochemical water splitting. Overall energy consumption and future energy demand contributed by present non-renewable energy sources apart from the need for renewable energy sources are discussed. A brief survey of current state-of-the-art scenario and challenges associated with the design and development of working electrode materials utilized for electrochemical water splitting are discussed. Several strategies used to enhance the surface reaction kinetics of metal oxide-based working electrodes are also discussed.

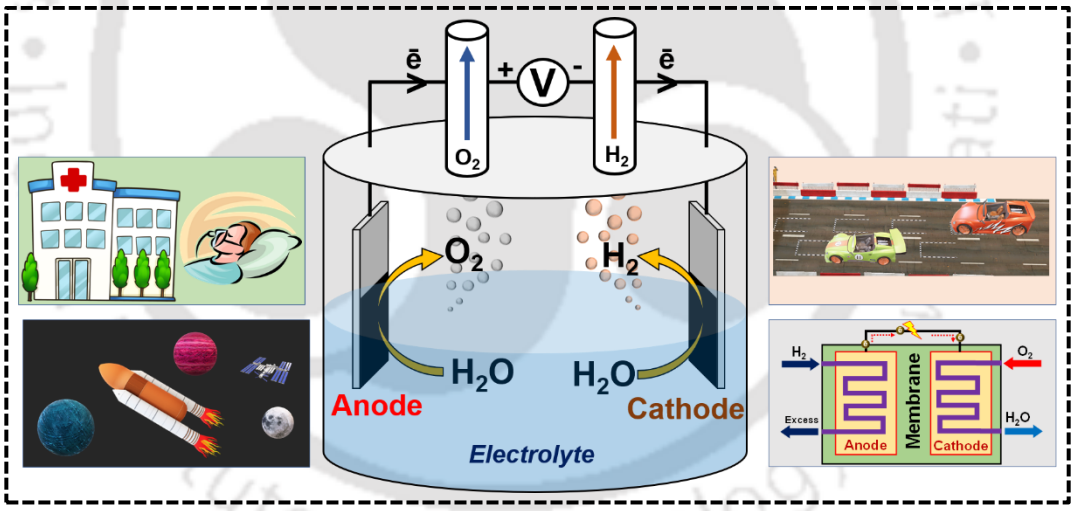

1.1. Renewable Energy Sources

The global energy crisis, and its associated environmental issues, has motivated scientists to search for renewable energy resources that can replace fossil fuels. The use of carbon-free renewable energy sources can significantly reduce the CO_2 emissions and restore the ecological balance. The distribution of the different renewable energy sources is not geological unlike the conventional non-renewable energy sources.[1] Among all the available sources, solar energy has the highest potential to meet all the energy demand as the Sun's annual flow of energy to the Earth's surface (1,73,000 TW) is thousand times than what is needed.[2] But till date, no economically feasible technology has been developed to harness the incoming solar energy to meet all the energy demand.[1] So, researchers have diverted to other alternatives which have zero carbon emission and are equally capable of producing energy in adequate amount.

Hydrogen gas (H_2), due to its high calorific value of ~141.7 MJ/kg has proven to be the alternate source of energy with zero carbon emission.[3] Till date most of the hydrogen gas is produced using the traditional methods like steam reforming of methane, coal gasification, etc., which equally contribute to the increase in the greenhouse gasses.[4] The secondary methods of hydrogen production include photolysis, electrolysis, and/or thermolysis of water and through biomass.[4,5] Among all, electrolysis is considered more effective due to its ability to produce hydrogen in large quantity, thereby has higher efficiency than other alternate routes. Electrochemical water splitting is thus considered as the boon of the modern era for requisite energy production.

1.2. Electrochemical Water Splitting

Electrochemical water splitting is a chemical process that converts water into hydrogen and oxygen with the help of electrical energy. It represents one of the most important reaction for hydrogen fuel production, as water is the most abundant hydrogen source on the Earth and the electricity required can be derived from the solar cells or any other green processes.[6] In a traditional electrochemical cell, there occurs two electrodes, anode and cathode producing the oxygen and hydrogen, respectively, embedded inside two separate cambers supported by electrolyte solution to complete the circuit loop (**Figure 1.1**). The electrochemistry involved in water electrolysis is relatively simple. The following equation is the simplest description of the electrochemical splitting of water into H_2 and O_2 in neutral conditions.

$$H_2O \rightarrow H_2 + \frac{1}{2} O_2 \ (\Delta G \sim 237.4 \text{ kJ/mol}, 1.23 \text{ V vs NHE})$$

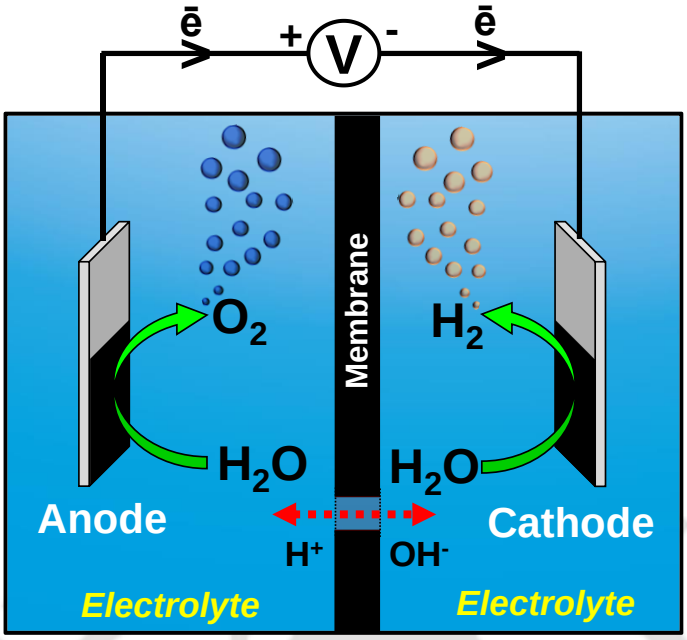

Figure 1.1. Schematic of an electrochemical cell. The water is reduced at the cathode to produce H_2, and oxidized at the anode to produce O_2 separating by a separator that allows electrolyte to pass through.

The accompanying energy losses are minimized by performing the water electrolysis either in highly acidic conditions or in highly alkaline conditions.[7,8] HER is highly efficient in acidic medium due to the availability of protons for immediate discharge and H_2 production. However, in acidic conditions, the efficient catalyst with minimum overpotential are the oxides/alloys of either Ir or Ru, which are of much high cost. For these reasons, electrocatalytic water splitting has mainly involved catalysts based on precious and scarce metals, such as Pt for HER and Ir and Ru for OER.[9,10]

Following are the proposed reactions that are to occur in acidic and alkaline electrolytes during electrochemical water splitting.[11,12]

In acidic:

$$2H_2O\ (l) \rightarrow 4H^+\ (aq.) + 4e^- + O_2\ (g)\ \text{(at anode)}$$

$$4e^- + 4H^+\ (aq.) \rightarrow 2H_2\ (g)\ \text{(at cathode)}$$

In alkaline:

$$4OH^-\ (aq.) \rightarrow 2H_2O\ (l) + 4e^- + 2O_2\ (g)\ \text{(at anode)}$$

$$4e^- + 4H_2O\ (l) \rightarrow 4OH^-\ (aq.) + 2H_2\ (g)\ \text{(at cathode)}$$

The reaction pathway followed by the HER suggests that the electrolyte medium to be acidic for the generation of H_2 by the electrocatalyst. The Tafel mechanism for HER is as follow (where **S** is the electro-active site),

$$H^+ (aq.) + S + e^- \rightarrow S–H \text{ (adsorption and discharge of proton)}$$
$$2S–H \rightarrow H_2 (g) + 2S \text{ (chemical desorption of } H_2)$$

Unlike HER, the reaction pathway for OER is the electrochemical oxide path stated as bellow.

In acidic:

$$S + H_2O \rightarrow S–OH + H^+ (aq.) + e^-$$
$$S–OH \rightarrow S–O + H^+ (aq.) + e^-$$
$$2S–O \rightarrow 2S + O_2 (g)$$

In alkaline:

$$S + OH^- (aq.) \rightarrow S–OH + e^-$$
$$S–OH + OH^- (aq.) \rightarrow S–O + H_2O + e^-$$
$$2S–O \rightarrow 2S + O_2 (g)$$

As mentioned, splitting of water is thermodynamically uphill process (ΔG = +237.4 kJ/mol = 1.23 V vs. NHE), thus an additional energy in the form of electricity is to be provided for the reaction to be spontaneous. In practical application, a potential much higher than 1.23 V is needed to initiate the electrolysis process and to acquire enough hydrogen gas, thus a huge amount of electrical energy is utilized. The prime objective of electrochemical water splitting is to design and fabricate a material which can minimize the energy need to initiate the reaction and upsurge the hydrogen production. Different strategies have been developed and utilized to supress the shortcomings of different materials and enhance the overall electrochemical performances.

1.3. Strategical Pathways to Enhance the Electrochemical Performances

The performance of an electrocatalyst towards water splitting depends on several parameters including both intrinsic and extrinsic properties of the material. Theoretically water splitting should commence at 1.23 V vs. RHE for oxygen production and 0 V vs. RHE for hydrogen production, but in practise the difference is much higher than 1.23 V. In general, water splitting occurs at the interface of solid catalyst, liquid electrolyte, and gaseous products.[13] For example, for an OER process in alkaline electrolyte occurring at solid-liquid-gas boundary region, the OH^- ions from the electrolyte adsorbs onto active sites while the

electrons get transferred from current collector to catalytic sites. After a series of surface reactions, like the bond cleavage/formation, oxygen molecules are produced which then desorbs off the surface into electrolyte. Thus, electrochemical process involves three vital steps: mass transport, charge transfer, and surface reaction.[13-15] An effective electrocatalyst therefore must have advanced active site concentration, intrinsic reactivity, charge transfer facility, mass transport capacity, and physical and chemical stability. In this regard several approaches have been recognized to encourage electrochemical performance, including morphological tuning, defect engineering, crystallography tailoring, construction of heterointerface, catalyst surface modification, and regulation of catalyst/electrolyte interface (**Figure 1.2**).[13, 16-20]

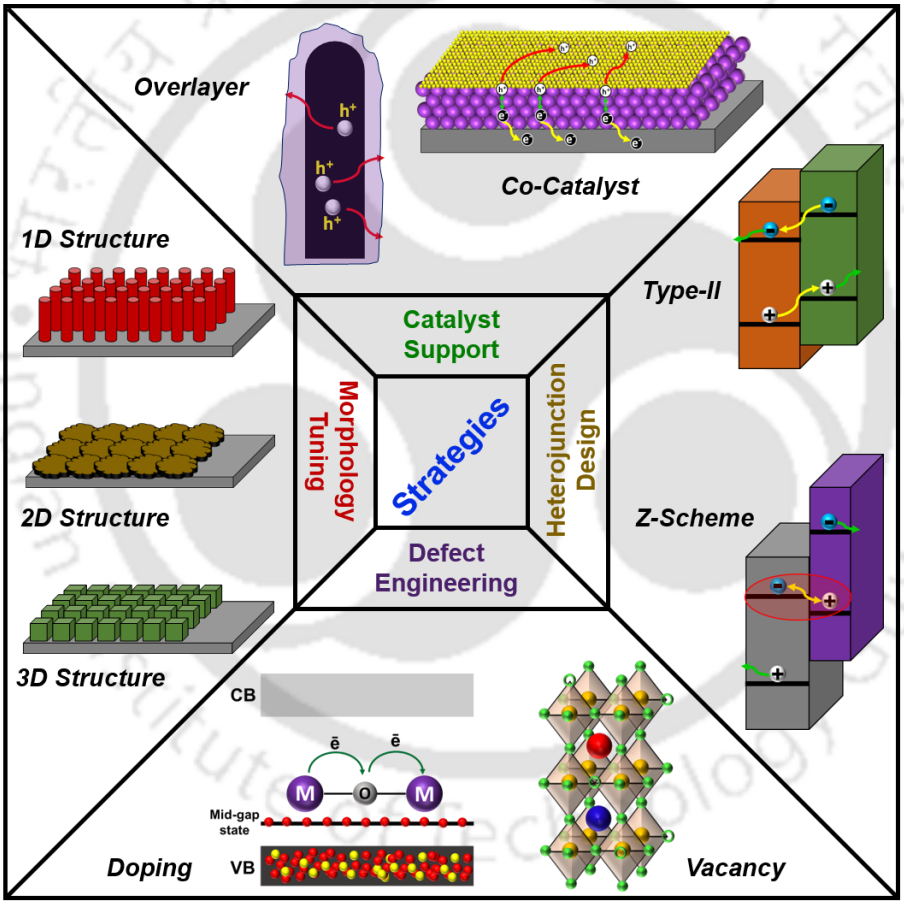

Figure 1.2. Schematic illustration of several active approaches for high-performing HER/OER electrocatalysts

1.3.1. Catalyst Support

OER and HER involves multi-step electron transfer processes for the electrolysis of water molecules, thus the complete utilization of the charged species at the electrode surface is quite tough. Oxygen evolution catalysts (OEC) and/or hydrogen evolution catalysts (HEC) are known to facilitate the electrocatalytic reactions at the electrode surface by accommodating the

charged species and undergoing redox reactions.[21-25] These catalysts when supported over the semiconductor catalyst, plays a crucial role by improving both the reliability and activity of electrochemical water-splitting. (i) HEC/OEC could lower the activation energy and/or overpotential for HER and OER on the surface of semiconductors, (ii) enhanced charge separation at the electrode/electrolyte interface, (iii) undergoes redox reactions thereby fastening the utilization of the charged species.[26,27] The O_2 and H_2 evolution in an OEC/HEC modified catalyst is affected by many reasons, such as the loading amount, structure, and particle size. Too much loading of catalysts on the surface of the semiconductor leads to the overcrowding of the particles thereby obstructing the transfer of charged species to the water molecules.[23-25] First-row transition metal hydroxides, phosphides, phosphates, borates, etc., are used as overlayers to overcome the sluggish reaction kinetics to accomplish a higher efficiency and decent reaction rates.[28-33] Amid several metal-based OECs, cobalt and nickel have known to be effective water oxidation catalysts and can operate under neutral and alkaline conditions. For instance, the electrocatalytic function of the well-known catalyst, cobalt phosphate, is accompanied with oxidation from Co(II) to Co(III) and Co(IV), leading to the creation of high-valence Co(IV)-O intermediates.[34,35] Similarly, nickel borate, another effective catalyst, undergoes redox cycle between +2, +3 and +4, thereby facilitating the overall reaction kinetics.[36-38] Thus, the mechanism of the overlayer catalysts lies in the redox capability of the constitute metal centre. The holes generated within the semiconductor are taken up by the overlayer catalyst where the metal centre gets oxidized. This oxidized species then interacts with water molecule at the electrolyte interface and easily releases the hole, oxidizing the water molecule and itself gets reduced to its native form to accept more generated holes from the semiconductor.

1.3.2. Heterojunction Design

Heterogeneous catalysts are known for their advanced water splitting performance of which the heterojunction catalysts occupy a very significant position.[39] In heterojunction catalysts, the active sites get modified due to the rearrangement of electrons on heterostructure interfaces, and the interaction of different active sites promotes the reaction kinetics, thus shows better water electrolysis activity than single component electrocatalysts.[40,41] The merits of heterojunction are as follows. Primarily, the lattice strain in heterojunction interface exposes higher active sites. Secondly, diversity in morphological design providing the scope for the improvement of the specific surface area and catalytical active sites.[42] Thirdly, the synergistic

effect promotes the efficiency in chemical reaction due to the charge transfer between the components in heterojunction catalysts.[43,44]

Non-noble metal heterojunction catalysts have gained more attention for electrolytic water performance due to their abundance and cost-effectiveness.[39,45] Transition metals (Ti, Ni, Fe, Mo, Co, W, etc.) have unfilled d-orbital and/or unpaired electrons in d-orbitals, making it favourable to adsorption/desorption of reactive groups.[46,47] The unfilled d-orbitals act as the Lewis acid sites making it reactive towards the incoming hydroxyl ions, while the unpaired electrons in d-orbitals act as Lewis base sites which are reactive towards the incoming protons.[46-48] The specific cooperativity of the heterojunction leads to higher electrical/ionic conductivity, catalytical activity and stability compared to the corresponding single-component transition metal/oxide.[48-50] For example, CoMo-hybrid precursor was obtained in one-pot solvothermal method using Co and Mo mixed precursor which upon further calcination resulted a hollow $Co_3O_4/CoMoO_4$ heterojunction thereby adding contact area between the electrode and electrolyte (**Figure 1.3b**).[49] Similarly, Zhu et al. synthesized Fe-V NPs covered with ultrathin NiO NSs on NF where the Fe and V ions gets substituted into NiO lattice, thereby producing more active ingredients getting exposed in electrochemical OER (**Figure 1.3a**).[51]

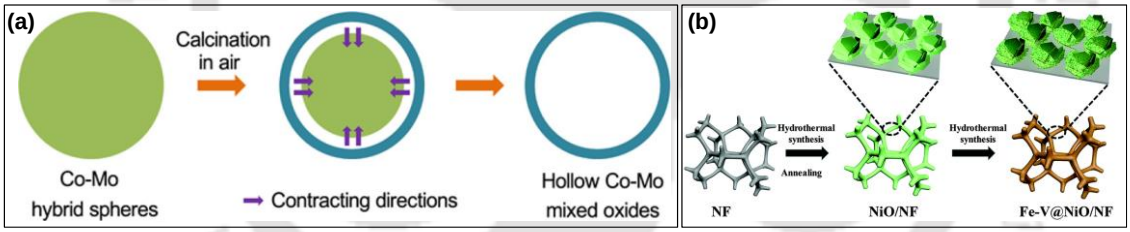

Figure 1.3. Schematics of the formation of the heterojunction structures for efficient OER (*Ref. 49 & 51*)

1.3.3. Defect Engineering

Defects in an electrocatalyst is an significant surface property, which affects the catalytic activity, thus altering the adsorption/desorption and charge distribution behaviours.[20,52] Defects can be considered as inhomogeneous composition in a material including vacancies, dopants, etc.[53] Metal ions doping (e.g., Fe, Sr, Cu, Mn, etc.) has been proven as an effective means for tailoring surface features.[20,54,55] Heteroatom doping favours the electron transfer in the catalyst, regulates adsorption/desorption behaviour and creates enormous active sites thereby enhancing the electrocatalytic performance.[56,57] For example, a recent work verified that the doping of Sr onto perovskite oxide led to oxygen over-stoichiometry enhancing the electrical conductivity and electrochemical performance.[58] Similarly, doping of Sr divalent ions into the crystal lattice of

$Pr_{1-x}Sr_xFeO_{3-\delta}$ perovskites increased the overall electrocatalytic activity due to the increased oxygen vacancy (δ) concentration, leading to enhanced availability of catalyst sites, and increased average oxidation state of Fe cations.[59] Another example where Mn atom doped onto cobalt carbonate hydroxide led to dual effect of electronic and morphological modulation.[60]

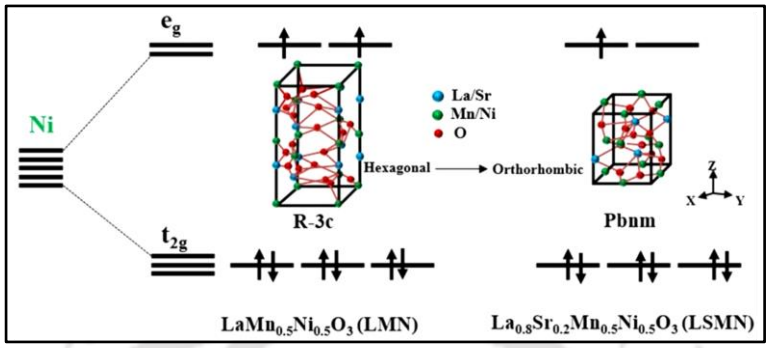

Figure 1.4. Schematic of the effect of Sr doping onto A-site of perovskite oxide (*Ref. 60*)

1.3.4. Morphology Tuning

Surface morphology engineering is observed as an effective method to manipulate surface features where the electrocatalytic materials are developed with 1D, 2D and 3D nanostructures (**Figure 1.5**) to enhance the exposed active sites and improve the mass transfer processes.[20,61,62] One-dimensional (1D) nanostructures enhances the electron transport by providing direct transfer pathway. The electrolyte can also infiltrate due to large specific surface area forming abundant accessible active sites, thereby enhancing the catalytic activity. Generally, the 1D nanostructures involve nanobelts, nanowires, nanofibers, nanorods, nanotubes, and so forth.[63-66] Unlike 1D materials, two-dimensional (2D) nanostructured materials possess high theoretical specific surface area thus providing scope to modify surface properties. The lateral size and thickness of 2D nanostructures play a crucial role in the alteration of chemical, physical, and electronic properties. Most probable 2D structures are the nanoplates and nanosheets which additionally provides better contact between the electrolyte and electrode.[67-69]

In case of three-dimensional (3D) nanostructures, significantly enhanced surface area and large active sites are attained for advanced electrochemical applications.[70-72] 3D nanostructures have the advantage of morphological versatility based on their synthesis methods and also have control of the facets-oriented crystallization.[73-75]

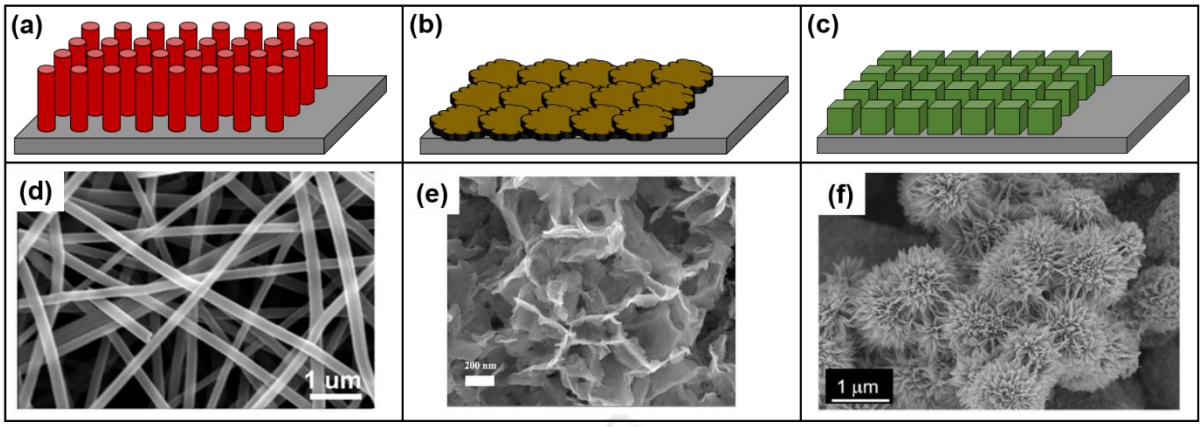

Figure 1.5. Schematics of (a) 1D, (b) 2D, (c) 3D morphological features, and the corresponding FESEM images (*Ref. 66, 68 & 72*)

1.4. Bipolar Membrane for Water Dissociation Process

The splitting of water into hydrogen and oxygen is quite advanced but yet challenged for commercialization where hydrogen and oxygen gasses needs to be separately collected. For this, the cathode and the anode are separated out using an ion-exchange membrane (IEM) to avoid mixing of the evolved gasses.[76,77] But the incorporation of IEM into the system adds to the solution resistance thereby restricting the efficiency of the electrocatalyst. In this regard bipolar membranes (BPM) have gained much attention due to its property of undergoing disproportionation reaction to dissociate H_2O molecules into H^+ and OH^- ions which are then efficiently converted respectively into H_2 and O_2 at the cathode and anode surfaces.[78-80]

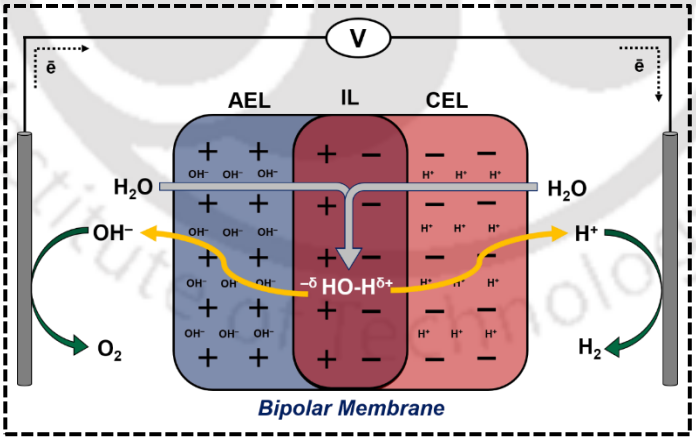

Figure 1.6. Schematic representation for the dissociation of water into H^+ and OH^- ions at the junctions of a bipolar membrane under reverse bias

Known HER related systems are most active in acidic conditions while OER activity is reported to be high in alkaline conditions, thus BPMs provides the opportunity in which the anode and cathode electrocatalyst to work at different pH.[81,82] Thus, the use of BPM in water electrolysis has shown promising results by (1) allowing operation of redox reactions

simultaneously under different pH conditions and (2) maintaining a pH gradient across the membrane, thereby reducing the total overpotential of the system. BPMs are generally polymeric membranes comprising of two layers, an anion-exchange layer (AEL) with positive charges, and a cation-exchange layer (CEL) with negative charges. The interface between AEL and CEL is denoted as the bipolar junction or "interfacial layer" (IL). At the IL, disproportionation reaction occurs where water is electro-dissociated into protons and hydroxyl ions without any gas formation (**Figure 1.6**). Upon application of current across a BPM, the ions in the bulk solution cannot sustain the ionic current through the membrane as either ions are unable to pass both the layers of a BPM. Hence, the generated H^+ and OH^- ions at the membrane interface carriers the ionic current.[80] With respect to the electrodes, the alignment of BPM is critical to ensure the flux of H^+ and OH^- ions along the electric field, thus the CEL should be towards the cathode while the AEL towards anode (reverse bias condition). Thereby, the generated ions exit the membrane through respective layers (i.e., OH^- through AEL, and H^+ through CEL), producing a base and an acid on opposite sides and generating a pH gradient over the BPM.[80,83]

1.4.1 Mechanism Involved in Water Dissociation

A BPM is an analogy with p-n junction under reverse bias condition as in the later holes and electrons are pulled away from the p-n junction creating a depletion layer leading to current ceasing.[84,85] The junction formed at the BPM interfacial layer (IL) contains a built-in potential due to the formation of depletion region when the BPMs are immersed into liquid electrolytes.[80,82] The potential across the BPM depend on the pH difference across it and given by the Nernst equation as follows,

$$\Delta V_{BPM} = 2.3\frac{RT}{F}(pH_{Anolyte} - pH_{Catholyte})$$

Thus, under extreme pH difference (ΔpH = 14) across BPM, the membrane potential reaches to ~ 0.83 V, representing the minimum potential for the initiation of water dissociation reaction.[80,86] Under reverse bias condition, a space charge region at the IL is generated resulting initially in high resistance (determined by a limiting current), thereby a region where current quickly increases with the voltage (**Figure 1.7**).[87,88] The rapid increase in the current is due to the generation of H^+ and OH^- ions at the junction depending upon the electric field at the bipolar junction.[80,89]

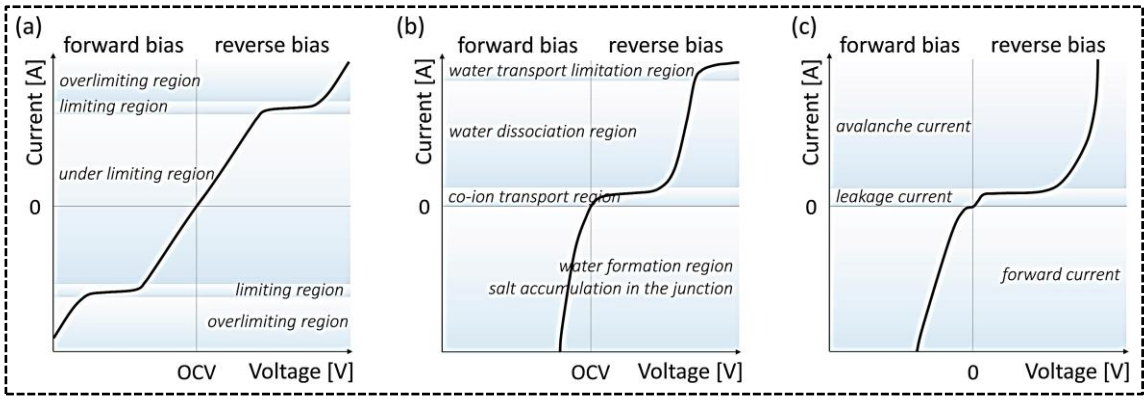

Figure 1.7. Qualitative I–V curves comparison for (a) an ion-exchange membrane, (b) bipolar membrane, and (c) p-n junction diode (*Ref. 80*)

The second Wien effect is one of the mechanisms of water dissociation describing the effect of strong electric fields on weak electrolytes.[90,91] There is increase in the dissociation degree and ion mobility of electrolytes at high electric fields. On application of this phenomenon to BPMs, a sharply limited bipolar junction is formed with thin space charge region where water dissociation takes place. The second Wien effect presumes the applied electric field to be the only cause of dissociation of water however other effects may appear with strong electric fields.[92] The protonation–deprotonation mechanism states the possibility of proton-transfer reactions between water and fixed charged groups of the involved water dissociation catalyst generating H^+ and OH^- ions.[93,94] Unlike second Wien effect theory, the protonation-deprotonation mechanism considers the dissociation of water to be dependent on catalytic activity of the fixed groups supporting the larger water dissociation after incorporation of a catalyst at the bipolar junction.[95-97] In case of a weak base (B), the protonation-deprotonation reaction can be written as;

$$B + H_2O \xrightarrow{k_1} BH^+ + OH^-$$

$$BH^+ + H_2O \xrightarrow{k_2} B + H_3O^+$$

where BH^+ is the catalytic centre (i.e., fixed charged groups of membrane), k_1, k_2 the forward rate constants.

In case of weak acid (AH), the reactions at the bipolar junction can be written as;

$$AH + H_2O \xrightarrow{k_1} A^- + H_3O^+$$

$$A^- + H_2O \xrightarrow{k_2} AH + OH^-$$

where A^- is the catalytic centre in the membrane.

The reactions can be summarized as;

$$2H_2O \xrightarrow{k_1} H_3O^+ + OH^-$$

Strathmann et al. established a model by merging the protonation-deprotonation theory and second Wien effect.[98] At low electric field, only salt ions are diffused through the BPM and with increasing electric field, the salt ion fluxing out the junction becomes larger than the flux into the junction resulting in depletions of ions. Thus, a limiting current is reached with increased resistance at the depleted junction, and to withstand the current dissociation of water takes place, generating H^+ and OH^- ions. A diffusive flux of water from the outer solution replaces the dissociated water in the junction. Overall, the protonation-deprotonation enhances the water dissociation while the electric field, as in the second Wien effect, accelerates the process.

1.4.2. Components of Bipolar Membrane

The key components of BPMs are the basis medium, functional groups, and a supporting matrix. The basis medium is generally a polymer matrix which provides the mechanical strength and carries the polyelectrolyte groups.[80] Aromatic monomer in basis matrix acts as a potential functionalization site for BPM performance and quality control.[99] Supporting matrix adds to the mechanical strength of a membrane.

a) Cation-Exchange Layer (CEL):

Cation-exchange layer generally contains anionic groups like sulphonic acid, phosphonic acid, or carboxyl groups. Some examples of crosslinked polymers with sulfonic acid groups are polyvinyl chloride, polysulphone, poly ether ketone, modified chitosan, etc.[100,101] Sulphonation can be done using sulphur trioxide, chlorosulphonic acid, oleum, sulfuric acid, or their mixtures.[102]

b) Anion-Exchange Layer (AEL):

Anion-exchange materials generally are positively charged with quaternary ammonium groups on polymer matrix. Other anionic groups include tertiary and secondary amines, and different di-amines.[80,103,104] Although various types of AELs have been prepared but yet the chemical stability in harsh alkaline conditions has remained an issue to date.

c) Water Dissociation Catalyst (EDC)

The protonation-deprotonation mechanism proposes that the dissociation of water in electrochemical systems which is influenced by ionic groups of ion-exchange membranes.[98] The dissociation constant (K_a) of the fixed groups determines the electric

potential difference of the BPMs with different ionic groups.[105] In this regard, weak ionic groups like phosphonic, phenolic, or carboxylic acid groups in CEL, and imidazole groups, primary to tertiary amino groups, or tertiary ammonium groups in AEL are recognized for their catalytic activity.[106] Additional catalysts (both inorganic and organic) are introduced into the bipolar junction to further accelerate the water dissociation reaction.[107-109] In case of organic catalysts, polymers and dendrimers occupy the largest share.[109-111] In case of inorganic catalysts oxides/hydroxides complexes and other compounds of metals are mostly used.[112-114] The catalytic activity for water dissociation reaction of ionic groups has been expanded with transition metal oxides/hydroxides.[80,115] Metal–organic frameworks (MOFs) are another class of compounds consisting of both organic ligands linked with inorganic metal ion centres thus having dual benefit towards the protonation-deprotonation reaction.[116-117]

1.4.3. Membrane Structure

Bipolar membranes are categorised into homogeneous and heterogeneous membranes of which homogeneous BPM layers are more preferable because of their evenly distribution of ionic groups. The BPM structure (i.e., the IL between the AEL and CEL) mainly depends on the method of membrane fabrication (**Figure 1.8**). A homogeneous BPM has a characteristic smooth interface.[80] Mechanically processing the interface forms a corrugated interface to enhance the adhesion of monopolar layers thus enhancing the overall water dissociation rate.[118,119] Heterogeneous interfaces are mainly obtained by hot pressing, where both anion- and cation-exchanger are present at the bipolar junction.[120,121] Heterogenous interface can also be obtained by electrospinning method.[122]

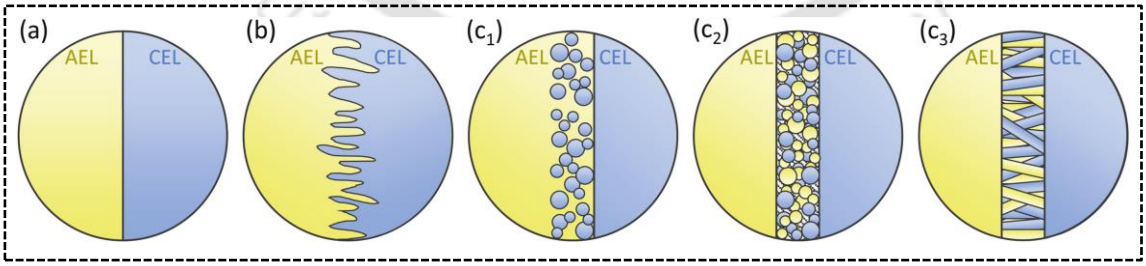

Figure 1.8. Schematic representation of the possible structures of the bipolar junction: (a) smooth, (b) corrugated, (c_1–c_3) heterogeneous (*Ref. 80*)

1.5. Motivation and Objectives of The Present Work

The electrolysis of water generating hydrogen and oxygen has been into research since long time but yet challenged for commercialization due to overall low efficiency. The cost and

stability are the prime factors along with high catalytic performance to be an effective electrocatalyst. In this regard, 3d transition metal oxides are the best candidates owing to its high stability, multi-valent states, ease of synthesis, tunable morphology, environmentally safe and economically abundant. Till date, several metal oxides based electrocatalysts have been reported for generation of oxygen and hydrogen but yet challenge remains to breach the thermodynamic barrier more efficiently thereby making the overall efficiency to unity. This led to search for better suited electrocatalytic material to enhance the overall water splitting efficiency. Thus, the prime objectives of the present thesis work are as follows:

(1) Selection of transition metal-based oxides for their high stability and bulk conductivity to be used as electrocatalytic material
(2) Doping foreign elements into the lattice of semiconductor to increase the bulk conductivity and electroactivity
(3) Incorporation of electroactive materials with the semiconductors to enhance the reaction kinetics at the electrolyte interface
(4) Introduction of desired morphological features to the metal oxides to increase the overall surface area and electroactive sites
(5) Design of combinational metal oxides to add up their abilities and suppress their individual shortcomings
(6) Construction of heterojunction semiconductor to ease the charge accumulation and separation boosting the overall electrocatalytic performance
(7) Design and fabrication of electrodes to demonstrate the practicality of the synthesized electrocatalysts
(8) Strategize the synthesis of conducting membrane in between the cathodic and anodic chambers to boost the overall water splitting performance of the system

1.6. References

[1] S. Yun, Y. Qin, A. R. Uhl, N. Vlachopoulos, M. Yin, D. Li, X. Han and A. Hagfeldt, *Energy Environ. Sci.*, 2018, **11**, 476.

[2] D. J. C. MacKay, *Phil. Trans. R. Soc. A.* 2013, **371**, 20110431.

[3] S. S. Lam, V. Nguyen, M. T. N. Dinh, D. Q. Khieu, D. D. La, H. T. Nguyen, D. V. N. Vo, R. S. Varma, M. Shokouhimehr, C. C. Nguyen, Q. V. Le and W. Peng. *J. Mater. Chem. A*, 2020, **8**, 10571.

[4] P. Nikolaidis and A. Poullikkas, *Renew. Sustain. Energy Rev.*, 2017, **67**, 597.

[5] S. E. Hosseini and M. A. Wahid, *Renew. Sustain. Energy Rev.*, 2016, **57**, 850.

[6] Y. Yan, B. Y. Xia, B. Zhao and X. Wang, *J. Mater. Chem. A*, 2016, **4**, 17587.

[7] S. Anantharaj, S. R. Ede, K. Sakthikumar, K. Karthick, S. Mishra and S. Kundu, *ACS Catal.*, 2016, **6**, 8069.

[8] J. Wang, W. Cui, Q. Liu, Z. Xing, A. M. Asiri and X. Sun, *Adv. Mater.*, 2016, **28**, 215.

[9] A. T. Marshall and R. G. Haverkamp, *Electrochim. Acta*, 2010, **55**, 1978.

[10] Y. Lee, J. K. Suntivich, J. May, E. E. Perry and Y. Shao-Horn, *J. Phys. Chem. Lett.*, 2012, **3**, 399.

[11] X. Zhou, H. Dong and A.-M. Ren, *Int. J. Hydrogen Energy*, 2016, **41**, 5670.

[12] J. O. Bockris and T. Otagawa, *J. Phys. Chem.*, 1983, **87**, 2960.

[13] C. Tang, H. F. Wang and Q. Zhang, *Acc. Chem. Res.*, 2018, **51**, 881.

[14] I. Roger, M. A. Shipman and M. D. Symes, *Nat. Rev. Chem.*, 2017, **1**, 0003.

[15] T. E. Mallouk, *Nat. Chem.*, 2013, **5**, 362.

[16] W.-J. Jiang, T. Tang, Y. Zhang and J.-S. Hu, *Acc. Chem. Res.*, 2020, **53**, 1111.

[17] T. Ling, D. Y. Yan, Y. Jiao, H. Wang, Y. Zheng, X. Zheng, J. Mao, X. W. Du, Z. Hu, M. Jaroniec and S. Z. Qiao, *Nat. Commun.*, 2016, **7**, 12876.

[18] J. Song, C. Wei, Z.-F. Huang, C. Liu, L. Zeng, X. Wang and Z. J. Xu, *Chem. Soc. Rev.*, 2020, **49**, 2196.

[19] L. Gao, X. Cui, C. D. Sewell, J. Li and Z. Lin, *Chem. Soc. Rev.*, 2021, **50**, 8428.

[20] P. C. Wang and B. G. Wang, *ACS Appl. Mater. Inter.*, 2021, **13**, 59593.

[21] L. Yu, H. Zhou, J. Sun, F. Qin, F. Yu, J. Bao, Y. Yu, S. Chen and Z. Ren, *Energy Environ. Sci.*, 2017, **10**, 1820.

[22] G. Ai, H. Li, S. Liu, R. Mo and J. Zhong, *Adv. Funct. Mater.*, 2015, **25**, 5706.

[23] J. Ran, J. Zhang, J. Yu, M. Jaroniec and S. Z. Qiao, *Chem. Soc. Rev.*, 2014, **43**, 7787.

[24] D. Li, J. Shi and C. Li, *Small*, 2018, **14**, 1704179.

[25] P. Munnik, P. E. Jongh and K. P. Jong, *Chem. Rev.*, 2015, **115**, 6687.

[26] J. Yang, D. Wang, H. Han and C. Li, *Acc. Chem. Res.*, 2013, **46**, 1900.

[27] L. Badia-Bou, E. Mas-Marza, P. Rodenas, E. M. Barea, F. Fabregat-Santiago, S. Gimenez, E. Peris and J. Bisquert, *J. Phys. Chem., C*, 2013, **117**, 3826.

[28] X. Ji, L. Cui, D. Liu, S. Hao, J. Liu, F. Qu, Y. Ma, G. Du, A. M. Asirif and X. Sun, *Chem. Commun.*, 2017, **53**, 3070.

[29] R. Ge, H. Du, K. Tao, Q. Zhang and L. Chen, *ACS Appl. Mater. Interfaces*, 2017, **9**, 15383.

[30] C. Z. Yuan, Y. F. Jiang, Z. Wang, X. Xie, Z. K. Yang, A. B. Yousaf and A. W. Xu, *J. Mater. Chem. A*, 2016, **4**, 8155.

[31] M. Pramanik, C. Li, M. Imura, V. Malgras, Y. M. Kang and Y. Yamauchi, *Small*, 2016, **12**, 1709.

[32] L. Yu, H. Zhou, J. Sun, F. Qin, F. Yu, J. Bao, Y. Yu, S. Chen and Z. Ren, *Energy Environ. Sci.*, 2017, **10**, 1820.

[33] D. Li, J. Shi and C. Li, *Small*, 2018, **14**, 1704179.

[34] D. A. Lutterman, Y. Surendranath, D. G. Nocera, *J. Am. Chem. Soc.*, 2009, **131**, 3838.

[35] Y. Surendranath, M. W. Kanan, D. G. Nocera, *J. Am. Chem. Soc.*, 2010, **132**, 16501.

[36] H. Zhang, W. Tian, Y. Li, H. Sun, M. O. Tadé and S. Wang, *J. Mater. Chem. A*, 2018, **6**, 24149.

[37] L. J. Enman, M. S. Burke, A. S. Batchellor and S. W. Boettcher, *ACS Catal.*, 2016, **6**, 2416.

[38] S. Anantharaj, S. R. Ede, K. Karthick, S. S. Sankar, K. Sangeetha, P. E. Karthik and S. Kundu, *Energy Environ. Sci.*, 2018, **11**, 744.

[39] Z. Li, M. Hu, P. Wang, J. Liu, J. Yao and C. Li, *Coord. Chem. Rev.*, 2021, **439**, 213953.

[40] A. Li, X. Chang, Z. Huang, C. Li, Y. Wei, L. Zhang, T. Wang and J. Gong, *Angew. Chem., Int. Ed.*, 2016, **55**, 13734.

[41] A. Wu, Y. Xie, H. Ma, C. Tian, Y. Gu, H. Yan, X. Zhang, G. Yang and H. Fu, *Nano Energy*, 2018, **44**, 353.

[42] D. Kim, Z. Zhang and K. Yong, *Nanoscale*, 2018, **10**, 20256.

[43] I. Ledezma-Yanez, W. D. Z. Wallace, P. Sebastián-Pascual, V. Climent, J. M. Feliu and M. T. M. Koper, *Nat. Energy*, 2017, **2**, 17031.

[44] S. Park, Y. Shao, J. Liu and Y. Wang, *Energy Environ. Sci.*, 2012, **5**, 9331.

[45] Y. Zheng, Y. Jiao, A. Vasileff and S.-Z. Qiao, *Angew. Chem., Int. Ed.*, 2018, **57**(26), 7568.

[46] Z. Wu, B. Fang, Z. Wang, C. Wang, Z. Liu, F. Liu, W. Wang, A. Alfantazi, D. Wang and D. P. Wilkinson, *ACS Catal.*, 2013, **3**, 2101.

[47] W. J. Zhou, X.-J. Wu, X. Cao, X. Huang, C. Tan, J. Tian, H. Liu, J. Wang and H. Zhang, *Energy Environ. Sci.*, 2013, **6**, 2921.

[48] L. Yang, W. Chen, R. Yang, A. Chen, H. Zhang, Y. Sun, Y. Jia, X. Li, Z. Tang and X. Gui, *ACS Appl. Mater. Interfaces*, 2020, **12**, 10755.

[49] Y. Yang, S. Wang, C. Jiang, Q. Lu, Z. Tang and X. Wang, *Chem. Mater.*, 2016, **28**, 2417.

[50] H. Lin, Z. Shi, S. He, X. Yu, S. Wang, Q. Gao and Y. Tang, *Chem. Sci.*, 2016, **7**, 3399.

[51] Y. X. Zhu, M. Y. Jiang, M. Liu, L. K. Wu, G. Y. Hou and Y. P. Tang, *Nanoscale*, 2020, **12**, 3803.

[52] Y. Zhu, X. Liu, S. Jin, H. Chen, W. Lee, M. Liu and Y. Chen, *J. Mater. Chem. A*, 2019, **7**, 5875.

[53] Y. Wang, P. Han, X. Lv, L. Zhang and G. Zheng, *Joule*, 2018, **2**, 2551.

[54] Z. Y. Cai, X. M. Bu, P. Wang, J. C. Ho, J. H. Yang and X. Y. Wang, *J. Mater. Chem. A*, 2019, **7**, 5069.

[55] L. Zhang, Q. Fan, K. Li, S. Zhang and X. Ma, *Sustainable Energy Fuels*, 2020, **4**, 5417.

[56] Y. Jiao, Y. Zheng, K. Davey and S.-Z. Qiao, *Nat. Energy*, 2016, **1**, 16130.

[57] X. W. Wang, G. Z. Sun, P. Routh, D. H. Kim, W. Huang and P. Chen, *Chem. Soc. Rev.*, 2014, **43**, 7067.

[58] M. M. Li, J. G. Cheng, Y. Gan, S. S. Li, B. B. He and W. Z. Sun, *J. Power Sources*, 2015, **275**, 151.

[59] S. Ward, M. A. Isaacs, G. Gupta, M. Mamlouk and S. S. Pramana, *Sustain. Energy Fuels*, 2021, **5**, 154.

[60] T. Tang, W.-J. Jiang, S. Niu, N. Liu, H. Luo, Y.-Y. Chen, S.-F. Jin, F. Gao, L.-J. Wan and J.-S. Hu, *J. Am. Chem. Soc.*, 2017, **139**, 8320.

[61] J. W. Xin Li, One-dimensional and two-dimensional synergized nanostructures for high-performing energy storage and conversion, *InfoMat*, 2020, **2**, 3.

[62] L. Shi, Y. Yin, S. Wang and H. Sun, *ACS Catal.*, 2020, **10**, 6870.

[63] Y. P. Zhu, T. Y. Ma, M. Jaroniec and S. Z. Qiao, *Angew. Chem.* 2017, **129**, 1344.

[64] J. Tian, N. Cheng, Q. Liu, X. Sun, Y. He and A. M. Asiri, *J. Mater. Chem. A*, 2015, **3**, 20056.

[65] E. Budiyanto, M. Yu, M. Chen, S. DeBeer, O. Rüdiger and H. Tüysüz, *ACS Appl. Energy Mater.*, 2020, **3**, 8583.

[66] P. Wei, X. P. Sun, Q. R. Liang, X. G. Li, Z. M. He, X. S. Hu, J. X. Zhang, M. H. Wang, Q. Li, H. Yang, J. T. Han and Y. H. Huang, *ACS Appl. Mater. Interfaces*, 2020, **12**, 31503.

[67] X. Yang, A.-Y. Lu, Y. Zhu, M. N. Hedhili, S. Min, K.-W. Huang, Y. Han and L.-J. Li, *Nano Energy*, 2015, **15**, 634.

[68] P. Wang, Z. Xu, Y. Lin, L. Wan and B. Wang, *ACS Sustainable Chem. Eng.*, 2020, **8**, 8949.

[69] F. L. Li, P. Wang, X. Huang, D. J. Young, H. F. Wang, P. Braunstein and J. P. Lang, *Angew. Chem.*, 2019, **131**, 7125.

[70] Y.-L. Ding, P. Kopold, K. Hahn, P. A. van Aken, J. Maier and Y. Yu, *Adv. Funct. Mater.*, 2016, **26**, 1112.

[71] L. Liu, J. Wang, Y. Hou, J. Chen, H. K. Liu, J. Wang and Y. Wu, *Small*, 2016, **12**, 602.

[72] S. V. Devaguptapu, S. Hwang, S. Karakalos, S. Zhao, S. Gupta, D. Su, H. Xu and G. Wu, *ACS Appl. Mater. Interfaces*, 2017, **9**, 44567.

[73] K. Zhou and Y. Li, *Angew. Chem., Int. Ed.*, 2012, **51**, 602.

[74] L. Li, C. Sun, B. Shang, Q. Li, J. Lei, N. Li and F. Pan, *J. Mater. Chem. A*, 2019, **7**, 18003.

[75] H. Yang, S. Luo, X. Li, S. Li, J. Jin and J. Ma, *J. Mater. Chem. A*, 2016, **4**, 18499.

[76] M. S. Kang, Y. J. Choi, H. J. Lee and S. H. Moon, *J. Colloid Interface Sci.*, 2004, **273**, 523.

[77] J. Lee, J. Yun, S. -R. Kwon, W. J. Chang, K. T. Nam and T. D. Chung, *Sci. Rep.*, 2017, **7**, 12281.

[78] L. Chen, Q. Xu, S. Z. Oener, K. Fabrizio and S. W. Boettcher, *Nat. Commun.*, 2022, **13**, 1.

[79] R. A. Tufa, M. A. Blommaert, D. Chanda, Q. Li, D. A. Vermaas and D. Aili, *ACS Appl. Energy Mater.*, 2021, **4**, 7419.

[80] R. Pärnamäe, S. Mareev, V. Nikonenko, S. Melnikov, N. Sheldeshov, V. Zabolotskii, H. Hamelers and M. Tedesco, *J. Membr. Sci.*, 2021, **617**, 118538.

[81] S. Z. Oener, M. J. Foster and S. W. Boettcher, *Science*, 2020, **369**, 1099.

[82] Z. Yan, R. J. Wycisk, A. S. Metlay, L. Xiao, Y. Yoon, P. N. Pintauro and T. E.Mallouk, *ACS Cent. Sci.*, 2021, **7** (6), 1028.

[83] F. Alvarez, R. Alvarez, J. Coca, J. Sandeaux, R. Sandeaux and C. Gavach, *J. Membr. Sci.*, 1997, **123**, 61.

[84] I. C. Bassignana and H. Reiss, *J. Membr. Sci.*, 1983, **15**, 27.

[85] H. G. L. Coster, *Biophys. J.*, 1965, **5**, 669.

[86] R. A. Tufa, M. A. Blommaert, D. Chanda, Q. Li, D. A. Vermaas and D. Aili, *ACS Appl. Energy Mater.*, 2021, **4** (8), 7419.

[87] B. Lovrecek, A. Despic and J. O. M. Bockris, *J. Phys. Chem.*, 1959, **63**, 750.

[88] V. J. Frilette, *J. Phys. Chem.*, 1956, **60**, 435.

[89] P. Ramirez, H. Rapp, S. Mafe and B. Bauer, *J. Electroanal. Chem.*, 1994, **375**, 101.

[90] L. Onsager, *J. Chem. Phys.*, 1934, **2**, 599.

[91] H. C. Eckstrom and C. Schmeltzer, *Chem. Rev*., 1939, **24**, 367.

[92] H. Strathmann, H. J. Rapp, B. Bauer and C. M. Bell, *Desalination*, 1993, **90**(1–3), 303.

[93] V. Zabolotskii, N. Sheldeshov and S. Melnikov, *Desalination*, 2014, **342**, 183.

[94] V.I. Zabolotskii, N. V Shel, N.P. Gnusin, *Russ. Chem. Rev.*, 1988, **57**, 801.

[95] Z. Yan, L. Zhu, Y. C. Li, R. J. Wycisk, P. N. Pintauro, M. A. Hickner and T. E. Mallouk, *Energy Environ. Sci.*, 2018, **11**, 2235.

[96] M. B. McDonald and M. S. Freund, *ACS Appl. Mater. Interfaces*, 2014, **6**, 13790.

[97] M. S. Kang, Y. J. Choi, H. J. Lee and S. H. Moon, *J. Colloid Interface Sci.*, 2004, **273**, 523.

[98] H. Strathmann, J. Krol, H.-J. Rapp and G. Eigenberger, *J. Membr. Sci.*, 1997, **125**, 123.

[99] L. T. C. Lee, G. J. Deg and K. -J. Liu, *U.S. Patent US4057481A*, 1977.

[100] A. Wang, S. C. Peng, Y. H. Wu, C. H. Huang and T. W. Xu, *J. Membr. Sci.*, 2010, **365**, 269.

[101] A. M. Rajesh, M. Kumar and V. K. Shahi, *J. Membr. Sci.*, 2011, **372**, 249.

[102] C. Vogel and J. Meier-Haack, *Desalination*, 2014, **342**, 156.

[103] N. V. Shel'deshov, N. P. Gnusin, V. I. Zabolotskii, N. D. Pis'menskaya, *Sov. Electrochem.*, 1985, **21**, 137.

[104] T. Sata, M. Tsujimoto, T. Yamaguchi and K. Matsusaki, *J. Membr. Sci.*, 1996, **112**, 161.

[105] V. P. Greben, N. Ya. Pivovarov, G. V. Nefedova, *J. Phys. Chem.*, 1978, **52**, 2641.

[106] R. Simons, *Electrochim. Acta*, 1985, **30**, 275.

[107] J. Balster, S. Srinkantharajah, R. Sumbharaju, I. Pünt, R. G. H. Lammertink, D. F. Stamatialis and M. Wessling, *J. Membr. Sci.*, 2010, **365**, 389.

[108] R. Simons, *J. Membr. Sci.*, 1993, **78**, 13.

[109] R. Q. Fu, Y. H. Xue, T. W. Xu and W. H. Yang, *J. Colloid Interface Sci.*, 2005, **285**, 281.

[110] R. Fu, T. Xu, G. Wang, W. Yang and Z. Pan, *J. Colloid Interface Sci.*, 2003, **263**, 386.

[111] R. Q. Fu, T. W. Xu, Y. Y. Cheng, W. H. Yang and Z. X. Pan, *J. Membr. Sci.*, 2004, **240**, 141.

[112] L. Jialin, W. Yazhen, Y. Changying, L. Guangdou and S. Hong, *J. Membr. Sci.*, 1998, **147**, 247.

[113] J. -H. Choi, H. -J. Lee and S. -H. Moon, *J. Colloid Interface Sci.*, 2001, **238**, 188.

[114] Y. H. Xue, R. Q. Fu, Y. Xun Fu, T. W. Xu, *Journal of Colloid and Interface Science*, 2006, **298**, 313.

[115] S. S. Melnikov, O. V. Shapovalova, N. V. Sheldeshov and V. I. Zabolotskii, *Petrol. Chem.*, 2011, 51, 577.

[116] Q. Y. Wang, B. Wu, C. X. Jiang, Y. M. Wang and T. W. Xu, *J. Membr. Sci.*, 2017, **524**, 370.

[117] P. K. Giesbrecht and M. S. Freund, *Chem. Mater.*, 2020, **32** (19), 8060.

[118] M. A. Blommaert, D. Aili, R. A. Tufa, Q. Li, W. A. Smith and D. A. Vermaas, *ACS Energy Lett.*, 2021, **6** (7), 2539.

[119] F. Hanada, K. Hiraya, N. Ohmura and S. Tanaka, *EP0459820B1***,** 1991.

[120] K. Umemura, T. Nagamura and H. Miyake, *US Patent US5401408*, 1995.

[121] G. J. Dege, F. P. Chlanda, L. T. C. Lee and K. -J. Liu, *US Patent US4253900*, 1981.

[122] R. Fu, T. Xu, W. Yang and Z. Pan, *J. Appl. Polym. Sci.*, 2003, **90**, 572.

CHAPTER 2

Experimental Section

This chapter illustrates the synthetic protocols employed for various electrocatalyts and their supports. Also, the step-by-step fabrication procedure for the working electrode has been described here. Lastly, various instrumentation techniques utilized for the characterization of the synthesized catalysts and the performance parameters of electrochemical performances are discussed in detail.

2.1. Introduction

This chapter describes the synthetic procedures of different electrocatalysts and techniques for the fabrication of working electrodes for electrochemical water-splitting. It also describes basic instrumental techniques which were used in the characterization of the synthesized materials. The chemicals and materials which were used during the synthesis and fabrication of the working electrode are also listed in the current chapter. The performance parameters which were used to define the performance of the electrocatalysts are also explained in detail.

2.2. Reagents and Chemicals Used

All the chemicals purchased are used without any further purifications, else mentioned.

Lanthanum oxide, strontium carbonate, copper acetate, ruthenium dioxide, manganese nitrate, potassium permanganate, manganese chloride, manganese (IV) oxide, manganese sulphate, manganese sulphate, alginic acid, ammonium fluoride, xanthan gum, polyvinyl alcohol, ammonium carbonate, manganese acetate, urea, fluorine-doped tin oxide (FTO) coated glass substrate, polysulphone, vanadium pentoxide, tin (IV) chloride, trimethylchlorosilane, paraformaldehyde, molecular sieves (4Å), are bought from **Sigma-Aldrich**.

Cobalt nitrate hexahydrate, potassium phosphate dibasic, ethylene glycol, nickel nitrate hexahydrate, boric acid, potassium hydroxide, hydrochloric acid, hydrogen peroxide, phosphoric acid, chloroform, potassium chromate, are bought from **Merck**. Dimethyl sulfoxide, dimethyl formamide, dimethyl acetamide, chlorosulphonic acid, are bought from **FINAR**. Sodium hydroxide, terpineol, ethyl cellulose, are bought from **Himedia**. Ethanol is bought from **TMEDA**. And for all the synthesis Milli-Q water (**18.2 MΩ cm^{-2}**) is used.

2.3. Characterization of the As-Synthesized Materials and Electrochemical Devices

Various analytical techniques were used to characterize the synthesized materials and fabricated electrochemical devices. Instrumental tools used in the present studies are listed below:

1) Powder X-ray diffraction (PXRD) analysis were done to determine, the crystalline structure and phase purity of all the materials using Rigaku Smartlab using Cu K_α (λ = 1.54 Å) as the source with 9kW power.

2) Micro-Raman spectroscopy analysis was done to determine different modes of vibration present in the sample, using a laser micro-Raman system (Horiba Jobin Vyon, LabRam HR) with 488 nm and 514 nm laser excitation
3) Perkin Elmer (Spectrum-II) instrument with KBr pellet was used to perform Fourier transformed infrared spectroscopic (FT-IR) studies.
4) Field emission scanning electron microscopic (FESEM) analysis was done to determine the surface morphology of as-synthesized materials using Zeiss (Gemini) and Zeiss (Sigma) instruments, operating at the voltages of 3 kV−10 kV.
5) Elemental mapping, morphology, *d*-spacing value, and selected area electron diffraction (SAED) patterns of the samples were determined through, Field emission transmission electron microscopy (FETEM) using JEOL (JEM-2100F) instrument with an operating voltage of 200 kV.
6) To determine the valance state, elemental composition, and change in the electronic environment around the elements, X-ray photoelectron spectroscopy (XPS) analysis were carried out using ESCALAB Xi+ (Made: Thermo Fisher Scientific Pvt. Ltd., UK) photoelectron spectrometer with a monochromatized Al-K_α ($h\nu$ = 1486.6 eV) source and Thermo Scientific (NEXA surface analysis with micro-focused, 72 W, 12 kV) with Al-K_α ($h\nu$ = 1486.6 eV) as X-ray source. C 1s spectrum (284.77 eV), as reference was used to compensate for the surface charging effect. XPSPEAK 4.1 software was used to fit and deconvolute the data.
7) The incorporation of the functional groups onto the material backbone was confirmed using nuclear magnetic resonance (NMR) spectroscopy recorded in 500MHz NMR spectrometer.
8) The contact angles were obtained to determine the surface condition of the synthesized materials. Kruss Drop Shape Analyser-DSA-25 instrument was used to measure the advancing and receding contact angles using deionized water droplet at four different locations for each sample.
9) Mechanical properties were analysed for the polymeric material (2 cm × 1 cm × 1 cm) that are synthesized using universal testing machine (Instron 5944, Norwood, MA, U.S.A.).
10) CHI1120B electrochemical workstation was used to record electrochemical analysis like linear sweep voltammetry (LSV), cyclic voltammetry (CV) and chronoamperometry.

11) Electrochemical work station from CH instruments model CHI760D, Inc., Austin, TX were used to perform electrochemical impedance spectroscopic (EIS) analyses of the devices.
12) Gamry Instrument model Interface1010 E was used to record all the electrochemical measurements including LSV, CV, chronoamperometry, electrochemical impedance spectroscopy (EIS), Mott-Schottky (MS), current-voltage curve (CVC), and chronopotentiometry plots.
13) The gas evolved (to calculate Faradaic yield) was measured by gas chromatography (GC) (Model-7820A, Agilent Technologies).

2.4. Steps Involved for the Fabrication of Working Electrode

The working electrodes were fabricated using the conventional Doctor-blade method (**Figure 2.1**) over conducting substrate by taking the as-synthesized powder materials (**chapters 3-6**). In **chapter 7**, the working electrodes used were platinum mesh. The steps involved for the fabrication of catalyst compound over conducting substrate are given below:

1) At first, the as-synthesized powder sample was weighed and ultra-sonicated in ethanol for 30 mins to break the particle agglomeration. Then, a homogenous paste was made using terpineol and ethyl cellulose in a mortar pestle.
2) For the casting of the paste, conductive glass substrate, i.e., FTO was utilized. The FTO substrate was cut into 2.5 cm x 1 cm dimensions, washed properly using soap solution, Milli-Q water, acetone and isopropanol, and then ozonized for 15mins. Active area of the electrode was fixed by masking with scotch tape.
3) A thin film of the as-prepared homogenous paste was casted over the masked FTO substrate using Doctor-blade technique and dried in oven at 100 °C for 1hour. After removing the scotch tape, the metal oxide films were calcined at 500 °C in a muffle furnace to remove the organic impurities.
4) Now, these electrocatalyst coated working electrodes were further modified by depositing other active catalysts via electrodeposition method (**chapter 3,5**) or drop-casting method (**chapter 6**) to fabricate the composite working electrode and then were subjected to measure their electrochemical performances.

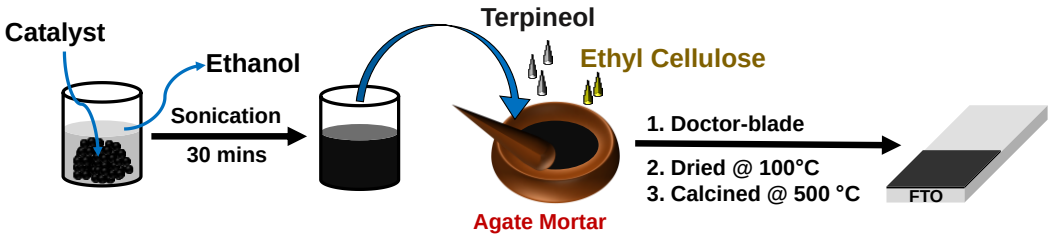

Figure 2.1: Schematic representation showing the fabrication procedure of the synthesized catalyst over the FTO substrate using Doctor-blade method

2.5. Electrochemical Measurements

Electrochemical measurements of the fabricated electrode were carried out utilizing electrochemical analysers (model-CHI1120B) (**chapters 3, 4 & 5**) and (model-Interface 1100E) (**chapters 6**) in a three-electrode system, using aqueous 1M NaOH as electrolyte (pH = 12.6) in a polypropylene electrochemical cell. The synthesized catalysts were fabricated on conducting substrate and used as the working electrode (**chapters 3-6**). For the reference electrode Ag/AgCl (saturated KCl) (**chapters 3 & 5**) and Hg/HgO (**chapters 4 & 6**) were used, while for counter electrode Pt wire (**chapters 3 & 5**) and graphite rod (**chapters 4 & 6**) were used. Prior to the electrochemical measurements, the electrolyte solution was purged using N_2 gas to remove any dissolved oxygen. **Figure 2.2** shows a schematic representation showing the experimental setup for electrochemical water-splitting.

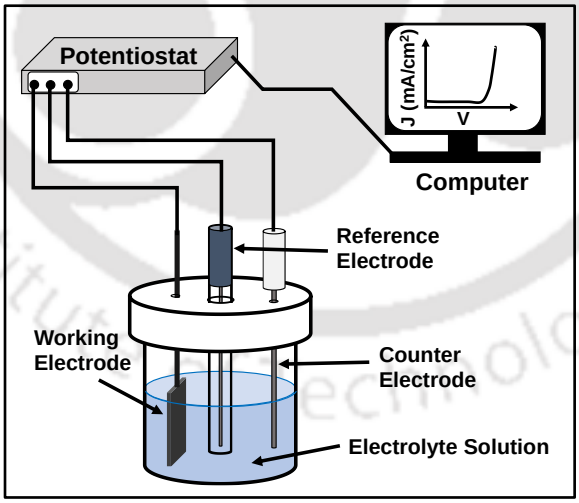

Figure 2.2: Schematic representation showing the experimental setup for electrochemical water-splitting where voltage is applied through potentiostat

All the applied potentials were converted to reversible hydrogen electrode (RHE) using the **equation 2.1** for measurements done by Ag/AgCl reference electrode and **equation 2.2** for measurements done by Hg/HgO reference electrode,

$$E_{RHE} = E_{Ag/AgCl} + 0.059pH + E^{0}_{Ag/AgCl} \quad \ldots (2.1)$$

Where, E_{RHE} is the RHE potential, $E^0_{Ag/AgCl}$ = 0.1976 V at 25 °C, $E_{Ag/AgCl}$ is the potential measured against the Ag/AgCl (saturated KCl) reference electrode, and pH is the pH of the electrolyte used.[1]

$$E_{RHE} = E_{Hg/HgO} + 0.059pH + E^0_{Hg/HgO} \quad \ldots (2.2)$$

Where, E_{RHE} is the RHE potential, $E^0_{Hg/HgO}$ = 0.098 V at 25 °C, $E_{Hg/HgO}$ is the potential measured against the Hg/HgO (saturated KCl) reference electrode, and pH is the pH of the electrolyte used.[2]

Linear sweep voltammetry of the catalysts was carried out in the range of 1.0 V to 1.8 V vs. RHE (**chapter 3**) and 1.0 V to 2.0 V vs. RHE at a scan rate of 10 mV/s (**chapter 5**), 1.3 V vs. 2.0 V vs. RHE at a scan rate of 5 mV/s (**chapter 4**), and 1.0 V to 2.0 V vs. RHE at a scan rate of 5 mV/s (**chapter 6**). To estimate the electrochemical active surface area (ECSA), double-layer capacitance (C_{dl}) was evaluated by measuring the cyclic voltammograms (CV) in the non-Faradaic region in the range of 0.30 V to 1.50 V vs. RHE (**chapter 3**), 0.65 V to 0.85 V vs. RHE (**chapter 5**), 0.90V to 1.10 V vs. RHE (**chapter 4**), and 0.70V to 0.90 V vs. RHE (**chapter 6**) at scan rates of 2-10 mV/s. The EIS measurements to obtain the Nyquist plots were performed in the frequency range of 0.1 Hz to 10^5 Hz at a fixed potential of 1.6 V vs. RHE (**chapters 3, 4 & 5**), 1.5 V & -0.3 V vs. RHE and open-circuit potential (OCP) (**chapter 6**). Mott-Schottky plots of the working electrodes were recorded at a fixed frequency of 1 kHz scanned from 0.3 - 1.0 V vs. RHE and -0.5 to 1.5 V vs. RHE (**chapter 6**).

The water dissociation capacity of the bipolar membrane was evaluated using galvanostatic mode (**Chapter 7**). The electrochemical measurements were performed in a 4-probe H-cell (as shown in **Figure 2.3**) with an active area of 1 cm^2 utilizing the Gamry Interface 1010E. Platinum mesh was used as the electrodes (cathode and anode), calomel electrodes ($Hg/HgCl_2$) as the reference electrode. The calomel electrodes were inserted in the Haber-Luggin capillaries for better detection of the developed potential between the membranes. The two chambers were separated by the fabricated BPM (1 cm x 1 cm) and 1M NaCl was used as the electrolyte solution in both anodic and cathodic chambers. Potentiodynamic analysis was performed to measure the voltage drop across the BPM with the increase in the applied current, while the chronopotentiometry was performed at the limiting current for BPM.

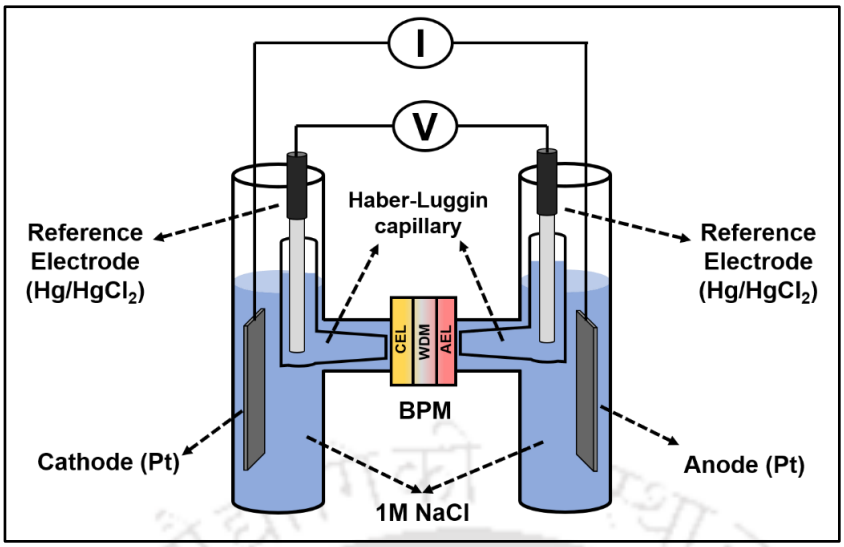

Figure 2.3: Schematic representation of the setup used during the electrochemical measurements

2.6. Electrochemical Performance Parameters

The effectiveness of a fabricated electrochemical devices was determined using the parameters as discussed in detail below:

2.6.1. Overpotential (η) at a defined current density

Overpotential of any electrochemical process can be defined as the additional potential required to sustainably drive an electrochemical reaction from its reversible potential. The reversible potentials for HER and OER are 0 and 1.23 V vs. standard hydrogen electrode (SHE), respectively. Hence, the equations

$$\eta_{OER} = E_{RHE} - 1.23\ V, \text{ and} \quad \ldots (2.3)$$

$$\eta_{HER} = E_{RHE} - 0\ V \quad \ldots (2.4)$$

was used for OER and HER, respectively, to calculate their overpotentials at a desired current density.[3,4]

The current density of 10 mA/cm^2 is accepted as the benchmark for evaluating the overpotential values (using **equations 2.3 & 2.4**) so as to compare and characterize various electrocatalytic materials for both HER and OER in all electrolytic medium.[3]

2.6.2. Tafel slope

Tafel analysis is one of the primary studies in the evaluation of activity of an electrocatalyst for water electrolysis. Tafel analysis of OER and HER processes is performed to gain information on the inherent kinetics of the electrocatalyst under study. The relationship

between current and overpotential at an electrical interface is given by the well-known Butler–Volmer equation, as follows; [3,5]

$$I = I_0 [\exp (\alpha_A \eta F / RT \times \eta) - \exp (-\alpha_C \eta F / RT \times \eta)] \quad \ldots (2.5)$$

In the above equation, I is the current, I_0 is the exchange current (current at equilibrium potential), α_A and α_C are the charge transfer coefficients for the anodic and cathodic reactions, respectively, n is the number of electrons transferred, F is the Faraday constant (96,485 C/mol), R is the ideal gas constant, T is the absolute temperature in K and η is the overpotential. In equilibrium conditions, the contributions of both the anodic and cathodic terms are equal where the observed current I is equal to I_0. Additionally, the high overpotential approximation of the above Butler–Volmer equation lead to the Tafel equations of the cathodic and anodic polarizations, respectively, as given below,[3,4]

$$\ln I = \ln I_0 + (-\alpha_C \eta F / RT) \eta \quad \ldots (2.6)$$

$$\ln I = \ln I_0 + (\alpha_A \eta F / RT) \eta \quad \ldots (2.7)$$

The **equations 2.6 & 2.7** have the form of y = b + mx and gave a linear line when log I was plotted vs. η, which is the well-known 'Tafel plot'. The slope of the linear line was given as follows for the cathodic and anodic polarizations, respectively,[3-5]

$$\text{Slope (d log j/d } \eta) \text{ for cathodic reaction} = (2.303RT / -\alpha_C \eta F) \quad \ldots (2.8)$$

$$\text{Slope (d log j/d } \eta) \text{ for anodic reaction} = (2.303RT / \alpha_A \eta F) \quad \ldots (2.9)$$

The Tafel slope was usually used to semi-quantitatively predict how much faster the reaction occurs on an electrocatalytic interface. The **equations 2.8 & 2.9** provided a clear view that the slope of the Tafel plot is inversely related to the charge transfer coefficient (α), which meant that the lower the Tafel slope, the faster the charge transfer across the electrocatalytic interface. In the electrocatalysis of water splitting, this was used as a fundamental activity parameter to relate the activities of various electrocatalysts, provided that the given experimental conditions are the same.

2.6.3. Electrochemically active surface area (ECSA)

ECSA is used to predict the activity trends when a set of similar catalytic materials is studied and to determine the reasons behind the differences in the activities of similar catalysts in the same study.[6] ECSA was calculated from the measurement of double-layer capacitance

(C_{dl}) value for the respective catalysts using cyclic voltammetry (CV) technique. ECSA is proportional to the C_{dl} value as follows,[4,6]

$$ECSA = C_{dl} / C_S \quad \ldots (2.10)$$

where, C_S is the specific capacitance of the material and C_{dl} value is obtained from the CV plots at non-Faradaic region. The value is equal to the half of the slope value obtained from the plot of the difference in current density between the anodic and cathodic sweeps ($J_{anodic} - J_{cathodic}$) at a particular potential as a function of the scan rate.

2.6.4. Turnover frequency (TOF)

The TOF provided information on the kinetics of HER and/or OER for the catalytic material. Hence, it was used in addition to Tafel analysis to obtain more insight into the kinetics of the gas evolution reaction with the given catalyst. As both HER and OER follow pseudo first order kinetics, their TOFs was given per unit time (s^{-1}). The **equation 2.11** was used to calculate the TOF of electrochemical reaction (**chapter 3**).[3,6]

$$TOF = \frac{J \times A}{n \times F \times N_S} \quad \ldots (2.11)$$

where J, A, n, F and N_S are, respectively, current density at a certain overpotential (A/cm^2), surface area of the working electrode (cm^2), number of electrons transferred to evolve a molecule of product (for H_2, it is 2 and for O_2, it is 4), Faraday constant (96458 C/mol), and concentration of active sites in the catalysts (mol/cm^2). N_S for oxygen evolution reaction (OER) was determined by CV measurements at different scan rates in the voltage range where redox reaction occurs. The peak current was plotted against scan rate where the slope had the linear relationship,[3,6]

$$Slope = n^2F^2AN_S/4RT \quad \ldots (2.12)$$

in which n, R, and T are, respectively, the number of electrons transferred, ideal gas constant and absolute temperature.

Turnover frequency value of an electrocatalyst was also calculated using the **equation 2.13** (**chapters 4, 5 & 6**);[7,8]

$$TOF = \frac{J \times A}{n \times m \times F} \quad \ldots (2.13)$$

where J is the current density at a given potential, A is the surface area of the electrode (1 cm^2 for the working electrode), n is the number of electrons transferred in the OER (n = 4) and/or

HER (n = 2), m is the number of moles of all metal ions available for the OER and/or HER, and F is Faraday's constant (96485 C mol^{-1}).

2.6.5. Faradaic efficiency (FE)

The faradaic efficiency reflected the selectivity of the catalyst under study for a particular electrochemical reaction. This provided information on how efficiently a catalytic system utilized the supplied electrical energy selectively for the desired electrochemical reaction. Selectivity is one of the three most desired criteria for an electrocatalyst; along with activity and stability, it forms the essential quality trio of an electrocatalyst.[3,6] Faradaic yield is the ratio of amount of experimentally evolved gasses (H_2 and O_2) to the theoretically calculated gasses (H_2 and O_2) as explained in the **equation 2.14**,[9]

$$\text{Faradaic Yield} = \frac{\text{Amount of experimentaly evolved gasses}}{\text{Amount of theoretically calculated gasses}} \quad \ldots (2.14)$$

The theoretical calculation for the amount of gas evolved was done by using **equation 2.15**,[9]

$$\text{Amount of gasses evolved} = \frac{J \times t}{n \times F} \quad \ldots (2.15)$$

Where J is current density in mA/cm^2, t is time in sec), n is no. of moles charge required to produced one mole of gas (n = 2 for H_2 and n = 4 for O_2), and F is the Faraday constant 96485 C/mol. The amount of gasses (experimental) that evolved during the water-splitting process was measured through an online gas chromatograph (GC).

2.6.6. Electrochemical impedance spectroscopy (EIS) analysis

Electrochemical impedance spectroscopy (EIS) is an important technique for understanding the kinetics of charge transfer at the semiconductor-electrolyte interface. It is an alternating current (AC) technique, where resistive and capacitive responses between semiconductor interfaces are distinguished based on the frequency dependence.[10] EIS experiments are composed of applying a small-amplitude sinusoidal signal to the electrodes at a certain fixed bias and measuring the response of the system to the perturbation. During the experiment, current density of the electrode is recorded while applying an alternating current signal with different frequencies (usually 0.1 Hz to 10^6 Hz) to the system.[11] By EIS characterization, Nyquist plot (real vs. imaginary impedance) can be obtained. Theoretically, a typical Nyquist plot can be divided into two parts: high-frequency (low impedance) and low-frequency (high impedance) region, as shown in **Figure 2.4 (a)**. In high frequency region, the electrochemical process is controlled by rate of charge transfer and the curve exhibits the shape

of a semicircle which hints at the existence of an interface. The characteristic semicircle arc arises from the parallel combination of a resistor and capacitor. In the low-frequency region, the process is determined by rate of mass transfer.[5] The shape of the curves could be affected by the intrinsic or electrochemical properties of electrodes, electrolytes, and the conditions of the experiments. **Figure 2.4 (b)** shows an equivalent circuit model, where frequency responses were fitted to determine parameters of the Nyquist plot. The parallel combination of charge transfer resistance (R_{ct}) and interfacial capacitance (C_{int}) describes the flow of Faradaic and non-Faradaic current through the interface, respectively. These two elements are represented in parallel to reflect the fact that total current is the sum of Faradaic and non-Faradaic pathways. The R_s term is included in series to account for any and all resistances associated with solution resistance, wires, clips, or other contacts. The simple Randles circuit can be extended to include multiple parallel R||C circuits in series to account for multiple observed semicircle arcs.[10]

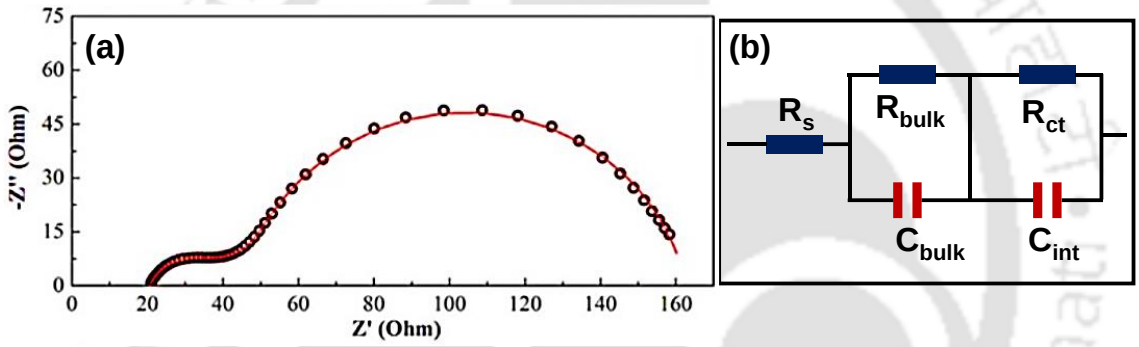

Figure 2.4: (a) A typical Nyquist plot, taken from (Ref. 10), and (b) equivalent circuit used to interpret the EIS data

2.6.7. Mott-Schottky analysis

Mott−Schottky (M-S) analysis was done to estimate key operational parameters of semiconductor electrodes, namely the flat-band potential (E_F), and the type of semiconductor (*n*-type or *p*-type).[12] The flat band potential is the potential at which the electric potential drop between the electrode surface and the bulk is zero. It establishes the position of the semiconductor energy bands with respect to the redox potentials of the electroactive species in the electrolyte. To obtain the value of E_F by M–S measurements, a potentiostat with a three-electrode system, similar to that used for current measurements, was used. Then, the M–S equation was used to obtain the value of E_F after obtaining the M–S plots. The flat band (E_F) potentials of the electrodes can be evaluated from the following **equation 2.16**:[13]

$$\frac{1}{C^2} = \frac{2}{A^2 N_D e \varepsilon \varepsilon^0}\left[E - E_{FB} - \frac{kT}{e}\right] \quad \ldots (2.16)$$

Where, C is the capacitance of the semiconductor, A is the surface area of the photoelectrode, N_D is the charge carrier density of semiconductor, e is the fundamental charge constant, ε^0 is the permittivity of the vacuum, ε is the relative permittivity of the semiconductor, E is the applied potential, k is the Boltzmann constant, and T is the temperature. Through the sign of M–S plot slope $\left({}^{1}/_{C^2}\text{ vs. E}\right)$, conductivity type in a semiconductor can be determined, positive for *n*-type and negative for *p*-type, as shown in **Figure 2.5**.

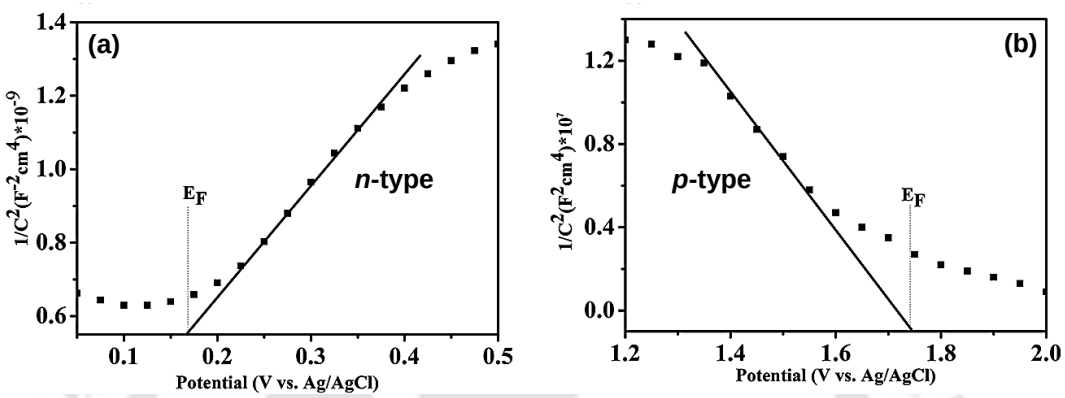

Figure 2.5: Typical Mott-Schottky plot for semiconductor photoanode, showing the nature of conductivity, (a) positive (n-type), (b) negative (p-type). Taken from (*Ref. 13*).

2.7. Fabrication steps for bipolar membrane

Bipolar membranes (BPL) can be fabricated using several methods but among all layer-by-layer (LBL) lamination technique was adopted (**Chapter 7**).[14,15] In this case single layered membranes are casted using the casting knife individually. The water dissociation catalyst (WDC) is deposited at the interfacial layer (IL) between the ion-exchange layers (IEL). The steps involved are mentioned below as shown in **Figure 2.6.**

1) Initially, the anion exchange membrane (AEM) has been laminated over a clean glass slide using casting method. The synthesized polymer (cationic) was dissolved in DMSO at certain temperature and then allowed to cool to room temperature.
2) Then the gel was casted over glass slide and laminated using casting-knife and was kept in vacuum oven at 40 °C overnight. After complete drying, the membrane was peeled off by dipping the glass slide in water.
3) Similarly, the cation exchange membrane (CEM) was laminated over glass slide and peeled off.
4) The water dissociation catalyst (WDC) was prepared by blending the synthesized catalyst with a hydrophilic polymer to form strong adhesion between the two layers in a BPM.

5) The cation exchange layer (CEL) was placed over glass slide and above it the dispersed WDC was drop-casted and evenly spread using casting knife. Then the anion exchange layer (AEL) was placed over it and pressed using another glass slide.
6) Finally, the fabricated CEL/WDC/AEL was allowed to dry in open air. After drying, the bipolar membrane (BPM) was utilized for the water dissociation process.

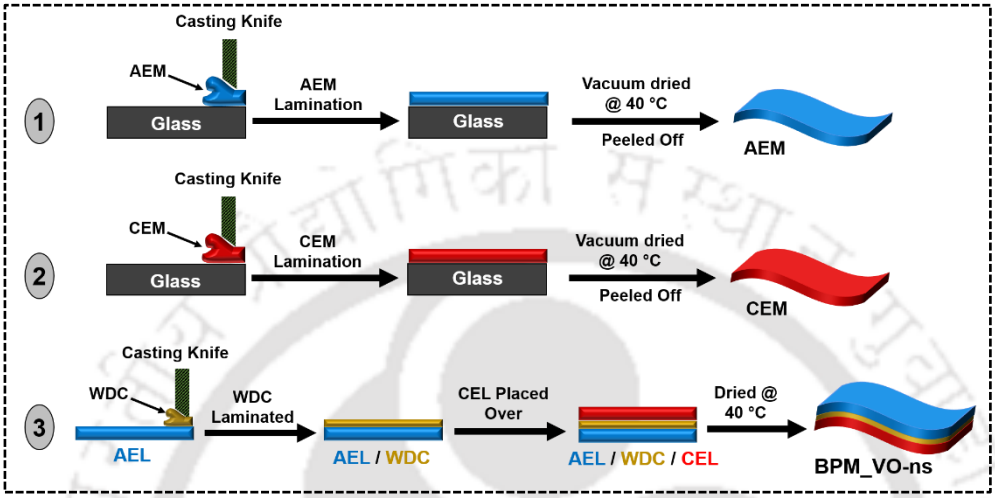

Figure 2.6: Schematic representation showing the LBL lamination method for the preparation of bipolar membrane with a WD catalyst at IL between the CEL and AEL

2.8. Water Dissociation Performance Parameters

Various methods can be used to study the process of water dissociation and ion transfer in membranes. Many of them were initially developed and applied to electrode systems. The essential methods are explained below.

2.8.1. Current-Voltage characteristics

The electrochemical property of BPMs is generally studied using voltammetry.[15-18] The current-voltage curve (CVC) is most convenient to determine the potential difference across the entire membrane system without dividing it into components. For the water dissociation to occur at the interfacial layer, the BPM is used under reverse bias condition.

The current-voltage curve in the reverse bias mode can be divided into four sections (**Figure 2.7a**),[15,19] where each section is characterized by specific parameters. The first region of the current-voltage curve gives the ohmic resistance of the membrane system (R_{Ohm}). The second region gives the value of first limiting current (I_{lim1}) characterizing the current density carried by co-ions, i.e., higher the membrane permselectivity, the lower is I_{lim1}. The slope of the third section characterizes the water dissociation resistance (R_{diss}) i.e., the BPM's ability to intensify water dissociation.[15,20] Thus, smaller the R_{diss} value, higher is the catalytic activity

towards water dissociation reaction. The fourth region is the second limiting current region (I_{lim2}) where the water diffusion limit occurs as the water transport towards the BPM interface is not enough to replenish the water dissociated thereby drying out the IL region.

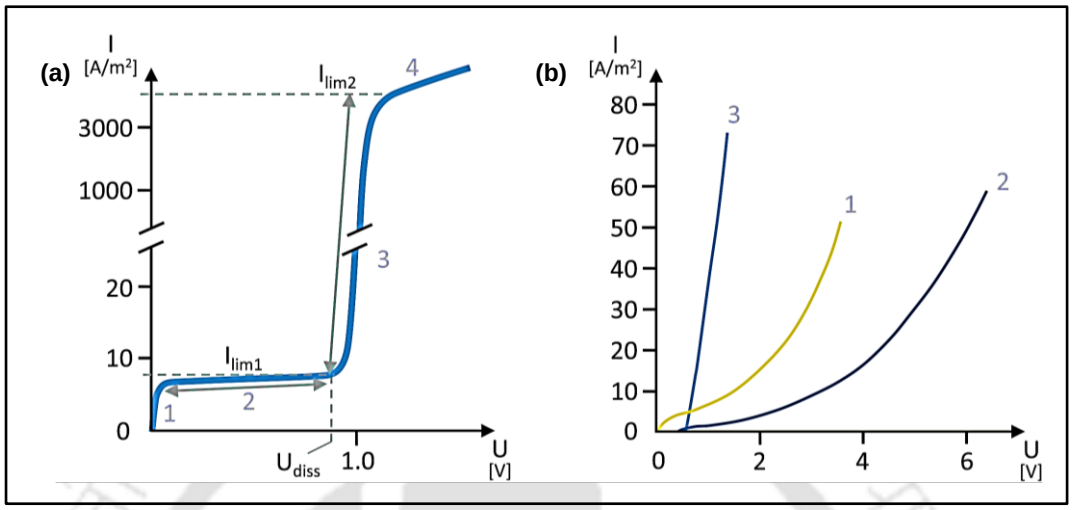

Figure 2.7: (a) Schematic current-voltage curve of a BPM in a salt solution, and (b) Current-voltage characteristic of asymmetric bipolar membranes (ABPM) 1) in a 0.01 M NaCl solution, 2) in a 0.01 M NaOH | ABPM | 0.01 M HCl system, and 3) CVC of an ABPM with a water dissociation catalyst measured in the same acid-alkali system. (*Ref. 15*)

The CVC characteristics of a BPM differ in shape when measured in a neutral salt solution and in an acid-alkali system (i.e., with an acidic solution on the CEL side, and alkali solution on the AEL side of the BPM) (**Figure 2.7b**). The CVC of a bipolar membrane in the acid-alkali system shows significant deviation of the potential from zero at small polarizing current (**Figure 2.7b**, curves 2, 3).[15,21] This is due to the emerging Donnan potential at the bipolar junction which is about 0.83 V. The closer this potential to the equilibrium, the higher the catalytic activity, and vice versa.

2.8.2. Chronopotentiometry

Chronopotentiometry of membrane systems provides information on the dynamic characteristics of ion transport and chemical reactions in the bulk of an ion-exchange membrane (IEM) and adjacent solution layers.[15,22,23] In chronopotentiometry the potential drop across the membrane system is recorded as a function of time, with application of constant current density. At an overlimiting current density, the potential drop sharply increases upon reaching the transition time, τ. The BPM resistance drastically increases due to the depletion of co-ions which leads to increasing voltage, and the rate of water dissociation becomes rather high. Further growth of the potential drop with time is due to an increase in the electric field at

the bipolar junction, which intensifies the water dissociation rate. When this rate becomes sufficient to supply the required current density, the system reaches a stationary state.

2.9. References

[1] M. Kato, J. Z. Zhang, N. Paul and E. Reisner, *Chem. Soc. Rev.*, 2014, **43**, 6485.

[2] S. Li, S. Sirisomboonchai, A. Yoshida, X. An, X. Hao, A. Abudula and G. Guan. *J. Mater. Chem. A*, 2018, **6**, 19221.

[3] S. Anantharaj, S. R. Ede, K. Karthick, S. S. Sankar, K. Sangeetha, P. E. Karthik and S. Kundu, *Energy Environ. Sci.*, 2018, **11**, 744.

[4] Y. Shi, B. Zhang, *Chem. Soc. Rev*., 2016, **45**, 1529.

[5] A. J. Bard, L. R. Faulkner, J. Leddy and C. G. Zoski, *Electrochemical methods: Fundamentals and Applications*, New York, Wiley, 1980, vol. 2.

[6] H. Han, H. Choi, S. Mhin and Y-R. Hong, *Energy Environ. Sci*., 2019, **12**, 2443.

[7] G. Li, S. Li, J. Ge, C. Liu and W. Xing, *J. Mater. Chem. A*, 2017, **5**, 17221.

[8] T. Zhou, Z. Cao, P. Zhang, H. Ma, Z. Gao, H. Wang, Y. Lu, J. He and Y. Zhao, *Sci. Rep.*, 2017, **7**, 46154.

[9] C. Jiang, S. J. Moniz, A. Wang, T. Zhang and J. Tang, *Chem. Soc. Rev.*, 2017, **46**, 4645.

[10] A. R. C. Bredar, A. L. Chown, A. R. Burton and B. H. Farnum, *ACS Appl. Energy Mater.*, 2020, **3**, 66.

[11] K. Sivula, F. Le Formal, M. Gratzel, *ChemSusChem.*, 2011, **4**, 432.

[12] A. Hankin, F. Bedoya-Lora, J. Alexander, A. Regoutz and G. Kelsall, *J. Mater. Chem. A*, 2019, **7**, 26162

[13] S. P. Berglund, F. F. Abdi, P. Bogdanoff, A. Chemseddine, D. Friedrich and R. van de Krol, *Chem. Mater.*, 2016, **28**, 4231.

[14] M. B. McDonald and M. S. Freund, *ACS Appl. Mater. Interfaces*, 2014, **6**, 13790.

[15] R. Pärnamäe, S. Mareev, V. Nikonenko, S. Melnikov, N. Sheldeshov, V. Zabolotskii, H. Hamelers and M. Tedesco, *J. Membr. Sci.*, 2021, **617**, 118538.

[16] V. I. Zabolotskii, N. V. Shel'deshov and N. P. Gnusin, *Russ. Chem. Rev.*, 1988, **57**, 801.

[17] F. G. Wilhelm, N. F. A. Van Der Vegt, H. Strathmann and M. Wessling, *J. Appl. Electrochem.*, 2022, **32**, 455.

[18] R. Simons and G. Khanarian, *J. Membr. Biol.*, 1978, **38**, 11.

[19] F. G. Wilhelm, I. Pünt, N. F. A. van der Vegt, H. Strathmann and M. Wessling, *Ind. Eng. Chem. Res.*, 2022, **41**, 579.

[20] J. Balster, S. Srinkantharajah, R. Sumbharaju, I. Pünt, R. G. H. Lammertink, D. F. Stamatialis and M. Wessling, *J. Membr. Sci.*, 2010, **365**, 389.

[21] S. S. Melnikov, N. V. Sheldeshov and V. I. Zabolotskii, *Desalin. Water Treat*, 2018, **123**, 1.

[22] J. H. Choi and S. H. Moon, *J. Membr. Sci.*, 2001, **191**, 225.

[23] S. A. Mareev, D. Y. Butylskii, N. D. Pismenskaya, V. V. Nikonenko, *J. Membr. Sci.*, 2016, **500**, 171.

CHAPTER 3

Doping and overlayer strategy: Strontium doped Lanthanum manganite overlayered with Cobalt Phosphate for oxygen evolution reaction

This chapter focusses on the effect of elemental doping and overlayer deposition on the performance of oxygen evolution reaction (OER). Here, lanthanum manganite (LMO) has been synthesized via solid-state method with different strontium doping. The optimized strontium doped lanthanum manganite (LSMO) was further modified by depositing cobalt phosphate, an electroactive material, over the surface and utilized for the oxygen evolution reaction (OER).

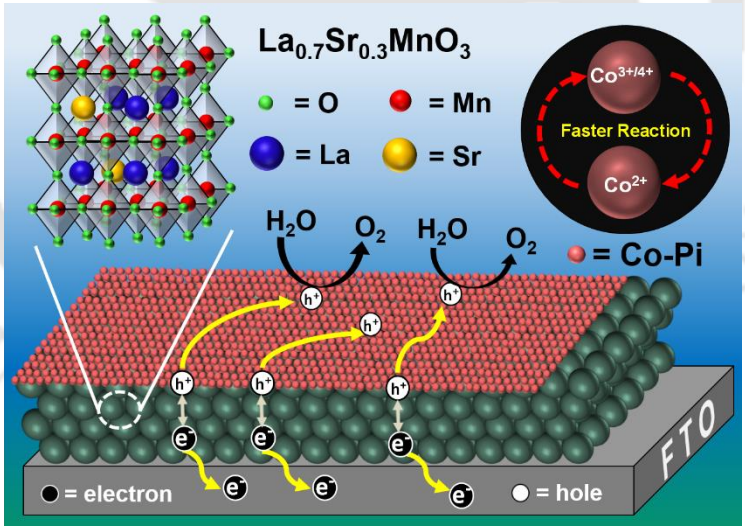

S. Bhowmick, et al., *ACS Appl. Energy Mater.* 2020, **3**, 1279−1285

3.1. Introduction

In the electrolysis of water process, OER is energetically more challenging due to its 4 e^- and 4 H^+ charge-transfer process, as compared to HER, which is a 2 e^- and 2 H^+ charge-transfer process.[1,2] In this regard, transition metals (like Mn, Co, Fe or Ni) with variable oxidation states, which can facilitate electron movement and tunable lattice structures by virtue of dopants create suitable electronic structures that are effective components to design OER electrocatalysts.[3,4] IrO_2 and RuO_2, considered as the benchmark OER catalysts in aqueous acidic conditions are the most effective and efficiently overcomes the kinetic barrier with low overpotential, but the scarceness and high cost of Ir and Ru lead to the exploration of alternate catalysts with comparable efficiency for the commercial purposes.[3,5] Recently, three dimensional (3D) perovskite oxides, with a general formula of ABO_3, where A is a rare-earth or alkali metal and B is a transition metal, are being investigated owing to its intrinsic properties such as low bandgap, low exciton binding energy, and high efficiency.[5,6] High flexibility of the elemental composition and rich electronic/defect structure of the 3D perovskites results in their usage as OER electrocatalysts with the intrinsic activity.[7,8] In Mn based perovskites, the oxidation state of Mn at the B-site can be tuned by substituting a larger cation at the A-site. For example, substituting Sr^{2+} for La^{3+} at the A-site results in an increase in the catalytic activity as it converts a proportion of the Mn^{3+} to Mn^{4+} in the B-site.[9,10] The advantage of doping a bivalent ion (Sr^{2+}) into trivalent ion (La^{3+}) in $LaMnO_3$ is the introduction of holes into the system, due to the well-known double exchange phenomenon,[11] which helps in oxidizing water by facilitating the conduction pathway via 2p orbital of oxygen species (O_{2p}) to the surface reaction site.[12]

To improve the OER by virtue of charge separation, the surface of electrocatalysts are modified with other active catalysts.[13-15] On comparing with various metal oxides, hydroxides and cobalt-based catalysts; cobalt phosphate (Co-Pi) is widely investigated as earth-abundant, low-cost and multipurpose material.[16,17] Being itself an OER electrocatalyst, Co-Pi emerges as a hot candidate to couple as a modifier[18,19] due to its exceptional redox ability resulting in Co^{2+} to Co^{3+}/ Co^{4+} species forming high valent Co^{4+}–O intermediate.[20,21]

Although the use of Sr doped $LaMnO_3$ in colossal magnetoresistance material (CMR) and oxygen reduction reaction (ORR) is known, it has been sparsely investigated for OER. In this work, A-site doped $LaMnO_3$ with Sr^{2+} is proposed as an electrocatalyst for excellent electrocatalytic OER, owing to improved bulk conductivity and interfacial charge transport kinetics due to formation of Mn^{3+}/Mn^{4+} redox pair. Subsequently, for further enhancing the

electrocatalytic activity, Co-Pi is electrodeposited over the $La_{1-x}Sr_xMnO_3$ surface. An overpotential of 220 mV @10 mA/cm^2 current density is attained for the modified system with a Tafel slope of 62 mV/decade. Additionally, the electrocatalyst showed durability of 16 hours with fourfold enhancement in the turnover frequency and a Faradaic yield of ~98%. Co-Pi being an electrocatalyst facilitates the surface reaction of OER by accepting the holes generated in the $La_{0.7}Sr_{0.3}MnO_3$ and transferring to the electrolyte interface with the continuous shuttling of the oxidation state of the Co^{3+}/Co^{4+} ion. The importance of this works lies in the fact that with the appropriate combination of stable metal oxide such as $La_{0.7}Sr_{0.3}MnO_3$ and cobalt phosphate enhances the surface kinetics of the overall system. This paves the path as a model system for the design and fabrication of a noble metal-free electrocatalyst with high OER activity at lower overpotential and can be useful for the development of several other perovskite based-electrocatalysts.

3.2. Experimental Section

3.2.1. Synthesis of strontium doped lanthanum manganites ($La_{1-x}Sr_xMnO_3$, $0 \leq X \leq 0.4$)

To synthesize the doped lanthanum manganites, conventional solid-state route method was performed.[12] Stoichiometric amounts of lanthanum, strontium and manganese precursors were weighed and grinded well in a mortar-pestle. The doping of strontium in lanthanum manganite were of the order 0%, 10%, 20%, 30% and 40% of the lanthanum stoichiometry. The well grinded precursors were calcined at 1050 °C for 24hrs to obtain black coloured solid powder.

3.2.2. Deposition of Co-Pi layer over $La_{1-x}Sr_xMnO_3$

Cobalt phosphate (Co-Pi) layer was electrodeposited using a three-electrode system.[22] The fabricated $La_{1-x}Sr_xMnO_3$ electrode (**Section 2.4** of **Chapter 2**) was used as the working electrode with Ag/AgCl and platinum as reference and counter electrode, respectively. The potential was fixed at 1.1V vs. Ag/AgCl. The electrolyte used was prepared using 15mM cobalt nitrate in 0.1M potassium phosphate dibasic solution. After the deposition the electrode was washed with DI water and dried in oven at 60 °C. A bare cobalt phosphate working electrode was also prepared using similar technique.

3.3. Results and Discussions

3.3.1. Phase and Structural Analysis

The different synthesized lanthanum manganites were examined using X-ray diffraction (XRD) technique to study the phase purity. The obtained XRD peaks for all the

materials (**Figure 3.3.1a**) are indexable to that of the orthorhombic phase of lanthanum manganite (ICSD no. 00-065-0076). As can be seen from the **Figure 3.3.1b**, with the increase in the doping percentage of strontium into lanthanum manganite, the peak at ~32° (2θ) is shifted towards higher angle. The shift in the peak position is due to the difference in the ionic radii of Sr^{2+} (132pm) and La^{3+} (117.2pm) leading to internal chemical pressure in the lattice causing the distortion.[9] **Figure 3.3.1c** shows the XRD pattern of the fabricated $La_{0.7}Sr_{0.3}MnO_3$ and $La_{0.7}Sr_{0.3}MnO_3$/Co-Pi electrode over the FTO substrate and the peaks well matched with the orthorhombic phase of the lanthanum manganite. The peaks for the Co-Pi overlayer are not assignable due to its amorphous nature. The schematic representation of the electrocatalytic system is shown in **Figure 3.3.1d**. The $La_{0.7}Sr_{0.3}MnO_3$ is fabricated by doctor-blade method over FTO and the Co-Pi is electrodeposited for the controlled systematic overgrowth onto the $La_{0.7}Sr_{0.3}MnO_3$.

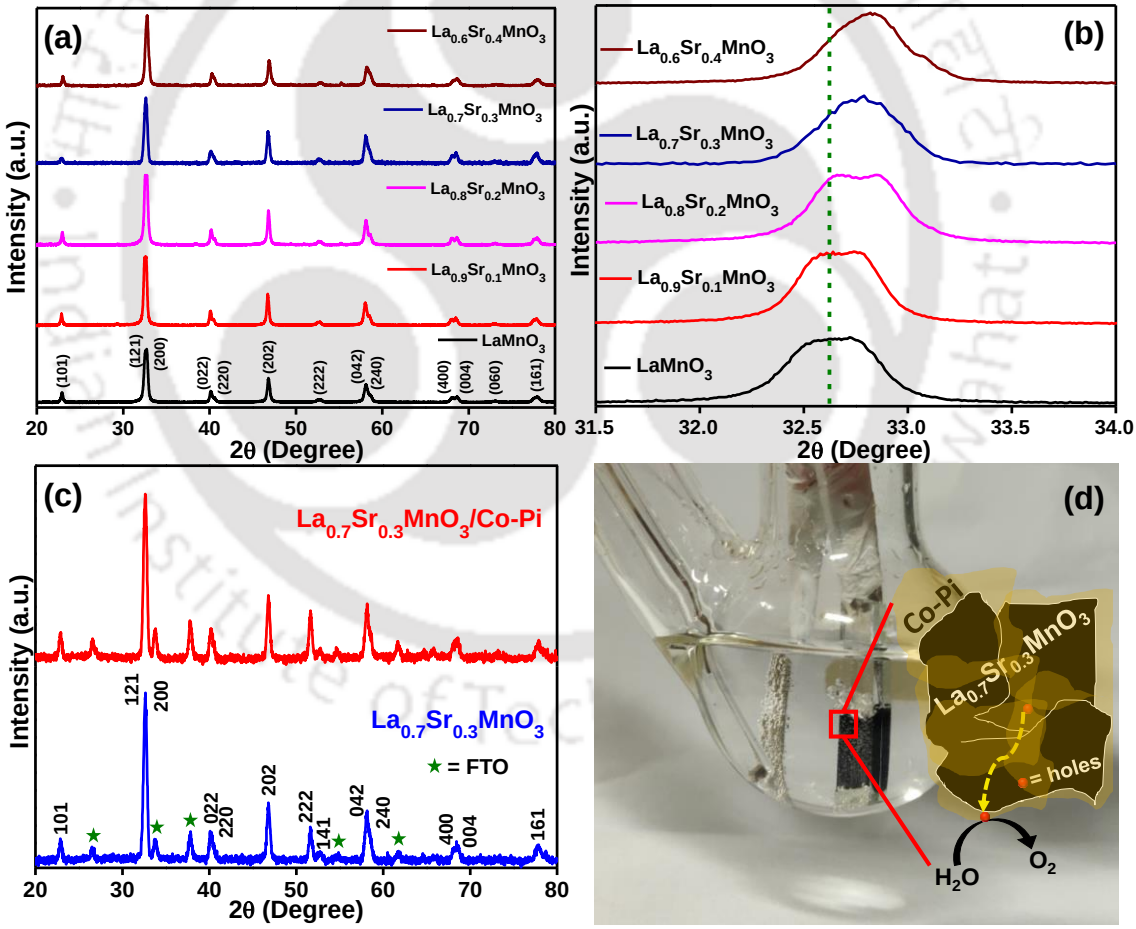

Figure 3.3.1. (a) p-XRD plots of the bare lanthanum manganite along with the different amount of strontium doped lanthanum manganites, (b) enlarged peak position at around 32° (2θ) showing the shift towards higher angle with increasing strontium concentration, (c) XRD analysis of the $La_{0.7}Sr_{0.3}MnO_3$ and $La_{0.7}Sr_{0.3}MnO_3$/Co-Pi fabricated over the FTO substrate, and (d) Schematic representation of the electrocatalytic OER by $La_{0.7}Sr_{0.3}MnO_3$/Co-Pi

3.3.2. Morphological Analysis

The morphological study was made using the field emission scanning electron microscopy (FESEM) technique. As can be seen from the FESEM images (**Figure 3.3.2a, b**) of both $La_{0.7}Sr_{0.3}MnO_3$ and $La_{0.7}Sr_{0.3}MnO_3$/Co-Pi, there is no morphological changes after the deposition of Co-Pi over the perovskite material. The presence of Co-Pi is not visible over the $La_{0.7}Sr_{0.3}MnO_3$ particles due to its very minimum deposition on the surface.

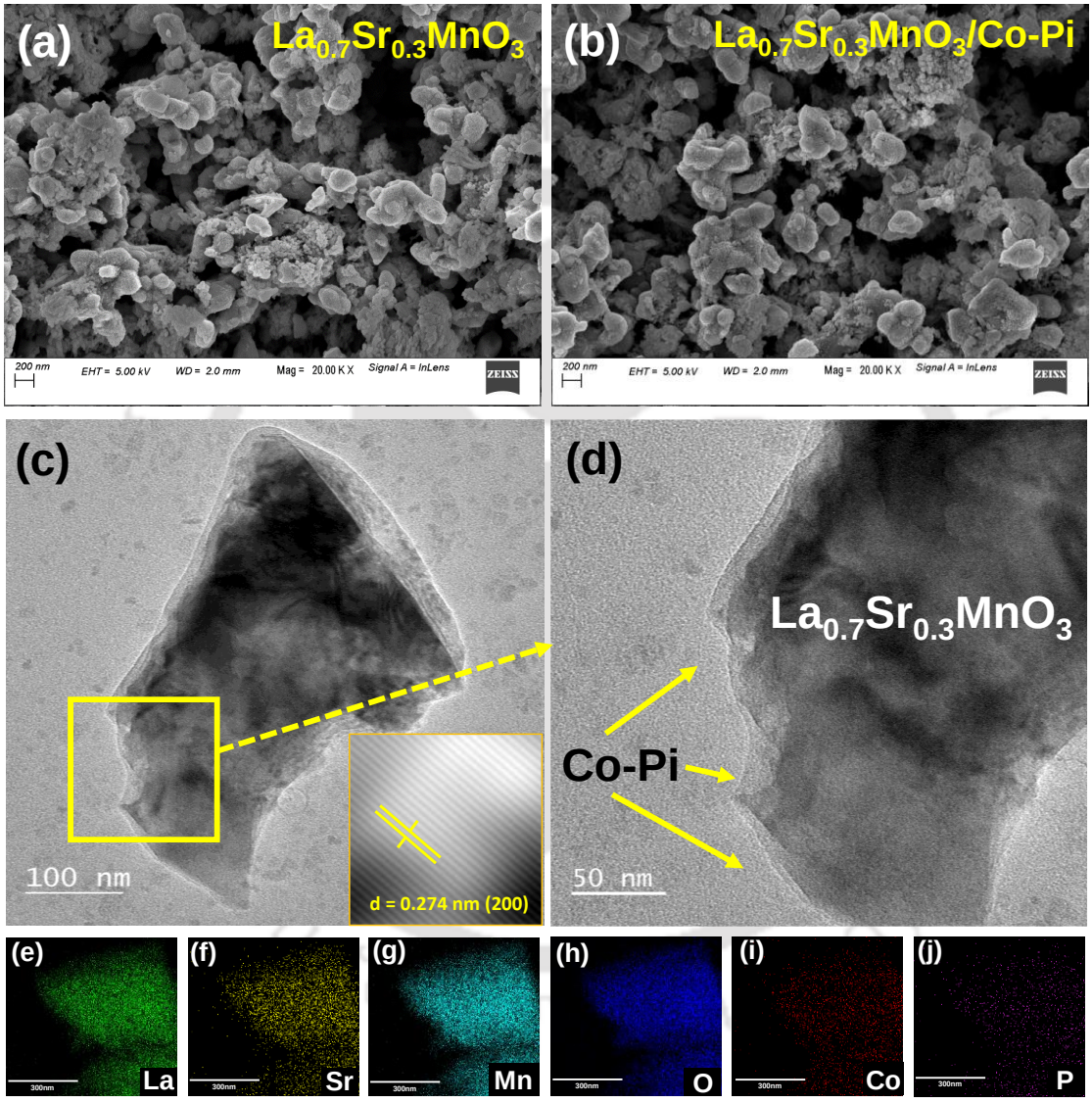

Figure 3.3.2. Morphological features of the fabricated electrocatalyst over FTO, (a) $La_{0.7}Sr_{0.3}MnO_3$ and (b) $La_{0.7}Sr_{0.3}MnO_3$/Co-Pi, (c) FETEM image of $La_{0.7}Sr_{0.3}MnO_3$/Co-Pi, (d) enlarged image of the same showing the layer of Co-Pi over the $La_{0.7}Sr_{0.3}MnO_3$, STEM-EDX elemental mapping of $La_{0.7}Sr_{0.3}MnO_3$/Co-Pi showing the uniform distribution of (e) **Lanthanum**, (f) **Strontium**, (g) **Manganese**, (h) **Oxygen**, (i) **Cobalt**, and (j) **Phosphorous**

To confirm the presence of the cobalt phosphate overlayer, field emission transmission electron microscopy (FETEM) analysis was performed, as shown in **Figure**

3.3.2c, d. A uniform layer over the $La_{0.7}Sr_{0.3}MnO_3$ particle (**Figure 3.3.2c**) confirms the presence of the deposited amorphous Co-Pi of about 5-10 nm thickness (**Figure 3.3.2d**). The high-resolution transmission electron microscopy (HRTEM) image of $La_{0.7}Sr_{0.3}MnO_3$ (**Figure 3.3.2c** inset) confirms the phase purity of the $La_{0.7}Sr_{0.3}MnO_3$ with *d*-spacing of ~0.274 nm corresponding to the (200) crystal plane. The scanning transmission electron microscopy energy-dispersive X-ray spectroscopy (STEM-EDX) elemental mapping of modified $La_{0.7}Sr_{0.3}MnO_3$, as shown in **Figure 3.3.2e-j** confirms the presence of all the elements. The presence of cobalt and phosphorous homogenously over the particle validates the uniform deposition of Co-Pi over $La_{0.7}Sr_{0.3}MnO_3$.

3.3.3. Electronic State Analysis

To investigate the electronic structure and the chemical state of the constituent elements X-ray photoelectron spectroscopy (XPS) analysis was performed. The XPS spectra of La 3d (**Figure 3.3.3a**) has been de-convoluted into $3d_{5/2}$ and $3d_{3/2}$. The peaks for $La_{0.7}Sr_{0.3}MnO_3$ at 834.3 eV and 838.1 eV are due to La^{3+} and satellite, respectively.[23] The shift in the peak for $La_{0.7}Sr_{0.3}MnO_3$/Co-Pi indicates interaction between $La_{0.7}Sr_{0.3}MnO_3$ and Co-Pi. In **Figure 3.3.3b** the XPS spectra for Sr 3d has been de-convoluted into respective $3d_{5/2}$ and $3d_{3/2}$. The peaks at 132.6 eV and 133.8 eV for $La_{0.7}Sr_{0.3}MnO_3$ are assigned to Sr^{2+} in the bulk and surface of the material, respectively.[23] **Figure 3.3.3c** shows the Mn 2p core-level spectra which is de-convoluted for $2p_{3/2}$ and $2p_{1/2}$ levels. The Mn $2p_{3/2}$ peak of $La_{0.7}Sr_{0.3}MnO_3$ featuring at 641.2 eV and 644.1 eV can be attributed to Mn^{3+} and Mn^{4+}, respectively. The peak at 642.5 eV is due to the Manganese in different coordination environments. The peak position at 645.9 eV is due to the satellite peak.[23] The shift in the peak positions for that of $La_{0.7}Sr_{0.3}MnO_3$/Co-Pi is due to the interaction of $La_{0.7}Sr_{0.3}MnO_3$ with the Co-Pi. **Figure 3.3.3d** shows the O1s core-level spectra. The peaks at 529.4 eV and 531.3 eV of $La_{0.7}Sr_{0.3}MnO_3$ are due to lattice oxygen O^{2-} associated with Mn and the surface oxygen species associated hydroxyl ions, respectively. The peak at 533.1 eV is due to the O, which is weakly bound to surface.[23] The additional fitted peak at 529.2 eV for $La_{0.7}Sr_{0.3}MnO_3$/Co-Pi is assigned to lattice Oxygen species, while the other peak at 530.2 eV corresponds to the lattice Oxygen corresponding to Co-Pi.[24] The **Figure 3.3.3e, f** corresponds to the Co 2p and P 2p core-level spectra, which are de-convoluted for $2p_{3/2}$ and $2p_{1/2}$ contributions. The characteristic peaks for Co $2p_{3/2}$ and Co $2p_{1/2}$ at around 780.4 eV and 796.1 eV, while the peaks at 785.0 eV and 803.0 eV corresponding to the satellite peaks.[24,25] The binding energy

of P $2p_{3/2}$ and $2p_{1/2}$ are at 132.3 eV and 133.8 eV, which is characteristic of P in the phosphate group, confirming that P exists in the form of PO_4^{3-}.[24,25]

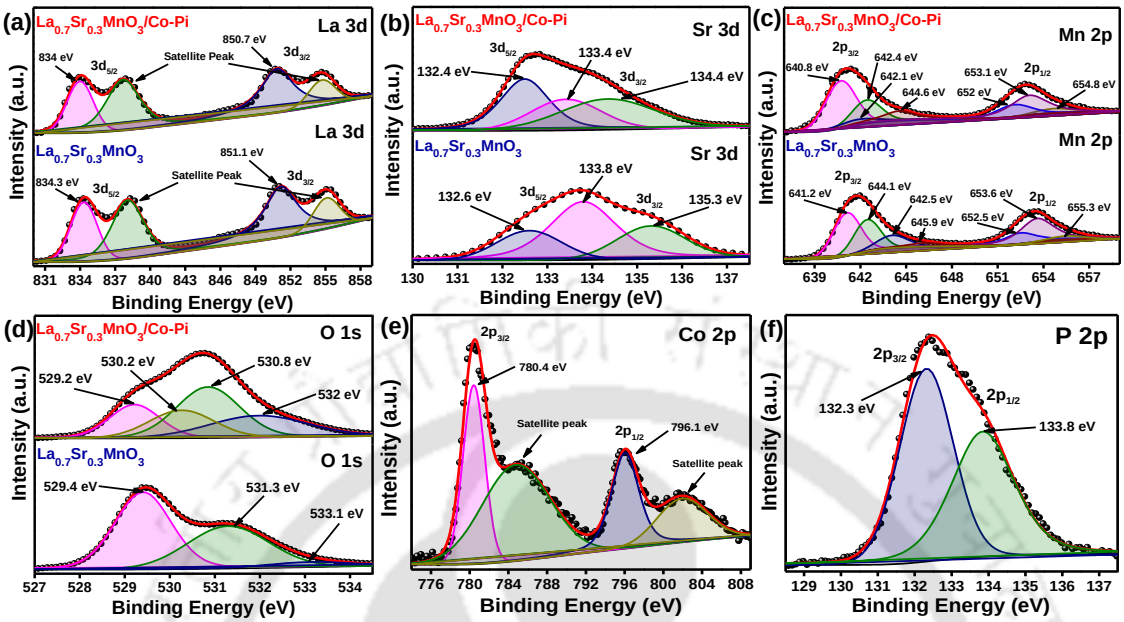

Figure 3.3.3. XPS spectra of (a) the La 3d core-level (b) the Sr 3d core-level, (c) the Mn 2p core-level, and (d) the O 1s core-level of $La_{0.7}Sr_{0.3}MnO_3$ and $La_{0.7}Sr_{0.3}MnO_3$/Co-Pi, and (e) the Co 2p core-level and (f) the P 2p core-level of $La_{0.7}Sr_{0.3}MnO_3$/Co-Pi

3.3.4. Electrochemical Analyses

To investigate the OER activity of the synthesized electrocatalyst, linear sweep voltammetry (LSV) was performed in alkaline solution (1 M NaOH) in a standard three-electrode configuration (**Figure 3.3.4**). The potential was swept between 0.1V and 1.0 V vs. Ag/AgCl (saturated KCl) reference electrode, converted to RHE (**Equation 2.1**) and the overpotential was calculated at 10 mA/cm^2 current density for the electrocatalysts. To choose for the optimized doped lanthanum manganite for OER, all the materials were subjected to electrochemical analysis. It can be seen from the plot (**Figure 3.3.4a**) the overpotential for $La_{0.7}Sr_{0.3}MnO_3$ is lowest among all other lanthanum manganites, which is due to the formation of optimum holes within the lattice upon conversion of Mn ions from +3 to +4 state due to the Sr^{2+} doping. Additionally, the 30 at% doping of Sr^{2+} into La^{3+} results in the facile transport of the charge carriers owing to the formation of optimum Mn^{3+}–O_{2p}–Mn^{4+} bong angle of ~180°. The optimum deposition of Co-Pi over the oxide material was evaluated by changing the deposition time keeping all other parameters constant. It was observed that the overpotential value @10mA/cm^2 decreases upto 10mins deposition time and again increases with more time (**Figure 3.3.4b**). The observed trend is due to the different concentration of Co ions deposited over the perovskite surface. The Co ions are responsible for the extraction

of the charge carriers from the perovskite surface and transferring the same to the electrolyte interface. Low concentration of Co ions reduces the effective extraction of the charge carriers, thus upon increasing the deposition time the concentration of the Co ions increases, enhancing the efficiency. With increase in Cobalt concentration with the excessive deposition of the Co-Pi onto the perovskite surface causes over-crowding of the Co ions and thus the Co^{3+}/Co^{4+} (Co^{2+} on accepting the holes) instead of reaching to the electrolyte surface collides with other Co^{2+} ions thereby releasing the holes and getting reduced to +2 state. Thus, we observe a decrease in the efficiency of the catalyst for higher deposition time.

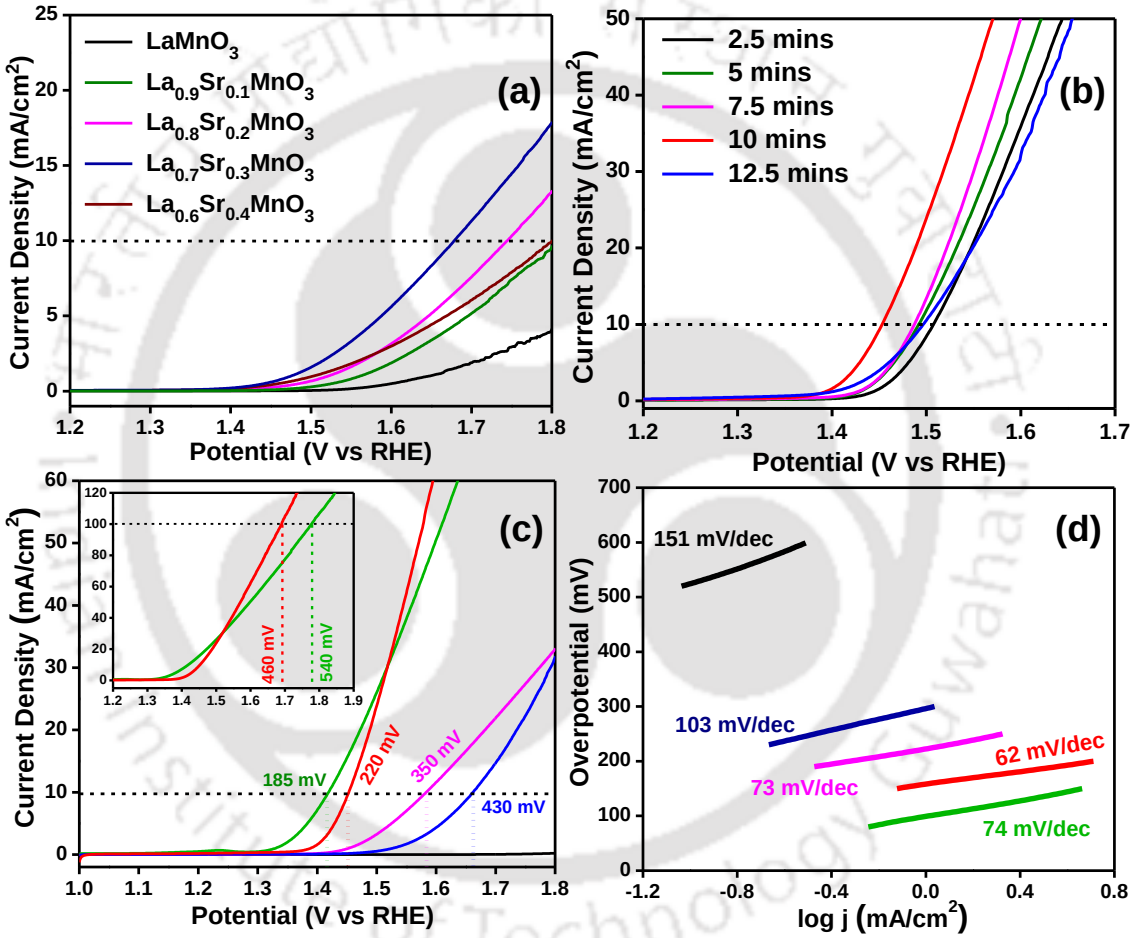

Figure 3.3.4. (a) Linear sweep voltammetry in 1M NaOH electrolyte solution of $LaMnO_3$, $La_{0.9}Sr_{0.1}MnO_3$, $La_{0.8}Sr_{0.2}MnO_3$, $La_{0.7}Sr_{0.3}MnO_3$, $La_{0.6}Sr_{0.4}MnO_3$, (b) different deposition time of Co-Pi over $La_{0.7}Sr_{0.3}MnO_3$, (c) Linear sweep voltammetry of the FTO (**black**), Co-Pi (**magenta**), RuO_2 (**green**), $La_{0.7}Sr_{0.3}MnO_3$ (**blue**) and $La_{0.7}Sr_{0.3}MnO_3$/Co-Pi (**red**) in 1 M NaOH electrolyte solution with inset showing the overpotential of the RuO_2 and $La_{0.7}Sr_{0.3}MnO_3$/Co-Pi at a current density of 100 mA/cm^2, and (d) the corresponding Tafel plots along with inset comparing the Tafel slopes of the catalysts

From **Figure 3.3.4c** an exceptional ~195% enhancement in the performance is observed for the modified $La_{0.7}Sr_{0.3}MnO_3$ electrode with Co-Pi overlayer resulting in an

improved overpotential from 430 mV to 220 mV, which is comparable to the commercial RuO_2 (185 mV), measured under conditions identical to our measurements. It is interesting to note that observed overpotential at a current density of 100 mA/cm^2 (**Figure 3.3.4c inset**) for $La_{0.7}Sr_{0.3}MnO_3$/Co-Pi (460 mV) shows a better electrocatalytic property than the commercial RuO_2 (540 mV) under identical alkaline conditions. The improved overpotential for the modified electrocatalyst is attributed to the Co-Pi overlayer. It enhances the surface oxidation kinetics by accepting the charge carriers generated in the perovskite material.

OER kinetics of the electrocatalysts were evaluated by the Tafel slope (**Figure 3.3.4d**). The reduction of the Tafel slope for the modified $La_{0.7}Sr_{0.3}MnO_3$/Co-Pi signifies the favorable kinetics at smaller overpotential. The Tafel slope of 62 mV/decade for $La_{0.7}Sr_{0.3}MnO_3$/Co-Pi depicts faster OER kinetics as compared to that of $La_{0.7}Sr_{0.3}MnO_3$ (103 mV/decade), Co-Pi (73 mV/decade) and commercial RuO_2 (74 mV/decade) at 1 M NaOH (aqueous). The observation of improved Tafel slope for the faster charge transfer across the electrocatalytic interfaces for the $La_{0.7}Sr_{0.3}MnO_3$/Co-Pi is well supported by the LSV plots.

3.3.5. Electrochemical Active Surface Area (ECSA) and Electrochemical Impedance Spectroscopy (EIS) Analyses

To further understand the number of active sites of the OER catalyst, ECSA analysis is carried out and can be evaluated from the electrochemical double-layer capacitance (C_{dl}) model.[28] The C_{dl} was calculated from the slope of the capacitive current vs scan rate obtained from the cyclic voltammograms (CV) of respective catalysts. **Figure 3.3.5a, b** shows the CV of the $La_{0.7}Sr_{0.3}MnO_3$ and $La_{0.7}Sr_{0.3}MnO_3$/Co-Pi recorded in the potential range of -0.6 to 0.6V vs. Ag/AgCl at different scan rates (10 to 100 mV/s). From the plots it is observed that the activity of the $La_{0.7}Sr_{0.3}MnO_3$ has increased upon deposition of Co-Pi over the surface. Also, with the increase in the scan rate the oxidation and reduction peaks in the non-Faradaic region shifts towards higher potential which infers that the electroactive species is confined to the electrode surface. From **Figure 3.3.5c** it is observed that the C_{dl} obtained for $La_{0.7}Sr_{0.3}MnO_3$/Co-Pi (85.22 mF/cm^2) is ~9.5 times higher than that for $La_{0.7}Sr_{0.3}MnO_3$ (8.915 mF/cm^2). The higher ECSA attributes to the larger active sites for the modified catalyst which is beneficial for the better adsorption of water molecules and intimate contact with the electrolyte, resulting in an enhanced OER activity.

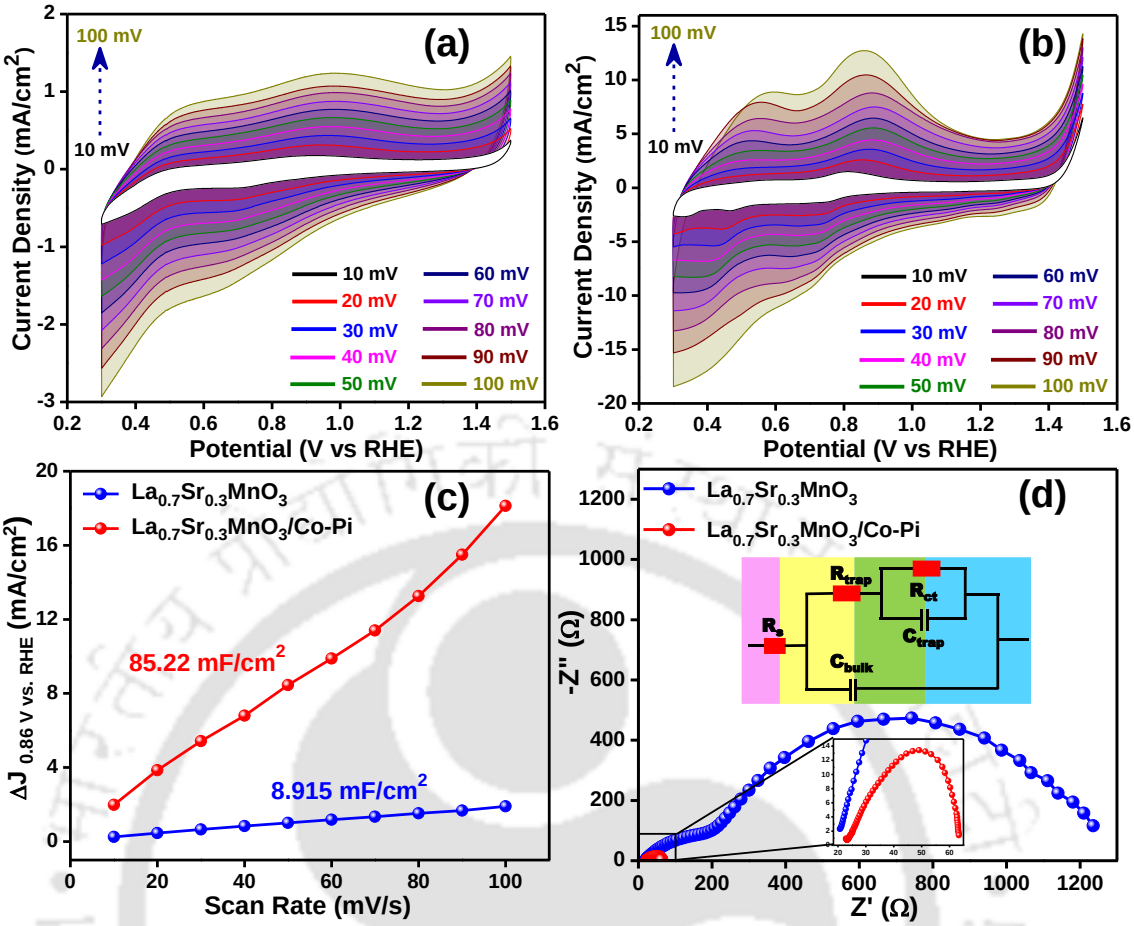

Figure 3.3.5. Cyclic voltammograms (CVs) of (a) $La_{0.7}Sr_{0.3}MnO_3$ and (b) $La_{0.7}Sr_{0.3}MnO_3$/Co-Pi, measured at different scan rates from 10 to 100 mV/s, (c) Plots of current density (at 0.86V vs RHE) vs. scan rates, and (d) Nyquist plots with inset showing the corresponding circuit at different interfaces.

Along with the surface activity, charge transfer kinetics within the bulk also plays a vital role in the betterment of OER activity. To evaluate the charge transfer kinetics, EIS was performed for both the bare perovskite and the modified catalyst. As can be seen from **Figure 3.3.5d**, the diameter in the mid-frequency region of the Nyquist plot for $La_{0.7}Sr_{0.3}MnO_3$/Co-Pi is much smaller than that for the $La_{0.7}Sr_{0.3}MnO_3$, which confirms the improved kinetics of the modified system. The charge transfer resistance (R_{ct}) for $La_{0.7}Sr_{0.3}MnO_3$/Co-Pi is 12.4 Ω while that for $La_{0.7}Sr_{0.3}MnO_3$ is 154.2 Ω. Additionally, the overall bulk capacitance (C_{bulk}) of the system was also evaluated using EIS measurements and found to be 5.5 μF/cm^2 for $La_{0.7}Sr_{0.3}MnO_3$/Co-Pi and 94.1 μF/cm^2 for the $La_{0.7}Sr_{0.3}MnO_3$. The 17-fold reduction of C_{bulk} of the $La_{0.7}Sr_{0.3}MnO_3$ upon the Co- Pi deposition implies the efficient extraction of the carriers from the $La_{0.7}Sr_{0.3}MnO_3$ by the Co-Pi molecules. Thus, the Co^{2+} ions over the $La_{0.7}Sr_{0.3}MnO_3$ surface accept holes from the perovskite material and transfer them to the electrolyte interface more rapidly, thus enhancing the electrocatalytic performance.

3.3.6. Electrochemical Efficiency Analyses

To check the efficiency of the modified electrocatalyst, turnover frequency (TOF) was calculated as explained in the supporting information. Upon calculation, it was found that the modified catalyst, $La_{0.7}Sr_{0.3}MnO_3$/Co-Pi, has a TOF of 3.17 s^{-1} and that for bare perovskite material, $La_{0.7}Sr_{0.3}MnO_3$, is 0.86 s^{-1} (**Figure 3.3.6a**). The four-folds enhancement in the TOF value for the modified catalyst infers that the number of cycles of catalytic activity at the surface per unit time has tremendously increased upon deposition of the Co-Pi overlay owing to its faster reaction kinetics as supported by the ECSA and EIS results.

In addition to the TOF, the Faradaic yield was also evaluated using the online gas chromatography technique (**Figure 3.3.6b**). From the figure, it can be seen that the amount of gas evolved for H_2 and O_2 is in the ratio of 2:1, which is in good accord with the theoretical prediction. The average Faradaic yield of the gas evolved (O_2 and H_2) was found to be ~98% on comparing the experimental and the theoretical yields, as explained in the supporting information. The high Faradaic yield infers that the charge carriers generated in the electrocatalyst are utilized in the oxidation of H_2O molecules producing the O_2 gas at the catalyst surface.

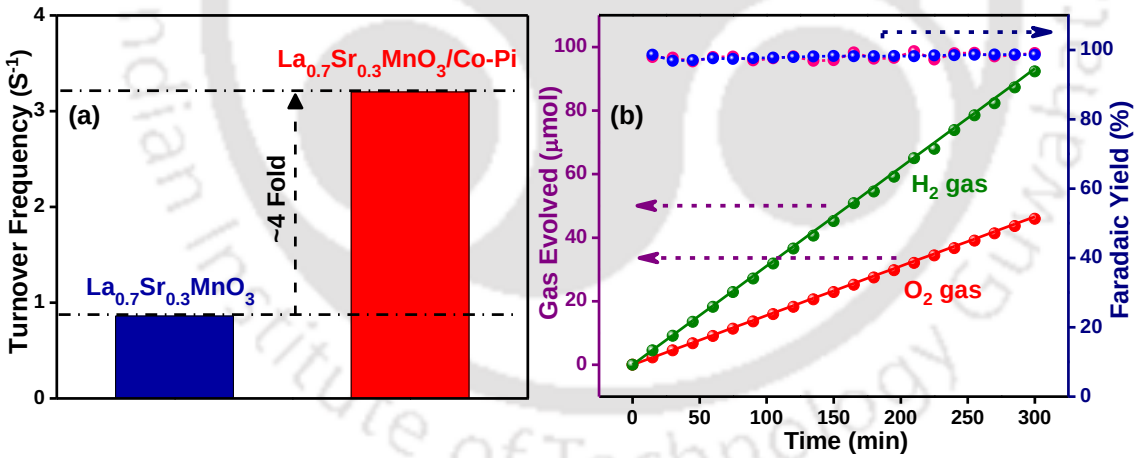

Figure 3.3.6. (a) Turnover frequency (TOF) of the $La_{0.7}Sr_{0.3}MnO_3$ (■) and $La_{0.7}Sr_{0.3}MnO_3$/Co-Pi (■), (b) Faradaic yield of $La_{0.7}Sr_{0.3}MnO_3$/Co-Pi measured at a current density of 10 mA/cm^2 using the gas chromatography technique. In the plot (▬) represents the theoretical yield of H_2 gas while (●) represents the experimental yield. Similarly, (▬) represents the theoretical yield of O_2 gas and (●) represents the experimental yield of O_2 gas. Also, the Faradaic yield of O_2 gas is represented by (●▬●) and that of H_2 by (●▬●)

3.3.7. Durability Test

To test for the durability of the fabricated electrodes, a long-term stability test has been performed by measuring the current density using chronoamperometry method at a

potential of 220 mV (i.e., 1.45 V vs RHE). From **Figure 3.3.7a** it is clear that the catalyst is quite stable even after 16 hours of continuous run. The inset shows the current density of the modified catalyst before and after the stability test. To check the decay in the current density, CV was measured between the potential 0.3 V to 1.5 V vs RHE at a scan rate of 100 mV/s for 500 cycles. Fig S8 shows the CV of $La_{0.7}Sr_{0.3}MnO_3$/Co-Pi at different numbers of cycles. The plot (**Figure 3.3.7b**) shows negligible reduction in the current density upon continuous run upto 500 cycles with no shift in the peak positions. Thus, it can be inferred that the $La_{0.7}Sr_{0.3}MnO_3$/Co-Pi is stable in the alkaline condition and can be utilized as electrocatalyst for long run.

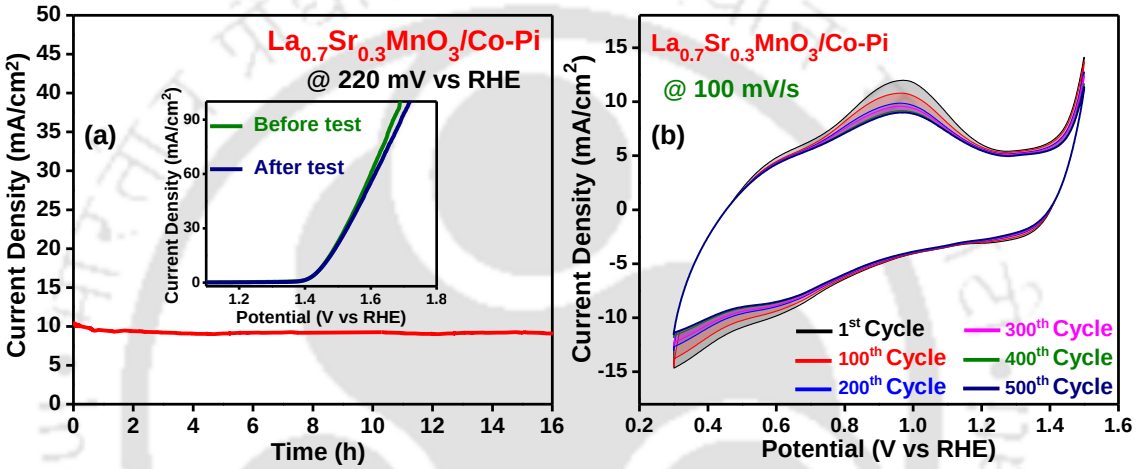

Figure 3.3.7. (a) Chronoamperometry plot of $La_{0.7}Sr_{0.3}MnO_3$/Co-Pi at an overpotential (OP) of 220mV vs RHE with inset the IV curve of the catalyst before and after the stability test, and (b) CV scan of $La_{0.7}Sr_{0.3}MnO_3$/Co-Pi measured at a scan rate of 100 mV/s

3.3.8. Mechanism Involved for Efficient OER Performance

The mechanism of the OER by the $La_{0.7}Sr_{0.3}MnO_3$/Co-Pi is depicted in the schematic diagram (**Figure 3.3.8**). The introduction of Sr^{2+} into the lattice of La^{3+} resulted in the formation of Mn^{4+} from Mn^{3+}, thus inducing the formation of holes into the lattice. With the increase in the doping concentration, the bond angle between Mn^{3+}–O_{2p}–Mn^{4+} increases and reaches to the optimum 180° at 30 at%, which aids the facile charge transport owing to the simplified conduction path.[27] Thus, $La_{0.7}Sr_{0.3}MnO_3$ shows better electrocatalytic behavior. The electro-deposition of Co-Pi over the $La_{0.7}Sr_{0.3}MnO_3$ layer enhances the OER. The Co^{2+} receives the holes generated in the $La_{0.7}Sr_{0.3}MnO_3$ from the surface and gets oxidized to Co^{3+}/Co^{4+} and moves to the electrolyte interface where it releases the hole on interacting with the H_2O molecule thus oxidizing it to O_2, and itself reduces to Co^{2+}. The rapid shuttling of the oxidation state of Co ions between +2 and +3/+4 state results in the faster kinetics of OER and results in superior efficiency.

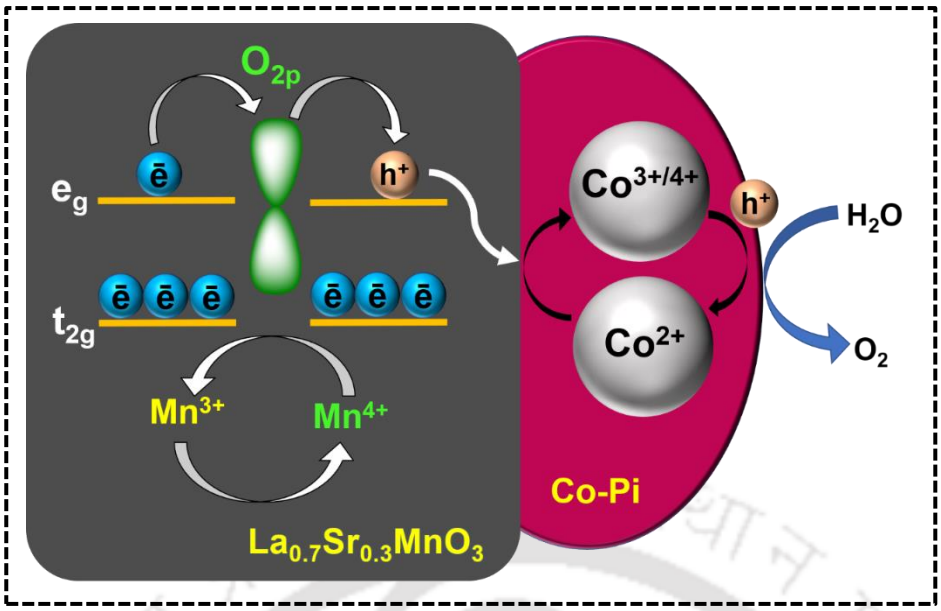

Figure 3.3.8. Schematic representation of plausible mechanistic pathway $La_{0.7}Sr_{0.3}MnO_3$/Co-Pi underwent for the oxygen evolution reaction

3.4. Conclusions

In summary, we proposed a model system of the perovskite material, $La_{0.7}Sr_{0.3}MnO_3$, over the FTO over-layered with Co-Pi via electrodeposition method and its potential as an efficient electrocatalyst. The obtained $La_{0.7}Sr_{0.3}MnO_3$/Co-Pi catalyst exhibits a low overpotential of 220 mV vs RHE attained at a current density of 10mA/cm^2 and a small Tafel slope of 62 mV/decade under alkaline conditions. Moreover, it shows an improved efficiency with a turnover frequency of 3.17 s^{-1}, which implies the high activity of the catalyst, which is in accord with the very low R_{ct} (12.36 Ω) value obtained from EIS and a high C_{dl} (85.22 mF/cm^2) value from ECSA. In addition, the average Faradaic yield of ~98 % implies that the generated holes within the electrocatalyst are utilized for H_2O oxidation evolving O_2 gas. The high stability for about 16 hours with a negligible decrease in the current density also supports the high potential of $La_{0.7}Sr_{0.3}MnO_3$/Co-Pi as a promising electrocatalyst to replace the high cost and scarce commercial noble metal catalysts for practical electrochemical water splitting.

3.5. References

[1] J. D. Blakemore, R. H. Crabtree and G. W. Brudvig, *Chem. Rev.*, 2015, **115**, 12974.

[2] C. Hu, L. Zhang and J. Gong, *Energy Environ. Sci.*, 2019, **12**, 2620.

[3] Y. Yan, B. Y. Xia, B. Zhao and X. Wang, *J. Mater. Chem. A*, 2016, **4**, 17587.

[4] L. Han, S. J. Dong and E. Wang, *Adv. Mater.*, 2016, **28**, 9266.

[5] L. Etgar, *Energy Environ. Sci.*, 2018, **11**, 234.

[6] H. Sun, X. Xu, Z. Hu, L. H. Tjeng, J. Zhao, Q. Zhang, H. J. Lin, C. T. Chen, T. S. Chan, W. Zhou and Z. Shao, *J. Mater. Chem. A*, 2019, **7**, 9924

[7] X. Xu, Y. Chen, W. Zhou, Z. Zhu, M. Liu and Z. Shao, *Adv. Mater.*, 2016, **28**, 6442.

[8] X. Xu, C. Su, W. Zhou, Y. Zhu, Y. Chen and Z. Shao, *Adv. Sci.*, 2016, **3**, 1500187.

[9] M. Zhi, G. Zhou, Z. Hong, J. Wang, R. Gemmen, K. Gerdes, A. Manivannan, D. Ma and N. Wu. *Energy Environ. Sci.*, 2011, **4**, 139.

[10] M. Yuasa, N. Yamazoe and K. Shimanoe, *J. Electrochem. Soc.*, 2011, **158**, A411.

[11] Zener C., *Phys Rev*, 1951, **2**, 403.

[12] A. S. Patra, N. V. Kumar, D. Barpuzary, M. De and M. Qureshi, *Materials Letters*, 2014, **131**, 125.

[13] J. Ran, J. Zhang, J. Yu, M. Jaroniec and S. Z. Qiao, *Chem. Soc. Rev.*, 2014, **43**, 7787.

[14] D. Li, J. Shi and C. Li, *Small*, 2018, **14**, 1704179.

[15] P. Munnik, P. E. Jongh and K. P. Jong, *Chem. Rev.*, 2015, **115**, 6687.

[16] M. W. Kanan, J. Yano, Y. Surendranath, M. Dinca, V. K. Yachandra and D. G. Nocera, J. *Am. Chem. Soc.*, 2010, **132**, 13692.

[17] M. W. Kanan and D. G. Nocera, *Science*, 2008, **321**, 1072.

[18] S. K. Pilli, T. E. Furtak, L. D. Brown, T. G. Deutsch, J. A. Turner and A. M. Herring, *Energy Environ. Sci.*, 2011, **4**, 5028.

[19] G. M. Carroll, D. K. Zhong and D. R. Gamelin, *Energy Environ. Sci.*, 2015, **8**, 577.

[20] D. A. Lutterman, Y. Surendranath and D. G. Nocera, *J. Am. Chem. Soc.*, 2009, **131**, 3838.

[21] Y. Surendranath, M. W. Kanan and D. G. Nocera, *J. Am. Chem. Soc.*, 2010, **132**, 16501.

[22] C. -Z. Yuan, Y. -F. Jiang, Z. Wang, X. Xie, Z. -K. Yang, A. B. Yousaf and A. -W. Xu, *J. Mater. Chem. A*, 2016, **4**, 8155.

[23] A. Giri, N. Goswami, M. S. Bootharaju, P. L. Xavier, R. John, N. T. K. Thanh, T. Pradeep, B. Ghosh and S. K. Pal, *J. Phys. Chem. C*, 2012, **116**, 25623

[24] L. Ai, Z. Niu and J. Jiang, *Electrochim. Acta*, 2017, **242**, 355.

[25] G. Ai, R. Mo, H. Li and J. Zhong, *Nanoscale*, 2015, **7**, 6722.

[26] L. Yu, H. Zhou, J. Sun, F. Qin, F. Yu, J. Bao, Y. Yu, S. Chen and Z. Ren, *Energy Environ. Sci.*, 2017, **10**, 1820.

[27] K. McBride, J. Cook, S. Gray, S. Felton, L. Stella and D. Poulidi, *CrystEngComm*, 2016, **18**, 407.

CHAPTER 4

Transcription strategy: Morphological transformation of Strontium doped lanthanum manganite for oxygen evolution reactions

This chapter focusses on the effect of morphological variation on the performance of oxygen evolution reaction (OER). Here, strontium doped lanthanum manganite (LSMO) has been utilized as the electrocatalyst, which in general is synthesized via high temperature solid-state route leaving no scope for induction of morphological features. Herein, a transcription methodology has been utilized, where its precursor, manganese oxide, is synthesized with desired morphology and later used as template during solid-state reaction for induction of the morphology onto the LSMO.

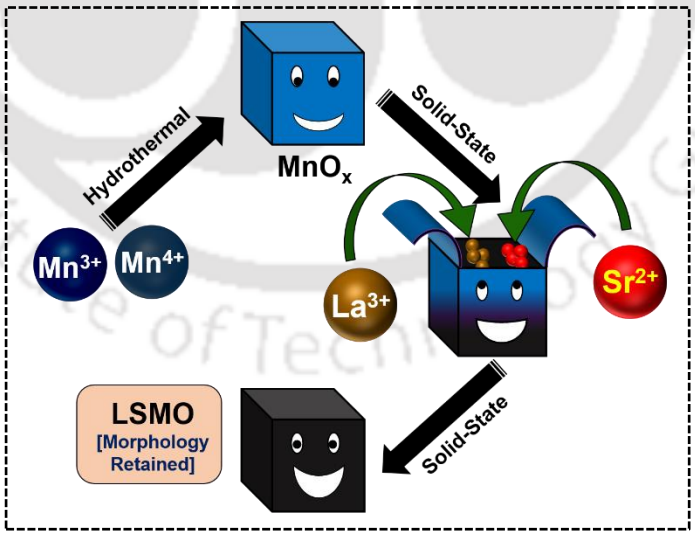

S. Bhowmick, et al., *Sustainable Energy Fuels*, 2021,**5**, 6392-6405

4.1. Introduction

Heterogeneous catalysis is a surface phenomenon where the catalyst provides the active sites for the conversion of the reactants to the products.[1] Apart from the stability and kinetics of the catalyst, the concentration of the electrochemical active sites determines the catalytic efficiency. Number of electrochemical active sites mainly depends on the extent of the exposed surface, governed by its morphology.[2,3] Thus, an important strategy to improve the efficacy of a catalyst is by increasing the electrochemical active sites by virtue of its rationally designed morphologies.[4,5] One of the guiding principles of the shape selectivity by a molecule is based on its crystalline energy of formation and intrinsic anisotropic growth behavior.[6-8] Several synthetic procedures such as templating methods, change in reaction conditions, and use of structure-directing agents have been utilized to prepare desired morphologies for the molecules.[9-11]

Among various heterogeneous catalysts, metal oxides are most widely employed, either as active phase or as a support, owing to their high activity and stability.[12] The high activity of metal oxides is due to the redox properties of the metal ion which eases the charge transfer process within the system.[12,13] Complex metal oxides containing two or more metal ions have better catalytic activity than the uni-metal oxides due to the presence of multiple redox centres.[14] The multivalent transition metal oxides belong to a predominant class of catalysts owing to their low cost of production, easy regeneration of the active species and selectivity.[12] In recent times, 3 D perovskite oxides (ABO_3), with alkaline or rare-earth metal ion in A-site and transition metal ion in the B-site are widely investigated for their applications due to their electronic, ionic, magnetic, catalytic and other environmentally friendly properties.[15-17] The high temperature solid-state synthetic route of the perovskite oxide results in non-uniform random morphology with less electrochemical active surface area.[14,18] Conventional solid-state reaction utilizes commercially available precursor molecules possessing no unique morphological feature thereby resulting in the formation of random morphology. Also, at high temperature, the stability of structure directing agents (SDA) is questionable and makes them unfavourable to be employed during the reaction. Although, few synthetic protocols have been exploited to design specific structures for the perovskite molecules but morphological flexibility is yet to be achived.[19-23] To achieve versatile morphological features of perovskite oxides which can lead to superior properties in terms of active surface area and transport phenomenon, transcription methodology is utilized, where one of the precursor molecules can be tuned with desired morphology and use the

obtained morphological precursor as a directing template during the solid-state reaction for the transcription of its morphology.

Among various applications of surface/morphology modification, electrochemical water splitting phenomena utilizes surface active sites formed for the production of hydrogen and oxygen from environmental benign source, water.[24] The four-electron transfer mechanism results in complex thermodynamic possibilities of the oxygen evolution reaction (OER), limits the overall efficiency of water splitting process.[25] Most of the metal oxides are designed to confront the kinetic barrier to surpass the performance of the state-of-art catalyst, such as IrO_2.[26] Perovskite oxides with the advantage of high flexibility of elemental composition, rich electronic/defect structure, high conductivity and chemical stability makes them good candidates for electrocatalytic OER activity.[27,28] Researchers have utilized ABO_3 type perovskites, e.g., $LaMnO_3$,[29] as water oxidation catalysts and found that the doped counterparts, ($La_{0.7}Sr_{0.3}MnO_3$,[30] $La_{0.5}Sr_{0.5}MnO_3$,[31] $(La_{0.8}Sr_{0.2})_{0.95}MnO_{3-\delta}$,[32] etc.) exhibits better OER activity on virtue of its increased conductivity due to the modification of Mn–O–Mn bond angle providing facile movement of charged species within the bulk. Water oxidation being a surface phenomenon, high electrochemical active surface area (ECSA), which is directly proportional to double-layer capacitance at the electrolyte interface, is also one of the key parameters for the enhancement of OER activity.[33-35] The synthetic procedure of perovskite oxides restricts the formation of high electrochemical active sites due to the inherent random non-uniform morphology. Sphere shaped perovskite oxide ($LaMn_{0.3}Co_{0.7}O_3$) exhibited better electrocatalytic activity that the random shaped perovskite oxide owing to higher electroactive sites.[36] In order to counter the limitation of electrochemical active sites, the morphology transcription methodology can be utilized during the solid-state process for the formation of desired morphology of the perovskite oxide.

In this work we have utilized strontium doped lanthanum manganite as the perovskite metal oxide and tuned its morphology for enhancement of its activity towards electrochemical water oxidation. 30 at. % strontium doped lanthanum manganite ($La_{0.7}Sr_{0.3}MnO_3$) is best known for its higher conductivity and activity towards OER compared to other doped counterparts.[18,30,37,38] The $La_{0.7}Sr_{0.3}MnO_3$ (**LSMO**) is conventionally synthesized using lanthanum, strontium and manganese precursors at high temperatures which results in the formation of no controlled morphology. Desirable morphologies of **LSMO** were attained by the utilization of our proposed transcription methodology. Here we have tuned the morphology of manganese oxide (Mn_xO_y) using

hydrothermal method under different reaction conditions and later utilized it as a template for transcription of respective morphology into the synthesized **LSMO**. The development of anisotropic/ isotropic morphologies for **LSMO** resulted in the enhancement of electrochemical active sites as confirmed by the double layer capacitance measurements and escalated water oxidation catalytic activity. We believe that this method can be utilized as a model system for other complex metal oxide/ chalcogenides, where morphological tuning is a critical component in improving the electrocatalytic properties. Also, a detailed report comparing the OER performances of various manganese-based perovskite oxides is tabulated (Table 3) supporting the importance of our methodology for the synthesis of morphological **LSMO**.

4.2. Experimental Section

4.2.1. Synthesis of morphological Mn_xO_y

The diversified morphologies of Mn_xO_y were obtained by utilizing the following synthetic protocols.

(i) Cuboidal shaped Mn_2O_3:

Manganese nitrate ($Mn(NO_3)_2$) (1 mmol) and urea (1 M) were dissolved in 30 mL H_2O. The mixture was stirred for 2h and transferred to stainless steel autoclave and reacted @ 180 °C for 20h, then centrifuged and washed using H_2O-EtOH mixture. Finally, it was calcined @ 550 °C for 2h with ramp of 10 °C/min.

(ii) Rod shaped Mn_2O_3:

Potassium permanganate ($KMnO_4$) (2.5 mmol) and manganese chloride ($MnCl_2$) (1 mmol) were dissolved in 30 mL H_2O. The mixture was stirred for 2 h and transferred to stainless steel autoclave and reacted @ 160 °C for 12 h, then centrifuged and washed using H_2O-EtOH mixture. Finally, it was calcined @ 550 °C for 2 h with ramp of 10 °C/min.

(iii) Flake shaped KMn_8O_{16}:

Potassium permanganate ($KMnO_4$) (1 mmol) was dissolved in 30 mL H_2O along with concentrated HCl (0.5 mL) and H_2O_2 (1 mL). The mixture was stirred for 2h and transferred to stainless steel autoclave and reacted @ 160 °C for 12h, then centrifuged and washed using H_2O-EtOH mixture. Finally, it was calcined @ 550 °C for 6h with ramp of 5 °C/min.

(iv) Nano-block shaped β-MnO_2:

Potassium permanganate ($KMnO_4$) (1 mmol) and manganese chloride ($MnCl_2$) (2.5 mmol) were dissolved in 30 mL H_2O. The mixture was stirred for 2 h and transferred to stainless steel autoclave and reacted @ 180 °C for 20 h, then centrifuged and washed using H_2O-EtOH mixture. Finally, it was calcined @ 400 °C for 2 h with ramp of 10 °C/min.

(v) Fused-rods shaped Mn_2O_3:

Manganese chloride ($MnCl_2$) (1 mmol) and potassium permanganate ($KMnO_4$) (2.5 mmol) were dissolved in 30 mL H_2O and later xanthan gum (30 mg) was added to it. After stirring for an hour, the mixture was transferred to stainless steel autoclave and reacted @ 160 °C for 24 h. Finally, it was centrifuged using H_2O-EtOH mixture and after drying calcined @ 550 °C for 6 h with ramp of 5 °C/min.

(vi) Fused-cubes shaped Mn_2O_3:

Manganese chloride ($MnCl_2$) (2.5 mmol) and potassium permanganate ($KMnO_4$) (1 mmol) were dissolved in 30 mL H_2O and later ammonium fluoride (30 mg) was added to it. After stirring for an hour, the mixture was transferred to stainless steel autoclave and reacted @ 160 °C for 24 h. Finally, it was centrifuged using H_2O-EtOH mixture and after drying calcined @ 550 °C for 6 h with ramp of 5 °C/min.

(vii) Spherical shaped Mn_2O_3:

Manganese sulphate ($MnSO_4$) (1 mmol), ammonium carbonate (3 mmol) and alginic acid (1 mg/mL) were dissolved in 30 mL H_2O. The mixture was stirred for 2h and transferred to stainless steel autoclave and reacted @ 80 °C for 4 h, then centrifuged and washed using H_2O-EtOH mixture. Finally, it was calcined @ 550 °C for 6 h with ramp of 5 °C/min.

(viii) Wire shaped α-MnO_2:

Potassium permanganate ($KMnO_4$) (3 mmol) was dissolved in 30 mL H_2O and kept for stirring. Then concentrated HCl (10 mmol) was added to it along with polyvinyl alcohol (1 mg/mL) and then the mixture was transferred to stainless steel autoclave and reacted @ 160 °C for 12 h. After the reaction the product was centrifuged using H_2O-EtOH mixture and dried in oven @ 60 °C overnight.

4.2.2. Transcription of morphological Mn_xO_y into corresponding $La_{0.7}Sr_{0.3}MnO_3$ (LSMO)

For the synthesis of morphological **LSMO** (**Scheme 4.2.1**), the different synthesized Mn_xO_y were utilized as the Mn source during the solid-state route. Here stoichiometric amount of La_2O_3, $SrCO_3$ and Mn_xO_y were taken in mortar-pestle and ground well and then subjected to calcination in a muffle furnace @ 1000 °C for 16 h at a heating rate of 5 °C/min. For comparing the morphological **LSMO** with conventionally synthesized **LSMO**, similar procedure was followed taking commercial MnO_2 as the Mn source alongside La_2O_3 and $SrCO_3$ in stoichiometric amount.

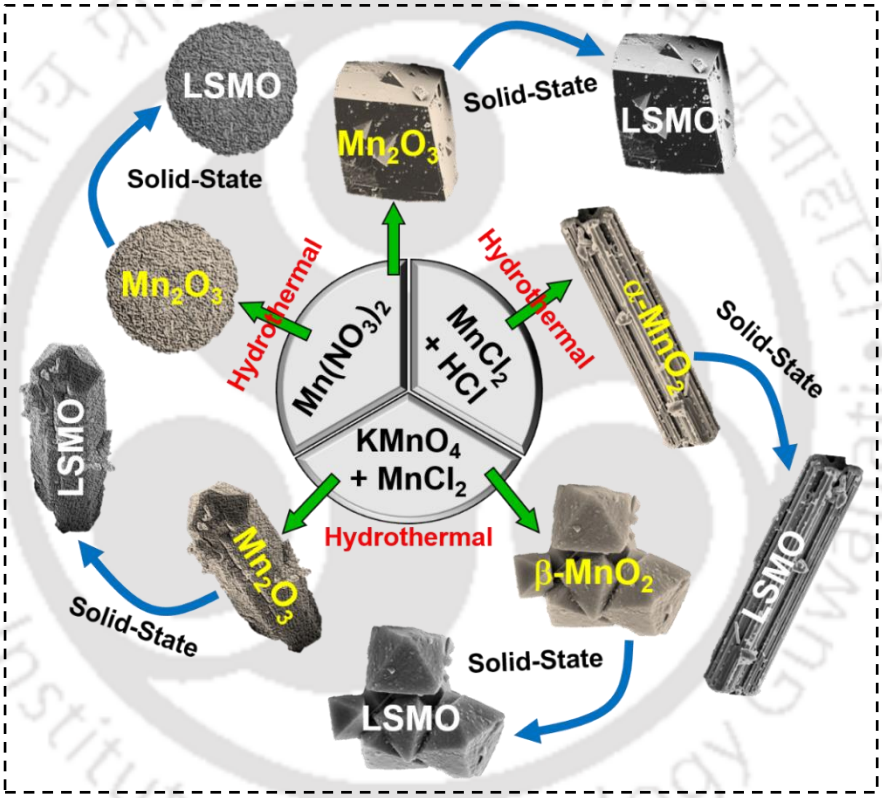

Scheme 4.2.1. Synthetic protocol for the formation of morphological Mn_xO_y synthesized via hydrothermal route which are used as template during the solid-state reaction for transcription of its morphology into the corresponding **LSMO**

4.2.3. Rietveld Analysis

The agreement of Rietveld refined data was evaluated with initial parameters in relation to the weighted and expected residual factors (R_{wp}, R_{ex}), and their ratio, corresponding to the goodness-of-fit (χ^2). The weighted-profile R value, R_{wp} was defined as

$$R_{wp} = [\Sigma_i W_i\{Y_i(obs) - Y_i(cal)\}^2 / \Sigma_i W_i\{Y_i(obs)\}^2]^{1/2} \quad \ldots (4.1)$$

where, Y_i (obs) was the observed intensity at step i, Y_i (cal) the calculated intensity, and W_i the weight. The expected R value (R_{exp}) was defined as

$$R_{exp} = \left[(N - P)\,\Sigma_i^N W_i\{Y_i(obs)\}^2\right]^{1/2} \quad \ldots (4.2)$$

where, N and P correspond to the number of observations and parameters respectively.

4.3. Results and Discussions

4.3.1. Experimental Modification Induced Morphological Features

A library of Mn_xO_y morphologies with different crystalline phases were synthesized for transcriptional purpose of its higher analogues by altering various experimental conditions. The morphological features of the Mn_xO_y and their respective analogues i.e. doped lanthanum manganites were analyzed by field emission scanning electron microscopy (**FESEM**) technique. From **Figure 4.3.1**, it can be seen that the inherent morphologies of Mn_xO_y were transcripted into the corresponding **LSMO** via a two-step process. The cuboidal Mn_2O_3 (**Figure 4.3.1(a)**) transcripted to form cuboidal **LSMO** (**Figure 4.3.1(e)**),

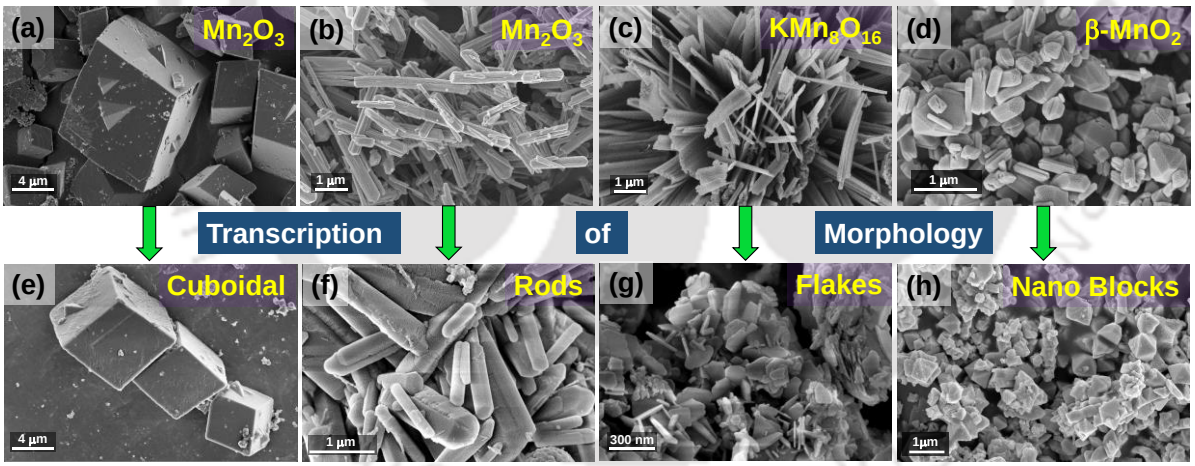

Figure 4.3.1. FESEM images of (a) cuboidal Mn_2O_3 (b) rod shaped KMn_8O_{16} (c) flake shaped Mn_2O_3 (d) nano-block shaped β-MnO_2 synthesized via modification in experimental conditions and (e-h), representing the corresponding morphological features of **LSMO** transcripted from their respective Mn_xO_y.

similarly, the rod-shaped Mn_2O_3 (**Figure 4.3.1(b)**), flake-shaped KMn_8O_{16} (**Figure 4.3.1(c)**), and nano-block shaped β-MnO_2 (**Figure 4.3.1(d)**) resulted in the formation of the **LSMO** with the corresponding morphologies; rods (**Figure 4.3.1(f)**), flakes (**Figure 4.3.1(g)**), and nano-blocks (**Figure 4.3.1(h)**).

The formation steps of a host of morphologies of the Mn_xO_y have been demonstrated schematically in **Figure 4.3.2**.

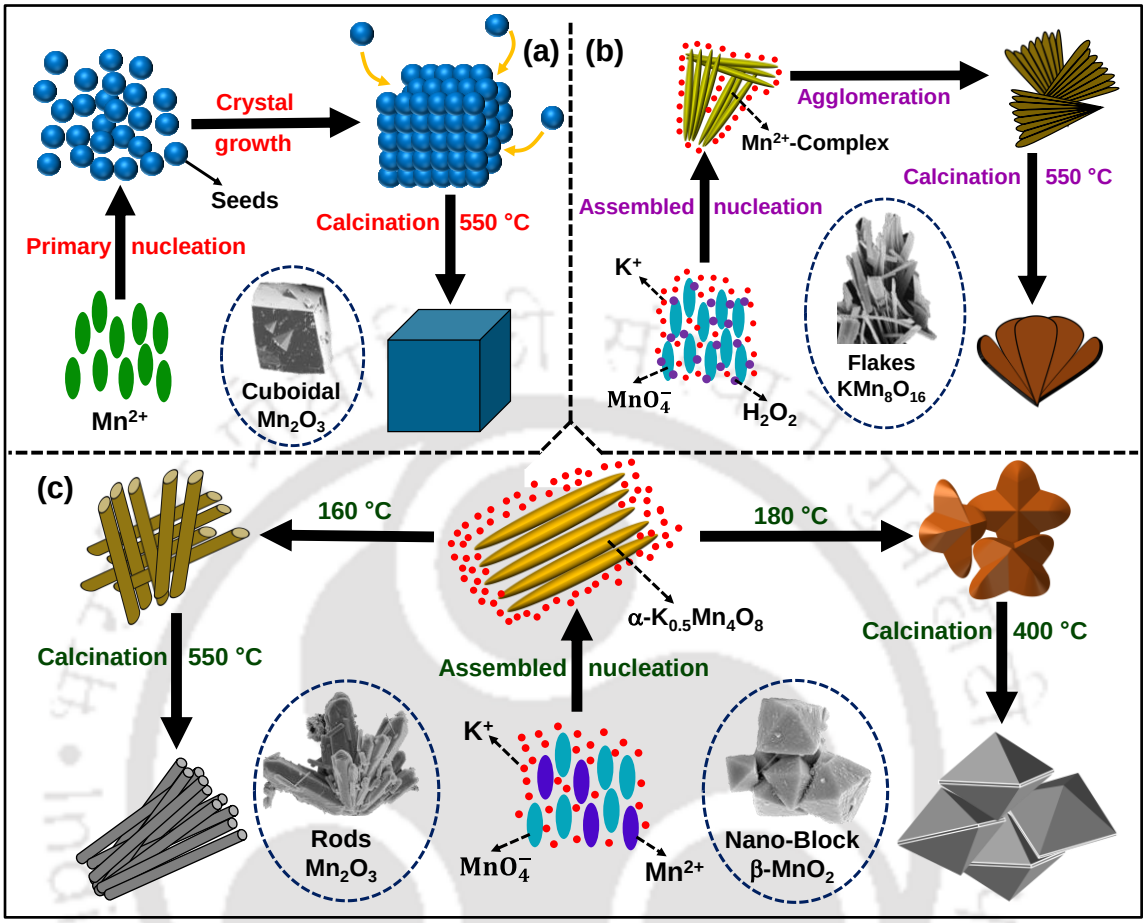

Figure 4.3.2: Schematic representation of the plausible mechanism for the formation of (a) cuboidal Mn_2O_3, (b) flake shaped KMn_8O_{16}, and (c) rod shaped Mn_2O_3 and nano-block shaped β-MnO_2

The formation steps of a host of morphologies of the Mn_xO_y have been demonstrated schematically in **Figure 4.3.2**. The crystal lattice of the Mn_2O_3 is cubic and upon reaction with Mn^{2+} ions, under no additional influence/ reagents, it prefers to form the thermodynamically stable cuboidal shape (**Figure 4.3.2(a)**).[39,40] In **Figure 4.3.2(b)**, $KMnO_4$ reacts with oxidizing agent H_2O_2 in acidic medium and results in the formation of nano wire shaped Mn^{2+}- adduct. The K^+ ions stabilizes the formed nanowire-adduct which gets self – assembled/agglomerates and transforms into the flake like structures upon calcination.[41] **Figure 4.3.2(c)** shows the formation of Mn_2O_3 rods and nano-block shaped β-MnO_2 under different thermal conditions starting from the same reaction precursors as shown in first two steps. In the initial step, the mixture of $KMnO_4$ and $MnCl_2$ undergoes nucleation, resulted in the formation of nanowire shaped α-$K_{0.5}Mn_4O_8$, stabilized by the K^+ cations. Further, the reaction at 160 °C it retains the rod shaped Mn_2O_3 upon calcination,[41,42] whereas, at high

temperature of 180 °C, the rod-shaped structures deformed and re-organize themselves into a pyramid like nano-block shaped β-MnO_2.[6,43]

4.3.2. Structure Directing Agents (SDA) Induced Morphological Transformation

Structure directing agents (SDA) are utilized for their ability to direct the growth of molecules in specific orientation thus defining its morphology. In the nucleation stage, the SDA organizes into small structural building fragments of a particular geometrical topology around itself and provides the initial seed points for a unique structure type. Thus, to further tune different morphologies for Mn_xO_y, SDA molecules were used during its hydrothermal synthesis and were then utilized as template for the synthesis of morphological **LSMO**. The compounds were analyzed using FESEM technique to visualize the morphological features (**Figure 4.3.3**). As can be seen the structure directing agent, xanthan gum (XG), forms fused-rod shaped Mn_2O_3 (**Figure 4.3.3(a)**) which further transcripted into fused-rod shaped **LSMO** (**Figure 4.3.3(e)**). Similarly, when ammonium fluoride (NH_4F) was used as SDA resulted the formation of fused-cube shaped Mn_2O_3 (**Figure 4.3.3(b)**) which transcribed into fused-cube shaped **LSMO** (**Figure 4.3.3(f)**). The use of SDA, Alginic acid (AÂ), results in spherical Mn_2O_3 (**Figure 4.3.3(c)**) which further transcribed into spherical **LSMO** (**Figure 4.3.3(g)**).

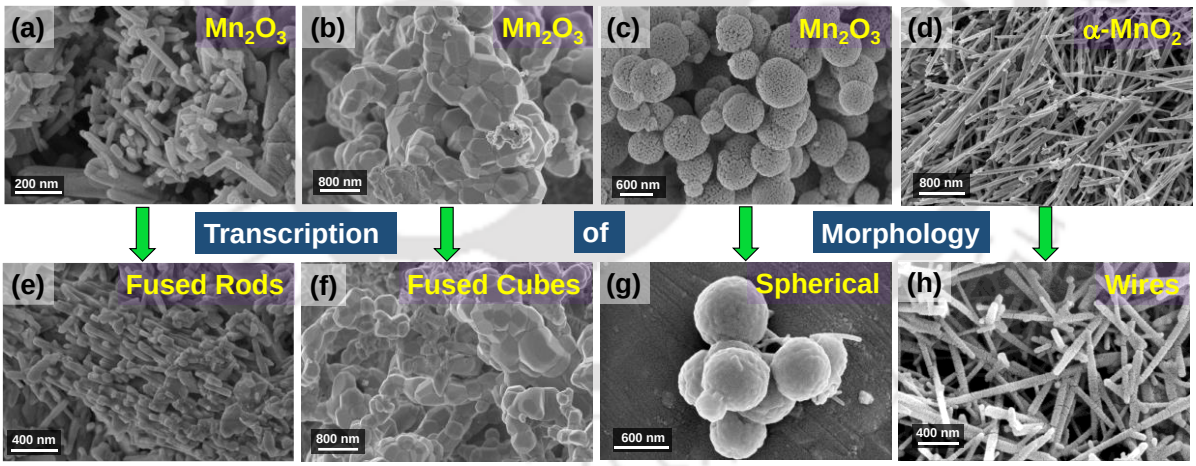

Figure 4.3.3. FESEM images of (a) fused-rod shaped Mn_2O_3, (b) fused-cube shaped Mn_2O_3, (c) spherical Mn_2O_3, (d) wire shaped α-MnO_2 synthesized hydrothermally utilizing the SDA molecules and (e-h) their corresponding transcripted morphological **LSMO**

Polyvinyl alcohol (PVA) resulted in the formation of wire shaped α-MnO_2 (**Figure 4.3.3(d)**) which transcribed into wire shaped **LSMO** (**Figure 4.3.3(h)**).

The formation of morphologies of Mn_xO_y synthesized using SDA molecules has been presented schematically in **Figure 4.3.4**.

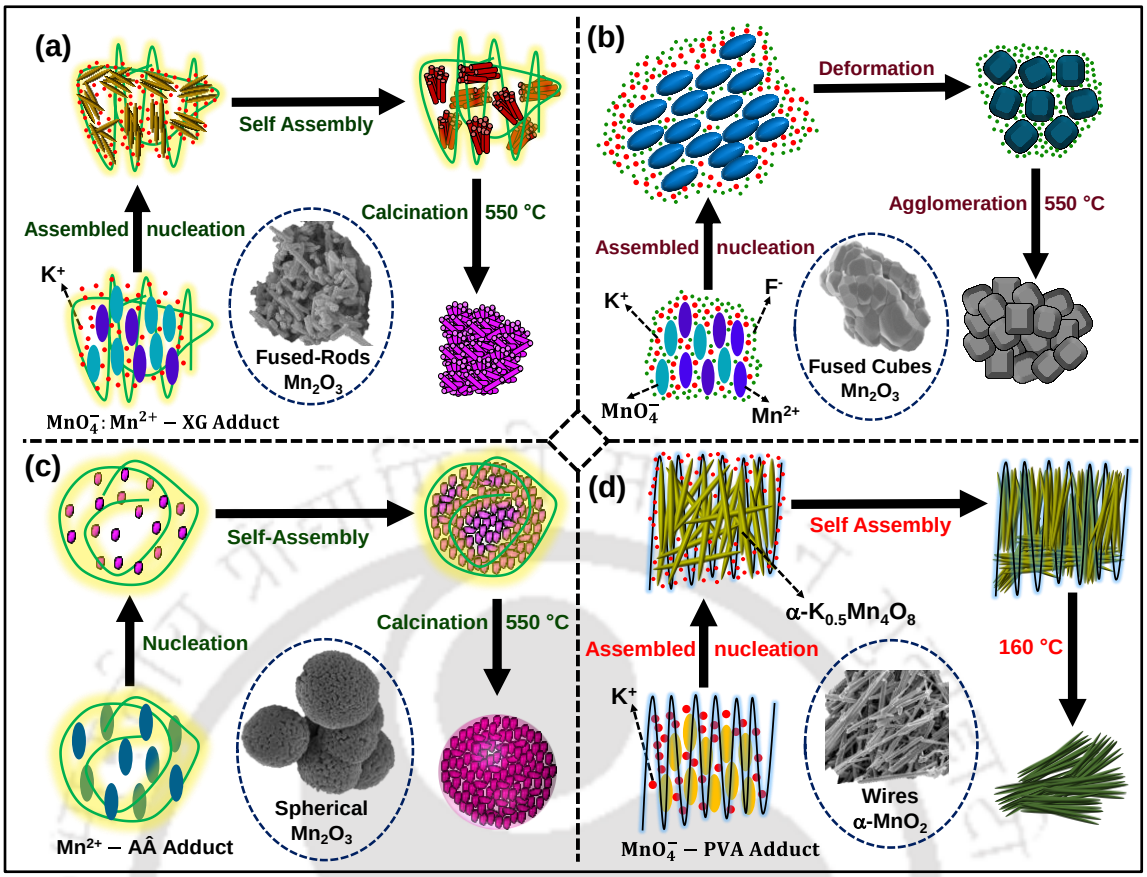

Figure 4.3.4: Schematic representation of the plausible mechanism for the formation of (a) fused-rod shaped Mn_2O_3, (b) fused-cube shaped Mn_2O_3, (c) spherical Mn_2O_3, and (d) wire shaped α-MnO_2

For the synthesis of fused-rod shaped Mn_2O_3 xanthan gum (XG) is used along with $KMnO_4$ and $MnCl_2$, where it forms an adduct complex, $MnO_4^-: Mn^{2+} - XG$ (**Figure 4.3.4(a)**). During the course of reaction, $KMnO_4$ and $MnCl_2$ undergoes nucleation forming nanowire shaped α-$K_{0.5}Mn_4O_8$ which in presence of XG molecule undergoes self-assembly and upon calcination results in Mn_2O_3 fused-rods. In **Figure 4.3.4(b)**, when the NH_4F is used as SDA, it resulted in the restricted growth of the α-$K_{0.5}Mn_4O_8$ upon the redox reaction of $KMnO_4$ and $MnCl_2$.[44] The α-$K_{0.5}Mn_4O_8$ forms a complex with the F^- ions and during the reaction it deforms into cube shaped entities. Further upon calcination the deformed cubes agglomerates and forms the fused-cube shaped Mn_2O_3.[45] For synthesizing spherical morphology of Mn_2O_3, alginic acid (AÂ) was used along with $MnSO_4$ and $(NH_4)_2CO_3$, where it forms an adduct, $MnCO_3$ – AA (**Figure 4.3.4(c)**). The nucleation of the formed $MnCO_3$ followed by self-assembly in presence of AÂ takes the spherical shape which upon calcination results into spherical Mn_2O_3.[39,40] In **Figure 4.3.4(d)**, polyvinyl alcohol (PVA) is used for the synthesis of nanowired α-MnO_2. $KMnO_4$ forms an adduct with PVA (MnO_4^- – PVA) and subsequently

upon the reaction forms α-$K_{0.5}Mn_4O_8$, which under the influence of PVA self-assembles to form nanowires.[41-43]

4.3.3. Conventional Solid-State Induced Random Morphological Features

The morphology of conventionally synthesized solid-state **LSMO** from commercially available MnO_2 (**Figure 4.3.5**) resulted in random and non-uniform morphologies. Thus, in the transcription methodology, the doped lanthanum manganites were successfully designed with preferred uniform morphologies by calcination of the predefined morphological Mn_xO_y as a template.

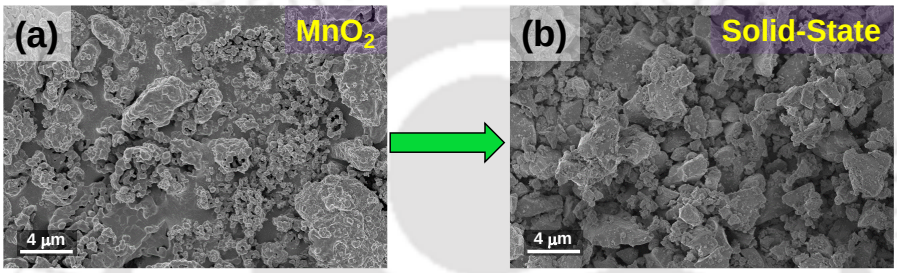

Figure 4.3.5. (a) FESEM image of commercial MnO_2 and (b) FESEM image of the LSMO synthesized using conventional solid-state method utilizing the commercial MnO_2

4.3.4. Experimental Modification Induced Crystal Phases & Rietveld Refinement

As-synthesized Mn_xO_y phase purity, crystallinity and their transcripted **LSMO** were examined using powder X-ray diffractometer (**PXRD**).

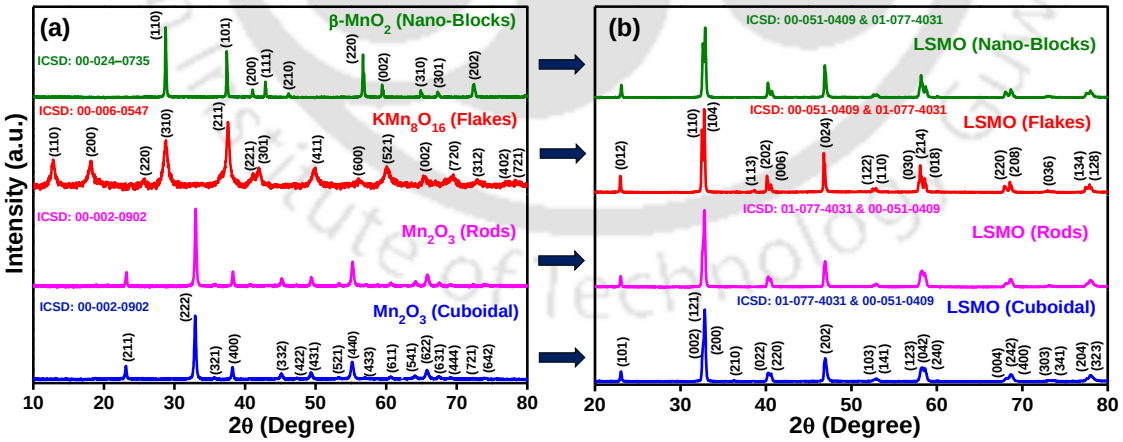

Figure 4.3.6. PXRD pattern of (a) the as-synthesized Mn_xO_y formed by the utilization of SDA, and (b) the corresponding transcripted morphological **LSMO**

From **Figure 4.3.6(a, b)** it can be seen that, for both Mn_xO_y and **LSMO**, the peaks are indexed to corresponding phases with no detectable impurities. In **Figure 4.3.6(a)** the synthesized cuboidal and rod-shaped Mn_2O_3 corresponds to the cubic phase (ICSD No. 00-

002-0902), the flake shaped KMn_8O_{16} and the β-MnO_2 corresponds to tetragonal phase (ICSD No. 00-006-0547 and 00-024–0735, respectively). **Figure 4.3.6(b)** demonstrates the PXRD patterns for the **LSMO** synthesized from their corresponding morphological Mn_xO_y.

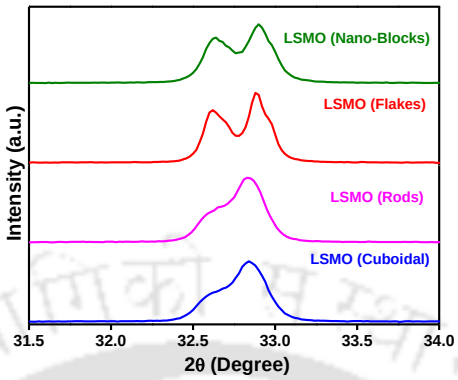

Figure 4.3.7. The enlarged XRD spectra at ~32° of the morphological LSMO demonstrating the pattern of the peak split

As can be observed, the ratio of splitting, an indication of mixed phases, in the major peak at ~32° (**Figure 4.3.7**) varies for **LSMO** synthesized from the different Mn_xO_y phases.

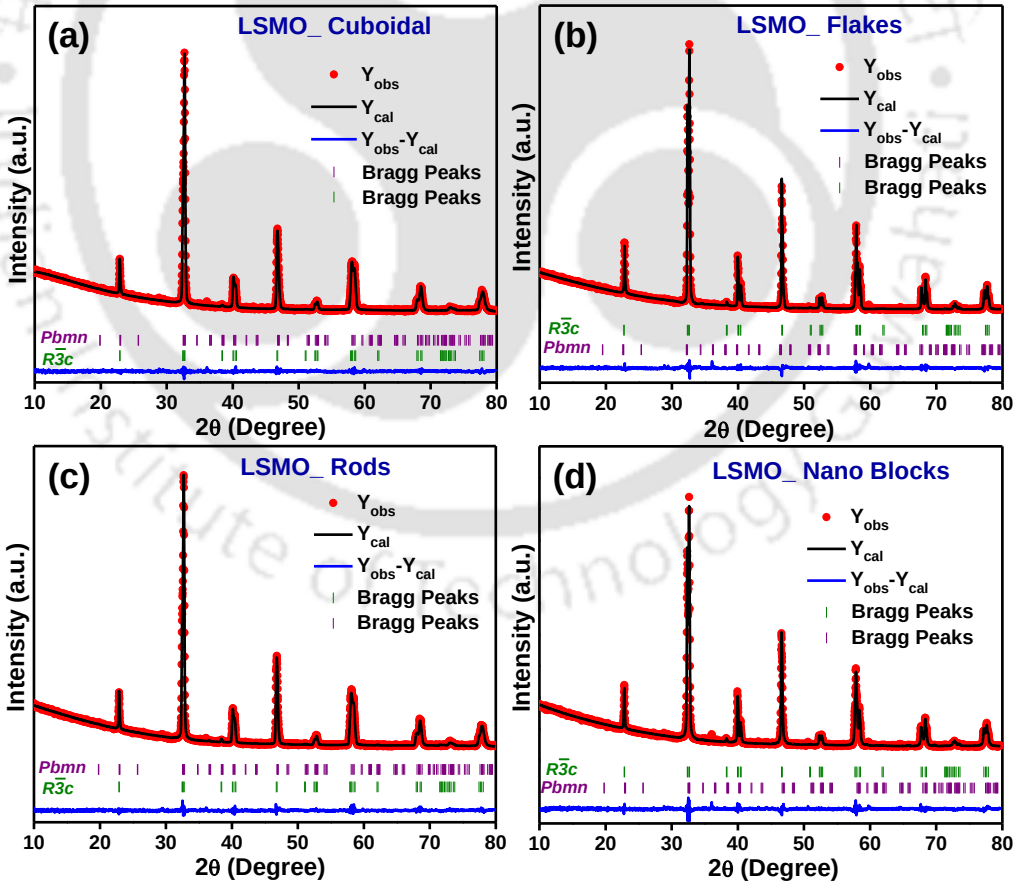

Figure 4.3.8. Rietveld refined XRD spectra of morphological LSMO synthesized from (a) cuboidal Mn_2O_3, (b) flake shaped KMn_8O_{16}, (c) rod shaped Mn_2O_3, and (d) nano-block shaped β- MnO_2 showing the presence of both rhombohedral and orthorhombic phases

The presence of mixed phases in the **LSMO** was also confirmed by Rietveld refinement corresponding to two different phases, namely, rhombohedral and orthorhombic (ICSD No. 00-051-0409 and 01-077-4031) as shown in **Figure 4.3.8**. The detailed results are tabulated in **Table 4.3.1** with the percentage of the formed phases in the **LSMO**. It is observed that the **LSMO** synthesized from cubic phase of Mn_2O_3 results in the formation of orthorhombic as the dominant phase, whereas the **LSMO** synthesized from tetragonal phase of KMn_8O_{16} and β-MnO_2 resulted in the formation of rhombohedral as the dominant phase.

Table 4.3.1. Summary of the Rietveld refinement of the morphological LSMO and the conventional solid-state LSMO demonstrating the percentage of the formed mixed phases

Template MnO_x			**Transcripted $La_{0.7}Sr_{0.3}MnO_3$**		
Compound	**Morphology**	**Phase**	**Goodness-of-fit (χ^2)**	**Rhombohedral (R3c)**	**Orthorhombic (Pbmn)**
Mn_2O_3	Cuboidal	Cubic	1.73	43.97%	56.03%
KMn_8O_{16}	Flakes	Tetragonal	3.00	99.98%	0.02%
Mn_2O_3	Rods	Cubic	2.02	38.93%	61.07%
β-MnO_2	Nano-Blocks	Tetragonal	2.79	95.68%	4.32%

4.3.5. Structure Directing Agents (SDA) Induced Crystal Phases & Rietveld Refinement

The phase purity and crystallinity of the as-synthesized Mn_xO_y and the transcripted **LSMO** were determined using PXRD technique.

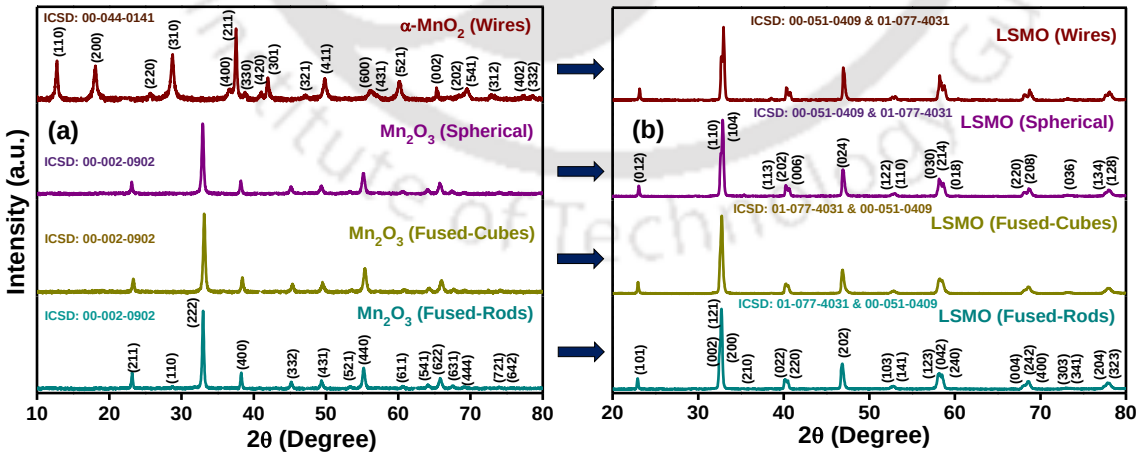

Figure 4.3.9. PXRD pattern of (a) morphological parent Mn_xO_y under different experimental conditions, and (b) the corresponding morphological **LSMO** transcripted from their parent Mn_xO_y.

The peaks of the synthesized fused-rod shaped, fused-cube shaped and spherical Mn_2O_3 (**Figure 4.3.9(a)**) are indexed to the cubic phase (ICSD No. 00-002-0902) while that of wire shaped α-MnO_2 to tetragonal phase (ICSD No. 00-044-0141). **Figure 4.3.9(b)** demonstrates the PXRD patterns of the correspondingly synthesized morphological **LSMO** with no detectable impurity peaks.

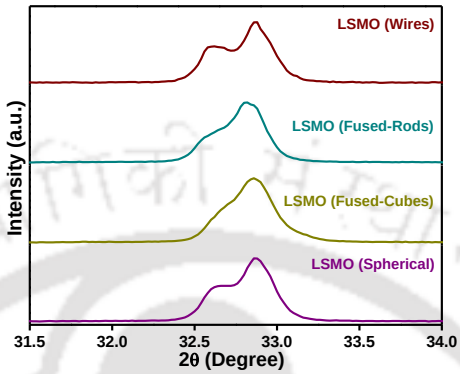

Figure 4.3.10. The enlarged XRD spectra at ~32° of the morphological LSMO demonstrating the pattern of the peak split

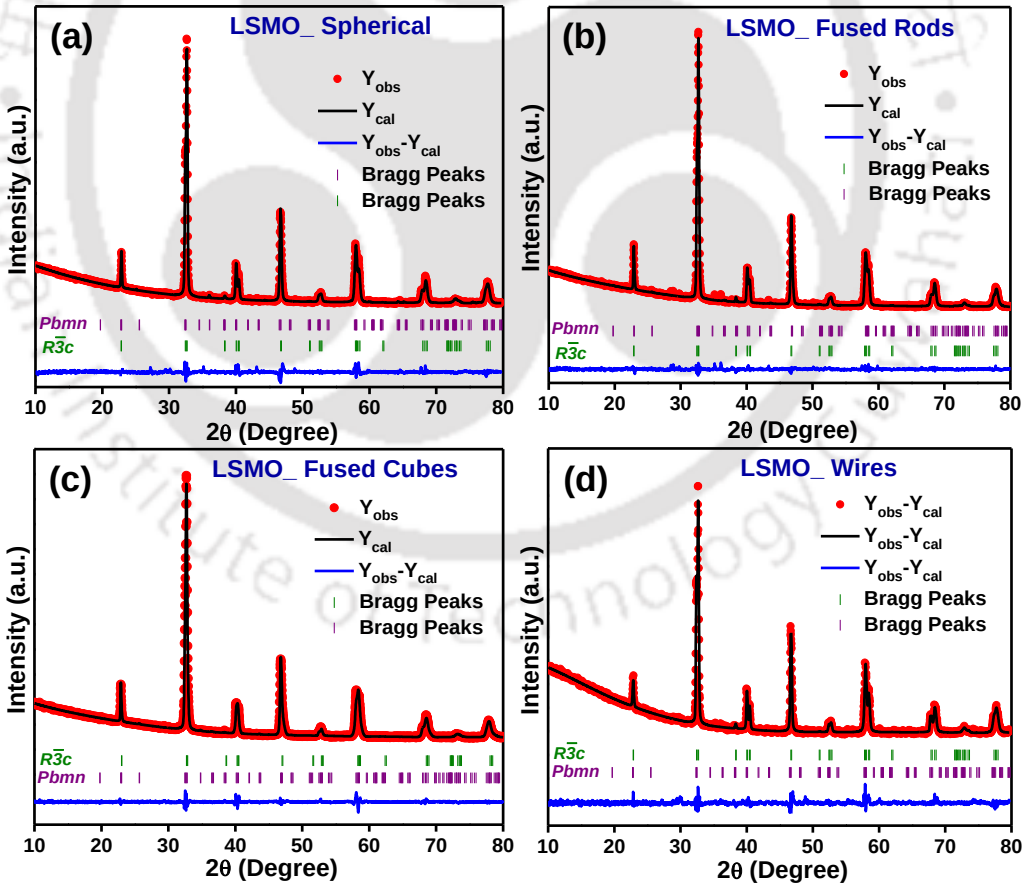

Figure 4.3.11. Rietveld refined XRD spectra of morphological LSMO synthesized from (a) spherical Mn_2O_3, (b) fused-rod shaped Mn_2O_3, (c) fused-cube shaped Mn_2O_3, and (d) wire shaped α-MnO_2 showing the presence of both orthorhombic and rhombohedral phases

The ratio of splitting in major peak at ~32° (**Figure 4.3.10**) is different for the **LSMO** synthesized from the Mn_xO_y of cubic and tetragonal phases, indicating the formation of mixed phases in the **LSMO**, which further confirmed by the Rietveld refinement, confirming the rhombohedral and orthorhombic phases (ICSD No. 00-051-0409 and 01-077-4031) as shown in **Figure 4.3.11** with the phase percentage details given in **Table 4.3.2**. The **LSMO** synthesized from the cubic phase of Mn_2O_3 resulted in the formation of orthorhombic as the dominant phase for fused-rod and fused-cube shaped **LSMO**, while for the spherical **LSMO** the dominant phase is rhombohedral. The wire shaped **LSMO** synthesized from tetragonal phase of α-MnO_2 resulted in the formation of rhombohedral as the dominant phase. Thus, the utilization of a pre-defined morphological Mn_xO_y as template for the transcription methodology results in the formation of desired phase in doped lanthanum manganites.

Table 4.3.2. Summary of the Rietveld refinement of the morphological LSMO and the conventional solid-state LSMO demonstrating the percentage of the formed mixed phases

Template MnO_x			**Transcripted $La_{0.7}Sr_{0.3}MnO_3$**		
Compound	**Morphology**	**Phase**	**Goodness-of-fit (χ^2)**	**Rhombohedral (R3̄c)**	**Orthorhombic (Pbmn)**
Mn_2O_3	Spherical	Cubic	3.30	69.87%	30.13%
Mn_2O_3	Fused-Rods	Cubic	2.44	33.50%	66.50%
Mn_2O_3	Fused-Cubes	Cubic	3.45	49.55%	50.45%
α-MnO_2	Wires	Tetragonal	2.58	99.99%	0.01%

4.3.6. Conventional Solid-State Induced Crystal Phases & Rietveld Refinement

The PXRD pattern of commercial MnO_2 and the LSMO synthesized utilising conventional solid-state route is shown in **Figure 4.3.12**. The commercial MnO_2 corresponds to the well-indexed tetragonal phase (ICSD No. 00-044-0141), and the LSMO to the rhombohedral phase (ICSD No. 00-051-0409). The peak at ~32° for conventional solid-state **LSMO** shows splitting like other synthesized morphological **LSMO** (**Figure 4.3.13(a)**). The Rietveld refinement of the conventional solid-state LSMO was similarly performed (**Figure 4.3.13(b)**) and it showed the presence of single rhombohedral phase (R3̄c).

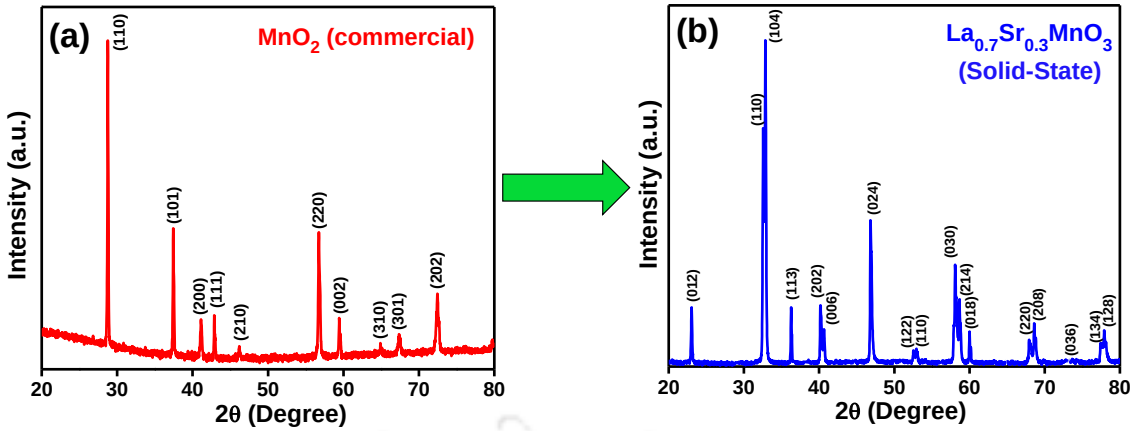

Figure 4.3.12. (a) PXRD plot of commercial MnO_2 and (b) PXRD of the synthesized LSMO using conventional solid-state method utilizing the commercial MnO_2 as Mn source

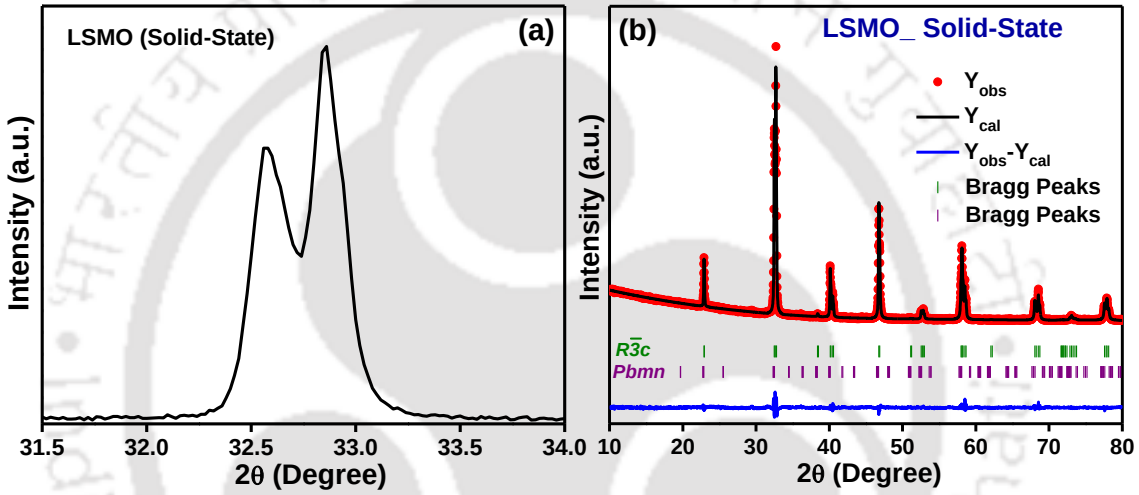

Figure 4.3.13. (a) The enlarged peak at ~32° for the conventional solid-state LSMO, and (b) Rietveld refined XRD spectra of LSMO synthesized from the commercial MnO_2

4.3.7. Mechanistic Insights into the Formation of Morphological LSMO Transcripted from Mn_xO_y

The formation of **LSMO** from the Mn_xO_y occurs via a diffusion controlled solid-state reaction as shown in **Figure 4.3.14**. The retainment of the inherent morphologies of the Mn_xO_y is due to the solid-state diffusions of the La^{3+} and Sr^{2+} ions into the lattice of the Mn_xO_y resulting in the formation of the stoichiometric $La_{0.7}Sr_{0.3}MnO_3$.[21,46-48] Thus, the Mn_xO_y with pre-defined structural morphologies when used as a template during the solid-state reaction along with lanthanum and strontium results in the transcription on its morphology onto the **LSMO**.

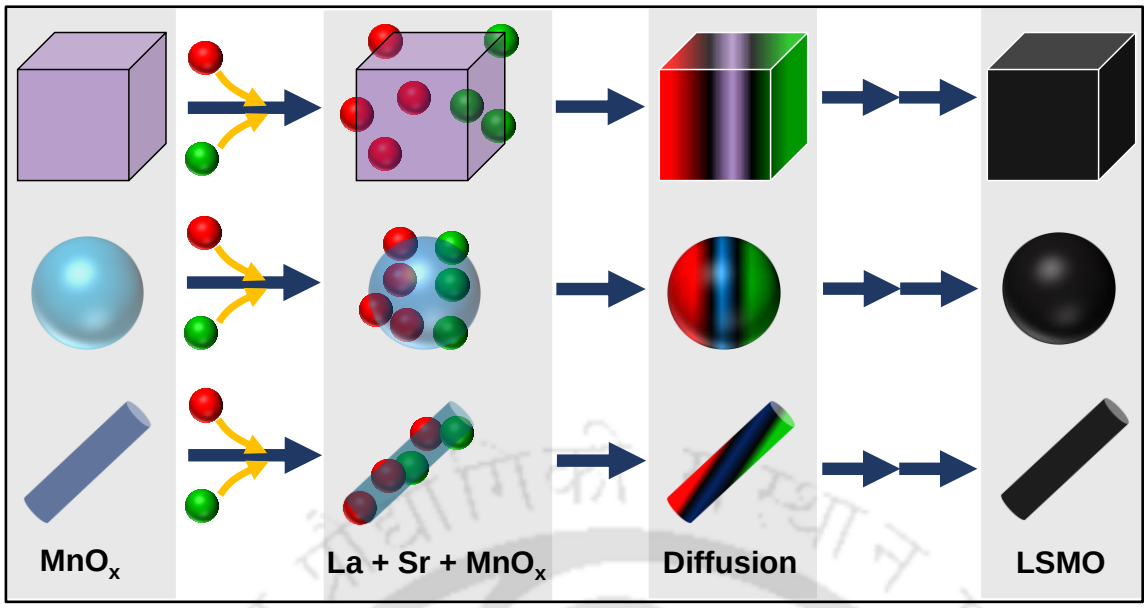

Figure 4.3.14. Schematic representation of the template assisted solid-state formation of morphological **LSMO**

4.3.8. X-Ray Photoelectron Spectroscopy (XPS) Analyses

To investigate the electronic structure and the chemical state of the constituent elements X-ray photoelectron spectroscopy (XPS) analysis was performed. The XPS core-level spectra of La 3d (**Figure 4.3.15(a)**) has been de-convoluted into $3d_{5/2}$ and $3d_{3/2}$. The peaks for at 834.3 eV and 851.3 eV are due to La^{3+} while the peaks at 838.2 eV, 842.8 eV and 855 eV are satellite peaks. Similarly, for the wire-shaped LSMO the peaks at 834.5 eV and 851.2 eV are ascribed to La^{3+} while the peaks at 838.1 eV, 846.8 eV and 854.8 eV are satellite peaks.[30] **Figure 4.3.15(b)** shows the Mn 2p core-level spectra which is de-convoluted into $2p_{3/2}$ and $2p_{1/2}$ levels. The Mn $2p_{3/2}$ peak of general solid-state LSMO featuring at 641.6 eV, 653.4 eV and 643.3 eV, 654 eV can be attributed to Mn^{3+} and Mn^{4+}, respectively. The peak position at 646.6 eV is due to the satellite peak.[19,30] For the wire-shaped LSMO the peaks at 641.5 eV, 653.2 eV and 643.5 eV, 654.2 eV corresponds to Mn^{3+} and Mn^{4+}, respectively, with the satellite peak at 647.3 eV. **Figure 4.3.15(c)** shows the O1s core-level spectra for general solid-state and wire-shaped LSMO. The peaks at 529.6 eV and 529.5 eV, respectively, are due to the lattice oxygen O^{2-} (O_L) associated with Mn atom. The peaks at 531.3 eV and 531.1 eV, respectively, corresponds to the surface adsorbed oxygen species (O_{ads}), like O^-, O^{2-}, or O_2^{2-}. While the respective peaks at 532.9 eV and 532.4 eV corresponds to hydroxyl groups ($O_{O\text{-}H}$) weakly bound to the surface.[19,30] The increase in the area of the peaks for O_{ads} and $O_{O\text{-}H}$ of the wire-shaped LSMO may be due to the enhanced surface area of the compound. In **Figure 4.3.15(d)** the XPS spectra for Sr 3d has been de-

convoluted into respective $3d_{5/2}$ and $3d_{3/2}$ with peak ratio of 3:2. The peaks at 132.9 eV, 132.3 eV and 133.8 eV, 133.5 eV are assigned to Sr^{2+} in the bulk and surface of the material, respectively for general solid-state and wire-shaped LSMO.[30]

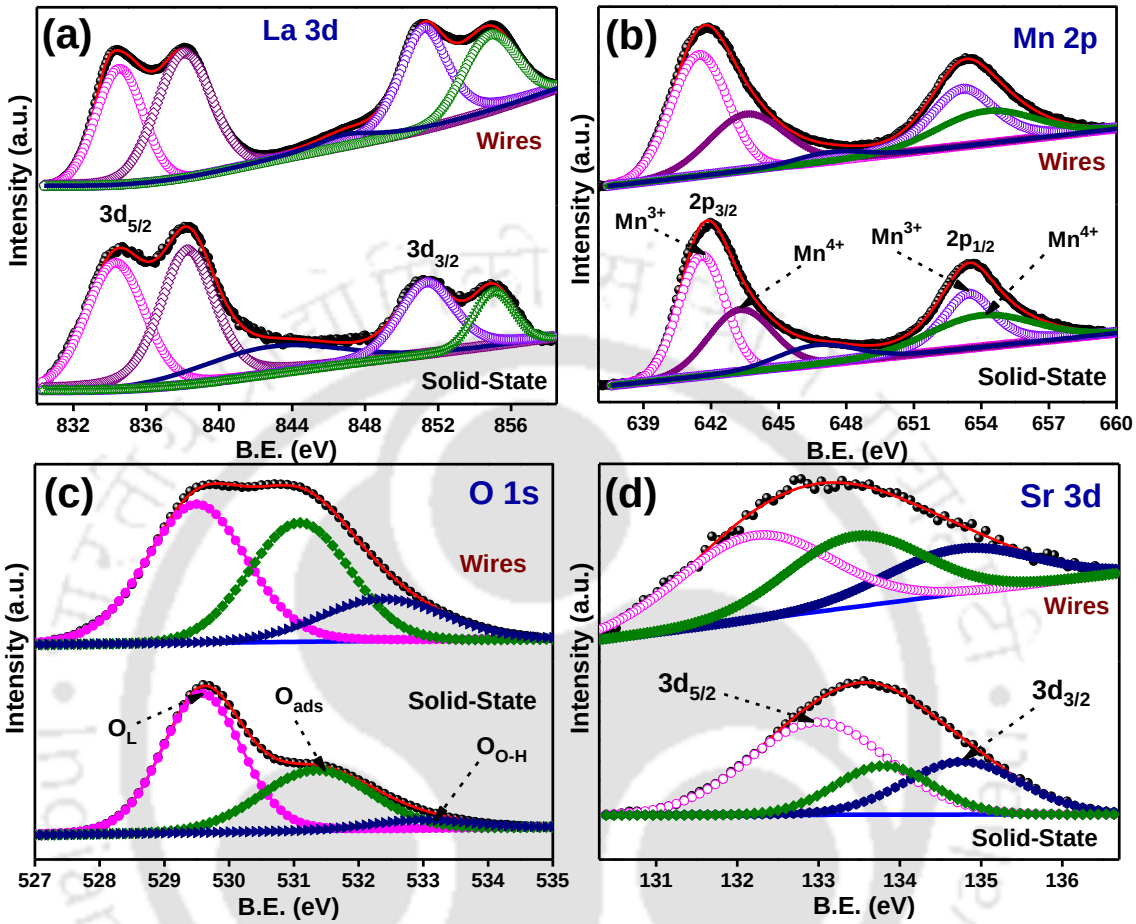

Figure 4.3.15. The core-level XPS spectra of (a) La 3d, (b) Mn 2p, (c) O 1s, and (d) Sr 3d of wire-shaped and conventional solid-state LSMO

4.3.9. Transcripted Morphology Induced Electrocatalytic OER Performance

The objective of tuning morphologies of complex metal oxide such as **LSMO** is to establish morphology – property correlations with reference to the electrocatalytic performance. To assess the electrocatalytic activity, water oxidation behaviour of the morphological **LSMO** were studied using the linear sweep voltammetry (LSV) technique in 1M NaOH (pH ~ 13) electrolytic solution. The as-synthesized **LSMO** over FTO substrate was used as the working electrode alongside Ag/AgCl as the reference and graphite rod as the counter electrode. **Figure 4.3.16(a, b)** demonstrates the polarization curves of the morphological **LSMO** along with the conventional solid-state synthesized **LSMO**. The overpotential (η_{10}) value, measured at current density of 10 mA/cm^2 for the morphological

LSMO was significantly improved than the solid-state synthesized **LSMO**. On comparing the overpotential values (η_{10}) of the **LSMO** (**Table 4.3.3**), it is seen that one-dimensional (1D) structures such as wires and rods have higher electrocatalytic activity compared to the three-dimensional (3D) structures of LSMO. The attained overpotential value for wire shaped **LSMO** is 330 mV, fused-rod shaped **LSMO** is 350 mV and rod shaped **LSMO** is 360 mV, i.e., **η_{10}: wires < fused-rods < rods**. The higher electrocatalytic activity of the 1D structures is due to better charge transport ability within the bulk resulting in the faster mobility of the holes responsible for water oxidation reaction. Among the formed 3D morphological structures, the spherical **LSMO** has a better electrocatalytic activity with η_{10} value of 380 mV followed by cuboidal **LSMO** with η_{10} value of 395 mV, nano-block shaped **LSMO** with 410 mV, flake shaped **LSMO** with 420 mV and fused-cube shaped **LSMO** with 430 mV, i.e., **η_{10}: spherical < cuboidal < nano-blocks < flakes < fused-cubes < solid-state (random)**. The higher electrocatalytic activity of the spherical **LSMO** is due to its smaller size (~ 600 nm) and more diffusion of electrolyte solution within the available pores. The η_{10} value for the **LSMO** synthesized using conventional solid-state method was found to be 450 mV.

Electrochemical kinetics is determined by the Tafel slope values which quantifies the relation between the current and the applied potential. A lower Tafel slope value implies higher charge transfer coefficient resulting in a faster water oxidation kinetics. The Tafel slope of the morphological **LSMO** were (**Figure 4.3.16(c, d)**) evaluated from their corresponding LSV curves. The lower Tafel slope value for the wire shaped **LSMO** (76 mV/decade) supports the faster electrocatalytic activity of the 1D structure. Similarly, the rod shaped **LSMO** and fused-rod shaped **LSMO** resulted in lower Tafel slope values of 85 mV/decade and 88 mV/decade, respectively compared to their morphological counterparts.

The 3D structures with lower charge transfer coefficient compared to the 1D structures resulted in higher Tafel slope. The attained Tafel slope values for the spherical **LSMO** is 102 mV/decade, for cuboidal **LSMO** is 124 mV/decade, for nano-block shaped **LSMO** is 126 mV/decade, for flake shaped **LSMO** is 137 mV/decade and for the fused-cube shaped **LSMO** is 157 mV/decade. The higher Tafel slope value of the conventionally synthesized solid-state **LSMO** (159 mV/decade) confirms its slower water oxidation kinetics due to lower charge transfer coefficient value. Thus, overall **Tafel slope value: wires < rods < fused-rods < spherical < cuboidal < nano-blocks < flakes < fused-cubes < solid-state (random)** as tabulated in **Table 4.3.3**.

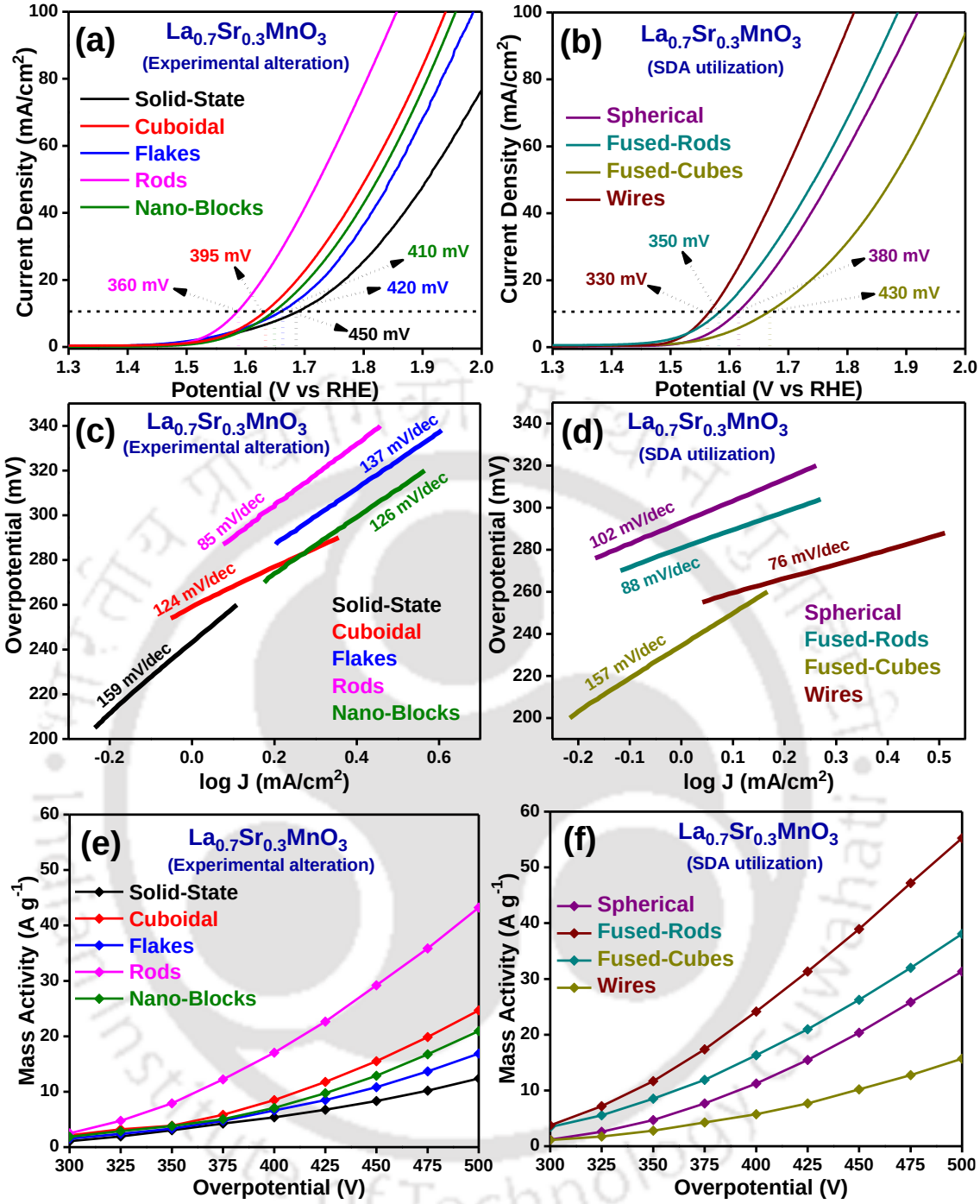

Figure 4.3.16. Polarization curves of morphological **LSMO** (a) synthesized from the Mn_xO_y formed by experimental condition alteration, (b) synthesized from the Mn_xO_y formed by utilization of SDA molecules, and (c, d) their corresponding Tafel slope values, (e, f) catalytic activities of the morphological LSMO normalized with the mass of the catalyst loading

Current normalized by loaded mass of the catalyst, known as mass activity, is crucial to understand the OER performance of nanostructured electrocatalyts. To evaluate the mass activity of the morphological **LSMO**, the loaded catalyst over the FTO was removed and

weighed. The average loaded mass of the catalyst was found to be ~1.2 mg. **Figure 4.3.16(e, f)** represents the mass activities of all the morphological LSMO and it can be seen that the trend of the OER performance, as obtained from the LSV curves, is maintained. Thus, **mass activity: wires > rods > fused-rods > spherical > cuboidal > nano-blocks > flakes > fused-cubes > solid-state(random)**.

Table 4.3.3: Overpotential (η_{10}) values at current density of 10 mA/cm^2 of the different morphological LSMO and their corresponding Tafel slope values

Compound	Morphology	Overpotential (η_{10})	Tafel Slope
$La_{0.7}Sr_{0.3}MnO_3$	Random	450 mV	159 mV/decade
$La_{0.7}Sr_{0.3}MnO_3$	Cuboidal	395 mV	124 mV/decade
$La_{0.7}Sr_{0.3}MnO_3$	Flakes	420 mV	137 mV/decade
$La_{0.7}Sr_{0.3}MnO_3$	Rods	360 mV	85 mV/decade
$La_{0.7}Sr_{0.3}MnO_3$	Nano-Blocks	410 mV	126 mV/decade
$La_{0.7}Sr_{0.3}MnO_3$	Spherical	380 mV	102 mV/decade
$La_{0.7}Sr_{0.3}MnO_3$	Fused-Rods	350 mV	88 mV/decade
$La_{0.7}Sr_{0.3}MnO_3$	Fused-Cubes	430 mV	157 mV/decade
$La_{0.7}Sr_{0.3}MnO_3$	**Wires**	**330 mV**	**76 mV/decade**

4.3.10. Transcripted Morphology Induced Electro-Active Sites (ECSA)

The water oxidation reaction is a surface dominated phenomenon, hence higher electro- active surface area will result in higher catalytic performance. The electrochemical active surface area (ECSA) of the morphological **LSMO** was assessed by measuring the double-layer capacitance values (C_{dl}) (directly proportional to ECSA) in the non-Faradaic region, where electroactive species does not undergo redox reactions. The C_{dl} values were evaluated from the capacitive currents obtained from the cyclic voltammograms measured in the range of 0.9 V and 1.1 V vs. RHE at different scan rates (**Figure 4.3.17**).

From the **Figure 4.3.18(a, b)** it can be seen that the morphological **LSMO** have higher C_{dl} values (**Table 4.3.4**) compared to the conventionally synthesized **LSMO** supporting the enhanced electrocatalytic performance. The faster water oxidation of the 1D structures is due to the enrichment of the electrochemical active surface area with C_{dl} values for the wire shaped **LSMO** (36 mF/cm^2), the fused-rod shaped **LSMO** (32 mF/cm^2) and the rod shaped **LSMO** (30 mF/cm^2) which are higher than the synthesized 3D structures, i.e., **C_{dl}: wires > fused-rods > rods**.

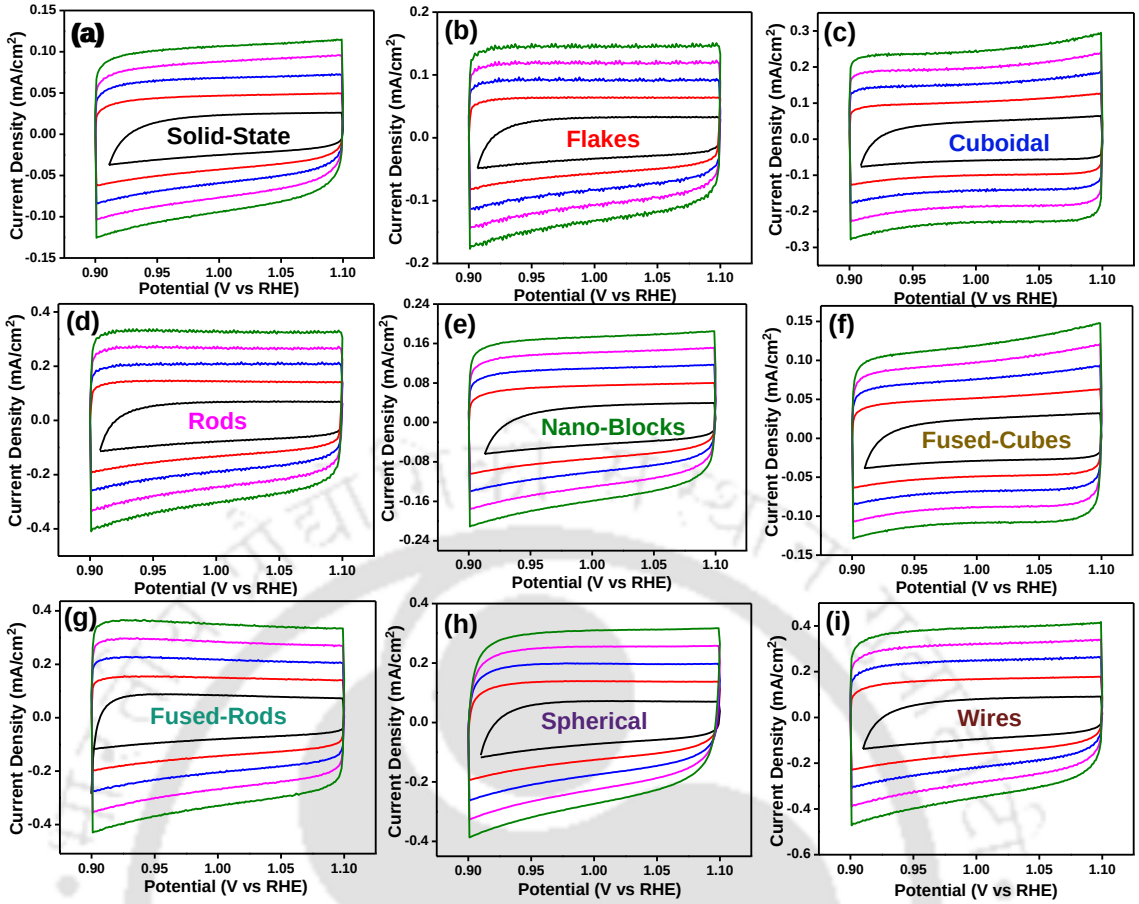

Figure 4.3.17. Cyclic Voltammograms of the different **LSMO** measured in the non-Faradaic region (0.9 V to 1.1 V vs. RHE) at scan rates of 2, 4, 6, 8 and 10 mV/s

Among the obtained 3D structures, the spherical **LSMO** has enriched electrochemical active surface area owing to its smaller size (~ 600 nm) and ease of diffusion of electrolyte solution within the available pores as the obtained C_{dl} value (27 mF/cm^2) is superior than the cuboidal **LSMO** (23 mF/cm^2), nano-block shaped **LSMO** (19 mF/cm^2), flake shaped **LSMO** (14 mF/cm^2) and fused-cube shaped **LSMO** (11 mF/cm^2).

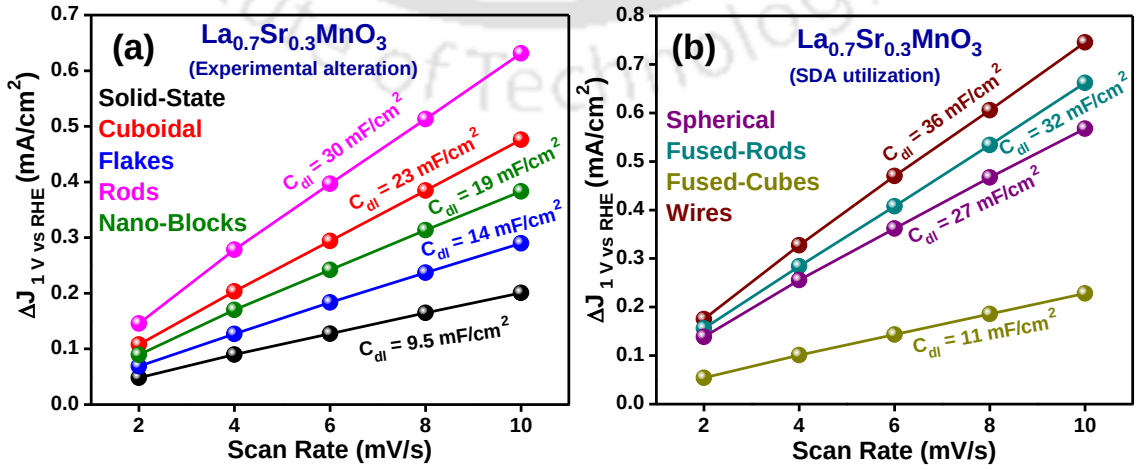

Figure 4.3.18. The plot of current density (at 1 V vs. RHE) vs. scan rate for the morphological **LSMO** (a) synthesized from the Mn_xO_y formed by synthetic protocol alteration, (b) synthesized from the Mn_xO_y formed by utilization of SDA molecules

Thus, **C_{dl}: spherical > cuboidal > nano-blocks > flakes > fused-cubes > solid-state (random)**. The obtained C_{dl} value for the conventional solid-state synthesized **LSMO** is 9.5 mF/cm^2 which depicts its lower OER performance compared to the as-synthesized morphological **LSMO**.

4.3.11. Transcripted Morphology Induced Impedance Spectroscopy (EIS)

To get an insight of the charge transfer kinetics of the catalyst, electrochemical impedance spectroscopy (EIS) technique was utilized and corresponding Nyquist plots for morphological **LSMO** alongside of solid-state synthesized **LSMO** were plotted as shown in **Figure 4.3.19(a, b)**. The charge transfer resistance (R_{ct}) values were evaluated by fitting the curves with equivalent circuit model (**Table 4.3.4**). The smaller the diameter of a semicircle in the Nyquist plot, the faster is the kinetics of water oxidation reaction due to lowering of the charge transfer resistance (R_{ct}) of the catalyst enabling faster mobility of the holes from the bulk to the electrolyte interface.

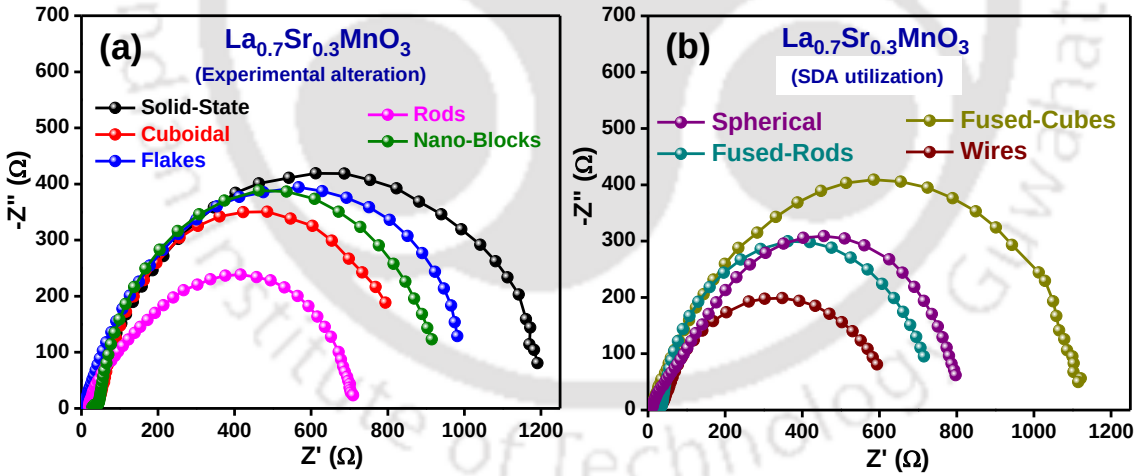

Figure 4.3.19. The Nyquist plots of the morphological **LSMO** (a) synthesized from the Mn_xO_y formed by synthetic protocol alteration, (b) synthesized from the Mn_xO_y formed by utilization of SDA molecules

On comparing the R_{ct} values of the as-synthesized morphological **LSMO**, it was found that the 1D structures have lower R_{ct} values compared to the 3D structures which depicts the higher charge transfer coefficient value supporting the faster water oxidation reaction kinetics. The obtained R_{ct} value for the wire shaped **LSMO** is 605.3 Ω, for rod shaped **LSMO** is 707.3 Ω and for fused-rod shaped **LSMO** is 723.5 Ω. Among the 3D

structures, the R_{ct} value of spherical **LSMO** is 803.1 Ω, cuboidal **LSMO** is 892.1 Ω, nano-block shaped **LSMO** is 950.1 Ω, flake shaped **LSMO** is 1007 Ω and fused-cube shaped **LSMO** is 1190 Ω. The higher R_{ct} value obtained for the conventional solid-state **LSMO** (1278 Ω) compared to the morphological **LSMO**, illustrates its slower water oxidation kinetics. Thus, overall **R_{ct}: wires < rods < fused-rods < spherical < cuboidal < nano-blocks < flakes < fused-cubes < solid-state (random)**. The lower R_{ct} value (**Table 4.3.4**) of the 1D structures also supports its lower Tafel slope value (**Table 4.3.3**) thus confirming the enhanced OER performance.

Table 4.3.4: The double-layer capacitance (C_{dl}) values of all the morphological LSMO alongside the charge transfer resistance (R_{ct}) values obtained from the Nyquist plot

Compound	Morphology	C_{dl} (mF/cm^2)	R_{ct} (Ω)
$La_{0.7}Sr_{0.3}MnO_3$	Random	9.5	1278
$La_{0.7}Sr_{0.3}MnO_3$	Flakes	14	1007
$La_{0.7}Sr_{0.3}MnO_3$	Cuboidal	23	892.1
$La_{0.7}Sr_{0.3}MnO_3$	Rods	30	707.3
$La_{0.7}Sr_{0.3}MnO_3$	Nano-Blocks	19	950.1
$La_{0.7}Sr_{0.3}MnO_3$	Fused-Cubes	11	1190
$La_{0.7}Sr_{0.3}MnO_3$	Fused-Rods	32	723.5
$La_{0.7}Sr_{0.3}MnO_3$	Spherical	27	803.1
$La_{0.7}Sr_{0.3}MnO_3$	**Wires**	**36**	**605.3**

4.3.12. Transcripted Morphology Induced Efficiency Measurements

The catalytic activity/efficiency of an electrocatalyst can be determined by its turnover frequency (TOF) which is an intrinsic property of the catalyst. The TOF values of all the **LSMO** (**Figure 4.3.20(a)**) were determined, as explained in the supporting information, at a potential of 1.6 V vs. RHE. An overall boosted TOF was attained for the morphological **LSMO** compared to the conventional solid-state **LSMO**. High TOF values of the wire shaped **LSMO** (0.78 s^{-1}), fused-rod shaped **LSMO** (0.59 s^{-1}) and rod shaped **LSMO** (0.43 s^{-1}) supports the higher electrocatalytic activity of the 1D structures owing to its higher electroactive surface area and faster kinetics. The 3D structures resulted in a TOF value of 0.33 s^{-1} for spherical **LSMO**, 0.29 s^{-1} for cuboidal **LSMO**, 0.27 s^{-1} for nano-block shaped **LSMO**, 0.23 s^{-1} for flake shaped **LSMO** and 0.20 s^{-1} for the fused-cube shaped **LSMO**. The lower TOF value for the conventional solid-state **LSMO** (0.19 s^{-1}) depicts the slower water

oxidation kinetics compared to the morphological **LSMO**. Thus, with the increment in the electrochemical active surface area, by virtue of its inherent morphology, the TOF values also increased signifying boosted water oxidation efficiency of the morphological **LSMO**.

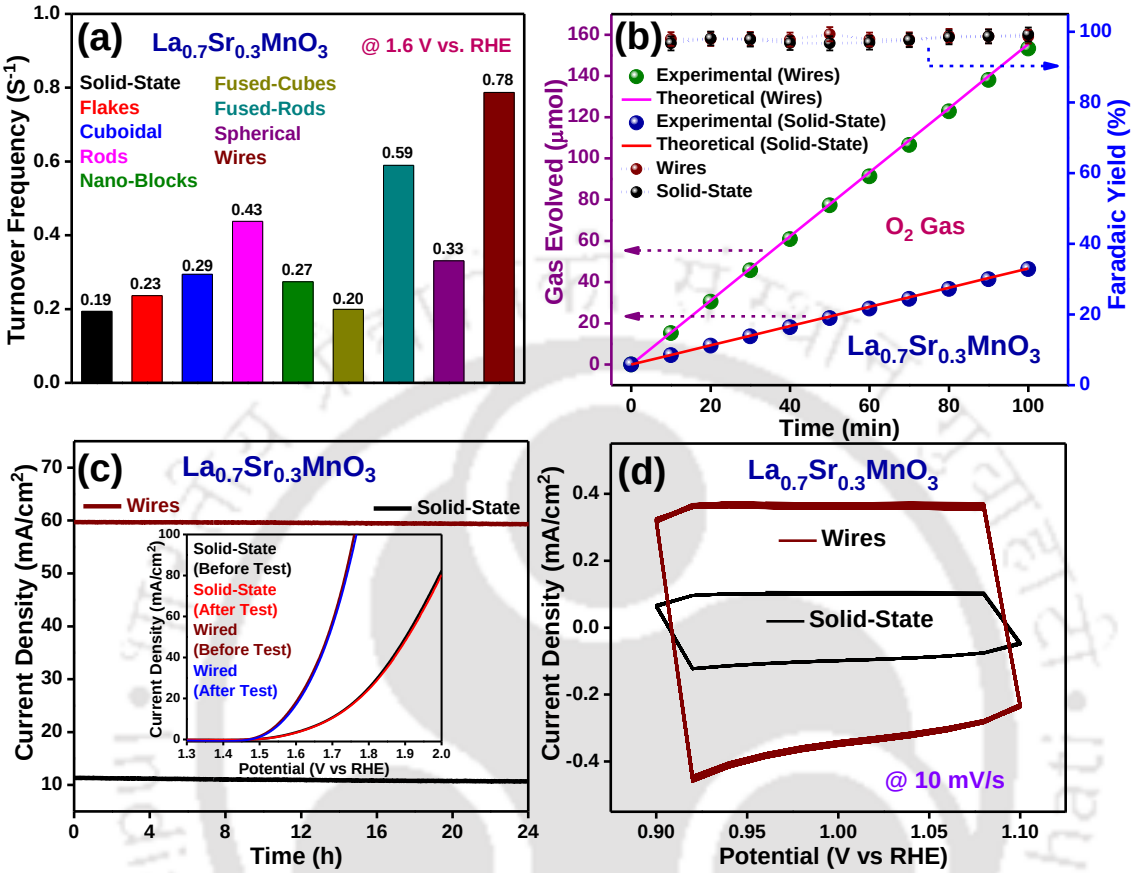

Figure 4.3.20. (a) Turnover frequencies of all the **LSMO** measure at a potential of 1.6 V vs. RHE, (b) the Faradaic-yield for both conventional solid-state and wire-shaped **LSMO**, (c) chronoamperometry analyses of conventional solid-state and wire-shaped **LSMO** at a potential of 1.7 V vs. RHE for 24 h with inset showing the LSV curves before and after the stability test, and (d) 500 CV cycles for conventional solid-state and wire-shaped **LSMO** measured between potential range of 0.9 and 1.1 V vs. RHE

In an electrochemical system, Faradaic yield is used to quantify the relation between the amount of gas evolved and obtained current density minimizing the influence of any side reactions. Faradaic yield was estimated for the high performing wire-shaped and conventional solid-state **LSMO** using gas chromatographic technique. From **Figure 4.3.20(b)**, an average Faradaic yield of ~97% was observed for both wire-shaped and conventional solid-state **LSMO** during 100 mins of continuous reaction. The high value of Faradaic yield suggests high efficacy of the compound towards water oxidation as the generated charge carriers are solely utilized for oxidation of water at the surface.

For an electrocatalyst to be exploited for practical applications, high durability of the compound is desired. To test long-term stability of the electrocatalyst, the wire-shaped and the conventional solid-state **LSMO** were subjected to chronoamperometric analyses at a fixed potential of 1.7 V vs. RHE for 24 h. From **Figure 4.3.20(c)** it can be seen that after 24 h of continuous water oxidation reaction there is insignificant decrease in the current density for both the compounds. Also, the comparison of the LSV curves before and after the durability test (inset of **Figure 4.3.20(c)**) supports the high stability and activity of **LSMO**. To further assess the stability of the compounds, 500 cycles of CV were measured between the potential of 0.9 and 1.1 V vs. RHE at a scan rate of 10 mV/s. **Figure 4.3.20(d)** shows a negligible decay in the current density and the double-layer capacitance values for both the wire-shaped and conventional solid-state **LSMO** signifying the robustness of the compounds.

4.3.13. Transcripted Morphology Induced Mechanism for OER

The water oxidation (OER) mechanism of the morphological **LSMO** is schematically illustrated in **Figure 4.3.21**.

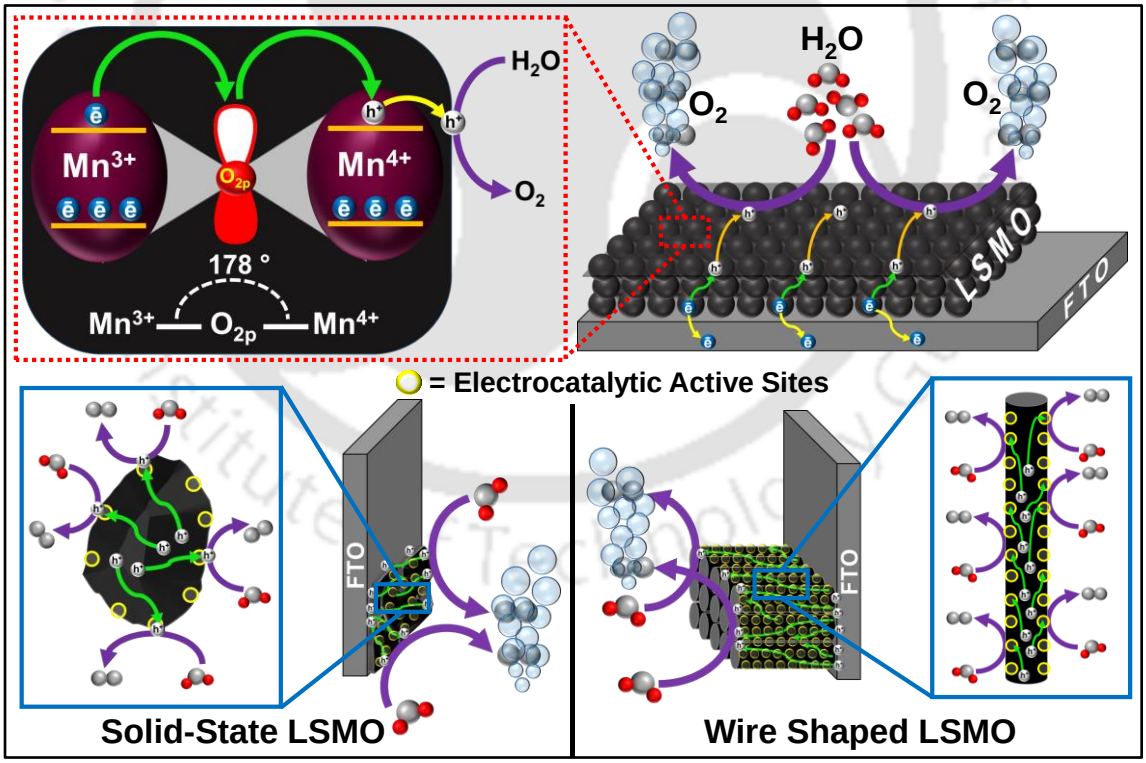

Figure 4.3.21. Schematic representation of the water oxidation mechanism of both the conventional solid-state **LSMO** and wire shaped **LSMO**

The doping of Sr^{2+} into the La^{3+} site results in the formation of holes in the lattice due to the formation of Mn^{4+} ($t_{2g}^3e_g^0$) from Mn^{3+} ($t_{2g}^3e_g^1$).[49] 30 at. % doping of Sr^{2+} into the lattice

changes Mn^{3+} – O_{2p} – Mn^{4+} bond angle to 178° which results into facile charge transport within the lattice due to simplified conduction path.[30,50] Conventionally synthesized solid-state **LSMO** results into formation of random morphology which has less electrochemical active sites (confirmed by lower ECSA value, 9.5 mF/cm^2) for the water molecules to get adsorbed and oxidize to oxygen upon accepting the holes. In case of wire shaped **LSMO**, the unique morphological feature enables higher electrochemical active sites (confirmed by higher ECSA value, 36 mF/cm^2) thereby more water molecules get adsorbed onto the surface and oxidizes to oxygen molecules upon accepting the generated holes. Also, the formation of 1D structure (wires) eases the movement of charged species through the electrode-electrolyte interface (confirmed by lower R_{ct} value, 605.3 Ω) thus increasing the kinetics of water oxidation resulting into higher TOF for the wire shaped **LSMO** compared to conventional solid-state **LSMO**.

4.4. Conclusions

In summary, the attained transcripted morphology of **LSMO** resulted in a ~4-fold increment of the electrochemical active sites confirmed by the ECSA analysis. This boosted the overall water oxidation performance of **LSMO** as depicted by the reduction in the overpotential and Tafel slope values. The ~4-fold enhancement in TOF value and the ~2-fold decrease in the charge transfer resistance value supports the escalated electrocatalytic activity of the morphologically modified **LSMO**. The test run for 24 h shows no significant decrease in current density, ascertains the high stability and activity of the catalyst. Thus, the adopted transcription methodology can be utilized for tuning desired morphological features onto high performing catalysts resulting in the enhancement of its overall performance.

4.5. References

[1] Le Bailly, *Nat. Rev. Chem.*, 2018, **2**, 0132.

[2] G. Ertl, *John Wiley & Sons, Inc.: Hoboken, NJ*, 2009.

[3] G. A. Somorjai, *John Wiley and Sons: New York,* 2010.

[4] F. R. Fan, R. Wang, H. Zhang and W. Wu, *Chem. Soc. Rev.*, 2021.

[5] F. Q. Liu, G. H. Li, S. W. Luo, W. H. Li, Z. G. Huang, W. Li, F. Su, C. Q. Li, Z. B. Ding and Q. Jiang, *ACS Appl. Mater. Inter.*, 2019, **11**, 691.

[6] Z. Hua, J. R. Jones, M. Thomas, M. C. Arno, A. Souslov, T. R. Wilks and R. K. O'Reilly, *Nat. Commun.*, 2019, **10**, 5406.

[7] Z. Zhou, X. Zhu, D. Wu, Q. Chen, D. Huang, C. Sun, J. Xin, K. Ni and J. Gao, *Chem. Mater.*, 2015, **27**, 3505.

[8] C. M. Coaty, A. A. Corrao, V. Petrova, T. Kim, D. P. Fenning, P. G. Khalifah and P. Liu, *Nanoscale*, 2021, **13**, 8242.

[9] N. Baig, I. Kammakakam and W. Falath, *Mater. Adv.*, 2021, **2**, 1821.

[10] B. H. Kim, M. J. Hackett, J. Park and T. Hyeon, *Chem. Mater.*, 2014, **26**, 59.

[11] J. Hwang, A. Ejsmont, R. Freund, J. Goscianska, B. Schmidt and S. Wuttke, *Chem. Soc. Rev.*, 2020, **49**, 3348.

[12] Y.-Y. Huang and L.-Y. Lin, *Adv. Energy Mater.*, 2018, **1**, 2979.

[13] A. A. S. Gonçalves, P. B. Faustino, J. M. Assaf and M. Jaroniec, *ACS Appl. Mater. Interfaces*, 2017, **9**, 6079.

[14] S. Bhowmick, S. Alam, A. K. Shah and M. Qureshi, *Sustainable Energy Fuels*, 2021, **5**, 2517.

[15] H. Wang, M. Zhou, P. Choudhury and H. Luo, *Appl. Mater. Today*, 2019, **16**, 56.

[16] X. Cheng, E. Fabbri, Y. Yamashita, I. E. Castelli, B. Kim, M. Uchida, R. Haumont, I. Puente-Orench and T. J. Schmidt, *ACS Catal.*, 2018, **8**, 9567.

[17] H. Sun, X. Xu, Z. Hu, L. H. Tjeng, J. Zhao, Q. Zhang, H. J. Lin, C. Te Chen, T. S. Chan, W. Zhou and Z. Shao, *J. Mater. Chem. A*, 2019, **7**, 9924.

[18] R. Xie, X. Hu, Y. Shi, Z. Nie, N. Zhang, E. Traversa, Y. Yu and N. Yang, *ACS Appl. Energy Mater.*, 2020, **3**, 7988.

[19] W. Xia, Z. Pei, K. Leng and X. Zhu, *Nanoscale Res. Lett.*, 2020, **15**, 9.

[20] Y. Liu, H. Dai, Y. Du, J. Deng, L. Zhang and Z. Zhao, *Appl. Catal., B*, 2012, **119–120**, 20.

[21] Y. Wang, S. Xie, J. Deng, S. Deng, H. Wang, H. Yan and H. Dai, *ACS Appl. Mater. Interfaces*, 2014, **6**, 17394.

[22] C. Zhou, K. Huang, L. Yuan, W. Feng, X. Chu, Z. Geng, X. Wu, L. Wang and S. Feng, *New J. Chem.*, 2015, **39**, 2413.

[23] K. Miyazaki, K. Kawakita, T. Abe, T. Fukutsuka, K. Kojima and Z. Ogumi, *J. Mater. Chem.*, 2011, **21**, 1913.

[24] I. Katsounaros, S. Cherevko, A. R. Zeradjanin and K. J. J. Mayrhofer, *Angew. Chem., Int. Ed.*, 2014, **53**, 102.

[25] N.-T. Suen, S.-F. Hung, Q. Quan, N. Zhang, Y.-J. Xu and H. M. Chen, *Chem. Soc. Rev.*, 2017, **46**, 337.

[26] S. Geiger, O. Kasian, B. R. Shrestha, A. M. Mingers, K. J. Mayrhofer and S. Cherevko, *J. Electrochem. Soc.*, 2016, **163**, F3132.

[27] X. Xu, Y. Chen, W. Zhou, Z. Zhu, C. Su, M. Liu and Z. Shao, *Adv. Mater.*, 2016, **28**, 6442.

[28] X. Xu, C. Su, W. Zhou, Y. Zhu, Y. Chen and Z. Shao, *Adv. Sci.*, 2016, **3**, 1500187.

[29] J. Bian, Z. Li, N. Li and C. Sun, *Inorg. Chem.*, 2019, **58**, 8208.

[30] S. Bhowmick, A. Dhankhar, T. K. Sahu, R. Jena, D. Gogoi, N. R. Peela, S. Ardo and M. Qureshi, *ACS Appl. Energy Mater.*, 2020, **3**, 1279.

[31] A. Seong, J. Kim, O. Kwon, H. Y. Jeong, R. J. Gorte, J. M. Vohs and G. Kim, *Nano Energy*, 2020, **71**, 104564.

[32] W. Li, Y. Yin, K. Xu, F. Li, K. Maliutina, Q. Wu, C. Li, B. Zhu and L. Fan, *Catalysis Today*, 2021, **364**, 148.

[33] S. Anantharaj, S. R. Ede, K. Sakthikumar, K. Karthick, S. Mishra and S. Kundu, *ACS Catal.*, 2016, **6**, 8069.

[34] S. Anantharaj, S. R. Ede, K. Karthick, S. Sam Sankar, K. Sangeetha, P. E. Karthik and Subrata Kundu, *Energy Environ. Sci.*, 2018, **11**, 744.

[35] H. Sun, X. Xu, Z. Hu, L. H. Tjeng, J. Zhao, Q. Zhang, H. J. Lin, C. Te Chen, T. S. Chan, W. Zhou and Z. Shao, *J. Mater. Chem. A*, 2019, **7**, 9924.

[36] J. Sun, L. Du, B. Y. Sun, G. K. Han, Y. L. Ma, J. J. Wang, H. Huo, C. Y. Du and G. P. Yin, *ACS Appl. Mater. Interfaces*, 2020, **22**, 24717.

[37] Y. Xue, H. Huang, H. Miao, S. Sun, Q. Wang, S. Li and Z. Liu, *J. Power Sources*, 2017, **358**, 50.

[38] Y. Xue, M. He, B. Li, S. Sun, Q. Wang, S. Li, L. Chen and Z. Liu, *J. Mater. Chem. A*, 2017, **5**, 6411.

[39] S. Z. Huang, J. Jin, Y. Cai, Y. Li, Z. Deng, J. Y. Zeng, J. Liu, C. Wang, T. Hasan and B. L. Su, *Sci. Rep.*, 2015, **5**, 14686.

[40] K. A. Khan, H. Ullah, P. Bonnet, M. Nawaz and M. Irfan, *Chemistry Select*, 2018, **3**, 6916.

[41] W. T. Yao, G. M. Odegard, Z. N. Huang, Y. F. Yuan, H. Asayesh-Ardakani, S. Sharifi-Asl, M. Cheng, B. Song, R. Deivanayagam, F. Long, C. R. Friedrich, K. Amine, J. Lu and R. Shahbazian-Yassar, *Nano Energy*, 2018, **48**, 301.

[42] P. -Y. Kuang, M. -H. Liang, W. -Y. Kong, Z. -Q. Liu, Y. -P. Guo, H.-J. Wang, N. Li, Y. -Z. Su and S. Chen, *New J. Chem.*, 2015, **39**, 2497.

[43] R. J. Yang, Y. Y. Fan, R. Q. Ye, Y. X. Tang, X. H. Cao, Z. Y. Yin and Z. Y. Zeng, *Adv. Mater.*, 2021, **33**, 2004862.

[44] J. Y. Kim, B. S. Kim, C. I. Oh, J. J. Ryu, H. J. Kim, E. Park, K. S. No and S. B. Hong, 2018, **8**, 12487.

[45] Y. Sun, J. J. Zhang, X. N. Sun and N. B. Huang, *CrystEngComm*, 2019, **21**, 7468.

[46] L. Fister and D. C. Johnson, *J. Am. Chem. Soc.* 1992**, 114**, 4639.

[47] R. E. Schaak and T. E. Mallouk, *Chem. Mater.*, 2002, **14**, 1455.

[48] A. Perejon, P. E. Sanchez-Jimenez, J. M. Criado and L. A. Perez-Maqueda, *J. Phys. Chem. B*, 2011, **115**, 1780.

[49] M. Zhi, G. Zhou, Z. Hong, J. Wang, R. Gemmen, K. Gerdes, A. Manivannan, D. Ma and N. Wu, *Energy Environ. Sci.*, 2011, **4**, 139.

[50] K. McBride, J. Cook, S. Gray, S. Felton, L. Stella and D. Poulidi, *CrystEngComm*, 2016, **18**, 407.

CHAPTER 5

Morphology and overlayer strategy: Oxygen evolution reaction performance of di-manganese copper oxide coupled with nickel borate

This chapter focusses on the effect of induced morphology and deposition of an electroactive layer over a complex metal oxide catalyst in the oxygen evolution reaction (OER) performance. Here, di-manganese copper oxide has been synthesized having petal like structures and fabricated into a working electrode, over which nickel borate, an electroactive compound, has been electrodeposited to prepare the composite material. Finally, the composite material was subjected to electrochemical measurements and 8-fold enhanced OER performance was observed compared to the bare counterpart.

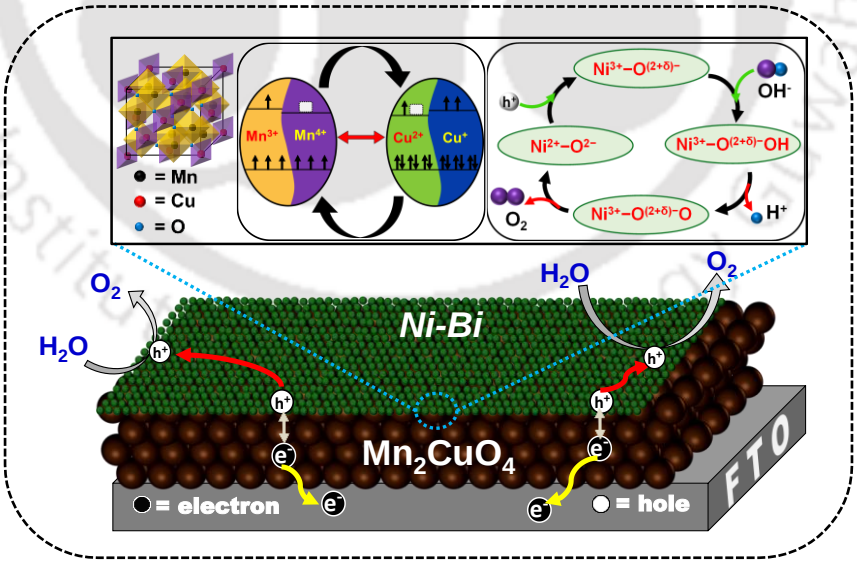

S. Bhowmick, et al., *Sustainable Energy Fuels*, 2021, **5**, 2517-2527

5.1. Introduction

During past decades, noble metal based electrocatalysts like RuO_2 and IrO_2, were widely explored, however, their high cost and low abundance limit their use for practical applications. The current trend is to look for an alternative, based on abundant and cheap 3d-transition metal oxides.[1,2] In this aspect, electrocatalysts using metal oxides, hydroxides, layered double hydroxides, based on 1st-row transition metals (Ni, Mn, Co, Cu, and Fe) have been reported with high efficiencies.[3-5] Among them, copper-based catalysts have attracted much attention. It being earth-abundant and cheap, shows an extensive redox property with variable oxidation states (Cu^0, Cu^+, and Cu^{2+}), beneficial in the development of the electrocatalysts. It is also an important metal center in the enzyme, where the dioxygen is activated as Cu–O_2, suitable for forming the Cu(III)-OOH intermediates during the water oxidation process.[6,7]

Usage of copper oxides and manganese oxides for the OER has been widely investigated, although the mixture of the two for the same has been sparsely studied.[8] It should be noted that these binary transition-metal oxides exhibit an enhanced electrochemical conductance and high specific surface area over the uni-metal oxides.[9,10] The presence of multivalent cations eases the electron-transfer process, enhancing the overall electrochemical performance.[11] Di-manganese copper oxide is a complex metal oxide with the presence of multivalent Mn and Cu and it is highly dependent on the synthetic conditions.[12] The co-existence of Cu(II) + Mn(III) ↔ Cu(I) + Mn(IV) mixed redox pairs in Cu and Mn species retains the activity of the catalysts even under higher applied bias for OER.[13,14]

To improve the overall efficiency of an electrocatalyst, they often over-layered using other electrocatalysts which mainly modifies the surface reaction kinetics and charge carrier transfer to the collecting electrode. OER catalysts based on composites such as metal-metalloids type, such as metal-borates,[15,16] metal-phosphates,[17,18] etc., are known to reduce the thermodynamic and kinetic barrier of the hydroxylation reaction during the water splitting.[19,20] In this regard, metal borates have been reported as the better OER electrocatalysts in the alkaline medium.[21-23] Unlike other metal borates, the utilization of nickel borate (Ni-B_i) for the modification of other catalysts is less studied and needs to be explored much. As known, the Ni ions in Ni- B_i takes the active role in OER due to its redox nature, i.e., rapid shuttling of the oxidation state of Ni ions between +2 and +3 on acceptance and then release of the holes.[24,25] Also, the formation of Ni^{3+} ions results in electron-deficient oxygen sites, which act as the electrophilic centers leading to the formation of a stable precursor state before O−O bond

formation.[22,26] Thus, Ni-B_i being used as a modifier for other electrocatalysts enhances the overall OER performance of the composite material.

In this work, we have synthesized di-manganese copper oxide and reported as an OER electrocatalyst with modification of nickel borate as an overlayer. Comparable electrocatalytic performance is noticed for the modified Mn_2CuO_4 with the benchmark RuO_2 under similar experimental conditions. A Tafel slope of 56 mV/decade is obtained for Mn_2CuO_4/Ni-B_i with a very small charge transfer resistance (R_{ct}) value of 13.15 Ω and a high double-layer capacitance (C_{dl}) value of 55 mF/cm^2. Also, the modified catalyst shows an excellent catalytic activity with turnover frequency (TOF) of 0.05 s^{-1} at 300mV overpotential and a high Faradaic yield of ~98%. The importance of this work lies in the fact that the utilization of di-manganese copper oxide as an OER electrocatalyst is for the first time and the nickel borate over the surface plays a very crucial role in the transfer of the charged species from the bulk to the electrolyte interface due to its fast-redox ability resulting in enhanced catalytic activity.

5.2. Experimental Section

5.2.1. Synthesis of di-manganese copper oxide (Mn_2CuO_4)

For the synthesis of the flake-like Mn_2CuO_4 hydrothermal method was utilized followed by calcination (**scheme 5.1**). 25mM copper acetate and 50mM manganese acetate were added to a 1:3 solvent mixture of ethylene glycol and water. Later, 0.1M urea was added to it and vigorously stirred for 1h. Then it was transferred to a Teflon-lined steel autoclave and reacted @ 160 °C for 12h. Thereafter, the sample was centrifuged and washed properly with water and ethanol and allowed to dry in oven at 60 °C. Finally, it was annealed in a muffle furnace at 450 °C for 2h at a heating rate of 5 °C/min.

5.2.2. Deposition of Ni-B_i layer over Mn_2CuO_4

Nickel Borate (Ni-B_i) layer was electrodeposited using a three-electrode system (**Scheme 5.1**). Fabricated Mn_2CuO_4 electrode (**Section 2.3** of **Chapter 2**) was used as the working electrode with Ag/AgCl and platinum as reference and counter electrodes, respectively. The potential was fixed at 1.1V vs. Ag/AgCl. The electrolyte used was prepared using 15mM nickel nitrate in 0.1M boric acid solution and the pH was adjusted to ~9.2 using KOH. After the deposition, the electrode was washed with DI water and dried in oven at 60 °C. A bare nickel borate working electrode was also prepared using a similar technique.

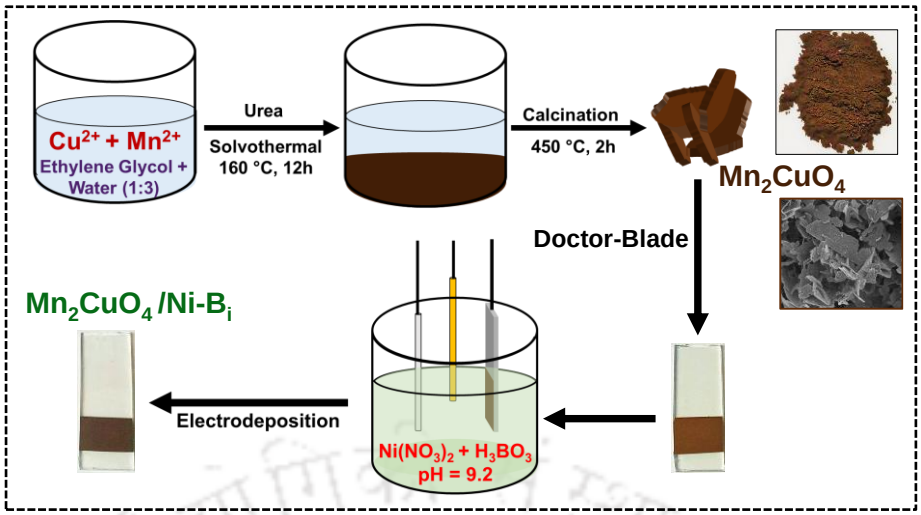

Scheme 5.1. Graphical representation of the synthesis and fabrication method of the working electrode

5.2.3. Purification of electrolyte to study the effect of trace Fe

A H_2SO_4 treated 50mL polypropylene (PP) centrifuge tube was taken and 2g of $Ni(NO_3)_2.6H_2O$ (99.99%) was dissolved in 4mL Milli-Q water and to it 20mL of 1M NaOH solution was added. The mixture was shaken well and centrifuged to separate the formed precipitates. The supernatant was decanted and $Ni(OH)_2$ precipitate was washed thrice by redispersing the solid into H_2O:NaOH mixture (10:1 v/v) and centrifuged. Finally, the tube was filled with 50mL 1M NaOH for purification and redispersed the solid and agitated the solution for 15 mins and kept undisturbed for 4 hrs. Then, it was centrifuged and the supernatant solution was used as the electrolyte.

5.3. Results and Discussions

5.3.1. Phase and Structural Analysis

To determine the phase purity and crystallinity of synthesized di-manganese copper oxide, powder X-ray diffraction (PXRD) technique was utilized. **Fig. 5.3.1 (a)** shows the PXRD of the as-synthesized Mn_2CuO_4 powder with all the peaks indexable to the cubic phase of di-manganese copper oxide (ICSD No. 01-076-2296). **Fig. 5.3.1 (b)** shows XRD plots of Mn_2CuO_4 and Mn_2CuO_4/Ni-B_i fabricated over the FTO surface. The peaks for Ni-B_i are not visible due to its amorphous nature and very thin layer deposition. To confirm the presence of Ni-B_i in the composite, Raman spectroscopy technique was used. In **Fig. 5.3.1 (c)**, Raman spectra of bare Mn_2CuO_4, Ni-B_i, and Mn_2CuO_4/Ni-B_i are shown. For Mn_2CuO_4, the peak at 124 cm^{-1} is due to the F_{1g} mode of vibration. The peaks at 433 cm^{-1}, 521 cm^{-1}, and 577 cm^{-1} are

$T_{2g}(2)$, $T_{2g}(1)$, and $A_{1g}(2)$ modes of vibrations, respectively, corresponding to the Cu-O and Mn-O bonds. For Ni-B_i, the peaks at 480 cm^{-1} and 560 cm^{-1} corresponds to Ni-O bending and stretching vibrations. Correspondingly, for the composite, the peaks for Mn_2CuO_4 are intact with additional peaks for the nickel borate confirming its presence. In **Fig. 5.3.1 (d)**, FT-IR spectra of Mn_2CuO_4, Ni-B_i, and Mn_2CuO_4/Ni-B_i are shown and the peaks for different vibrations of the bonds are indicated. For Mn_2CuO_4, the peaks at 510 cm^{-1} and 735 cm^{-1} are due to stretching frequencies of Mn–O and Cu–O bond, respectively. The peak at 1630 cm^{-1} is due to the vibration of the -OH group. For Ni-B_i, the peaks at 685 cm^{-1}, 1195 cm^{-1}, and 1385 cm^{-1} correspond respectively to the symmetric stretching of B–O and Ni–O and asymmetric stretching of B–O bonds in nickel borate. The peaks for the nickel borate are also observed in the composite (Mn_2CuO_4/Ni-B_i) confirming the presence of the Ni-B_i layer over the Mn_2CuO_4 surface.

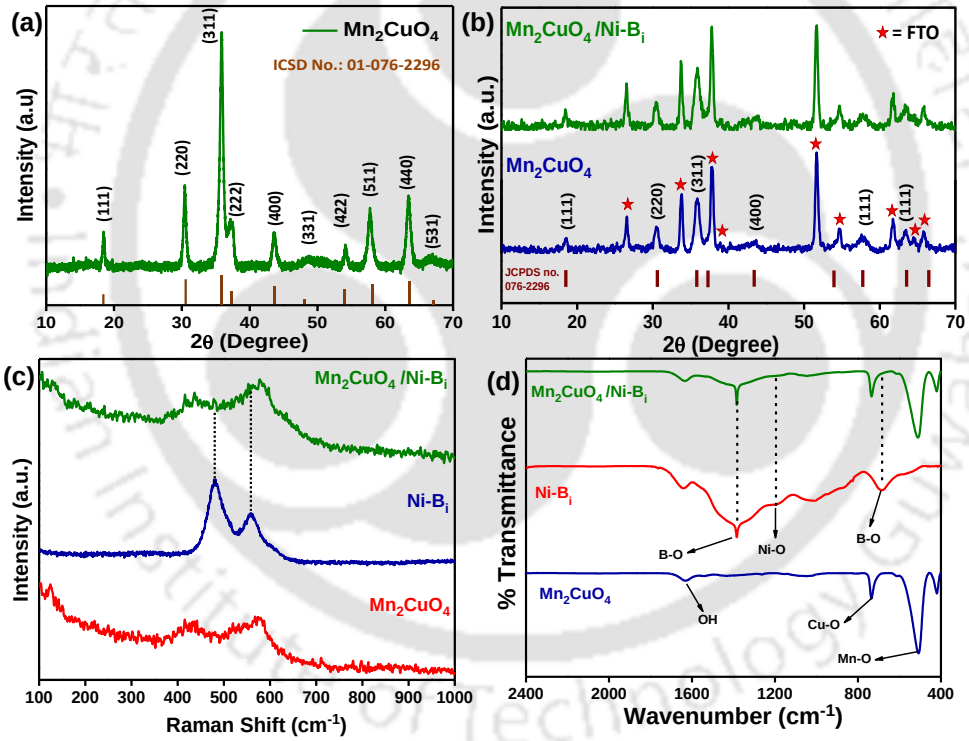

Figure 5.3.1. (a) PXRD of the synthesized Mn_2CuO_4 powder with all the peaks indexable to the cubic phase of di-manganese copper oxide (ICSD No. 01-076-2296), (b) X-ray diffractogram of Mn_2CuO_4 and Mn_2CuO_4/Ni-B_i fabricated over the FTO surface, (c) Raman spectra of Mn_2CuO_4, Ni-B_i and Mn_2CuO_4/Ni-B_i, and (d) FT-IR spectra of Mn_2CuO_4, Ni-B_i, and Mn_2CuO_4/Ni-B_i

5.3.2. Morphological Analysis

The morphological study was made using the field emission scanning electron microscopy (FESEM) technique. **Fig. 5.3.2 (a)** shows the FESEM images of the as-synthesized

Mn_2CuO_4 powder demonstrating the flake-like structures. **Fig. 5.3.2 (b)** shows the FESEM images of the fabricated Mn_2CuO_4/Ni-B_i films over FTO substrate, and it is observed that upon deposition of Ni-B_i over the surface, the morphological features remain intact. The presence of Ni-B_i is not visible due to the very thin layer deposition of the same over the surface. To further confirm the presence of the nickel borate layer over the Mn_2CuO_4 surface, field emission transmission electron microscopy (FETEM) technique was utilized. **Fig. 5.3.2 (c)** shows the FETEM image of Mn_2CuO_4 with an over-layer of Ni-B_i. The nickel borate overlayer is uniformly deposited over the Mn_2CuO_4 particle with an average thickness of ~4 nm. The high-resolution transmission electron microscopy (HRTEM) image of Mn_2CuO_4 is shown in **Fig. 5.3.2 (d)** with *d*-spacing of ~0.2 nm corresponding to the (311) crystal plane and ~0.3 nm corresponding to the (220) crystal plane of the cubic (Fd-3m(227)) phase. In **Fig. 5.3.2 (e-j)**, the scanning transmission electron microscopy energy-dispersive X-ray spectroscopy (STEM-EDX) elemental mapping of Mn_2CuO_4/Ni-B_i is shown. It is clear that all the elements are present in the composite, also nickel and boron are homogeneously distributed over the Mn_2CuO_4 surface.

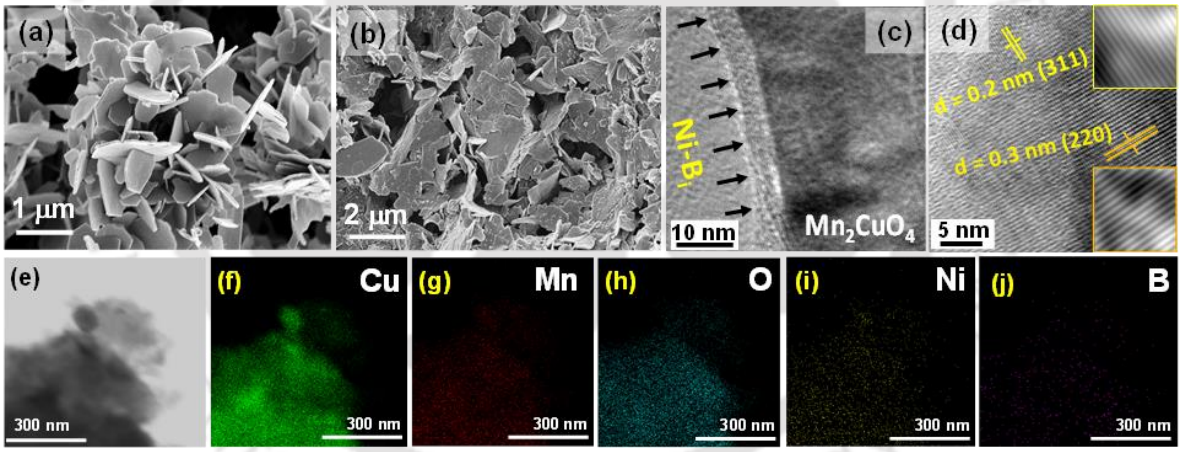

Figure 5.3.2. FESEM images of (a) as-synthesized Mn_2CuO_4, (b) fabricated Mn_2CuO_4/Ni-B_i, (c) FETEM image of Mn_2CuO_4/Ni-B_i with inset showing the presence of the Ni-B_i overlayer of ~4nm thick, (d) HRTEM image of Mn_2CuO_4 showing the *d*-spacing of ~0.2 nm corresponding to the (311) plane and of ~0.3nm corresponding to the (220) plane, (e) STEM-EDX elemental mapping of Mn_2CuO_4/Ni-B_i showing the uniform distribution of (f) **Copper**, (g) **Manganese**, (h) **Oxygen**, (i) **Nickel**, and (j) **Boron**

5.3.3. Electronic State Analysis

To get an insight of the electronic state of elements presents in the electrocatalyst, X-ray photoemission spectroscopy (XPS) technique was utilized. The presence of all the respective elements is confirmed from the survey spectra (**Fig. 5.3.3 (a)**). The Mn2p spectra

for Mn_2CuO_4 and Mn_2CuO_4/Ni-B_i are shown in **Fig. 5.3.3. (b)** with $2p_{3/2}$ and $2p_{1/2}$ at an energy difference of 11.5 eV analogous to the literature.[8] In bare Mn_2CuO_4, the $2p_{3/2}$ peak at 641.7 eV and $2p_{1/2}$ peak at 653.1 eV confirms the presence of Mn^{3+} while the $2p_{3/2}$ peak at 643.8 eV and $2p_{1/2}$ peak at 655.2 eV confirms the Mn^{4+}. The peaks at 648.7 eV and 657.8 eV are the satellite peaks of Mn^{4+}.[8,27] Similarly, for Mn_2CuO_4/Ni-B_i, the $2p_{3/2}$ peak at 641.9 eV and $2p_{1/2}$ peak at 653.3 eV corresponds to Mn^{3+}, while the $2p_{3/2}$ peak at 644 eV and $2p_{1/2}$ peak at 655.3 eV corresponds to Mn^{4+} ions. The peaks at 648.4 eV and 657.3 eV are the satellite peaks. In **Fig. 5.3.3 (c)**, the 2p core-level XPS spectra for Cu is shown with $2p_{3/2}$ and $2p_{1/2}$ at an energy difference of 20 eV. The $2p_{3/2}$ peak at 931.1 eV and $2p_{1/2}$ peak at 951 eV confirms the Cu^{+}, whereas, the $2p_{3/2}$ peak at 934 eV and $2p_{1/2}$ peak at 953.9 eV confirms the Cu^{2+} for the bare Mn_2CuO_4.[11] While for the Mn_2CuO_4/Ni-B_i, the $2p_{3/2}$ peak at 931 eV and $2p_{1/2}$ peak at 950.8 eV attributes to the Cu^{+}, whereas, the $2p_{3/2}$ peak at 934.1 eV and $2p_{1/2}$ peak at 954 eV attributes to the Cu^{2+}. The O 1s core-level XPS spectra are shown in **Fig. 5.3.3. (d)** of bare Mn_2CuO_4, Ni-B_i, and Mn_2CuO_4/Ni-B_i. For Mn_2CuO_4, the peaks at 530 eV, 531.5 eV, and 532.7 eV are due to the lattice oxygen (metal-oxygen bonding, O^{2-}), oxygen vacancies, and adsorbed oxygen at the surface, respectively.[18,28] For the Ni-B_i, the peaks at 531.6 eV, 532.3 eV, and 532.7 eV corresponds to the lattice oxygen (B-O bonding), oxygen vacancies and the surface adsorbed oxygen species.[15,29] While for the Mn_2CuO_4/Ni-B_i, the peaks at 529.7 eV, 531.4 eV, 532 eV, and 532.7 eV attributes to the lattice oxygen (metal-oxygen bonding, O^{2-}), lattice oxygen (B-O bonding), oxygen vacancies, and adsorbed oxygen at the surface, respectively. The Ni 2p core-level spectra are shown in **Fig. 5.3.3. (e)** for Ni-B_i and Mn_2CuO_4/Ni-B_i which is de-convoluted into $2p_{3/2}$ and $2p_{1/2}$. The peaks at the binding energy of 856 eV ($2p_{3/2}$) and 873.7 eV ($2p_{1/2}$) for the bare nickel borate confirm the presence of Ni in a high oxidation state (Ni^{2+}). The shake-up satellite peaks are observed at 861.3 eV and 879.2 eV for Ni $2p_{3/2}$ and Ni $2p_{1/2}$, respectively.[15,29] Similarly, for the composite, the de-convoluted peaks are observed at the binding energy of 856.2 eV (Ni $2p_{3/2}$) and 874 eV (Ni $2p_{1/2}$) with the satellite peaks at 861.5 eV and 879.5 eV, respectively. The observed shifts in the peak position are due to the interaction of Mn_2CuO_4 with nickel borate. The 1s core-level spectra of boron are shown in **Fig. 5.3.3 (f)**. The peak at a binding energy of 192.01 eV is for bare nickel borate, and for the composite, Mn_2CuO_4/Ni-B_i, the peak is shifted to 192.05 eV.[29,30] The shift in the peak position towards higher binding energy is due to the interaction of nickel borate with di-manganese copper oxide.

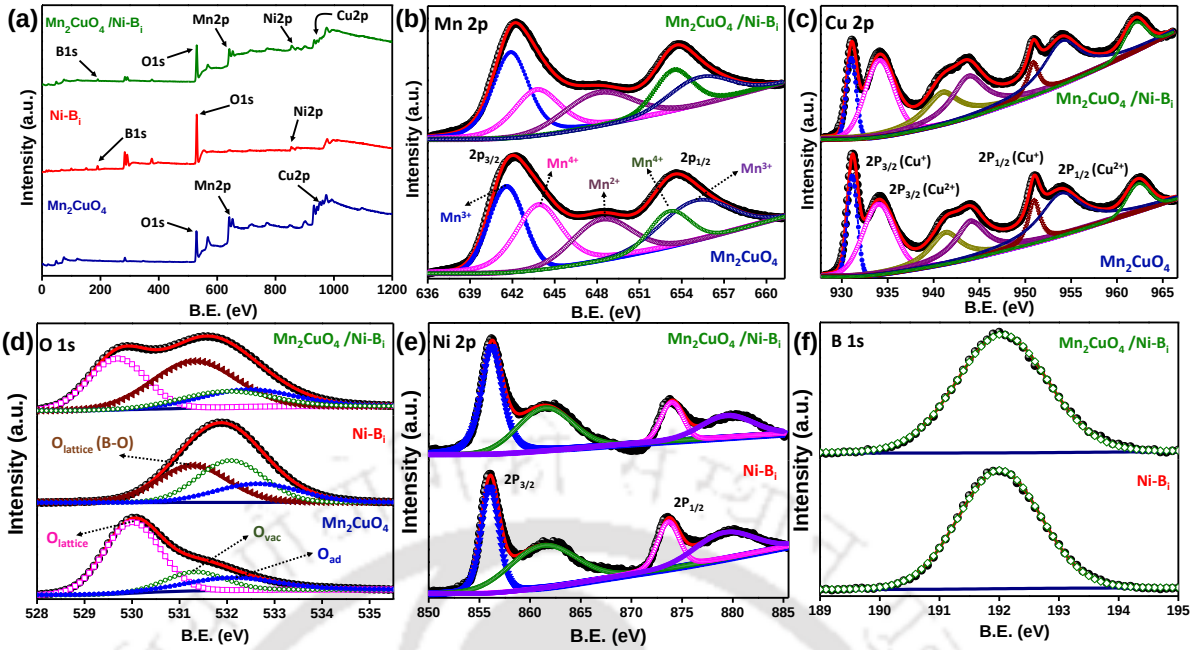

Figure 5.3.3. (a) XPS survey spectra of Mn_2CuO_4, Ni-B_i, and Mn_2CuO_4/Ni-B_i confirming the presence of all the respective elements, XPS core-level spectra of (b) Mn2p, (c) Cu2p, (d) O1s, (e) Ni2p, and (f) B1s for bare Mn_2CuO_4, Ni-B_i, and Mn_2CuO_4/Ni-B_i

5.3.4. Electrochemical Analyses

To study the electrochemical property (OER activity) of the electrocatalysts, linear sweep voltammetry (LSV) method was performed in 1M NaOH electrolyte solution. The electrodeposition of the nickel borate over the surface of Mn_2CuO_4 is optimized using different deposition time (**Fig. 5.3.4 (a)**). As can be seen from the figure, the performance of the electrocatalyst is dependent on the time of deposition of Ni-B_i over the Mn_2CuO_4 surface. The optimum deposition time is found out to be 5 min (300 sec). The excessive deposition of Ni-B_i overcrowds the surface leading to the decrease in the active surface area for the catalytic reaction, henceforth the performance decreases with the increase in the deposition time (400 sec and 500 sec). **Fig. 5.3.4 (b)** shows the LSV curves of the corresponding electrocatalysts and the overpotential of the same are marked at a current density of 10 mA/cm^2. To compare the modified electrocatalyst with a benchmark catalyst, a film of RuO_2 is fabricated using doctor-blade technique and used as a working electrode under similar experimental conditions. As can be seen from the figure, the overpotentials for bare Mn_2CuO_4 and bare Ni-B_i are 420 mV and 300 mV, respectively, while that for Mn_2CuO_4/Ni-B_i is 230 mV. So, there is an improvement in OER performance for the modified electrocatalyst than the bare di-manganese copper oxide as well as bare nickel borate. The overpotential at 10 mA/cm^2 for RuO_2 (190 mV) is marginally better than that for Mn_2CuO_4/Ni-B_i (230 mV), but at 100 mA/cm^2 the

overpotential of Mn_2CuO_4/Ni-B_i (440mV) supersedes RuO_2 (540 mV). Although, the OER activity of RuO_2 is superior at a lower potential, at a higher potential the OER activity of the Mn_2CuO_4/Ni-B_i is much better than the benchmark RuO_2. This flip in the activity of the Mn_2CuO_4/Ni-B_i and RuO_2 at the potential of 1.55 V vs RHE is due to the better charge transfer kinetics of the composite material over the benchmark RuO_2.

To study the kinetics of the electrocatalysts, Tafel plot has been evaluated from the LSV curves (overpotential vs log (current density)). **Fig. 5.3.4 (c)** represents the Tafel plot with the slope value defining the OER kinetics of the electrocatalysts and it is observed that the reaction kinetics of Mn_2CuO_4/Ni-B_i is faster than the other catalysts. The slope value for Mn_2CuO_4/Ni-B_i is 56 mV/decade and that for RuO_2, Ni-B_i, and Mn_2CuO_4 are 73 mV/decade, 85 mV/decade, and 104 mV/decade, respectively. As we know, the lower the Tafel slope value higher is the charge transfer coefficient value and thus the enhanced OER kinetics. This explains the alteration of performance of RuO_2 and Mn_2CuO_4/Ni-B_i at a higher potential.

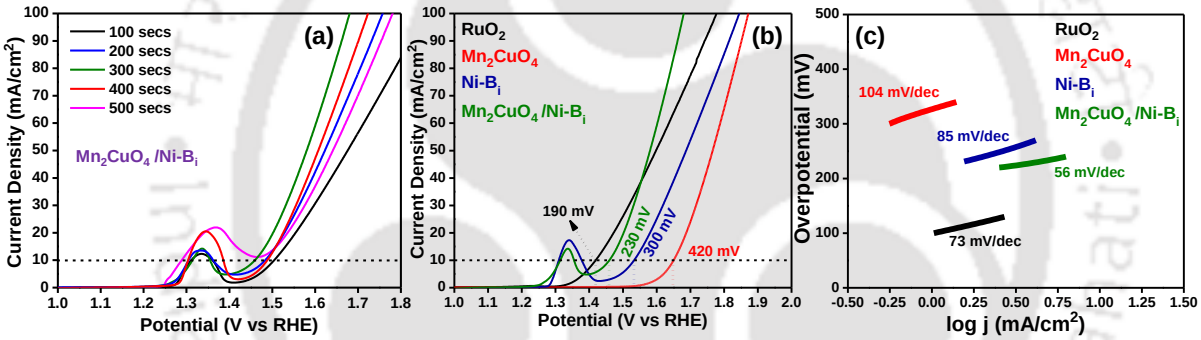

Figure 5.3.4. (a) Linear sweep voltammetry plot of Mn_2CuO_4, bare Ni-B_i, Mn_2CuO_4/Ni-B_i, and RuO_2 measured in 1M NaOH electrolyte solution, (b) the corresponding Tafel plot of all the electrocatalysts

5.3.5. Electrochemical Impedance Spectroscopy (EIS) Analyses

To get an insight into the charge transfer kinetics within the electrocatalyst, electrochemical impedance spectroscopy (EIS) was performed for bare Mn_2CuO_4, RuO_2, bare Ni-B_i, and Mn_2CuO_4/Ni-B_i. The flip in the LSV plot (Fig. 4 a) of RuO_2 and Mn_2CuO_4/Ni-B_i with the increase in potential can be explained based on their charge transfer kinetics. As can be seen from the Nyquist plots of RuO_2 and Mn_2CuO_4/Ni-B_i (**Fig. 5.3.5 (a-c)**), the kinetics vary with the applied potential. At 1.5 V vs RHE, before the cross-over, the charge transfer resistance (R_{ct}) value of RuO_2 (97.24 Ω) is lower than that of Mn_2CuO_4/Ni-B_i (144.9 Ω) supporting the low overpotential to drive a current density of 10 mA/cm^2. At 1.55 V vs RHE, the cross-over point, the R_{ct} values for both are comparable, 48.3 Ω (Mn_2CuO_4/Ni-B_i) and 49.54 Ω (RuO_2), thus resulting in the same current density value. While at 1.6 V vs RHE, after the

cross-over, the modified catalyst, Mn_2CuO_4/Ni-B_i, has a much lower R_{ct} value (13.15 Ω) compared to the RuO_2 (23.47 Ω) resulting in high current density supporting its high activity. Interestingly, di-manganese copper oxide is only among a few oxide structures available in the literature which are stable at higher potentials for performing OER without change in their structural and electronic properties.

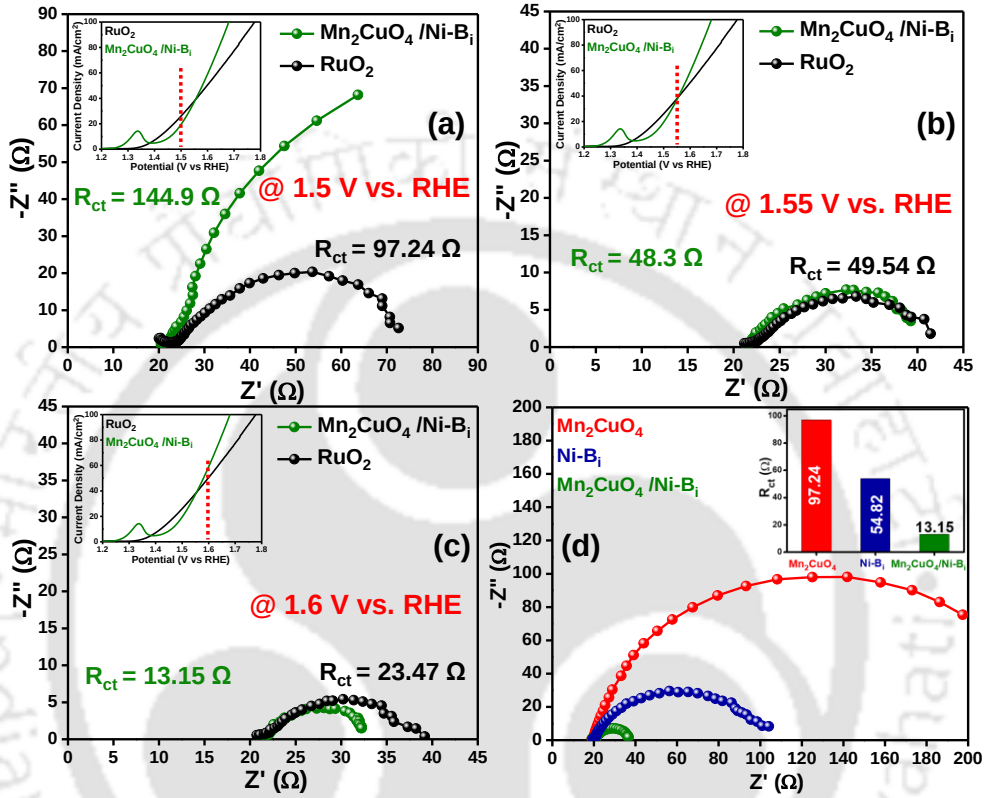

Figure 5.3.5. (a-c) Nyquist plots of Mn_2CuO_4/Ni-B_i, and RuO_2 at different potentials with the fitted R_{ct} values for the corresponding catalysts, Mn_2CuO_4/Ni-B_i (**olive**), and RuO_2 (**black**), (d) Nyquist plot of Mn_2CuO_4, bare Ni-B_i, and Mn_2CuO_4/Ni-B_i measured at a potential of 1.6V vs RHE with their corresponding R_{ct} values as shown in the inset

Fig. 5.3.5 (d) represents the Nyquist plot of Mn_2CuO_4, bare Ni-B_i, and Mn_2CuO_4/Ni-B_i, measured at a potential of 1.6 V vs RHE, and it can be seen that the diameter of the semicircle at mid-frequency region for Mn_2CuO_4/Ni-B_i is much smaller than that for bare Mn_2CuO_4 and Ni-B_i, supporting the improved performance of the modified catalyst. On fitting the curve, we evaluated the charge transfer resistance (R_{ct}) value (as shown in the inset) at the semiconductor-electrolyte interface for the catalysts and the obtained R_{ct} value for bare Mn_2CuO_4 is 97.24 Ω, bare Ni-B_i is 54.82 Ω while that for Mn_2CuO_4/Ni-B_i is 13.15 Ω. The lowering of the R_{ct} value for Mn_2CuO_4/Ni-B_i is due to the presence of Ni-B_i over the Mn_2CuO_4 surface which facilitates the transfer of charge carriers from the bulk to the surface at the electrolyte interface due to its redox property (Ni(II) ↔ Ni(III)).

5.3.6. Electrochemical Active Surface Area (ECSA) Evaluation

To understand the surface-active sites of the electrocatalysts, electrochemical active surface area (ECSA) analysis was carried out. ECSA can be calculated from the measurement of double-layer capacitance (C_{dl}) value for the respective catalysts using cyclic voltammetry (CV) technique. ECSA is equal to the double-layer capacitance (C_{dl}) per specific capacitance of the material (C_S). Thus, ECSA is directly proportional to the double-layer capacitance (C_{dl}) value evaluated from the slope value of the plot of capacitive current and scan rate measured using cyclic voltammetry (CV) technique at non-Faradaic region.[26] **Fig. 5.3.6 (a, b)** shows the CV plot of Mn_2CuO_4 and Mn_2CuO_4/Ni-B_i in the non-Faradaic region, and the C_{dl} value was estimated from the slope of current density and scan rate. The value is equal to half of the slope value obtained from the plot of the difference in current density between the anodic and cathodic sweeps ($J_{anodic} - J_{cathodic}$) at a potential of 0.75 V vs. RHE as a function of the scan rate. In **Fig. 5.3.6 (c, d)**, the ~3-folds increase in the C_{dl} value for Mn_2CuO_4/Ni-B_i (55 mF/cm^2) than that for Mn_2CuO_4 (18 mF/cm^2) is attributed to the deposited Ni-B_i layer over the Mn_2CuO_4 surface.

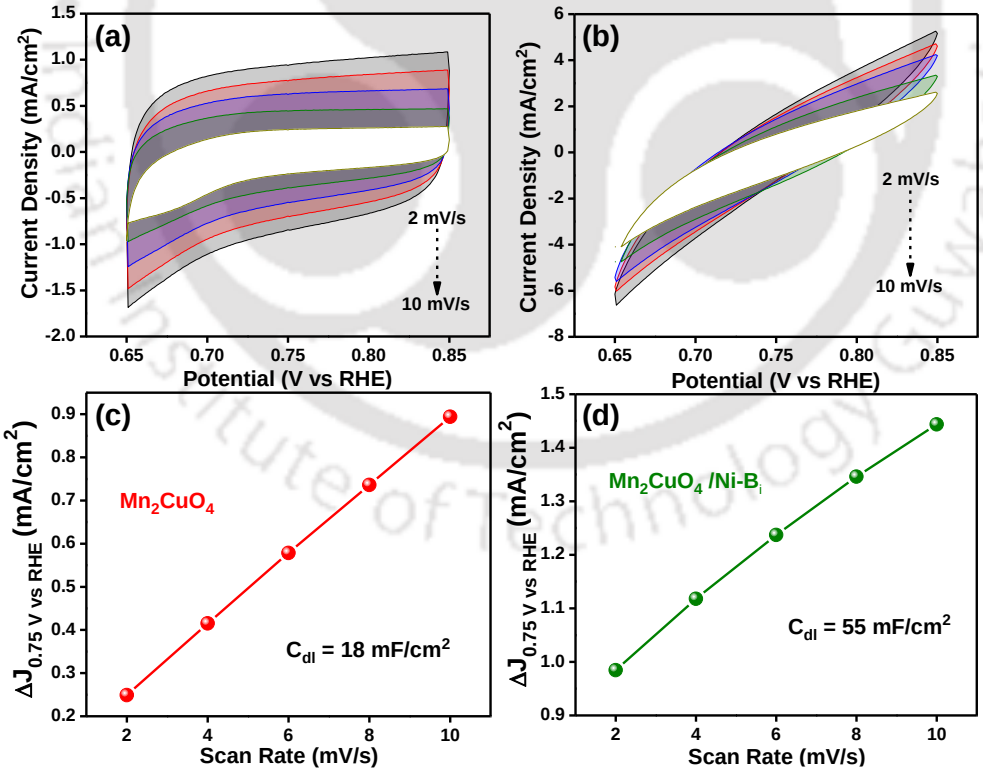

Figure 5.3.6. CV plots of (a) Mn_2CuO_4, and (b) Mn_2CuO_4/Ni-B_i measured at different scan rates in the non-Faradaic region, plot of current density (at 0.75 V vs RHE) vs the scan rate of (c) Mn_2CuO_4, and (d) Mn_2CuO_4/Ni-B_i for the determination of C_{dl} values

To calculate the ECSA value, we have to determine the C_s value by synthesizing an atomically smooth planar surface, which is not practical. But it has been found that for alkaline medium (NaOH) the C_s value for all the materials vary in range of 0.022–0.130 mF/cm^2 and for general, the average C_s value considered is 0.040 mF/cm^2.[25,26] Thus, the ECSA value is found to be 450 cm^2 for bare Mn_2CuO_4 and 1375 cm^2 for modified Mn_2CuO_4/Ni-B_i. The higher surface-active sites are beneficial for better adsorption of the water molecules on the surface of the modified catalyst resulting in enhanced OER activity.

5.3.7. Electrochemical Efficiency Analyses

To further comment on the efficacy of the electrocatalyst, turnover frequency (TOF) was calculate, as explained in the **chapter 2** (**Equation 2.13**). **Fig. 5.3.7 (a)** represents the TOF values of Mn_2CuO_4 and Mn_2CuO_4/Ni-B_i at an overpotential of 300 mV (i.e., 1.53 V vs RHE). TOF is defined as the amount of product converted from the reactant per mole of the effective catalyst per unit time. The ~8-fold increase in the value of TOF for the Mn_2CuO_4/Ni-B_i suggests higher catalytic ability than the bare Mn_2CuO_4 in the generation of O_2 gas from the water molecules per unit time. Thus, deposition of Ni-B_i over the surface of Mn_2CuO_4 enhanced the number of the catalytic cycle due to its faster reaction kinetics.

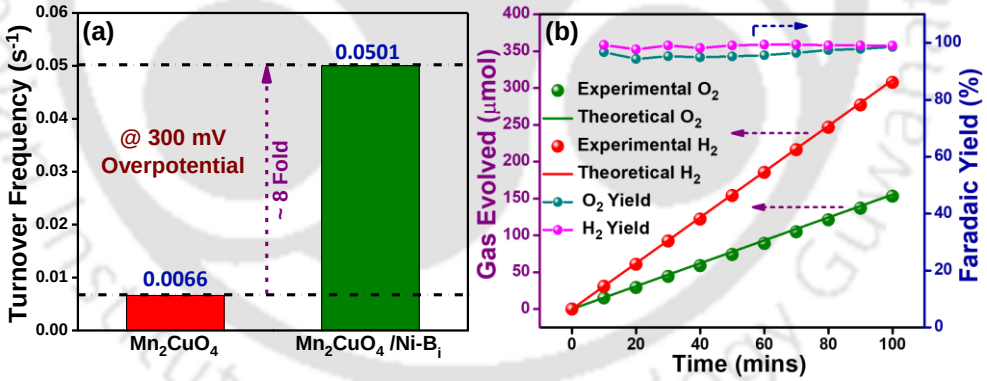

Figure 5.3.7. (a) Turnover frequencies of Mn_2CuO_4 and Mn_2CuO_4/Ni-B_i at an overpotential of 300 mV (1.53 V vs RHE), (b) Faradaic yield for Mn_2CuO_4/Ni-B_i measured at a current density of 10 mA/cm^2 using gas chromatography technique

In an electrochemical cell, on the application of high potential for longer duration across the semiconductor material, there is a possibility of side reactions within the system resulting in a decrease of O_2 yield. To check the amount of the gasses evolved and the efficiency of the electrocatalyst during the reaction time, Faradaic yield was determined using gas chromatography technique. From **Fig. 5.3.7 (b)**, it can be seen that the ratio of H_2 gas evolved to that of O_2 gas is 2:1, which is in accord with the theoretical approach. The figure represents both the amount of gasses evolved and also the Faradaic yield percentage during the reaction

course. The average Faradaic yield of the gasses evolved (H_2 and O_2) was found to be ~98% on comparing the theoretical and the experimental yields for the same. The high Faradaic yield suggests that the charge carriers generated within the system is solely consumed for the oxidation of H_2O molecules producing O_2 gas and there are no side reactions at high potential.

5.3.8. Durability Test

Among the criteria for being an efficient electrocatalyst, it should also perform in long run without compromising on its activity. To check the durability of the synthesized electrocatalysts, chronoamperometry analysis was performed at a fixed potential of 1.6 V vs. RHE for 20 hours. From **Fig. 5.3.8 (a)**, it can be seen that both the bare Mn_2CuO_4 and the modified Mn_2CuO_4/Ni-B_i exhibit good stability for 20 hours with a negligible drop in the current density.

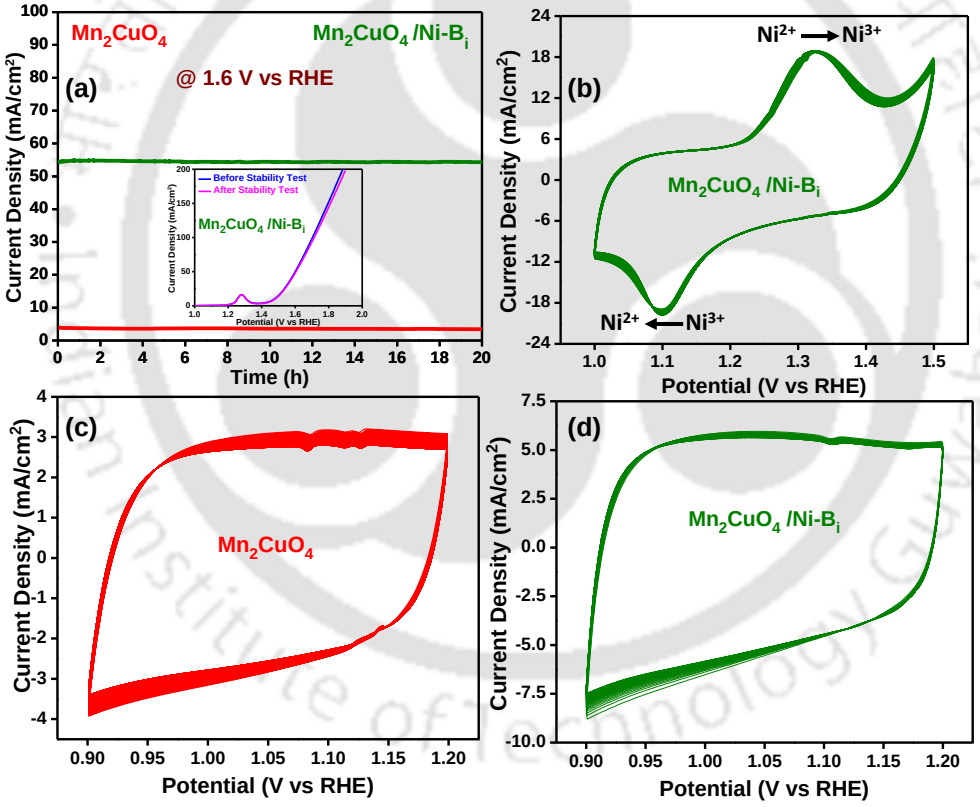

Figure 5.3.8. (a) Chronoamperometry plot at 1.6 V vs. RHE for testing the durability of the electrocatalysts with inset of LSV of Mn_2CuO_4/Ni-B_i measured before and after the stability test, (b) CV plot (500 cycles) of Mn_2CuO_4/Ni-B_i measured at a scan rate of 100 mV/s showing the redox cycle of the Ni ion in nickel borate, CV plots of 1000 cycles for testing the durability of (c) Mn_2CuO_4 and (d) Mn_2CuO_4/Ni-B_i measured at a scan rate of 100 mV/s

The high stability of the catalyst is due to the redox cycle of the Mn-Cu pair in the di-manganese copper oxide and the Ni ion in nickel borate. To check the stability of the redox

cycle of Ni ion in nickel borate, CV measurement was performed for Mn_2CuO_4/Ni-B_i at the potential range of redox behaviour of nickel. As can be seen from **Fig. 5.3.8 (b)**, the Ni ion in nickel borate undergoes the redox cycle (Ni(II) ↔ Ni(III)), and after a continuous run of 500 cycles, there is negligible change in its performance. Thus, the nickel borate is stable as an overlayer over the di-manganese copper oxide enhancing its OER activity. From **Fig. 5.3.8 (c & d)**, it can be inferred that the durability of both bare Mn_2CuO_4 and modified Mn_2CuO_4/Ni-B_i is high even after a continuous run of 1000 cycles. The high stability of both the catalyst is due to the self-healing redox cycle of bimetallic Cu and Mn in di-manganese copper oxide and Ni in nickel borate.

5.3.9. Mechanism Involved for Efficient OER Performance

To ensure the bimetallic redox cycle within the bare di-manganese copper oxide, Mn_2CuO_4, CV measurements were performed in the potential range of the redox behaviour of copper and manganese ions at a scan rate of 5 mV/s. **Fig. 5.3.9 (a)** shows the CV of Cu ion where it undergoes the redox cycle (Cu(II) ↔ Cu(I) ↔ Cu(0)) on application of potential in negative direction. Similarly, **Fig. 5.3.9 (b)** shows the CV plot of manganese undergoing the redox cycle (Mn(III) ↔ Mn(IV)). This implies that Mn_2CuO_4 has the property of charge transfer process between Mn and Cu, undergoing the bimetallic redox cycle ensuring its high activity and stability. In **Fig. 5.3.9 (c)**, we illustrate the schematic representation of the plausible mechanism involved in the OER activity of the modified catalyst. The di-manganese copper oxide (Mn_2CuO_4) oxide is known for the electronic transfer between the copper and manganese ions within the lattice, undergoing the redox cycle, Cu(II) + Mn(III) ↔ Cu(I) + Mn(IV).[19,20] So, upon application of potential, excitons are generated in the bulk, electrons move towards the FTO substrate and the holes are accepted by the Ni ions lying over the surface. The Mn_2CuO_4 then undergoes the self-redox mechanism to neutralize the charge compensation and to stabilize the lattice structure.[19,20] The Mn^{3+} transfers an electron to the Cu^{2+} reducing it to Cu^{+} and itself oxidizing to Mn^{4+}. Similarly, the Cu^{+} transfers the electron to the Mn^{4+} reducing it back to Mn^{3+} and itself oxidizing back to Cu^{2+}. While in nickel borate, the Ni^{2+} ions on accepting the holes from the bulk readily oxidize to Ni^{3+}, and under the influence of high potential charge, redistribution occurs between O_{2p} and Ni_{3d} resulting in the electron-deficient oxygen sites correlated to the Ni ions.[39,40] Thus the Ni^{3+} sites make the bounded O species electrophilic resulting in the formation of $Ni^{(3)+}$–$O^{(2+\delta)-}$OH species, which are further oxidized to $Ni^{(3)+}$–$O^{(2+\delta)-}$O species which subsequently release the O_2 gas.[27,40] After the OER, the Ni^{3+}

ions get reduced to Ni^{2+} ions which further accepts the holes generated and undergoes similar steps resulting in the formation of O_2 molecules until the potential is applied.

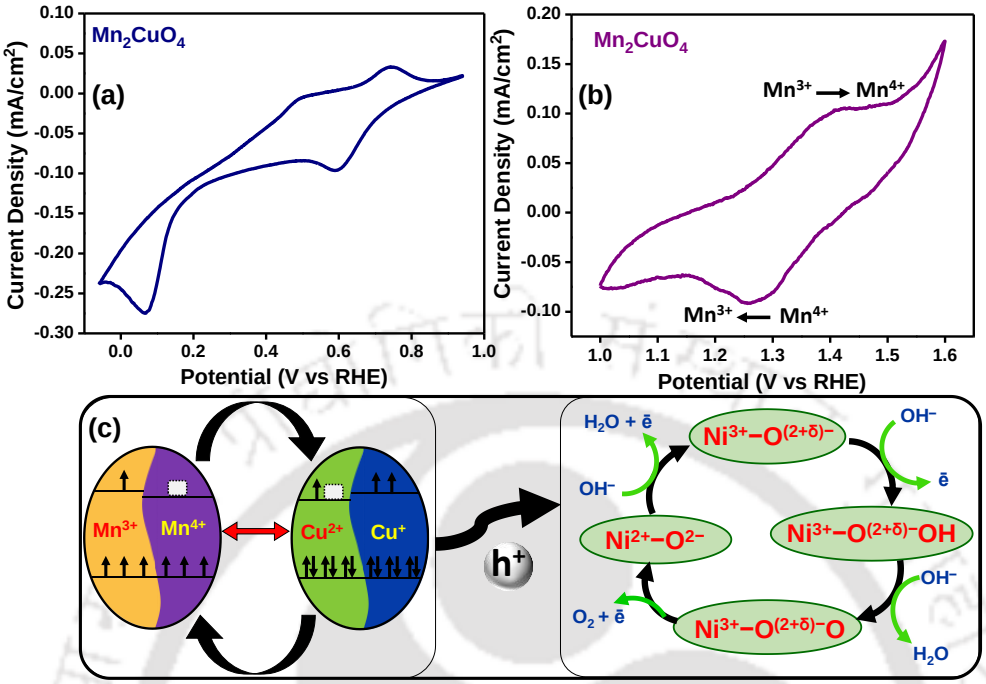

Figure 5.3.9. CV plots of bare Mn_2CuO_4 measured at a scan rate of 5 mV/s to support the redox property of (a) copper, and (b) manganese present within the system, and (c) the schematic representation of the plausible mechanistic pathway undergoing in the system for the OER activity

5.3.10. Effect of Presence of Trace Iron

To further understand the effect of trace iron impurity in the standard reagents, the modified catalyst, Mn_2CuO_4/Ni-B_i, has been synthesized using 99.99% $Ni(NO_3)_2.6H_2O$ and utilized for OER using the purified electrolyte solution, as explained in the experimental section.

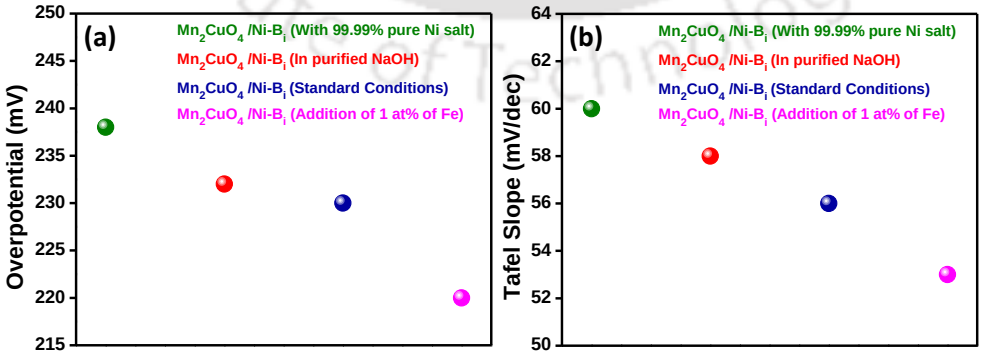

Figure 5.3.10. (a) The overpotential values measured at current density value of 10mA/cm^2 for modified catalyst, Mn_2CuO_4/Ni-B_i, in different conditions, (b) the corresponding Tafel slope values

It was found that the activity of the modified catalyst has slightly reduced for pure Ni-B_i and purified electrolyte (**Fig. 5.3.10**), suggesting that there might be trace amount of Fe impurity present in the standard chemicals. Also, with the intentional incorporation of Fe impurity into the nickel borate solution, the activity of the modified catalyst has increased which supports the fact that Fe enhances the activity of Ni ions in nickel borate.[28,41]

5.4. Conclusions

In summary, we propose the use of di-manganese copper oxide (Mn_2CuO_4) as an OER catalyst in alkaline conditions for the first time with modification using electrodeposited Ni-B_i overlayer. The modified catalyst, Mn_2CuO_4/Ni-B_i, showed an overpotential of 230 mV at a current density of 10 mA/cm^2 and a Tafel slope of 56 mV/decade comparable to the benchmark RuO_2, under similar experimental conditions. The increased performance of Mn_2CuO_4 upon deposition of Ni-B_i is well supported by the low R_{ct} and high C_{dl} values of 13.15 **Ω** and 55 mF/cm^2, respectively. Also, the high Faradaic yield of ~98% and a TOF of 0.05 s^{-1} proves the high activity of the catalyst for the long run. The redox cycle of Ni-B_i and the self-redox property of Mn_2CuO_4 play a vital role in the enhancement of the OER activity of the electrocatalyst and serves as a role model for its use in the future to replace the high cost and scarce noble metal catalysts.

5.5. References

[1] S. Anantharaj, S. R. Ede, K. Sakthikumar, K. Karthick, S. Mishra and S. Kundu, *ACS Catal.*, 2016, **6**, 8069.

[2] Y. Yan, B. Y. Xia, B. Zhao and X. Wang, *J. Mater. Chem. A*, 2016, **4**, 17587.

[3] L. Lv, Z. Yang, K. Chen, C. Wang and Y. Xiong, *Adv. Energy Mater.*, 2019, **9**, 1803358.

[4] F. Song, L. Bai, A. Moysiadou, S. Lee, C. Hu, L. Liardet and X. Hu, *J. Am. Chem. Soc.*, 2018, **140**, 7748.

[5] M. Okamura, M. Kondo, R. Kuga, Y. Kurashige, T. Yanai, S. Hayami, V. K. Praneeth, M. Yoshida, K. Yoneda, S. Kawata and S. Masaoka, *Nature*, 2016, **530**, 465.

[6] N. Supanchaiyamat and A. J. Hunt, *ChemSusChem.*, 2019, **12**, 397.

[7] W. Zhang, W. Lai and R. Cao, *Chem. Rev.*, 2017, **117**, 3717.

[8] P. Balasubramanian, M.Annalakshmi, S.-M. Chen, T. Sathesh, T.-K. Peng and T. S. T. Balamurugan, *ACS Appl. Mater. Interfaces*, 2018, **10**, 43543.

[9] Y. Zhang, L. Li, H. Su, W. Huang and X. Dong, *J. Mater. Chem. A*, 2015, **3**, 43.

[10] C. Z. Yuan, H. B. Wu, Y. Xie and X. W. Lou, *Angew. Chem., Int. Ed*., 2014, **53**, 1488.

[11] Q. Zhao, Z. Yan, C. Chen and J. Chen, *Chem. Rev*., 2017, **117**, 10121.

[12] J. Du, C. C. Chen, F. Y. Cheng and J. Chen, *Inorg. Chem*., 2015, **54**, 5467.

[13] S. Y. Chen, W. Tang, J. He, R. Miao, H. J. Lin, W. Song, S. Wang, P. X. Gao and S. L. Suib, *J. Mater. Chem. A*, 2018, **6**, 19047.

[14] M. R. Morales, M. P. Yeste, H. Vidal, J. M. Gatica and L. E. Cadus, *Fuel*, 2017, **208**, 637.

[15] X. Ji, L. Cui, D. Liu, S. Hao, J. Liu, F. Qu, Y. Ma, G. Du, A. M. Asirif and X. Sun, *Chem. Commun*., 2017, **53**, 3070.

[16] R Ge, H Du, K Tao, Q Zhang and L Chen, *ACS Appl. Mater. Interfaces*, 2017, **9**, 15383.

[17] C. Z. Yuan, Y. F. Jiang, Z. Wang, X. Xie, Z. K. Yang, A. B. Yousaf and A. W. Xu, *J. Mater. Chem. A*, 2016, **4**, 8155.

[18] M. Pramanik, C. Li, M. Imura, V. Malgras, Y. M. Kang and Y. Yamauchi, *Small*, 2016, **12**, 1709.

[19] D. K. Bediako, Y. Surendranath and D. G. Nocera, *J. Am. Chem. Soc*., 2013, **135**, 3662.

[20] R. Ge, H. Du, K. Tao, Q. Zhang and L. Chen, *ACS Appl. Mater. Interfaces*, 2017, **9**, 15383.

[21] L. Xi, M. Schellenberger, R. F. Praeg, D. Gao, D. Drevon, P. Plate, P. Bogdanoff, R. Krol and K. M. Lange, *ACS Appl. Energy Mater*., 2019, **2**, 4126.

[22] D. K. Bediako, B. Lassalle-Kaiser, Y. Surendranath, J. Yano, V. K. Yachandra and D. G. Nocera, *J. Am. Chem. Soc*., 2012, **134**, 6801.

[23] C. L. Farrow, D. K. Bediako, Y. Surendranath, D. G. Nocera and S. J. L. Billinge, *J. Am. Chem. Soc*., 2013, **135**, 6403.

[24] H. Zhang, W. Tian, Y. Li, H. Sun, M. O. Tadé and S. Wang, *J. Mater. Chem. A*, 2018, **6**, 24149.

[25] L. J. Enman, M. S. Burke, A. S. Batchellor and S. W. Boettcher, *ACS Catalysis*, 2016, **6**, 2416.

[26] S. Anantharaj, S. R. Ede, K. Karthick, S. S. Sankar, K. Sangeetha, P. E. Karthik and S. Kundu, *Energy Environ. Sci.*, 2018, **11**, 744.

[27] C. Xu, J. Y. Ge, Z. Feng, F. Chen, B. Kang, J. Zhang and S. Cao, *Ceram. Int.*, 2019, **45**, 20613.

[28] C. Dong, Z. Qu, Y. Qin, Q. Fu, H. Sun and X. Duan, *ACS Catal.*, 2019, **9**, 6698.

[29] M. Ma, D. Liu, S. Hao, R. M. Kong, G. Du, A. M. Asiri, Y. D. Yao and X. P. Sun, *Inorg. Chem. Front.*, 2017, **4**, 840.

[30] X. Ji, L. Cui, D. Liu, S. Hao, J. Liu, F. Qu, Y. Ma, G. Du, A. M. Asiri and X. Sun, *Chem. Commun.*, 2017, **53**, 3070.

[31] C. C. L. McCrory, S. Jung, I. M. Ferrer, S. M. Chatman, J. C. Peters and T. F. Jaramillo, *J. Am. Chem. Soc.*, 2015, **137**, 4347.

[32] Z. Qian, Y. Chen, Z. Tang, Z. Liu, X. Wang, Y. Tian and W. Gao, *Nano-Micro Lett.*, 2019, **28**, 11.

[33] X. Su, Y. Wang, J. Zhou, S. Gu, J. Li and S. Zhang, *J. Am. Chem. Soc.*, 2018, **140**, 11286.

[34] D. K. Bediako, Y. Surendranath and D. G. Nocera, *J. Am. Chem. Soc.*, 2013, **135**, 3662.

[35] L. Trotochaud, S. L. Young, J. K. Ranney and S. W. Boettcher, *J. Am. Chem. Soc.*, 2014, 136, 6744.

CHAPTER 6

Morphology, heterojunction and overlayer strategy: Oxygen evolution reaction performance of di-manganese copper oxide coupled with nickel borate

This chapter emphases on the utilization of morphological and overlayer strategy for both OER and HER, i.e., overall water splitting. In the present work, Mn_2O_3 and CuO were chosen due to their differences in diffusion coefficients thereby enabling morphological transformation via ion-exchange diffusion method, and the formation of n-p type heterojunction. The intentional morphological transformation was to increase the surface-active sites, while the heterojunction formation was to enhance the charge carrier separation and accumulation at the semiconductor interface for bifunctional behaviour (HER and OER). The overall water splitting capacity was further boosted by deposition of two-dimensional vanadyl phosphate hexahydrate over the semiconductor particles.

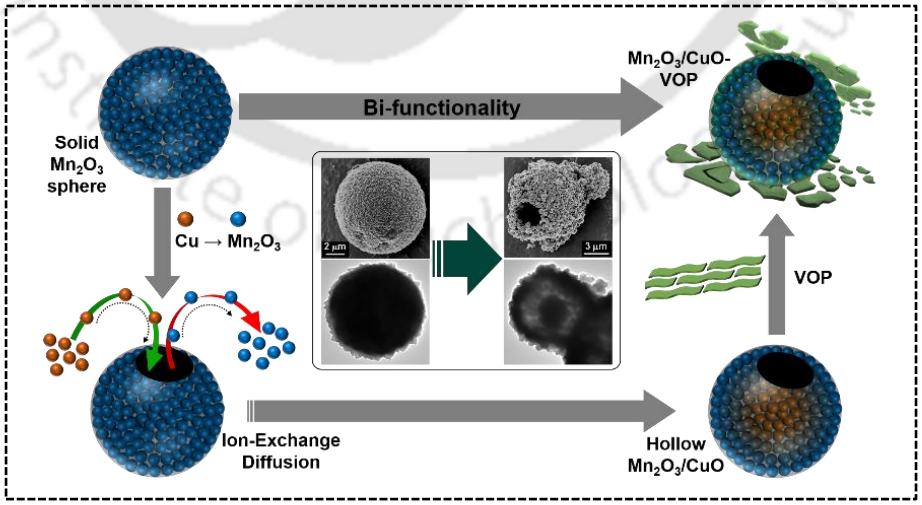

S. Bhowmick, et al., *ACS Appl. Mater. Interfaces*, 2022, **14**, 52204–52215

6.1. Introduction

Bi-functional electrocatalysts are considered one of the effective strategies in modern energy technology, where in nanomaterial-based catalysts based on their band energy alignments rationale are utilized for overall water splitting involving both hydrogen evolution reaction (HER) and oxygen evolution reaction (OER).[1–3] Extensive research has been focused on noble metal and noble metal-free based electrocatalytic nanomaterials for efficient HER and OER, but in recent times bi-functional electrocatalysts for both HER and OER has been the trending research topic.[1,3–10] Presently, Pt-group metals are promising HER catalysts, while Ir/Ru-based compounds are effective for OER, but the cost and scarcity of these metals have limited their extensive usage. In this regard, several non-precious and efficient electrocatalysts; including transition metal sulfides, carbides, and phosphides for HER,[11–13] and transition metal oxides, hydroxides, and phosphates for OER; have been developed.[14–16] An ideal electrocatalyst should be equally effective and stable for both HER and OER at a particular pH so as to simplify the overall system design and minimize the cost towards commercialization. But construction of efficient bi-functional HER-OER electrocatalyst is challenging as most of the non-noble metal catalysts are either efficient in acidic medium for HER and alkaline for OER, or vice versa. In recent time, researchers have developed 3d transition metal-based catalysts which integrates the merits of HER and OER possessing the binding force to both hydrogen- and oxygen-containing intermediates making it an efficient bifunctional HER-OER electrocatalyst.[1,3,5,7,9,10,17–23]

Among different 3d transition metal oxides, MnO_x are promising OER electrocatalyst due to the following inherent properties; (1) large number of unsaturated edge sites on the surface improves the exposed surface-active sites facilitating the adsorption of water molecules, and (2) huge morphological and structural versatility favours the OER.[24–26] But MnO_x deprives from being an efficient HER electrocatalyst due to its less stability and activity in the cathodic potential region.[24] Thus, to ensure the bi-functionality of MnO_x electrocatalyst, they can be coupled with the strategically designed HER active catalysts.

Copper, a 3d transition metal, has wide range of oxidation states (Cu^0, Cu^I, Cu^{II}, and Cu^{III}), which enables its reactivity via both one- and two-electron pathways, making it a good bi-functional electrocatalytic candidate for both HER and OER.[27–29] The coupling of Mn_2O_3 with CuO is one of the strategies to supress the shortcomings of Mn_2O_3 by virtue of their synergistic effect to improve the overall water splitting performance.[30] Integrating the merits of Mn_2O_3 and CuO in the formation of *n-p* heterojunction (Mn_2O_3 being *n-type* and CuO

being *p-type* semiconductors) is likely to advance the conductivity, electrochemical performance, cycling stability, and other important properties of the composite material.[30] In addition to the synergistic effect of Mn and Cu oxides, the ion-exchange diffusion process between the Cu and Mn ions, due to their differences in diffusion coefficient, paves the opportunity towards the morphological transformation during the synthesis of CuO over the Mn_2O_3 particles.[31–34] This results in strong interaction between the two metal oxides supporting the bi-functionality HER-OER of the formed composite.

Although metal oxides are highly stable and active, their electrocatalytic performance is yet challengeable as the charge transfer kinetics at the interface is slow as compared to their hydroxides, and/or chalcogenides.[35] To counter this ambiguity, metal oxides are often fused with other electro-active catalysts like metal phosphates, hydroxides, borates, etc., known for reducing the thermodynamic and kinetic barriers of hydroxylation reaction at the electrolyte interface and inherent faster charge-transfer coefficient values.[23,36,37] Vanadyl phosphate, a 2D material, known for its high electroactivity in other applications is yet to be explored for its water splitting performance.[38–41] High oxidation state of vanadium (V^{4+}) optimizes the water adsorption energy by forming optimal bond strength between the cation and water molecules.[42,43] Additionally, vanadyl phosphate being a 2D material provides more active sites for water adsorption onto its surface and the faster reaction kinetics of metal phosphates provides the scope for further enhancing the bi-functionality; HER-OER of the metal oxide by virtue of better charge transfer and extraction at the interface.[44–46]

In the present work, apart from designing the heterojunction for their bi-functionality based on their band energy alignments, we took advantage of their manoeuvrability in forming different morphological structures for enhanced charge transfers and injections. Solid spherical Mn_2O_3 have been synthesized and impregnated with CuO using solvothermal process forming the *n-p* heterojunction to enhance the bi-functional electrocatalytic performances compared to the individual metal oxides. The *in-situ* generation of CuO over the Mn_2O_3 took place via ion-exchange diffusion process (Kirkendall effect), where the higher flux of Mn^{2+} ions diffusing out from the core compared to the Cu^{2+} ions diffusing into the bulk of Mn_2O_3 resulted in the transformation of the solid spheres into hollow spherical structures.[31,47,48] This morphological transformation, resulting in more diffusion of electrolyte into the surface, and the formation of *n-p* type heterojunction aids the bi-functional HER-OER electrocatalytic performance of Mn_2O_3/CuO. Further modification was done by two-dimensional vanadyl phosphate hexahydrate ($(VO)_3(PO_4)_2.6H_2O$), denoted as VOP, over the

fabricated Mn_2O_3/CuO working electrode and utilizing the composite as the working electrode. This resulted in the deposition of an electroactive overlayer over semiconductor surface aiding better charge extraction at the electrolyte interface to be utilized for both water oxidation and reduction procedures. The 10-*fold* enhancement in the turnover frequency for both OER and HER infers the accomplishment of the desired strategy to improve the bi-functionality of the composite material.

6.2. Experimental section

6.2.1. Synthesis of manganese oxides (Mn_2O_3) microspheres

Manganese oxide microspheres were synthesized utilizing the hydrothermal method. 1.0 mmol of manganese acetate was dissolved in 30mL of DI water at room temperature and after 30 mins of stirring, 0.5M urea was added to it. Alginic acid was used as structure directing agent and was added (2mg/mL) to the solution. The solution was then transferred into a 50mL teflon vessel, kept inside stainless-steel autoclave and reacted @ 160 °C for 24h. The obtained product was washed with water-ethanol solution and after drying in oven was calcined @ 550 °C for 6 hours at a scan rate of 20 °C/min.

6.2.2. Formation of copper oxide coating over manganese oxide microspheres (Mn_2O_3/CuO)

The synthesized Mn_2O_3 were used as precursor material along with copper acetate during the solvothermal process (as shown in Scheme 1). Equimolar (1.0 mmol) amount of Mn_2O_3 and $Cu(OAc)_2$ were dissolved in ethylene glycol-water solution (1:1) and later 0.5 M urea was added to the solution. The solution was transferred to a teflon vessel kept in stainless steel autoclave and reacted @ 160 °C for 4 hours. After reaction the obtained product was washed with ethanol-water mixture and after drying in oven overnight it was calcined @ 450 °C for 2 hours at a scan rate of 5 °C/min.

6.2.3. Synthesis of vanadyl phosphate hydrate ($(VO)_3(PO_4)_2.6H_2O$)

The crystalline phase of vanadyl phosphate ($(VO)_3(PO_4)_2.6H_2O$) was synthesized utilizing the hydrothermal method. 1 g of V_2O_5 was dissolved in 24 mL water and to it 12 mL of concentrated H_3PO_4 was added under constant stirring. The solution mixture was transferred to 100 mL Teflon vessel and reacted @ 100°C for 20 hours. After the reaction the formed product was washed using ethanol-water mixture and dried overnight in oven @ 60°C.

6.2.4. Deposition of vanadyl phosphate hydrate over the Mn_2O_3/CuO working electrode

The synthesized $(VO)_3(PO_4)_2.6H_2O$ (5mg) was dispersed in isopropanol (30mL) via ultrasonication process until no precipitate was left. Then the solution was centrifuged @ 8000 rpm for 30mins and the supernatant solution was decanted out and labelled as VOP solution. 100 µL of the decanted VOP solution was drop-casted over the Mn_2O_3/CuO working electrode (fabricated using doctor-blade method) and let dry in vacuum oven @ 50 °C to prepare the composite working electrode, Mn_2O_3/CuO-VOP (Scheme 1).

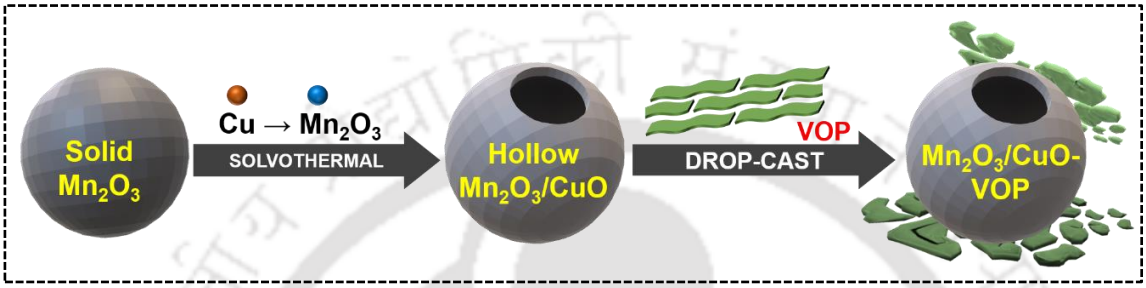

Scheme 6.1: Schematic representation of the morphological transformation into hollow spheres via ion-exchange diffusion of Cu ions into Mn_2O_3 particles and the formation of the composite material, Mn_2O_3/CuO-VOP

6.2.5. Computational Methodology

We have carried out density functional theory (DFT) based electronic structure calculations,[49,50] as implemented in the Vienna *ab-initio* simulation package (VASP) code throughout the theoretical investigation.[51] The projector augmented-wave (PAW) formalism is used to describe the interaction between ion cores and valence electrons,[52] while the exchange and correlation potential is described through generalized gradient approximation using Perdew- Burke-Ernzerhof (PBE) functional.[53] Van der Waals (VdW) interaction is applied to total energies and forces by means of DFT-D2 method. The kinetic energy cut-off corresponding to the plane-wave basis set has been used as 500 eV. The convergence criteria is set to be 1E-5 eV for the self-consistent process, and all the surface configurations are fully relaxed while achieving the minimum-energy criteria until the Hellman-Feynman forces become less than 0.01 eV/Å. We have constructed the surface along [100] direction while considering 15 Å vacuum along x-direction to avoid artificial inter-layer interactions, which will in turn remove the interaction between periodic images. The Brillouin zone has been sampled using 2×2×1 Monkhorst-Pack *k*-mesh for structural optimization of surface calculations.[54]

6.3. Results and discussions

6.3.1. Morphological Analyses through Scanning Electron Microscope (SEM) technique

Electrochemical activity of a catalyst is dependent on the concentration of the exposed surface-active sites, tuneable by varying the morphological features. The structural features of the synthesized electrocatalysts were visualized using field emission scanning electron microscope (FESEM) technique. The morphology of bare Mn_2O_3 and Mn_2O_3/CuO are shown in **Figure 6.3.1**. Mn_2O_3 forms spherical morphologies (**Figure 6.3.1a**) due to the presence of structure directing agent, alginic acid.[55] In **Figure 6.3.1b**, it is observed that the Mn_2O_3 spheres underwent more structurally sought out morphological transformation into hollow spherical structures upon reaction with CuO. The Mn_2O_3 particles in presence of the Cu ions in hydrothermal conditions at 160 °C leads to opening up of the solid sphere and creating a hollowness in the structure, as schematically demonstrated in **Figure 6.3.1c**. The morphology transformation of Mn_2O_3 from solid spheres to hollow spheres after reacting with CuO occurred through an ion exchange diffusion process (Kirkendall effect).[31,47,48,56]

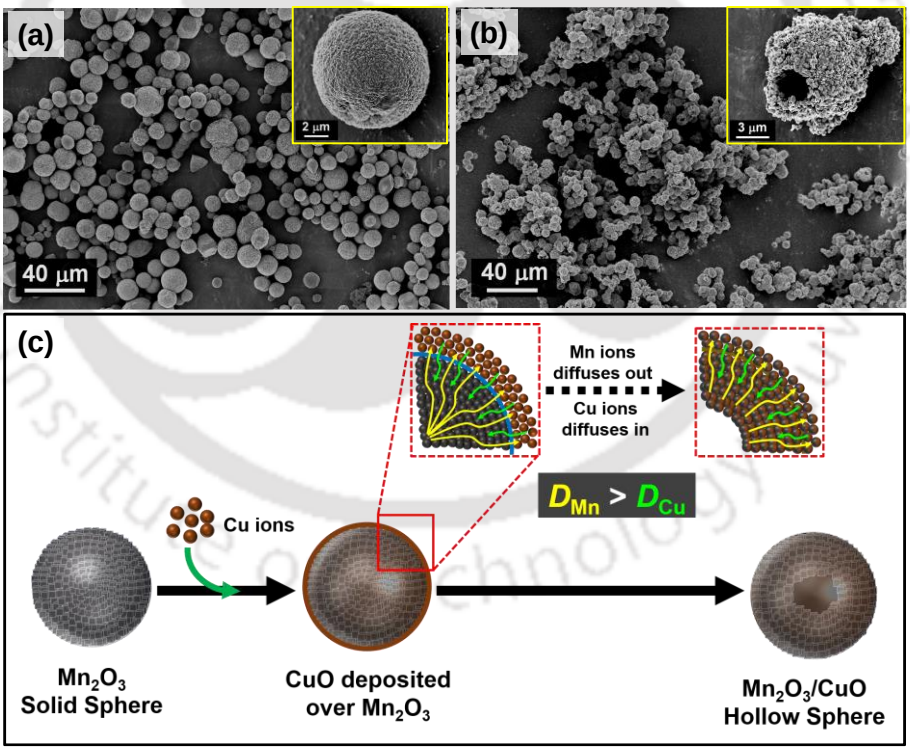

Figure 6.3.1: FESEM images of (a) solid spherical Mn_2O_3, (b) hollow sphere of Mn_2O_3/CuO, and (c) schematic representation of the morphological transformation of solid spheres into hollow spherical structures

The difference in the diffusion coefficients (*D*) of the two ions (Mn and Cu) is the crucial factor for the transformation of solid sphere into hollow sphere. The rate of diffusion

of Mn ions is known to be faster than that of Cu ions.[57] During the hydrothermal reaction, the Cu ions gets deposited over the Mn_2O_3 sphere and at high temperature and pressure the Mn ions diffuses out from the core through the interface (Mn-Cu) while the Cu ions diffuses inside the sphere through the interface. But as $D_{Mn} > D_{Cu}$, the Cu ions cannot compensate the flux of Mn ions diffusing out of the sphere resulting in the formation of void at the core. Thus, the solid sphere gets transformed into hollow sphere via Kirkendall-based ion exchange process.

The interaction of the Mn_2O_3 particles and Cu ions for the morphological transformation was optimized by varying the reaction temperature (140 - 180 °C) and reaction time (2 - 8 hours). **Figure 6.3.2** demonstrates the FESEM images of bare CuO synthesized by hydrothermal method at different temperatures (140 - 180 °C). It can be seen that the CuO particles have formed spherical structures at lower temperatures (140 °C and 160 °C), but at higher temperature (180 °C) it took the form of cuboidal structures. At temperature of 160 °C, there was the formation of hollow spherical structures, thus was chosen as the optimum temperature for the morphological transformation of Mn_2O_3 solid spheres into hollow spheres of Mn_2O_3/CuO.

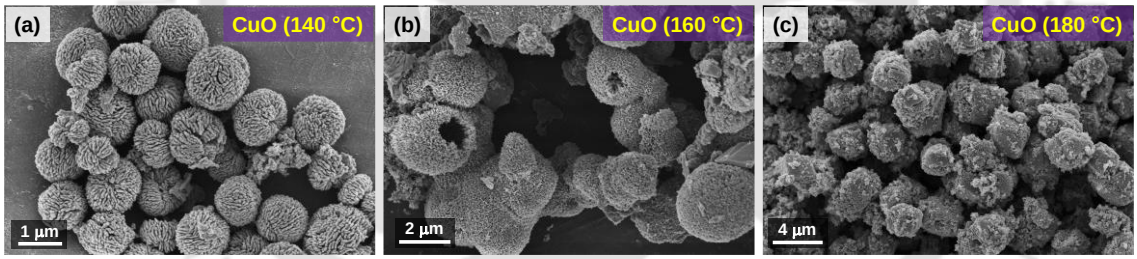

Figure 6.3.2: FESEM images showing the morphological features of hydrothermally synthesized CuO at different temperatures of (a) 140 °C, (b) 160 °C, and (c) 180 °C

In **Figure 6.3.3**, the optimization time for the morphological transformation of solid spheres of Mn_2O_3 into the hollow spherical structures of Mn_2O_3/CuO has been depicted. After 2 hrs of reaction time (**Figure 6.3.3a**), it can be observed that the transformation into hollow structure has commenced confirmimg the initiation of the ion-exchange diffusion between Cu ions Mn_2O_3 particles. After 4 hrs of reaction time (**Figure 6.3.3b**), it seems like the Cu ions have completely underwent the ion-exchange diffusion at the surface of the Mn_2O_3 sphere resulting in the hollowness in the structure. After 6 hrs of reaction (**Figure 6.3.3c**), there is the formation of ideal hollow spheres of Mn_2O_3/CuO formed due to the ion-exchange diffusion process between the Cu ions and Mn_2O_3 particles. On further reaction, 8 hrs (**Figure 6.3.3d**), the hollow spheres start to disintegrate causing in breakdown of the

structures. Thus, 6 hour of reaction time was chosen as optimum time for the morphological transformation of Mn_2O_3 solid spheres into the hollow spherical structures of Mn_2O_3/CuO.

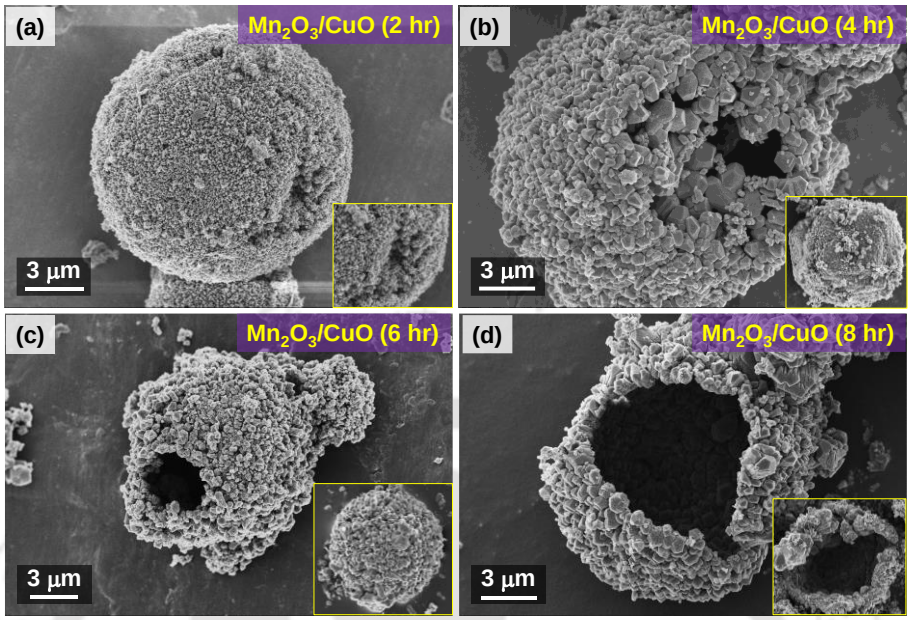

Figure 6.3.3: FESEM images of optimization for the morphological transformation into hollow spheres of Mn_2O_3/CuO at different time of (a) 2 hrs, (b) 4 hrs, (c) 6 hrs, and (d) 8 hrs reacted at the temperature of 160 °C

To facilitate swift charge transfer from the surface of the metal oxide at the electrolyte interface, a 2D oxygen evolution catalyst (OEC) layer of vanadyl phosphate hexahydrate was incorporated over the surface of Mn_2O_3/CuO hollow spheres.

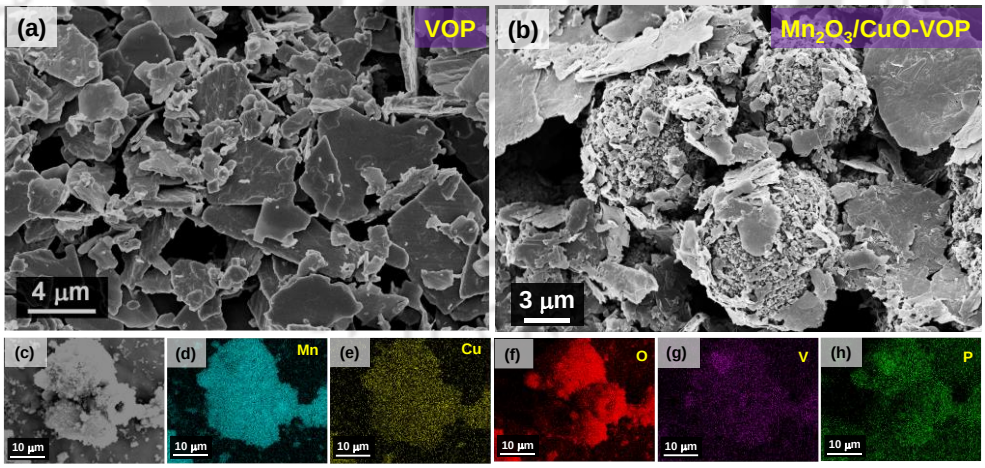

Figure 6.3.4: FESEM images of (a) bare 2D sheets of $(VO)_3(PO_4)_2.6H_2O$ (VOP), (b) the composite working electrode, Mn_2O_3/CuO-VOP, fabricated over the FTO, and (c) EDX spectra showing the uniform distribution of (d) manganese, (e) copper, (f) oxygen, (g) vanadium, and (h) phosphorous over surface of the composite

The FESEM images of bare VOP sheets and that of composite has been shown in **Figure 6.3.4a**. **Figure 6.3.4b** depicts the FESEM image of the composite working electrode

fabricated over FTO substrate confirming the homogenous deposition of VOP sheets over Mn_2O_3/CuO particles. The uniform distribution of VOP over the Mn_2O_3/CuO particle is confirmed by the energy dispersive X-ray spectroscopy (EDS) method, where in **Figure 6.3.4c-h** displays the presence of all the elements uniformly over the hollow spherical structure.

6.3.2. Morphological Analyses through Transmission Electron Microscope (TEM) technique

Field emission transmission electron microscope (FETEM) technique was further utilized to verify the morphological transformation from solid to hollow spheres in the synthesized compounds.

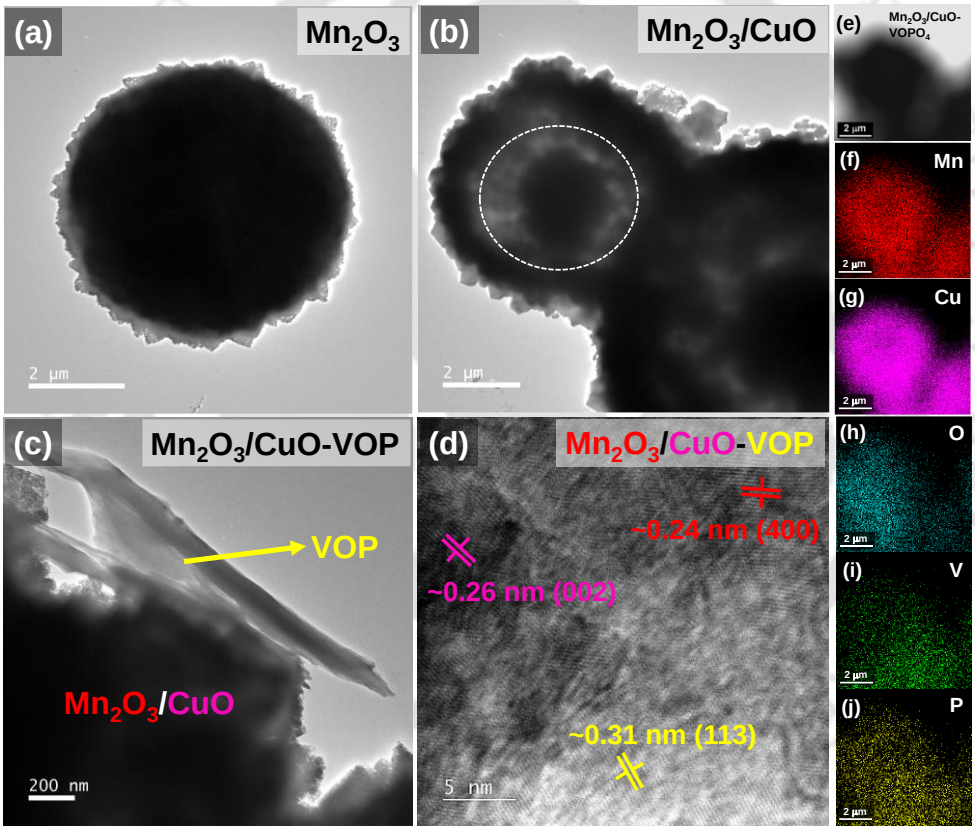

Figure 6.3.5: FETEM images of (a) solid-spherical Mn_2O_3, (b) morphologically transformed hollow-spherical Mn_2O_3/CuO, (c) the composite, Mn_2O_3/CuO particle with overlying 2D VOP sheet, (d) HRTEM image of the composite showing the lattice fringes with the *d*-spacing values corresponding to respective crystal planes of Mn_2O_3, CuO, and VOP, (e) STEM-EDS elemental mapping of the composite showing the uniform presence of the respective elements, (f) manganese, (g) copper, (h) oxygen, (i) vanadium, and (j) phosphorous

Figure 6.3.5a shows the FETEM images of Mn_2O_3 demonstrating the solid spherical structures of ~6μm average diameter. **Figure 6.3.5b** confirms the morphological

transformation from solid spheres to hollow spherical structures upon in-situ growth of CuO over the Mn_2O_3 particles. In the composite (**Figure 6.3.5c**), the deposition of the VOP sheet over the Mn_2O_3/CuO surface is clearly visible suggesting distribution of the OEC layer over the bare electrocatalyst. **Figure 6.3.5d** shows the HRTEM image of the composite, Mn_2O_3/CuO-VOP, where the lattice fringes of Mn_2O_3, CuO and VOP corresponding to the (400), (002) and (113) planes with d-spacing value of ~0.24 nm, ~0.26 nm and ~0.31 nm, respectively are demonstrated. This further confirms the presence of VOP sheets over the Mn_2O_3/CuO particles. The scanning transmission electron microscopy energy dispersive spectrometry (STEM-EDS) technique was utilized to obtain the elemental mapping (**Figure 6.3.5e-j**) for the composite, Mn_2O_3/CuO-VOP, to show the uniform deposition of VOP over the Mn_2O_3/CuO particles.

6.3.3. Phase and Structural Analyses

The phase formation of the synthesized materials and the composite has been confirmed by X-ray diffractometer (XRD) technique. **Figure 6.3.6a**, depicts the XRD spectra of all the synthesized powder compounds. All the peaks are well indexed corresponding to cubic phase of Mn_2O_3 (ICSD No. 01-071-3820) and monoclinic phase of CuO (ICSD No. 00-002-1040). From the XRD spectrum of Mn_2O_3/CuO, it can be ascertained that CuO has been formed over the surface of Mn_2O_3 particles without altering the phase of the Mn_2O_3. **Figure 6.3.6b** shows the XRD spectrum of vanadyl phosphate hexahydrate [$(VO)_3(PO_4)_2.6H_2O$] (mentioned as VOP) corresponding to the triclinic phase (ICSD No. 00-049-1256). In **Figure 6.3.6c** the XRD spectra of the working electrodes fabricated over FTO substrate of bare Mn_2O_3, Mn_2O_3/CuO, bare VOP and composite Mn_2O_3/CuO-VOP are shown with all the peaks indexed to their respective planes.

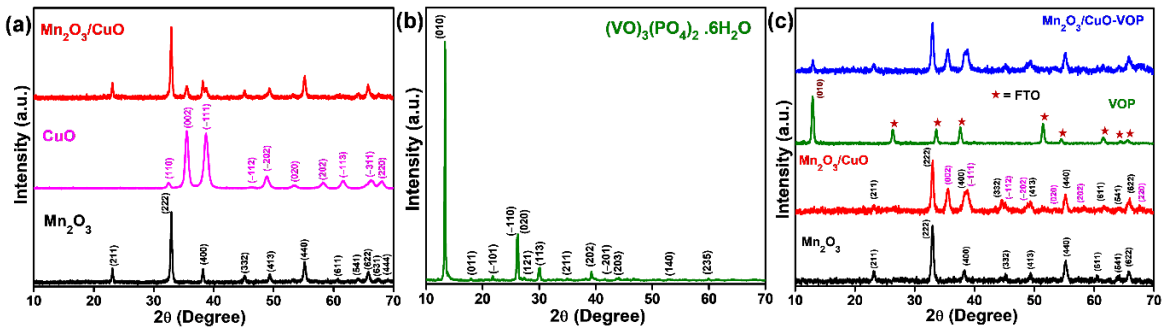

Figure 6.3.6: PXRD pattern of (a) all the synthesized compounds, Mn_2O_3, CuO and Mn_2O_3/CuO, in powder form, (b) bare vanadyl phosphate hexahydrate, and (c) all the fabricated working electrodes over the FTO substrate

6.3.4. Electronic Structure Analyses

The electronic and elemental features of bare and composite compounds are examined utilizing the X-ray photoelectron spectroscopy (XPS) technique. **Figure 6.3.7a** is the survey spectra of Mn_2O_3/CuO, VOP and the composite Mn_2O_3/CuO-VOP confirming the presence of all the elements in the respective compounds. **Figure 6.3.7b** is the Mn2p core-level spectra for Mn_2O_3/CuO and Mn_2O_3/CuO-VOP where the peak for both has been deconvoluted into $2p_{3/2}$ and $2p_{1/2}$ with energy difference of ~11.5 eV.[58,59] **Figure 6.3.7c** is core-level spectra of Cu2p for Mn_2O_3/CuO and Mn_2O_3/CuO-VOP where the peak for both has been deconvoluted into $2p_{3/2}$ and $2p_{1/2}$ with energy difference of ~20 eV.[58,59] In the core-level spectra of O1s (**Figure 6.3.7d**), the lattice oxygen ($O_{lattice}$), oxygen vacancies (O_{vac}) and surface adsorbed oxygen (O_{ads}) peaks are demonstrated for bare Mn_2O_3/CuO, VOP and the composite Mn_2O_3/CuO-VOP.[58–62] It is seen that the $O_{lattice}$ peaks for M-O bond (529.5 eV) and that for PO_4^{3-} group (530.5 eV) are both present in the composite O1s spectra with the shifts suggesting the electronic interactions between them. The shifts in the peak positions suggests the possible electronic interactions between the bare electrocatalyst (Mn_2O_3/CuO) and the OEC (VOP).

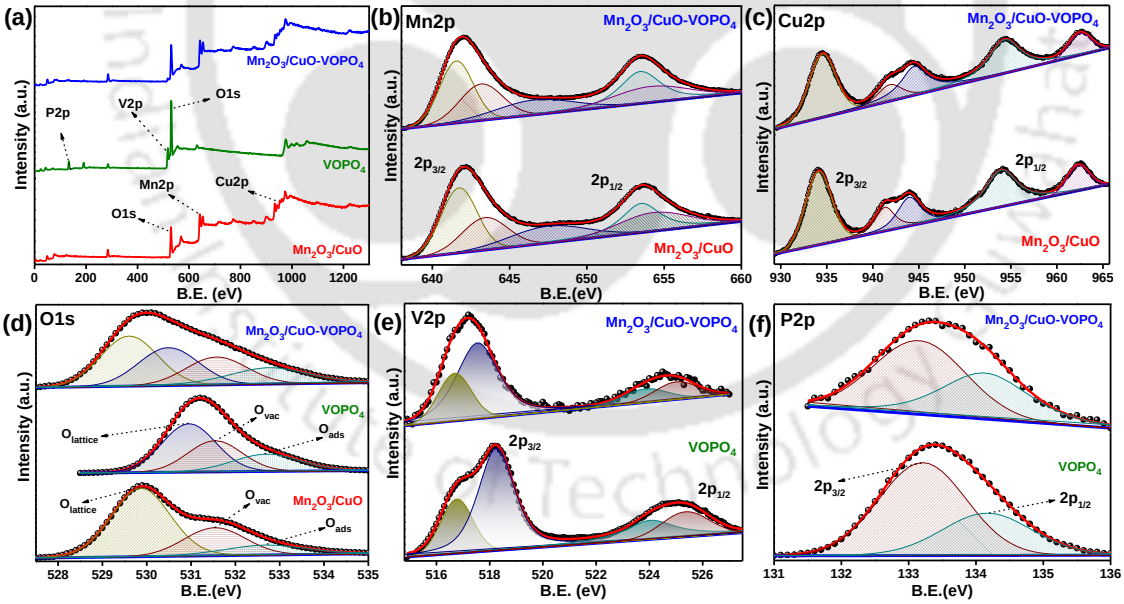

Figure 6.3.7: (a) XPS survey spectra of Mn_2O_3/CuO, VOP and Mn_2O_3/CuO-VOP confirming the presence of all the elements, and XPS core-level spectra of (b) Mn2p, (c) Cu2p, (d) O1s, (e) V2p, and (f) P2p in the electrocatalyts

Figure 6.3.7e depicts the core-level spectra of V2p for bare VOP and composite Mn_2O_3/CuO-VOP deconvoluted into their respective $2p_{3/2}$ and $2p_{1/2}$ peaks.[61,62] As can be seen the $2p_{3/2}$ peak for VOP at 518.25 eV is shifted to lower binding energy for Mn_2O_3/CuO-VOP

at 517.54 eV. The red shift in the binding energy (B.E.) suggests the accumulation of electron density around the V atom of VOP from Mn_2O_3/CuO. The **Figure 6.3.7f** depicts the core-level spectra of P2p for bare VOP and composite Mn_2O_3/CuO-VOP deconvoluted into their respective $2p_{3/2}$ and $2p_{1/2}$ peaks.[61,62] The red shift in the B.E. of $2p_{3/2}$ peak from 133.21 eV for VOP to 133.01 eV for Mn_2O_3/CuO-VOP confirms the shift of electron density around the P atom of VOP. The transfer of electron density from Mn_2O_3/CuO to the VOP in the composite, Mn_2O_3/CuO-VOP, confirms the strong interaction between the semiconductor and the overlayer.

6.3.5. Mott-Schottky Analyses

The main motive for the synthesis of Mn_2O_3/CuO catalyst is to form *n-p* type heterojunction to enhance the bi-functional behaviour of the semiconductor. The formation of the *n-p* type heterojunction has been proved using Mott-Schottky (M-S) measurement. From **Figure 6.3.8**, it can be inferred that Mn_2O_3 is *n*-type semiconductor due to the obtained positive slope, CuO is *p*-type semiconductor due to the obtained negative slope, and VOP is *n*-type semiconductor due to its positive M-S slope.[63–65] By extrapolating the slope to Y-axis = 0, the flat-band potential (E_{FB}) values were determined, and the obtained E_{FB} for Mn_2O_3 is 0.58 V, CuO is 0.84 V, and VOP is 0.47 V. Thus, it was observed that Mn_2O_3 and CuO forms the *n-p* heterojunction as confirmed from **Figure 6.3.8a**, and VOP forms an overlayer over the Mn_2O_3/CuO particles. Thus, in the composite material there is formation of *n-p* heterojunction having favourable band positions with *n-type* electroactive overlayer for water oxidation reactions.[66–68]

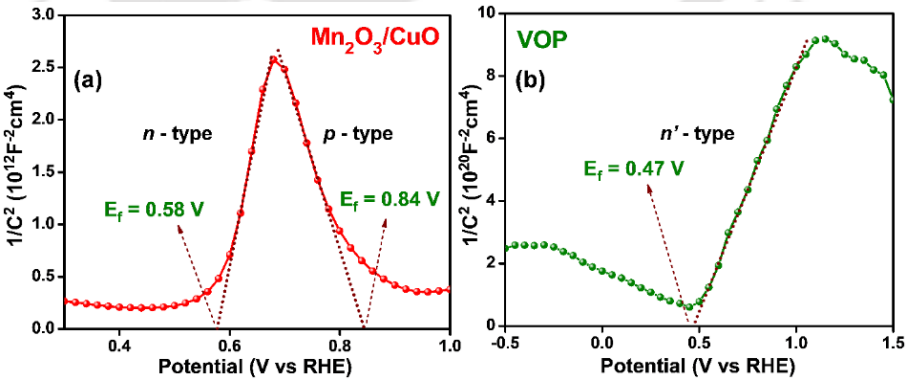

Figure 6.3.8: Mott-Schottky plots of (a) Mn_2O_3/CuO, and (b) VOP showing their respective semiconductor behaviours

6.3.6. Electrochemical Performance for Oxygen Evolution Reaction

The electrocatalytic performances of the compounds were examined using the linear sweep voltammetry (LSV) technique, where the compounds fabricated over FTO were

utilized as a working electrode, Hg/HgO (due to its activity and stability in alkaline conditions) and graphite rod as reference and counter electrodes, respectively, in 1 M NaOH electrolyte solution. To determine the best electrocatalyst, all the synthesized Mn_2O_3/CuO material were subjected to the LSV measurement. From **Figure 6.3.9a**, it can be seen that with the increase in the reaction time, the OER performance of the electrocatalyst also increases suggesting the availability of more exposed electro-active surfaces with the generation of hollownes in the structure. Thus, the Mn_2O_3/CuO formed after 6 hours of reaction time was chosen as the best material for electrocatalysis. Further, for the formation of the composite material, the exfoliated VOP was drop-casted over the Mn_2O_3/CuO surface and oven dried. The amount of VOP was varied from 25 µL to 125 µL and all were subjected to LSV measurement under similar conditions. From **Figure 6.3.9b**, it can be seen that with increase in concentration of VOP, the OER performance also increases and the optimum amount of deposited VOP was found to be 100 µL. Further increase in the amount of VOP hampers the performance due to over deposition restricting the charge transfer at the interface.

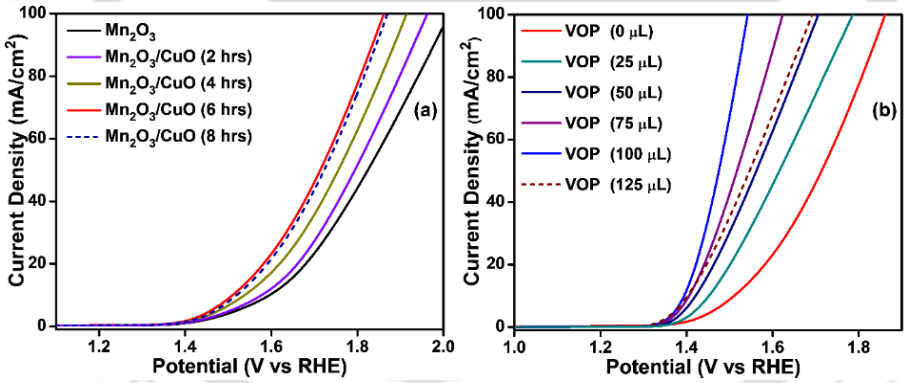

Figure 6.3.9: Optimization curve for (a) the reaction time CuO over the Mn_2O_3 particles and (b) the deposition of VOP over the surface of Mn_2O_3/CuO

After determination of the optimized electrocatalyst, its catalytic performance was evaluated via LSV curves. The obtained LSV curves for OER of bare Mn_2O_3, Mn_2O_3/CuO, VOP and Mn_2O_3/CuO-VOP are shown in **Figure 6.3.10a**. The measured overpotential (η_{10}) at current density of 10 mA/cm^2 for the composite, Mn_2O_3/CuO-VOP, shows an excellent value at 190 (±2) mV whereas that for bare Mn_2O_3/CuO is 280 (±3) mV, VOP is 340 (±3) mV, and Mn_2O_3 is 370 (±2) mV. The improvement in the overpotential value for Mn_2O_3/CuO compared to its bare counterpart is due to the structural transformation from solid to hollow sphere aiding incorporation of more electrolyte solution into the active sites. This increases the amount of water molecules getting converted to oxygen leading to boosted OER activity.

Additionally, the formation of *n-p* heterojunction between Mn_2O_3 and CuO, also aids the enhanced electrochemical performance due to better charge separation and accumulation at the electrolyte interface. The enhanced performance in the composite Mn_2O_3/CuO-VOP is due to the 2D vanadyl phosphate hexahydrate which increases the adsorption of water molecules to the surface (owing to the high valence V^{4+} ions) and also fasters the reaction kinetics of the material (also confirmed by enhanced OER activity of Mn_2O_3-VOP).

The water oxidation kinetics of the electrocatalyts were examined by determining the Tafel slope which states about their charge transfer coefficient values (**Equation 2.8 & 2.9**). The obtained Tafel slope value (**Figure 6.3.10b**) for the composite Mn_2O_3/CuO-VOP is 60 mV/decade which is much lower than Mn_2O_3/CuO (124 mV/decade), and bare counterparts VOP (106 mV/decade) and Mn_2O_3 (152 mV/decade). The formation of *n-p* type heterojunction in Mn_2O_3/CuO is responsible for the decrease of Tafel slope value compared to the bare Mn_2O_3. The heterojunction (*n-p* type) formation results in better charge separation in the bulk and faster extraction at the electrolyte interface leading to faster rate of the electrochemical reaction. The lower Tafel slope of bare VOP compared to bare Mn_2O_3 and Mn_2O_3/CuO explains its higher charge transfer coefficient value (**Equation 2.8 & 2.9**). Thus, the lowering of the Tafel slope in the composite is due to the faster reaction kinetics of the 2D vanadyl phosphate species at the electrolyte interface owing to its higher charge transfer coefficient value.

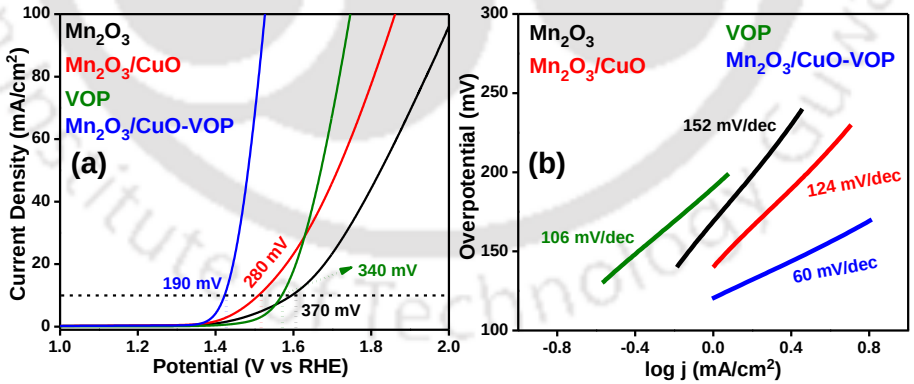

Figure 6.3.10: (a) Linear sweep voltammograms (LSV) of Mn_2O_3, Mn_2O_3/CuO, VOP and Mn_2O_3/CuO-VOP during OER, (b) their corresponding Tafel slope values

6.3.7. Electrochemical Performance for Hydrogen Evolution Reaction

The presence of CuO in the composite, forming a *n-p* heterojunction allows the material to act as HER (hydrogen evolution reaction) catalyst. In Mn_2O_3/CuO-VOP, the type-II heterojunction between Mn_2O_3 and CuO allows facile charge transfer and accumulation due to their favourable band alignments, suitable to reduce the water molecules generating

hydrogen with 2D VOP overlayer accelerating the reaction process.[66–68] Thus, the synthesized electrocatalysts were subjected to HER in the alkaline medium by varying the potential from 0.1 to -1 V vs. RHE. **Figure 6.3.11a** depicts the LSV curves of all the electrocatalysts, and can be seen that with the incorporation of CuO into the Mn_2O_3, the overpotential value (η_{10}) shifts from 550 (±2) mV for Mn_2O_3 to 310 (±4) mV for Mn_2O_3/CuO. The improvement in the electrocatalytic performance is due to the formation of *n-p* type heterojunction (aiding the charge separation and transfer to electrolyte interface) and morphological transformation into hollow spheres (more exposed active sites). Further advancement in performance of the composite, Mn_2O_3/CuO-VOP (η_{10} = 220 (±3) mV), attributes to the faster charge transfer kinetics of VOP leading to better charge separation and extraction at the electrolyte interface.

To probe the reaction rate (i.e., how efficiently the electrocatalyst can produce current in response to change in potential), Tafel slope of the corresponding electrocatalyts were evaluated (**Figure 6.3.11b**) and the obtained results for bare Mn_2O_3 is 187 mV/dec, Mn_2O_3/CuO is 160 mV/dec, bare VOP is 142 mV/dec and the composite Mn_2O_3/CuO-VOP is 105 mV/dec. It can be seen that for HER, similar trend in the reaction kinetics was observed for the electrocatalysts.

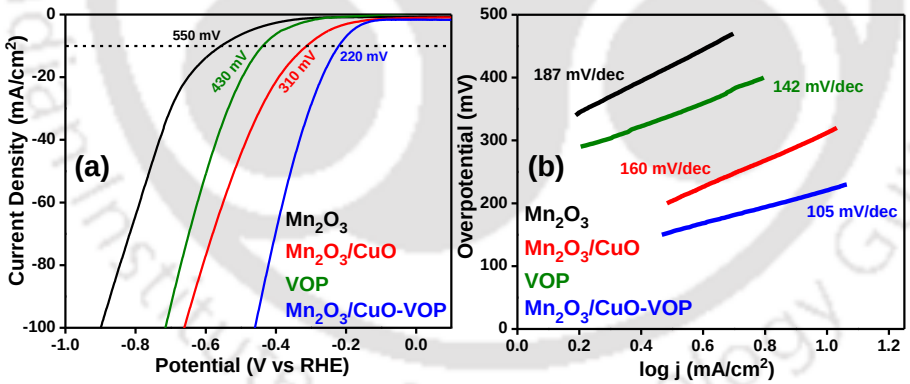

Figure 6.3.11: (a) LSV plots for Mn_2O_3, Mn_2O_3/CuO, VOP and Mn_2O_3/CuO-VOP during the HER, (b) their corresponding Tafel slope values

6.3.8. Electrochemical Active Surface Area (ECSA) Analyses

The enhancement in the electrochemical performances is often the result of the increased electroactive sites in the compounds. To determine amount of electrochemical active sites (ECSA) for all the electrocatalyts, double-layered capacitance (C_{dl}) value has been evaluated by measuring the cyclic voltammograms (CV) (**Figure 6.3.12a-d**) in the non-Faradaic region varying the scan rates. For the estimation of the C_{dl} values, the CVs were carried out at low scan rates as it would allow the charged species to completely get adsorbed

over the surface of the electrode material giving more insight of the double-layer formation. From **Figure 6.3.12e**, it can be seen that the C_{dl} values for all the electrocatalyts are in accord with the obtained overpotential values. The ~3-fold increase in the ECSA for the Mn_2O_3/CuO (34 (±2.5) mF/cm^2) compared to bare Mn_2O_3 (12 (±1) mF/cm^2) can be attributed to the morphological transformation from the solid spherical structures to hollow spheres which resulted in more exposed active sites. The high ECSA value for the composite, Mn_2O_3/CuO-VOP, (55 (±2) mF/cm^2) is due to the hollowness in the structure (Mn_2O_3/CuO) exposing more active sites and also the additional active sites of the 2D sheets of vanadyl phosphate.

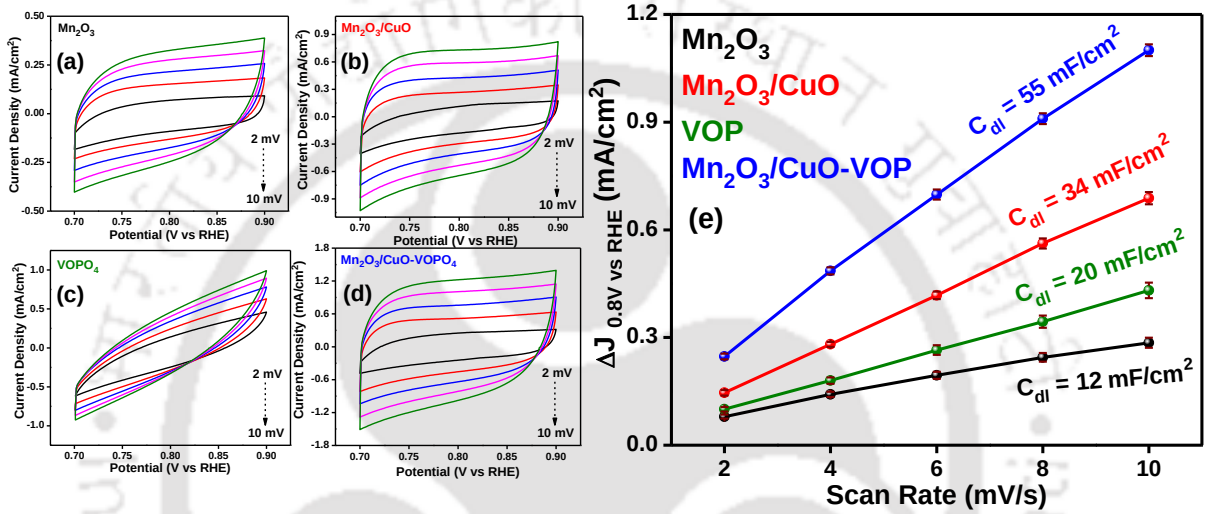

Figure 6.3.12: Cyclic voltammograms of (a) Mn_2O_3, (b) Mn_2O_3/CuO, (c) VOP and (d) Mn_2O_3/CuO-VOP measured at scan rate from 2 mV/s to 10 mV/s in the non-Faradaic region, and (e) current density vs the scan rate plots for determination of the C_{dl} values

6.3.9. Electrochemical Impedance Spectroscopy (EIS) Analyses

Charge transfer kinetics at the electrolyte interface is one of the criteria for the enhancement in the electrochemical performances. Electrochemical impedance spectroscopy (EIS) technique is utilized for the resolution of the charge mobility at the electrode-electrolyte interface by evaluating the charge transfer resistance (R_{ct}) value. In **Figure 6.3.13a**, EIS was performed at an open circuit potential (OCP) to evaluate the Nyquist plots of individual catalysts and the calculated R_{ct} values at the electrolyte interface are in trend with the obtained Tafel slopes, explaining the advancement in the reaction kinetics. As explained by **Equation 2.8 & 2.9**, the Tafel slope value is inversely proportional to the charge transfer coefficient of the material (i.e., $\text{Tafel slope} \propto 1/\alpha$). The R_{ct} value at the electrolyte interface for bare Mn_2O_3 is 29.2 Ω, and that for bare VOP is 12.2 Ω explaining the inherent higher charge transfer coefficient value of 2D OEC materials. The lowering of the R_{ct} value for the Mn_2O_3/CuO (17.8 Ω) is due to the morphological transformation into hollow

sphere providing the reactants access to more exposed surfaces and also the formation of *n-p* heterojunction provides better charge separation, resulting into the faster charge transfer at the electrolyte interface. Further lowering of the R_{ct} value for the composite, Mn_2O_3/CuO-VOP (8.4 Ω), is due to the overlying VOP sheets which accelerates the charge transfer at the electrolyte interface (due to its inherent higher charge transfer coefficient) enhancing the overall water oxidation process.

Figure 6.3.13b represents the Nyquist plots obtained for the electrocatalyts measured at a potential of 1.5 V vs RHE. The calculated R_{ct} values for the electrocatalyts are in trend with their obtained Tafel slopes explaining the advancement in the reaction kinetics. The R_{ct} value for bare Mn_2O_3 is 274 Ω, Mn_2O_3/CuO is 173 Ω, bare VOP is 125 Ω, and the composite, Mn_2O_3/CuO-VOP, is 66 Ω. The obtained R_{ct} value are in similar trend as obtained at OCP, stating the improvement in electrochemical performance of the composite is due to the morphological transformation into hollow spheres and faster charge transfer kinetics of the 2D vanadyl phosphate sheets.

The advancements in the HER performance of the modified electrocatalysts were further confirmed by the Nyquist plots obtained by performing the EIS at -0.4 V vs. RHE. The R_{ct} values (**Figure 6.3.13c**) provides the extent of charge transfer kinetics at the electrolyte interface, where in for bare Mn_2O_3 it is 418 Ω, Mn_2O_3/CuO is 252 Ω, bare VOP is 196 Ω and the composite Mn_2O_3/CuO-VOP is 128 Ω. The lowering of the R_{ct} value for Mn_2O_3/CuO is due to the availability of more electroactive sites, generated by the hollowness in the structure, which acts as the surface adsorption sites for the water molecules to undergo reduction process. Further lowering of R_{ct} value for the composite is due to the inherent higher charge transfer coefficient value of the 2D VOP sheets.

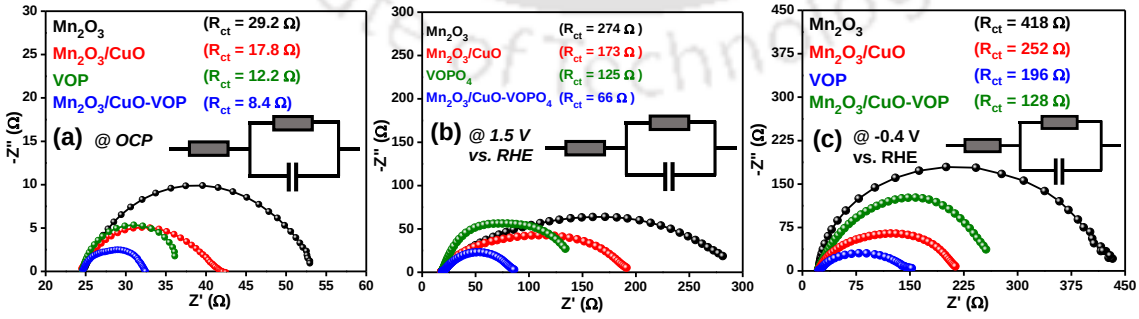

Figure 6.3.13: (a) Nyquist plots of all the electrocatalyts measured at open circuit potential, (b) Nyquist plot with respective R_{ct} values measured at a potential of 1.5 V vs. RHE, and (c) Nyquist plots of all the electrocatalyts measured at a potential of -0.4 V vs. RHE with the obtained R_{ct} values at the electrolyte interface and the corresponding circuit

6.3.10. Electrocatalytic Efficiency Analyses

The insight into the catalytic activity of an electrocatalyst can be determined by calculating the turnover frequency (TOF) value at a fixed potential. **Figure 6.3.14a** shows the TOF values of the electrocatalysts, Mn_2O_3, Mn_2O_3/CuO, VOP, and Mn_2O_3/CuO-VOP, calculated at a potential value of 1.4 V vs RHE. As seen, with the morphological transformation there is ~2.5 folds increment in the TOF for Mn_2O_3/CuO due to the generation of more surface-active sites in the hollow sphere. For the composite material, the ~10 folds increment in TOF ascribes to both the generated active sites due to hollowness in the structure and the faster kinetics of 2D sheets of vanadyl phosphates.

The turnover frequencies (TOF) of the synthesized materials were evaluated to determine its electrocatalytic activity for HER at a fixed potential of -0.15 V vs. RHE. **Figure 6.3.14b** shows the TOF values of all the electrocatalyts, and it can be observed that there is ~4 folds increment in the electrochemical performance for hollow spherical Mn_2O_3/CuO and ~10 folds advancement for composite Mn_2O_3/CuO-VOP compared to the solid Mn_2O_3 spheres.

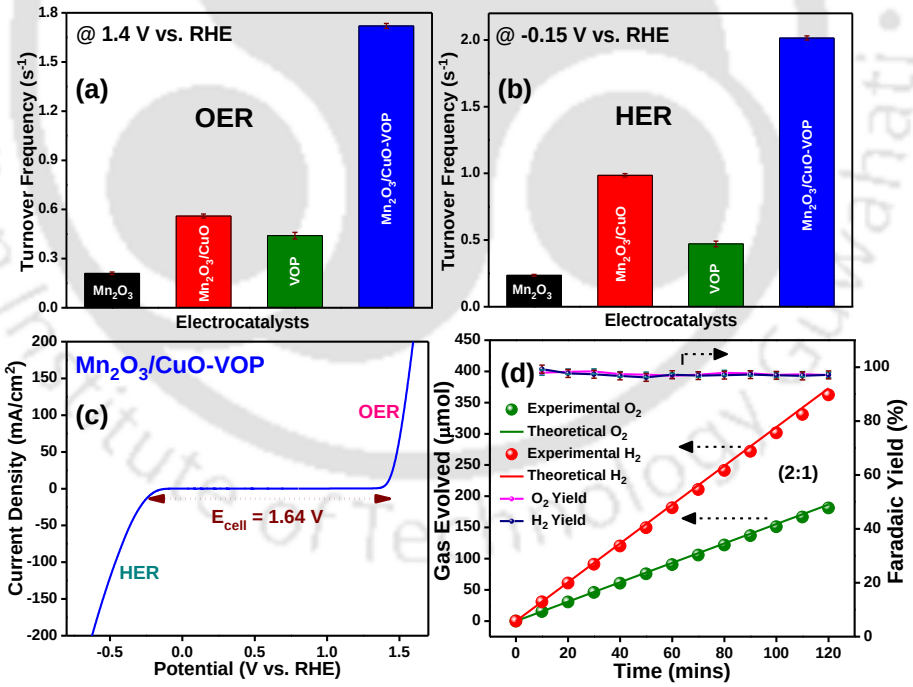

Figure 6.3.14: Turnover frequencies of all the electrocatalysts determined at a potential of (a) 1.4 V vs RHE (OER), (b) -0.15 V vs RHE (HER), (c) overall water splitting utilizing the composite, Mn_2O_3/CuO-VOP, depicting the cell voltage and (d) Faradaic yield for Mn_2O_3/CuO-VOP measured at a current density of 10 mA cm^{-2} using gas chromatography

For demonstration of the bifunctional behaviour of the composite electrocatalyst, it was subjected to electrochemical analysis by evaluating the LSV taking the fabricated

electrode both as anode and cathode during water splitting reaction. **Figure 6.3.14c** shows the overall water splitting comprising both OER and HER with overpotential values (at +/-10 mA/cm^2) of 190 (±2) mV and 220 (±3) mV, respectively. This confirms that the synthesized composite material can be utilized efficiently for both water oxidation and reduction in alkaline medium due to its bifunctional property.

Faradaic yield is estimated to quantify the relation between the amount of gasses evolved and the obtained current density, minimizing the influence of any side reactions. From **Figure 6.3.14d**, it can be seen that the ratio of evolved H_2 gas to O_2 gas is 2:1, which is in accord with the theoretical approach. During the measurement, the composite (Mn_2O_3/CuO-VOP) electrode was taken as both cathode and anode, and the evolved gasses were measured using online gas chromatography technique. The figure represents both the amount of gasses evolved and also the faradaic yield percentage during the reaction course. The average Faradaic yield obtained for HER was ~97 (±1) % and while for OER was ~98 (±1) % suggesting that the charge carriers generated within the system are consumed solely for the reduction and oxidation of H_2O molecules, producing H_2 and O_2 gas, respectively, and there are no side reactions at high potential.

6.3.11. Long-term Stability Analyses

A good electrocatalyst should have high stability to be used for long run in harsh conditions. To test the durability of the synthesized electrocatalyst, chronoamperometry measurements were performed at a fixed potential (1.5 V vs RHE). **Figure 6.3.15a** shows the stability for both Mn_2O_3/CuO and Mn_2O_3/CuO-VOP with negligible decrease in the current density even after 36 hours of continuous operation. The inset shows the constancy in the LSV curve of the composite material towards OER measured before and after the stability test.

The composite, Mn_2O_3/CuO-VOP, was also tested for stability utilizing the chronoamperometry technique at a negative potential of -0.3 V vs. RHE for 36 hours of continuous run (**Figure 6.3.15b**) and was found that there is negligible decrease in the current density confirming its high durability for HER. The inset shows the constancy in the LSV curve of the composite material towards HER measured before and after the stability test.

To further test the durability of the catalyst, the composite material was tested for 1000 cycles of cyclic voltammetry measurement in the non-Faradaic region. From **Figure**

6.3.15c it can be confirmed that the electrocatalyst is highly stable as there is no negligible decrease in the current density value.

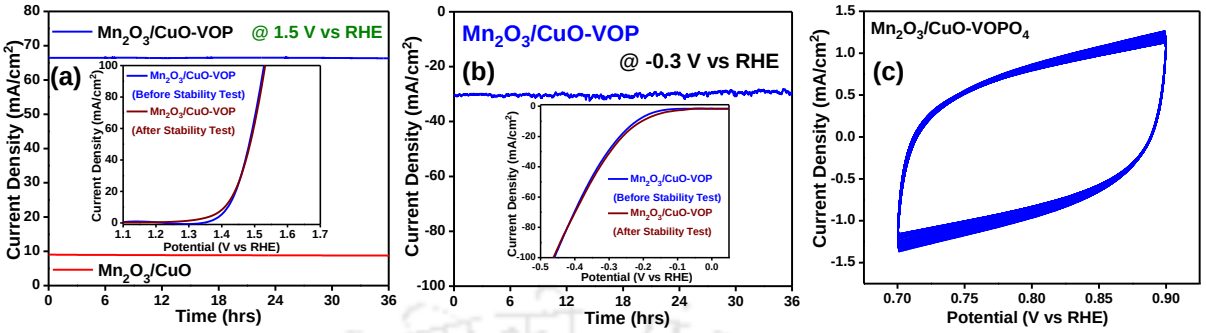

Figure 6.3.15: (a) chronoamperometric analysis measured at a potential of 1.6 V vs. RHE for Mn_2O_3/CuO and Mn_2O_3/CuO-VOP with inset of LSV curves of composite before and after the stability test, (b) chronoamperometric analysis measured at a fixed potential of -0.3 V vs. RHE for the composite with inset of LSV plot measured before and after the stability test, and (c) CV curve of 1000 cycles measured in non-Faradaic region for the composite Mn_2O_3/CuO-VOP

6.3.12. Post-Stability Analyses

To analyse the structural and electronic property integrity, the composite material was re-examined utilizing XRD, FESESM, FETEM and XPS techniques.

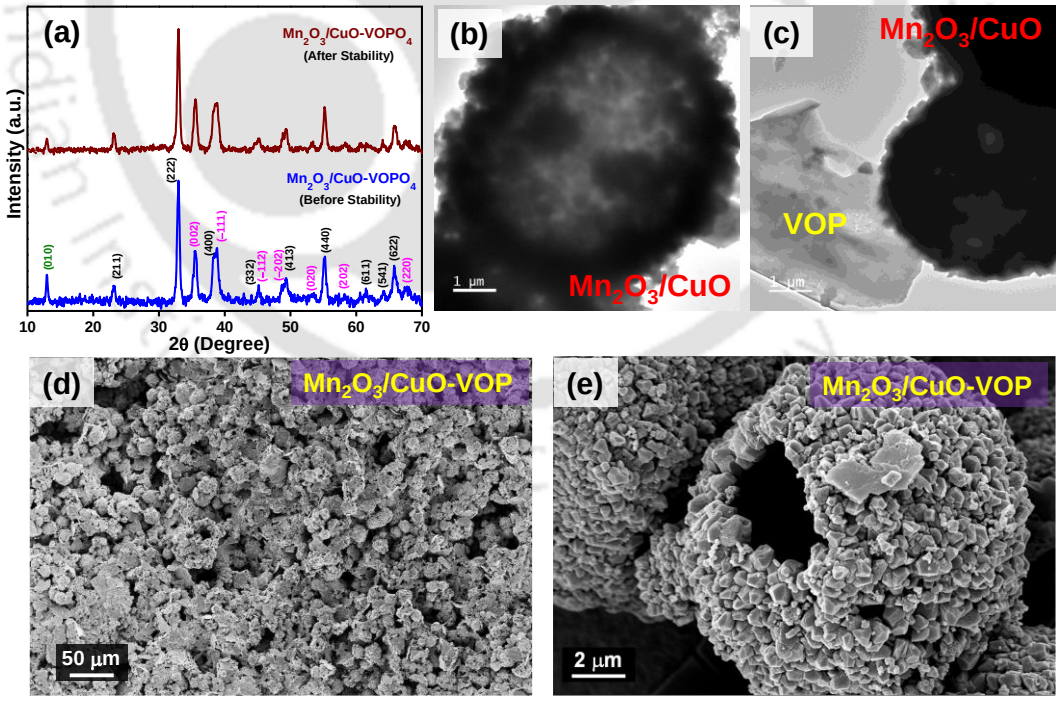

Figure 6.3.16: (a) PXRD of the composite Mn_2O_3/CuO-VOP before and after the stability test, (b) FETEM images showing the hollow spherical structure of Mn_2O_3/CuO after the stability test, (c) FETEM image of the composite showing the presence of VOP sheet over the surface of Mn_2O_3/CuO, (d, e) FESEM image of the composite, Mn_2O_3/CuO-VOP, showing the adhesion of VOP sheets over Mn_2O_3/CuO particles and retention of hollow structures

In **Figure 6.3.16a**, the XRD spectra of the composite Mn_2O_3/CuO-VOP, before and after stability test, has been shown. It can be seen that there are no shifts and change in the peak positions suggesting the intact of the phase of the individual material in the composite. Also, from the FETEM (**Figure 6.3.16b & c**) and FESEM (**Figure 6.3.16d & e**) images of the composite after the stability test, it can be commented that the material is highly durable and can be utilized without any loss in the structural features. Thus, as-observed that there were no changes in the electronic and structural features confirming the high stability of the composite material.

6.3.13. Density Functional Theory (DFT) Analyses

For better understanding of the materials features, DFT based theoretical analysis has been performed where we have considered three materials CuO, Mn_2O_3, VOP (vanadyl phosphate hexahydrate) for our present study. The morphological transformation in Mn_2O_3/CuO from solid sphere to hollow spherical structure, and the presence of VOP overlayer on its surface enhancing the overall water splitting performance needs more attention from scientific community. In this work, VOP overlayer has been added to morphologically transformed Mn_2O_3/CuO and observed its influence on the electrocatalytic process. For our theoretical analysis, we have optimized surface in (100) plane of all three individual structures. The lattice mismatch is also considered while making the supercell of individual structures. The vacuum barrier at surface and the energy barrier between the junction can be modulated using materials with different work function (φ). The key for designing a type-II heterojunction for high performance is to efficiently modulate the carrier transfer at the junction in a controlled manner. The band alignment at the interface is of great importance, thus favourable band alignment to balance the carrier separation, confinement, as well as recombination, from the application-oriented point of view has to be taken care of. During the junction formation, it is thought that there is a vacuum potential barrier between Mn_2O_3 and CuO surface. Such vacuum barrier can be regarded as the driving force for charge transfer near the junction. Mn_2O_3/CuO heterostructure forms a type-II band alignment along with the calculated work function (φ) to be 6.05 eV and 5.77 eV for Mn_2O_3 and CuO, respectively (**Figure 6.3.17a & b**). In order to analyse the modulation in work function with the presence of third structure, we have constructed VOP overlayer which has comparatively low work function (φ) than the other two (4.34 eV) as shown in **Figure 6.3.17c**. This large difference in work function (φ) has a profound effect on the band formation near the junction which eventually affects electrocatalysis, serving our purpose.

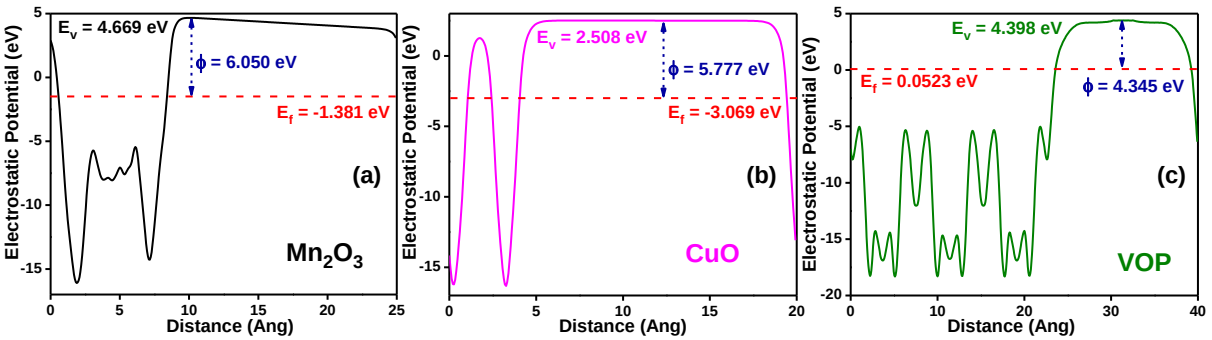

Figure 6.3.17: Work function values of (a) Mn_2O_3, (b) CuO and (c) VOP evaluated from the DFT calculations

6.3.14. Plausible Mechanism for Overall Water Splitting

The plausible mechanism in the composite, Mn_2O_3/CuO-VOP, for the bi-functionality in terms of OER and HER is schematically displayed in **Figure 6.3.18**. The advancement in the OER and HER performances of Mn_2O_3/CuO compared to bare Mn_2O_3 is due to the morphological transformation from solid to hollow spheres.[31,47,48,56] The hollowness in the structure increases the number of electroactive sites (confirmed by the ECSA measurements) giving better access to electrolyte diffusion resulting in more adsorption of water molecules at the surface to undergo the electrocatalytic reactions. In case of the composite, VOP is most catalytically active compared to Mn_2O_3 and CuO, acting as the reaction sites for both water oxidation and reduction. The shift in the electron density from the Mn_2O_3/CuO semiconductor to the VOP overlayer (as depicted by XPS spectra of V2p and P2p) and the lower φ value of VOP confirms the electroactive nature of the VOP molecule. Also, there is formation of the *n-p* heterojunction by virtue of favourable band alignments between the Mn_2O_3 and CuO (confirmed from the M-S plot and DFT calculations) along with overlayer of 2D VOP having inherent faster charge transfer kinetics, which allows facile water oxidation and reduction reactions.[66–68] As can be seen that there is formation of type-II heterojunction between Mn_2O_3 and CuO resulting in the availability of more electrons and holes at the electrolyte interface for both OER and HER. The generated holes in the valence band of Mn_2O_3 transfers to the valence band of CuO due to the favourable band alignment leading to the accumulation of charge carriers at the semiconductor-electrolyte interface to be effectively utilized for OER. Similarly, the electrons in the conduction band of CuO moves to that of Mn_2O_3 thereby accumulating charge carriers effective for water reduction at the electrolyte interface. The 2D VOP catalyst deposited onto the Mn_2O_3/CuO surface acts as the overlayer to enhance the bi-functional behaviour, OER and HER, of the semiconductor material owing to its inherent faster charge transfer coefficient. The holes and electrons that

are accumulated at the surface of Mn_2O_3/CuO particles are effectively extracted to the electrolyte interface by 2D VOP sheets resulting in accelerated OER/HER processes owing to its faster reaction kinetics due to reduced charge transfer resistance.[69,70] The DFT calculation also supports VOP overlayer to be efficient for charge carriers extraction from semiconductor interface and transfer to the electrolyte interface due to its lower work function (φ) value.[69,71,72] Additionally, VOP consists of V-atom at higher oxidation state (+4) which is suitable for lowering the water adsorption energy at the surface thereby providing more reactant species to undergo the oxidation and reduction reactions.[42,43] Therefore, the enhanced electrocatalytic performances of the bi-functional material, Mn_2O_3/CuO-VOP, are due to firstly, the morphological transformation of Mn_2O_3/CuO into hollow spherical structures generating more electroactive sites and better access to electrolyte diffusion; secondly, the formation of *n-p* heterojunction facilitating into better charge accumulation at the semiconductor interface; and lastly, the faster charge transfer kinetics at the electrolyte interface due to the inherent high charge transfer coefficient and lower work function (φ) value of the overlying 2D vanadyl phosphate hexahydrate sheets.

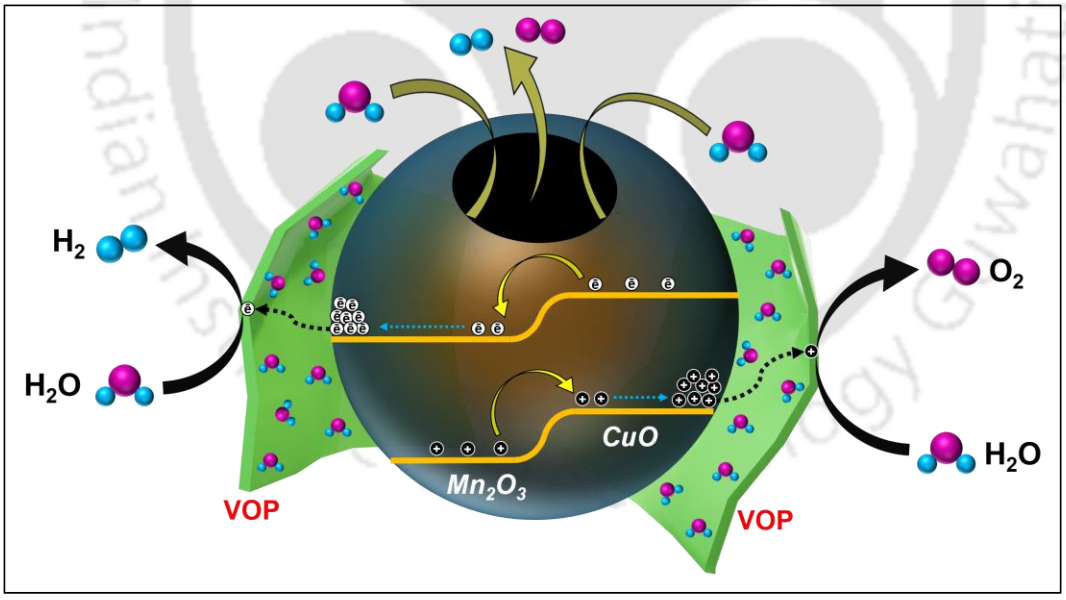

Figure 6.3.18: Plausible mechanistic pathway for the observed bi-functionality of the composite, Mn_2O_3/CuO-VOP, due to the morphological transformation and formation of *n-p* heterojunction in Mn_2O_3/CuO aided by the 2D VOP overlayer sheets

6.4. Conclusions

The diffusion mediated morphological transformation from solid spheres to hollow spherical structures due to the ion-exchange (Kirkendall effect) provided an effective bi-functional electrocatalytic performance for overall water splitting. The hollow space in the spherical structure of Mn_2O_3/CuO generated more exposed surface-active sites (supported by the high ECSA value) causing more adsorption of water molecules on the surface resulting in enhanced bi-functional behaviour (HER-OER) of the electrocatalyst. Also, the work function values (obtained from DFT calculations) showed the formation of type-II heterojunction between Mn_2O_3 and CuO which enhanced the charge separation and accumulation at the semiconductor interface. This improved the overpotential (η_{10}) values for both the OER and HER processes compared to the bare counterparts and also enhanced the reaction kinetics supported by reduced Tafel slope values due to increased charge transfer kinetics at the electrolyte interface (lower R_{ct} value). Further advancement in the electrocatalytic behaviour of the hollow Mn_2O_3/CuO spheres was achieved by overlayering the surface with 2D VOP sheets which accelerated the reaction kinetics at the electrolyte interface due to its inherent high charge transfer coefficient value (as depicted by its lower Tafel slope value). In addition to the faster charge transfer kinetics, the V^{4+} ions in VOP aids the adsorption of water molecules onto its surface, providing more reactant molecules. Thus a ~10-fold increment in the TOF value was obtained for both the OER and HER processes in the alkaline electrolytic medium. The lower work function value of VOP also supports its high efficiency towards the enhancement in the bifunctional behaviour of Mn_2O_3/CuO particles.

6.5. References

[1] Y. Yan, B. Y. Xia, B. Zhao and X. Wang, *J. Mater. Chem. A*, 2016, **4**, 17587.

[2] S. Ghosh and R. N. Basu, *Nanoscale*, 2018, **10**, 11241.

[3] X. Shang, J.-H. Tang, B. Dong and Y. Sun, *Sustain. Energy Fuels*, 2020, **4**, 3211.

[4] X. Li, X. Hao, A. Abudula and G. Guan, *J. Mater. Chem. A*, 2016, **4**, 11973.

[5] B. You and Y. Sun, *Acc. Chem. Res.*, 2018, **51**, 1571.

[6] X. Zhang, X. Cheng and Q. Zhang, *J. Energy Chem.*, 2016, **25**, 967.

[7] J. Yu, Y. Dai, Q. He, D. Zhao, Z. Shao and M. Ni, *Mater. Reports Energy*, 2021, **1**, 100024.

[8] J. Wang, X. Yue, Y. Yang, S. Sirisomboonchai, P. Wang, X. Ma, A. Abudula and G. Guan, *J. Alloys Compd.*, 2020, **819**, 153346.

[9] Y. Yan, B. Y. Xia, B. Zhao and X. Wang, *J. Mater. Chem. A*, 2016, **4**, 17587.

[10] X. Shang, J.-H. Tang, B. Dong and Y. Sun, *Sustain. Energy Fuels*, 2020, **4**, 3211.

[11] Y. Zhu, Q. Lin, Y. Zhong, H. A. Tahini, Z. Shao and H. Wang, *Energy Environ. Sci.*, 2020, **13**, 3361.

[12] J. Zhu, L. Hu, P. Zhao, L. Y. S. Lee and K.-Y. Wong, *Chem. Rev.*, 2020, **120**, 851.

[13] H. Du, R.-M. Kong, X. Guo, F. Qu and J. Li, *Nanoscale*, 2018, **10**, 21617.

[14] Z. Cai, X. Bu, P. Wang, J. C. Ho, J. Yang and X. Wang, *J. Mater. Chem. A*, 2019, **7**, 5069.

[15] N. -T. Suen, S. -F. Hung, Q. Quan, N. Zhang, Y. -J. Xu and H. M. Chen, *Chem. Soc. Rev.*, 2017, **46**, 337.

[16] C. C. L. McCrory, S. Jung, J. C. Peters and T. F. Jaramillo, *J. Am. Chem. Soc.*, 2013, **135**, 16977.

[17] S. Kumaravel, K. Karthick, S. S. Sankar, A. Karmakar, R. Madhu, K. Bera and S. Kundu, *Sustain. Energy Fuels*, 2021, **5**, 6215.

[18] N. Han, P. Liu, J. Jiang, L. Ai, Z. Shao and S. Liu, *J. Mater. Chem. A*, 2018, **6**, 19912.

[19] S. Anantharaj, S. R. Ede, K. Sakthikumar, K. Karthick, S. Mishra and S. Kundu, *ACS Catal.*, 2016, **6**, 8069.

[20] S. Gopi, A. Panda, A. G. Ramu, J. Theerthagiri, H. Kim and K. Yun, *Int. J. Hydrogen Energy*, 2022, **47**, 42122.

[21] S. Anantharaj, S. R. Ede, K. Sakthikumar, K. Karthick, S. Mishra and S. Kundu, *ACS Catal.*, 2016, **6**, 8069.

[22] L. Ji, J. Wang, X. Teng, T. J. Meyer and Z. Chen, *ACS Catal.*, 2020, **10**, 412.

[23] R. Guo, X. Lai, J. Huang, X. Du, Y. Yan, Y. Sun, G. Zou and J. Xiong, *ChemElectroChem*, 2018, **5**, 3822.

[24] L. Tian, X. Zhai, X. Wang, J. Li and Z. Li, *J. Mater. Chem. A*, 2020, **8**, 14400.

[25] Y. Tang, S. Zheng, S. Cao, H. Xue and H. Pang, *J. Mater. Chem. A*, 2020, **8**, 18492.

[26] S. Park, Y. H. Lee, S. Choi, H. Seo, M. Y. Lee, M. Balamurugan and K. T. Nam, *Energy Environ. Sci.*, 2020, **13**, 2310.

[27] X. Liu, H. Zheng, Z. Sun, A. Han and P. Du, *ACS Catal.*, 2015, **5**, 1530.

[28] J. D. Rodney, S. Deepapriya, M. C. Robinson, C. J. Raj, S. Perumal, B. C. Kim, S. Krishnan and S. J. Das, *Int. J. Hydrogen Energy*, 2021, **46**, 27585.

[29] D. Yao, L. Gu, B. Zuo, S. Weng, S. Deng and W. Hao, *Nanoscale*, 2021, **13**, 10624.

[30] K. Mohamed Racik, A. Manikandan, M. Mahendiran, P. Prabakaran, J. Madhavan

and M. Victor Antony Raj, *Phys. E Low-dimensional Syst. Nanostructures*, 2020, **119**, 114033.

[31] L. F. Garcia-Herrera, H. P. McAllister, H. Xiong, H. Wang, R. W. Lord, S. K. O'Boyle, A. Imamovic, B. C. Steimle, R. E. Schaak and K. E. Plass, *Chem. Mater.*, 2021, **33**, 3841.

[32] A. Almazouzi, M.-P. Macht, V. Naundorf and G. Neumann, *Phys. status solidi*, 1998, **167**, 15.

[33] K. Suzumura, K. Kawamura and T. Yokokawa, *J. Chem. Soc., Faraday Trans.*, 1991, **87**, 307.

[34] K. Hoshino, Y. Iijima and K.-I. Hirano, *Metall. Trans. A*, 1977, **8**, 469.

[35] J. Yin, J. Jin, H. Lin, Z. Yin, J. Li, M. Lu, L. Guo, P. Xi, Y. Tang and C. Yan, *Adv. Sci.*, 2020, **7**, 1903070.

[36] P. Bhanja, Y. Kim, B. Paul, J. Lin, S. M. Alshehri, T. Ahamad, Y. V. Kaneti, A. Bhaumik and Y. Yamauchi, *ChemCatChem*, 2020, **12**, 2091.

[37] D. K. Bediako, Y. Surendranath and D. G. Nocera, *J. Am. Chem. Soc.*, 2013, **135**, 3662.

[38] R. Sen, R. Bera, A. Bhattacharjee, P. Gütlich, S. Ghosh, A. K. Mukherjee and S. Koner, *Langmuir*, 2008, **24**, 5970.

[39] M. Alhumaimess, Z. Lin, N. F. Dummer, S. H. Taylor, G. J. Hutchings and J. K. Bartley, *Catal. Sci. Technol.*, 2016, **6**, 2910.

[40] K. Li, Y. Li, Z. Xie, X. Tan, X. Zhang, R. Liu, Y.-F. Song and S. Zhang, *ACS Appl. Nano Mater.*, 2021, **4**, 2503.

[41] C. Wu, X. Lu, L. Peng, K. Xu, X. Peng, J. Huang, G. Yu and Y. Xie, *Nat. Commun.*, 2013, **4**, 2431.

[42] K. N. Dinh, P. Zheng, Z. Dai, Y. Zhang, R. Dangol, Y. Zheng, B. Li, Y. Zong and Q. Yan, *Small*, 2018, **14**, 1703257.

[43] Y. Hu, Z. Wang, W. Liu, L. Xu, M. Guan, Y. Huang, Y. Zhao, J. Bao and H. Li, *ACS Sustain. Chem. Eng.*, 2019, **7**, 16828.

[44] Z. Wu, C. Lu, F. Ye, L. Zhang, L. Jiang, Q. Liu, H. Dong, Z. Sun and L. Hu, *Adv. Funct. Mater.*, 2021, **31**, 2106816.

[45] F. Rouvet, J.-M. Herrmann and J.-C. Volta, *J. Chem. Soc. Faraday Trans.*, 1994, **90**, 1441.

[46] A. M. Wernbacher, P. Kube, M. Hävecker, R. Schlögl and A. Trunschke, *J. Phys. Chem. C*, 2019, **123**, 13269.

[47] Y. Lim, C.-H. Lee, C.-H. Jun, K. Kim and J. Cheon, *J. Am. Chem. Soc.*, 2020, **142**, 9130.

[48] Z. Yang, N. Yang and M.-P. Pileni, *J. Phys. Chem. C*, 2015, **119**, 22249.

[49] P. Hohenberg and W. Kohn, *Phys. Rev.*, 1964, **136**, B864.

[50] W. Kohn and L. J. Sham, *Phys. Rev.*, 1965, **140**, A1133.

[51] G. Kresse and J. Furthmüller, *Phys. Rev. B*, 1996, **54**, 11169.

[52] P. E. Blöchl, *Phys. Rev. B*, 1994, **50**, 17953.

[53] J. P. Perdew, K. Burke and M. Ernzerhof, *Phys. Rev. Lett.*, 1996, **77**, 3865.

[54] H. J. Monkhorst and J. D. Pack, *Phys. Rev. B*, 1976, **13**, 5188.

[55] S. Bhowmick, M. K. Mohanta and M. Qureshi, *Sustain. Energy Fuels*, 2021, **5**, 6392.

[56] J. Park, H. Zheng, Y. Jun and A. P. Alivisatos, *J. Am. Chem. Soc.*, 2009, **131**, 13943.

[57] J. H. Ellis, R. I. Barnhisel and R. E. Phillips, *Soil Sci. Soc. Am. J.*, 1970, **34**, 866.

[58] P. Balasubramanian, M. Annalakshmi, S.-M. Chen, T. Sathesh, T.-K. Peng and T. S. T. Balamurugan, *ACS Appl. Mater. Interfaces*, 2018, **10**, 43543.

[59] S. Bhowmick, S. Alam, A. K. Shah and M. Qureshi, *Sustain. Energy Fuels*, 2021, **5**, 2517.

[60] C. Dong, Z. Qu, Y. Qin, Q. Fu, H. Sun and X. Duan, *ACS Catal.*, 2019, **9**, 6698.

[61] X. Zhang, D. Yang, W. Liu and X. Rui, *Front. Energy Res.*, 2020, **8**, 211.

[62] Y. He, X. Yang, Y. Bai, J. Zhang, L. Kang, Z. Lei and Z.-H. Liu, *Electrochim. Acta*, 2015, **178**, 312.

[63] H. Yang, B. Wang, S. Kou, G. Lu and Z. Liu, *Chem. Eng. J.*, 2021, **425**, 131589.

[64] G. Swain, S. Sultana, J. Moma and K. Parida, *Inorg. Chem.*, 2018, **57**, 10059.

[65] Q. Li, F. Shan, B. Sun, Y. Song, F. Wang and J. Ji, *Int. J. Hydrogen Energy*, 2017, **42**, 5549.

[66] L. Heymann, M. L. Weber, M. Wohlgemuth, M. Risch, R. Dittmann, C. Baeumer and F. Gunkel, *ACS Appl. Mater. Interfaces*, 2022, **14**, 14129.

[67] Z. Li, M. Hu, P. Wang, J. Liu, J. Yao and C. Li, *Coord. Chem. Rev.*, 2021, **439**, 213953.

[68] T. Li, J. Yin, D. Sun, M. Zhang, H. Pang, L. Xu, Y. Zhang, J. Yang, Y. Tang and J. Xue, *Small*, 2022, **18**, 2106592.

[69] T. Qin, Z. Wang, Y. Wang, F. Besenbacher, M. Otyepka and M. Dong, *Nano-Micro Lett.*, 2021, **13**, 183.

[70] Z. Wang, H. Wu, Q. Li, F. Besenbacher, Y. Li, X. C. Zeng and M. Dong, *Adv. Sci.*,

2020, **7**, 1901382.

[71] P. Gayen, S. Saha, K. Bhattacharyya and V. K. Ramani, *ACS Catal.*, 2020, **10**, 7734.

[72] H. Radinger, V. Trouillet, F. Bauer and F. Scheiba, *ACS Catal.*, 2022, **12**(10), 6007.

CHAPTER 7

Membrane Strategy: Vanadium oxide nanosheets infused functionalized polysulphone bipolar membrane for water dissociation

This chapter focusses on the strategy to enhance water dissociation process generating H^+ and OH^- utilizing bipolar membrane (BPM) to provide surplus reactant species to undergo reduction and oxidation (overall water splitting) at the cathode and anode, respectively. Dissociation of water molecules occurs at the interfacial region between the two ion-exchange layers (IEL) of a BPM. Herein, functionalized polysulphone membranes were chosen as the IEL and 2D V_2O_5 nanosheets blended with polyvinyl alcohol was incorporated in between them to act as the water dissociation catalyst.

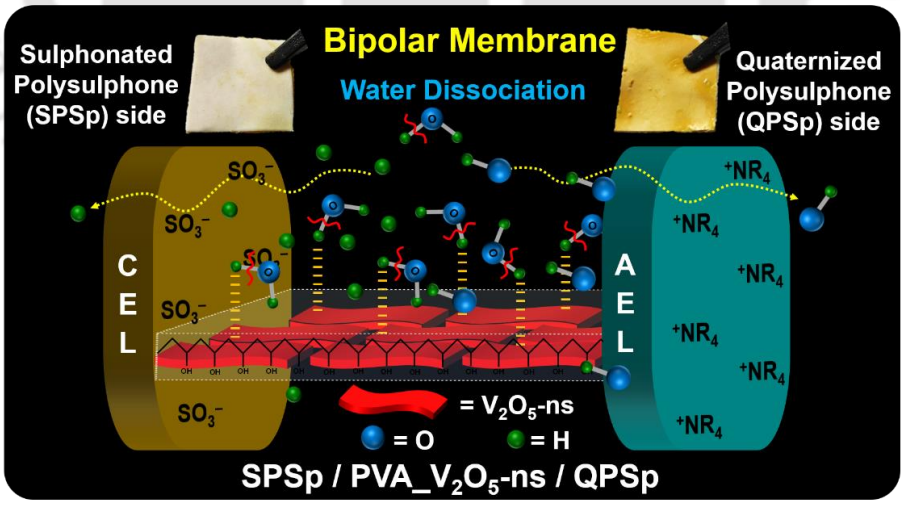

S. Bhowmick, et al., *ACS Appl. Mater. Interfaces*, 2023, DOI: 10.1021/acsami.2c20090

7.1. Introduction

Electrolysis of water is one of the most trending research topics due to the production of the green hydrogen gas, a substitute to meet the energy demand. Bipolar membranes (BPM) have emerged as alternative to the conventional anion- and cation exchange membrane (A/CEM) separators due to its advantage to meet all the challenges associated in electrolytic cells.[1–4] Ionic groups of respective membranes are directly involved in the WD process occurring at interfacial layer (IL) region and groups with smaller dissociation constant leads to lower potential difference thus increasing the dissociation rate.[2] Although weak ionic groups accelerates WD, strong ionic groups are required to obtain BPM with high current yields for H^+ and OH^- ions generation.[3] IEM are generally long polymer chains with functional groups for efficient migration of the ions towards the bulk of the IEM.[5] Polysulphone is known for its cost-effectiveness, outstanding thermal, mechanical, and chemical stability. The polymer can readily be modified to induce specific charged groups thus functionalizing the membranes as AEM and/or CEM thereby enhancing the performance of the ion-exchange membranes.[6–9] Functionalized polymer with ionic groups is preferred due to increased conductivity and hydrophilicity which aids the permselectivity of the membranes thereby maintaining the rate of water intake and inhibiting drying out of the IL region at higher current density during water dissociation reaction.[6,10,11] Thus, the polysulphone was sulphonated and quaternized to introduce the anionic and cationic functional groups in the polymer backbone.

Water dissociation reaction can further be improved at the BPM junction by introduction of additional catalysts at the IL region.[12] Catalysts are known to suppress the high activation energy of water dissociation by forming reactive activated complexes, providing alternative reaction paths.[13–15] In addition to the incorporation of water dissociation catalysts (WDC), a good contact between the AEL and CEL is well desired for reduced interfacial resistance. Polyvinyl alcohol (PVA) is a cost-effective synthetic semi-crystalline polymer, which has significant properties such as good film forming ability, high water holding capacity, excellent thermal and mechanical stability, and favourable chemical cross-linking ability.[9,16,17] The hydroxyl group in the PVA has the tendency to interact with the ionic groups of IEM thus strongly binding to the surfaces of ion-exchange layers (IEL) of BPM.[9] Thus, PVA in the IL act as binder between the AEL and CEL providing better contact between the two layers and also avoiding the bubbling of BPMs.[17] But the low conductivity of PVA adds to the search for a catalyst to enhance the conductivity and WD performance of BPM. As known, proton transfers are induced by hydrogen bonding of bulk water in contact with oxide surfaces leading

to reduced activation energy for water dissociation process.[18,19] Vanadium pentoxide is a well-known transition metal oxide having high catalytic and water adsorption capabilities.[20,21] Additionally, V_2O_5 exhibits redox and Lewis acid/base properties, resulting in strong interaction with water molecules.[22,23] The surface exposed oxygen atoms of V_2O_5 has the tendency to form H-bond with the adjacent water molecule leading to the physisorption of water molecules onto its exposed surface.[20,21,24] Theoretical studies showed that dissociation of an isolated water molecule is kinetically hindered, whereas dissociation of a water molecule that forms an interaction with lattice oxygen or other water molecule is more facile, thereby promoting the water dissociation process.[24,25] Compared to bulk and other nanostructured counterparts, two-dimensional (2D) V_2O_5 nanosheets (V_2O_5-ns) proves to be better candidate as WDC in virtue of its high specific surface area and exposed active sites ideal for better water adsorption thus exhibiting enhanced electrochemical and catalytic properties.[26–28] This general WD mechanism with 2D metal oxides and reorganization of O−H bonds in the presence of electric field, led to idea to use V_2O_5-ns blended with PVA as the WD catalyst.

In the present work, polysulphone has been functionalized by incorporating $–SO_3^-$ and R_4N^+ groups to synthesize sulphonated and quaternized polysulphones, respectively. These were then fabricated into membranes to form the CEL and AEL of the BPM. The two layers were then strongly adhered together by incorporating polyvinyl alcohol (PVA) in the IL which act both as binder and catalyst for the WD process. The IL region was further modified by blending the PVA with transition metal oxide, V_2O_5-ns, to enhance conductivity of the IL and catalytic activity towards water dissociation. It has been observed that when the composite BPM (SPSp/PVA_V_2O_5-ns/QPSp) was utilized, it showed a good WD performance with water dissociation reaction initiating at current density of 1.02 mA/cm^2 at transmembrane potential of 1.11 V.

7.2. Synthetic Methodologies

7.2.1. Sulphonation of polysulphone (SPSp)

The sulphonated polysulphone (SPSp) was synthesized by utilization of chlorosulphonic acid (**Scheme 7.1**).[11,29] Here, 3.5g of polysulphone was weighed and dissolved in 35 mL dichloro ethane (DCE) at temperature of 60 °C. The reaction medium was subjected to inert N_2 atmosphere to avoid the interference of water during the reaction. Then 2mL of chlorosulphonic acid was dissolved separately in 10mL DCE under ice-cold condition. Then the solution was added drop-wise into the reaction over a time span of 30 mins keeping the

temperature constant at 60 °C. The reaction was allowed to run for 4 hours and then the formed precipitate was separated out from the reaction medium. It was then washed to neutralize the pH and dried in vacuum oven at 40 °C to obtain the sulphonated polysulphone (SPSp).

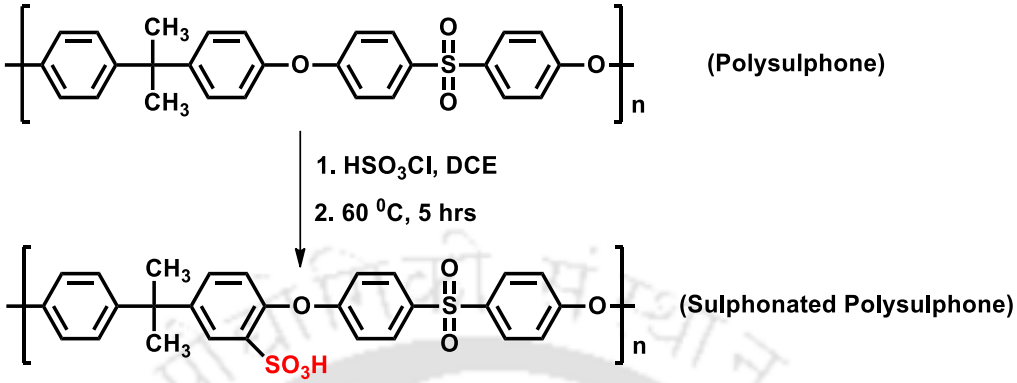

Scheme 7.1: Sulphonation of the polysulphone utilizing chemical process

7.2.2. Quaternization of polysulphone (QPSp)

Quaternized polysulphone (QPSp) was synthesized in a two-phase process with chloromethylation of polysulphone as the initial step (**Scheme 7.2**).[30–32] For the chloromethylation of polysulphone, paraformaldehyde, chlorotrimethylsilane and tin (IV) chloride were used as catalyst. Initially, 2g of PSp was dissolved in 100 mL of $CHCl_3$ (stored in presence of 4Å molecular sieves). After dissolution, 1.2g of paraformaldehyde and 5g of Me_3SiCl were added to the reaction mixture. Subsequently, 0.2 mL $SnCl_4$ (anhydrous) in 5 mL $CHCl_3$ was slowly added under stirring at 55 °C and then the reaction was continued for 72 hours at 55 °C under reflux condition. Lastly, the solution was transferred into 200 mL ethanol and the precipitated polymer was collected via filtration, washed and dried under vacuum condition. The white powder obtained was analysed using ^{1}H-NMR recorded in $CDCl_3$ solvent to confirm the chloromethylation of PSp (**Figure 7.4.1**).

The quaternization of the PSp-CH_2Cl was done using triethylamine. 1g of PSp-CH_2Cl was dissolved in 10 mL DMA solvent and 1 mL TEA was added dropwise under N_2 atmosphere. Then it was reacted @ 40 °C for 24 hrs. After the reaction, the mixture was poured into 50 mL diethyl ether and the precipitate was obtained using vacuum filtration. After drying the sample overnight, it was utilized for the preparation of anion exchange layer (AEL).

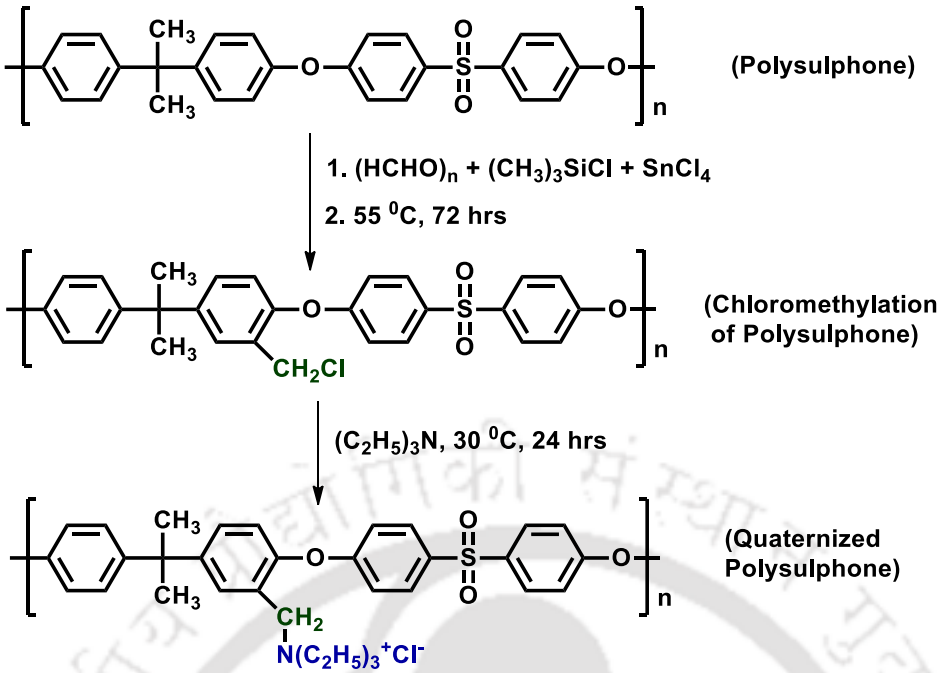

Scheme 7.2: Quaternization of the polysulphone utilizing a two-step chemical process

7.2.3. Synthesis of vanadium pentoxide nanosheets (V_2O_5-ns)

V_2O_5 nanosheets (V_2O_5-ns) were prepared by treating V_2O_5 powder with H_2O_2 solution in ice-cold condition.[33,34] For the synthesis, 0.30 g of V_2O_5 powder was dissolved in 3 mL of DI water under ice-bath condition followed by dropwise addition of 3 mL H_2O_2 (50%) with continuous stirring. Soon after the light brown solution turned into dark brown gel, it was ultra-sonicated for an hour and diluted to 50 mL with DI water. About 20 mL of the solution (6mg/mL) was poured in a petridish and dried in oven to fabricate free-standing V_2O_5-ns membrane for further characterizations.

7.2.4. Fabrication of the bipolar membrane (BPM)

Bipolar membrane (BPM) has been fabricated using solution casting method as discussed in **Section 2.8**. The composite bipolar membrane was fabricated with functionalized polysulphones as the IEL and V_2O_5-ns as WDC, and laminated as SPSp/PVA_V_2O_5-ns/QPSp (**BPM_VO-ns**). For comparison two more bipolar membranes were fabricated, one without any WDC (**BPM_1**) and another with only PVA in the IL region (**BPM_PVA**). The thickness of the layers of BPM and the amount of V_2O_5-ns catalyst was optimized by varying each alternatively. Finally, the laminated bipolar membranes were cut (2cm x 2cm) using a razor-sharp blade and utilized for the water dissociation process. The digital images of the individual membranes and the fabricated bipolar membrane, BPM_VO-ns, is shown in **Figure 7.2.1**.

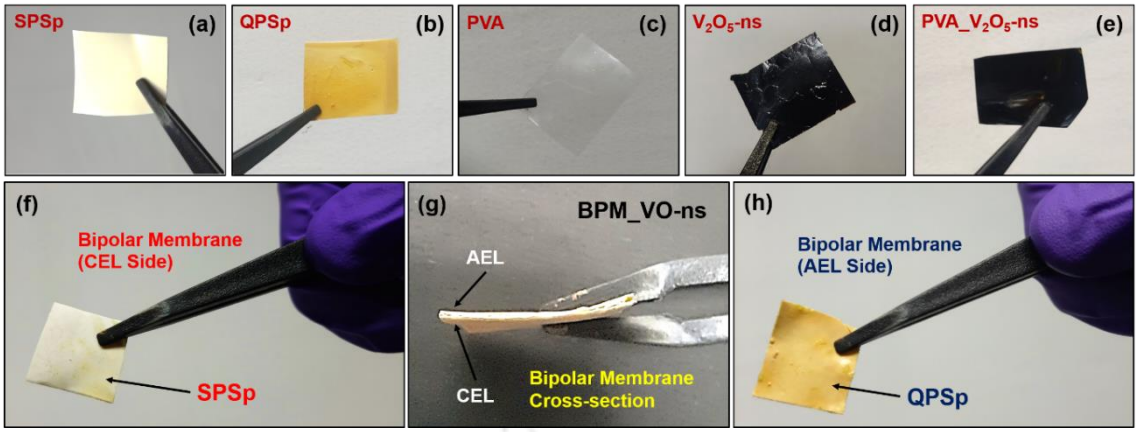

Figure 7.2.1: The digital images of the individual membranes of (a) SPSp, (b) QPSp, (c) PVA, (d) V_2O_5-ns and (e) PVA_V_2O_5-ns, and also of the fabricated bipolar membrane with (f) the CEL side, (g) cross-section, and (h) AEL side of BPM_VO-ns

7.3. Membrane Characterization

7.3.1. Water-uptake capacity

The water uptake (WU%) capacity of the membranes was measured by initially calculating the weight of the membranes in totally dry condition (W_{dry}) and then was immersed in DI water for 24hrs. After that the membranes were wiped clean to remove excess water off the surfaces and the weight was measured (W_{wet}). The WU% is given as;

$$WU\% = \frac{W_{wet} - W_{dry}}{W_{dry}} \times 100 \quad \ldots (7.1)$$

7.3.2. Ion-conductivity

A Gamry interface 1010E was utilized to obtain the Nyquist plot of the membranes. A two-probe cell was used where the membrane was sandwiched between two copper plates and the electrochemical impedance spectroscopy (EIS) was measured between the frequency range of 1 to 1MHz. The ionic conductivity was then determined as:

$$\sigma = \frac{l}{R \times A} \quad \ldots (7.2)$$

where, l (cm) is the separation between the two electrodes, R(Ω) is the resistance obtained from Nyquist plot, and A (cm^2) is the surface area.

7.3.3. Ion-exchange capacity

The ion-exchange capacity (IEC) of the functionalized polysulphone membranes were evaluated using the titration method. The AEM (QPSp) prior to the measurement was

completely dried in vacuum oven and was weighed (W_{dry}). It was then immersed in 1M HCl solution and kept undisturbed for 48 hrs to convert to the Cl^- form. The excess Cl^- was removed by washing with DI water. The sample was then immersed in 50 mL of 1M KNO_3 solution for 48 hrs. The amount of displaced Cl^- ions were determined by titrating the solution with $AgNO_3$ (0.05 M) using K_2CrO_4 as indicator. The IEC was then calculated as,

$$IEC = \frac{C_{AgNO_3} \times V_{AgNO_3}}{W_{dry}} \quad \ldots (7.3)$$

The CEM (SPSp) was also completely dried in vacuum oven and was weighed. Then soaked in 1M HCl solution and kept undisturbed for 48 hrs to convert to the H^+ form. The excess ions were removed by washing with DI water. The membrane was then immersed in 50 mL of 1M NaCl solution for 48 hrs to convert the H^+ form to Na^+ form. The solution was then titrated with NaOH (0.05 M) using phenolphthalein as an indicator. The IEC was then calculated using the following formula,

$$IEC = \frac{C_{NaOH} \times V_{NaOH}}{W_{dry}} \quad \ldots (7.4)$$

7.4. Results and discussions

7.4.1. ^{1}H-Nuclear Magnetic Resonance (NMR) Spectroscopy Analyses

The chloromethylation of polysulphone was confirmed using ^{1}H-NMR technique using $CDCl_3$ solvent.

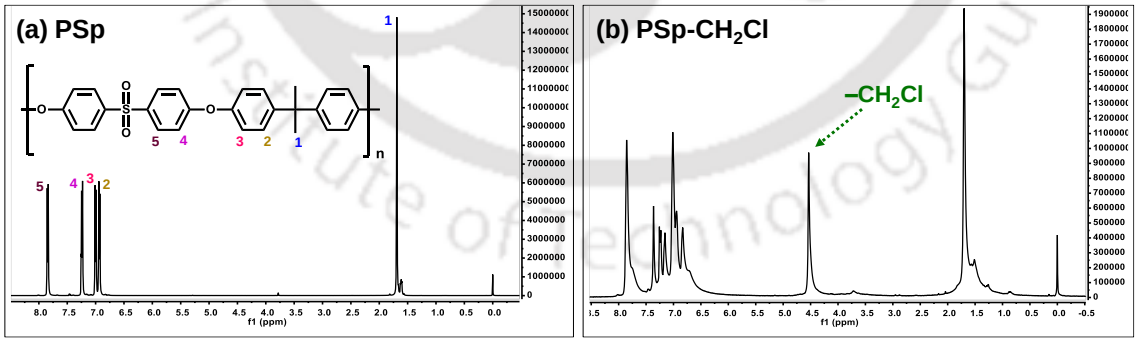

Figure 7.4.1: ^{1}H-NMR spectra of (a) PSp and (b) PSp-CH_2Cl showing the successful synthesis of chloromethyl polysulphone

The ^{1}H-NMR spectra of PSp has been shown in **Figure 7.4.1a** where the peak at 1.68 ppm is due to the ^{1}H(1) of -CH_3 groups. The first doublet at 6.93 ppm corresponds to the ^{1}H(2) of benzene ring close to the -CH_3(1) group. The second doublet at 7.00 ppm corresponds to the ^{1}H(3) of benzene ring adjacent to ^{1}H(2) close to oxo group. The next doublet at 7.24 ppm is

assigned to $^{1}H(4)$ of the adjacent benzene ring close to the oxo group. The far deshielded doublet at 7.84 ppm is assigned to $^{1}H(5)$ of benzene ring close to the sulfoxide group. The singlet at ~1.6 ppm and the four doublets ~7 ppm confirms the skeleton structure of the PSp polymer. From the ^{1}H-NMR spectra of PSp-CH_2Cl (**Figure 7.4.1b**) it can be seen that there is substitution of –CH_2Cl group in the polysulphone backbone, confirmed by the new peak at 4.5 ppm. The peak at 4.5 ppm corresponds to the ^{1}H present in benzyl chloride group (Ph-CH_2Cl). Thus, the chloromethylation of polysulphone was successfully carried out.

7.4.2. Characterization of the As-Synthesized

a) Functionalized Polysulphones

The functionalization of the polysulphone, i.e., sulphonation and quaternization, was confirmed using Fourier-Transform Infrared spectroscopy (FT-IR) technique. The FT-IR spectra of PSp, SPSp and QPSp are shown in **Figure 7.4.2a** where the peak at 1040 cm^{-1} for SPSp corresponds to the symmetric stretching of sulphonate group and broad peak at 3400 cm^{-1} corresponds to the OH bond stretching of the –SO_3H group.[11,29] In QPSp additional peaks at 1028 cm^{-1} corresponds to the C–N bond stretching while a sharp peak at 1670 cm^{-1} and a broad peak at 3370 cm^{-1} corresponds to the quaternary ammonium group.[30–32] The phase purity of the functionalized polysulphones were confirmed using X-ray diffraction (XRD) technique (**Figure 7.4.2b**). It can be seen that the amorphous nature of the PSp polymer is intact without any impurity peaks.

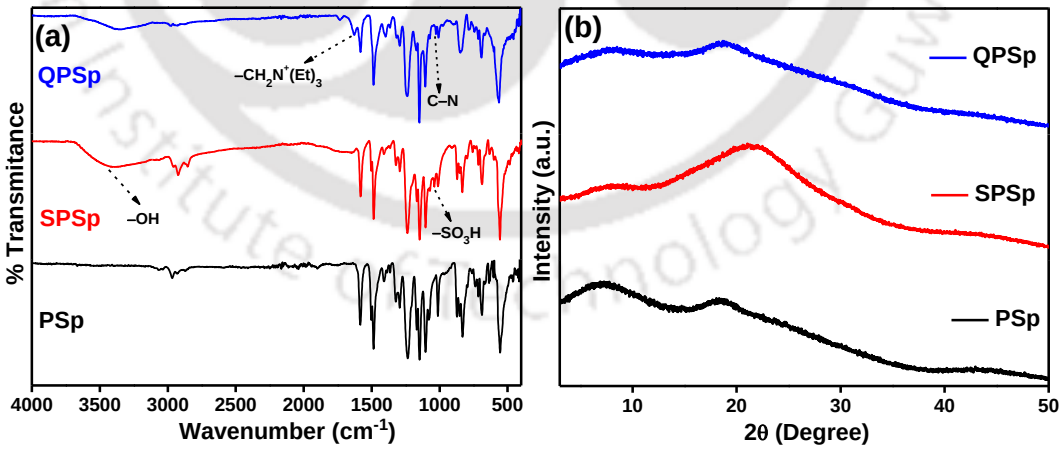

Figure 7.4.2: (a) FT-IR spectra of PSp, SPSp and QPSp, (b) XRD spectra of PSp, SPSp and QPSp

b) Two-Dimensional V_2O_5 nanosheets

The field emission transmission electron microscope (FETEM) image of the V_2O_5-ns (**Figure 7.4.3a**) shows that the V_2O_5 are formed in the size ranging from 50-100 nm. The

formation of 2D nanosheets of V_2O_5 (V_2O_5-ns) was confirmed from the XRD spectra (**Figure 7.4.3b**) where the peak at 7.4° (2θ) corresponds to the interlayer spacing of V_2O_5 sheets in the "*c*" direction (001 plane) with interplanar spacing of ~1.19 nm. The 2D sheet structure of the V_2O_5-ns was further proved by the cross-sectional field emission scanning electron microscope (FESEM) image (**Figure 7.4.3c**). **Figure 7.4.3d** shows the FETEM image of a single nanosheet of V_2O_5-ns confirming its 2D nature.

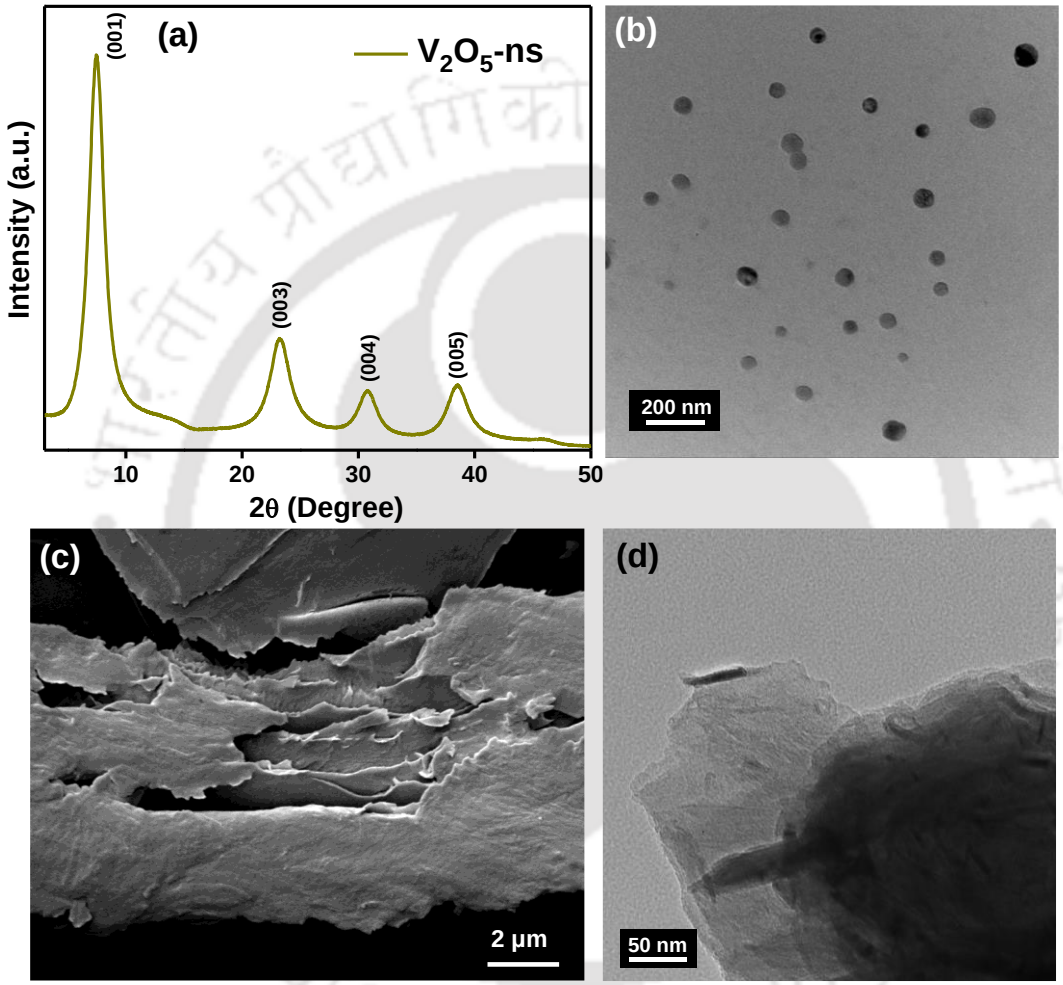

Figure 7.4.3: (a) XRD spectra of the V_2O_5 nanosheets, (b) FETEM image of the synthesized V_2O_5-ns, (c) FESEM image of V_2O_5-ns depicting its 2D sheet structures, and (d) FETEM image of V_2O_5-ns showing single nanosheet structure

7.4.3. Cross-Sectional Images of

a) Individual Membranes

Field emission scanning electron microscope (FESEM) was utilized to obtain the cross-sectional image of the individual membranes. The thickness of the individual membranes was evaluated from the obtained cross-sectional images of each membrane separately (**Figure 7.4.4**). As can be seen the thickness of SPSp membrane (**Figure 7.4.4a**) is 97.17 µm and that

of QPSp membrane (**Figure 7.4.4b**) is 108.64 µm. A set of 5 membranes were fabricated and the average thickness was found to be 100 (±10) µm for both SPSp and QPSp. Also, the presence of porous structure aids the water intake during the water dissociation process. The thickness of the PVA membrane (**Figure 7.4.4c**) is 12.37 µm and that of PVA_V_2O_5-ns membrane (**Figure 7.4.4d**) is 11.81 µm. The PVA and PVA_V_2O_5-ns membranes were fabricated this thick to form free standing membranes for their characterizations.

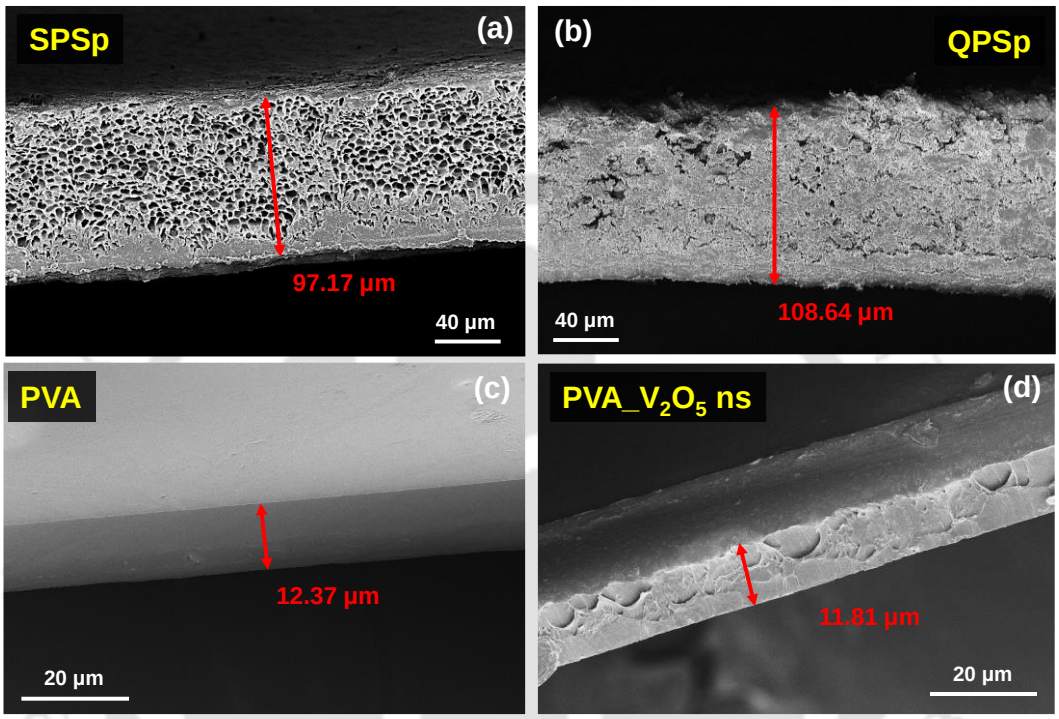

Figure 7.4.4: Cross-sectional FESEM images of individual membranes of (a) SPSp, (b) QPSp, (c) PVA, (d) PVA_V_2O_5-ns depicting their thickness

b) Fabricated Bipolar Membranes

Field emission scanning electron microscope (FESEM) was utilized to obtain the cross-sectional image of the fabricated bipolar membranes to demonstrate the strong adhesion of the layers. The structural feature of the bipolar membrane **BPM_1** (i.e., SPSp/QPSp) is shown in **Figure 7.4.5a**, where the thickness of each IEL were ~100 (± 10) µm. As the two layers have been placed over each other (SPSp at top and QPSp at bottom), strong adhesion was missing confirmed from the gap of ~80 µm at the IL region. **Figure 7.4.5b** shows the cross-sectional view of **BPM_PVA** (i.e., SPSp/PVA/QPSp) with PVA layer of ~6 (± 2) µm thick between SPSp and QPSp. Due to the presence of PVA at the IL region, strong adhesion between the IEL was possible. Similarly, in **Figure 7.4.5c** the cross-sectional view of **BPM_VO-ns** (i.e., SPSp/PVA_V_2O_5-ns/QPSp) with PVA_V_2O_5-ns layer of ~8 (± 2) µm thick between SPSp and QPSp is shown. Here also a strong adhesion between AEL and CEL is achieved due to the

incorporation of WDC at the IL region. To confirm the presence of V_2O_5-ns as WDC at the IL region, energy dispersive X-ray spectroscopy (EDS) was performed for BPM_VO-ns (**Figure 7.4.5d**). As can be seen the red colour (**Figure 7.4.5e**) corresponds to C atom present in PSp and PVA molecules, the yellow colour (**Figure 7.4.5f**) corresponds to the O atom present in all the PSp, PVA and V_2O_5, the green colour (**Figure 7.4.5g**) corresponds to the S atom of sulphonyl group in PSp and sulphonic acid group in SPSp, the cyan colour (**Figure 7.4.5h**) corresponds to the N atom of the R_4N^+ group of QPSp, and the purple colour (**Figure 7.4.5i**) corresponds to the V atom of V_2O_5-ns present as WDC in IL region.

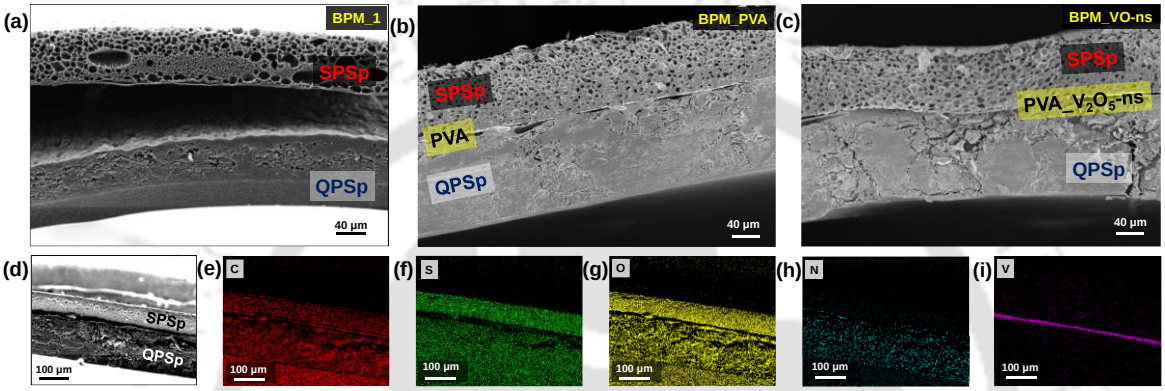

Figure 7.4.5: Cross-sectional FESEM images of (a) BPM_1, (b) BPM_PVA, (c) BPM_VO-ns, and EDS spectra of (d) BPM_VO-ns, showing the presence of the individual elements (e) carbon, (f) oxygen, (g) sulphur, (h) nitrogen and (i) vanadium in the bipolar membrane

7.4.4. Mechanical Strength Analyses of

a) Individual Membranes

The mechanical strength of the fabricated membranes was examined using the universal testing machine (UTM). All the membranes were cut in equal dimensions (2 cm x 1 cm) and the thickness were determined from the cross-sectional FESEM images. **Figure 7.4.6b** provides the ultimate tensile strength (UTS) of the individual membranes determined from the Stress vs. Strain plots (**Figure 7.4.6a**).

As can be seen, with functionalization (SO_3^- & R_4N^+) of PSp the mechanical strength was still intact for SPSp and QPSp. For the PVA molecule with incorporation of V_2O_5-ns there has been improvement in its mechanical strength due to the interaction of the –OH groups of PVA with the oxide molecule.

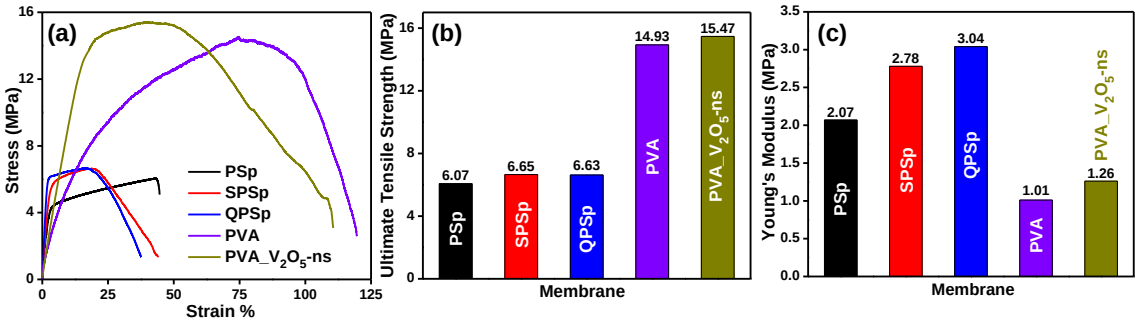

Figure 7.4.6: (a) Stress vs. Strain plots, (b) Ultimate tensile strength, and (c)Young's Modulus values of the individual membranes of PSp, SPSp, QPSp, PVA & PVA_V_2O_5-ns

Figure 7.4.6c depicts the Young's modulus (*E*) values obtained from the slope of linear portion of Stress vs. Strain plots (**Figure 7.4.6a**). With the functionalization the PSp, the polymers became stiffer (higher *E* values) which may be due to the strong interaction of the ionic groups within the polymer. Similar behaviour is seen for the PVA_V_2O_5-ns membrane which is due to the possibility of H-bonds between the hydroxyl groups and oxide molecule.

b) Fabricated Bipolar Membranes

A high performing BPM must be mechanically strong enough to withstand the high interlayer voltage generated at high current density during the water dissociation reaction. On fabrication of the BPM_1, the UTS (**Figure 7.4.7b**) has increased thus due to the combinational effect of the two layers. Further increase in the UTS for BPM_PVA and BPM_VO-ns is due to the effect of PVA and PVA_V_2O_5-ns in the IL region which strongly adheres the two layers together. The Young's Modulus (*E*) of the fabricated membranes were also determined from the linear slope of the Stress vs. Strain plots (**Figure 7.4.7a**) and shown in **Figure 7.4.7c**. The lower value for the BPM states its elasticity as compared to the individual membranes which is much needed for the stability of the BPM at adverse conditions.

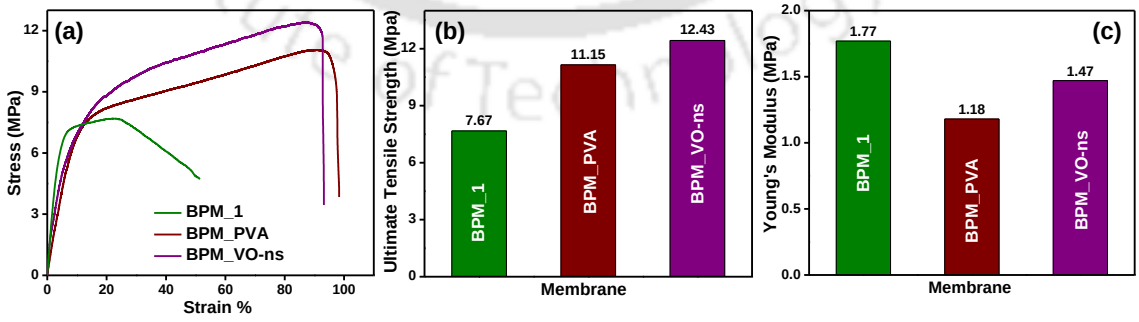

Figure 7.4.7: (a) Stress vs. Strain plots, (d) Ultimate tensile strength, (e)Young's Modulus values of the fabricated BPMs of BPM_1, BPM_PVA & BPM_VO-ns

7.4.5. Wettability and Thermal Stability Analyses

The optimum wettability of individual layers in a BPM system is much crucial for the efficient WD process, as less water uptake capacity will lead to drying up of the IL reducing the efficiency whereas too much water uptake will swell up the IL which may lead to the tearing and/or detachments of the layers. The wettability of the membranes was evaluated by measuring the contact angles of the individual membranes (**Figure 7.4.8a-e**). With functionalization of the polysulphone, hydrophilicity of the membrane surface increased, as depicted by the lowering of the contact angle for SPSp and QPSp due to the presence of ionic groups, SO_3^- & R_4N^+ on the polysulphone backbone (**Figure 7.4.8a-c**). The lower contact angle for SPSp may be due to the formation of H-bonds between the sulphonyl group and water molecule. In addition to the contact angle measurements, water uptake (WU%) capacity was also evaluated using **Equation 7.1**. **Figure 7.4.8f** displays the WU% of the individual membranes and PVA_V_2O_5-ns has the highest water holding capacity owing to the intrinsic property of water adsorption onto the surface of 2D V_2O_5 nanosheets.

The water uptake capacity of the fabricated BPMs has been shown in **Figure 7.4.8g**. A high performing BPM must be able to hold optimum amount of water during the WD process to inhibit drying up of the IL region. The WU% of BPM_1 (SPSp/QPSp) has enhanced due to the presence of both AEL and CEL and the interlayer space which can also hold onto water molecules. In case of BPM_PVA (SPSp/PVA/QPSp), the PVA layer in the IL adds up to the water uptake capacity along with the SPSp and QPSp. For the composite BPM_VO-ns (SPSp/PVA_V_2O_5-ns/QPSp), the WU% further increased due to the presence of V_2O_5-ns which also has the capacity to hold up the water molecules between the sheets.

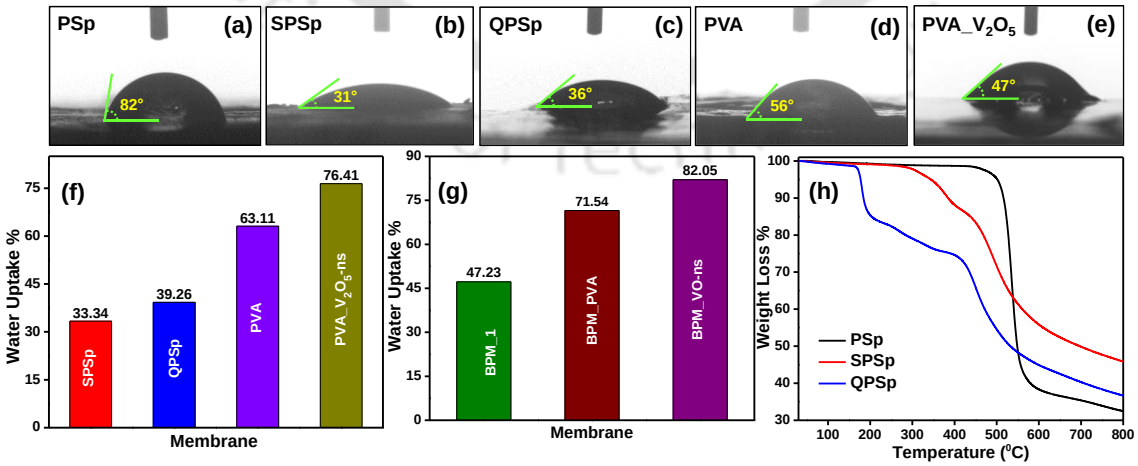

Figure 7.4.8: The contact angles of (a) PSp, (b) SPSp, (c) QPSp, (d) PVA & (e) PVA_V_2O_5-ns, water uptake capacities of the (f) individual membranes, (g) bipolar membranes, and (h) Thermal gravimetric analysis (TGA) plot of PSp, SPSp and QPSp

The thermal stability of the membrane, another crucial parameter of high performing BPM, was determined using thermal gravimetric analysis (TGA). As can be seen from **Figure 7.4.8h**, it can be observed that the polymer membranes, PSp, SPSp and QPSp, are stable upto ~150 °C without any loss in its mass. Thus, SPSp and QPSp have great potential to be utilized as IEL during the fabrication of a BPM for stable and efficient water dissociation process. At higher temperatures the PSp was stable upto ~500 °C while the functionalized PSp started to degrade earlier due to the presence of $-SO_3^-$ & R_4N^+ functional groups.

7.4.6. Ionic Conductivity Analyses

The ion-exchange capacity (IEC) is an important parameter of a BPM to quantify the total active sites or functional groups responsible for ion exchange in polymer electrolyte membrane. For the synthesized SPSp (CEL) and QPSp (AEL), the IEC was determined using titration method and **Equations 7.3 and 7.4**. Another important parameter of BPM for efficient WD process is the ion-conductivity of the individual layers. The ion-conductivity of the individual membranes (SPSp, QPSp, PVA and PVA_V_2O_5-ns) and bipolar membranes (BPM_1, BPM_PVA and BPM_VO-ns) was evaluated by measuring the resistance using EIS technique in a two-probe cell sandwiched between two copper plates. The ionic-conductivity (σ) was thereby calculated from the resistance value obtained from the Nyquist plots (**Figure 7.4.9**) using **Equation 7.2**.

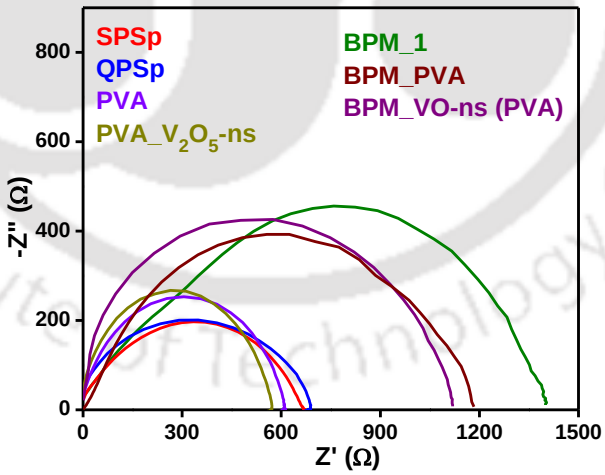

Figure 7.4.9: Nyquist plots of the individual membranes (SPSp, QPSp, PVA and PVA_V_2O_5-ns) and the bipolar membranes (BPM_1, BPM_PVA and BPM_VO-ns) obtained from the EIS technique for ion-conductivity measurement

The obtained IEC values, ionic conductivity and water uptake % of all the individual membranes and layers have been tabulated in **Table 7.1**.

Table 7.1: Ion exchange capacity (IEC), ion-conductivity (σ), water uptake (WU%), ultimate tensile strength (UTS) & Young's Modulus (*E*) of all the membranes

Membrane	IEC (mmol/g)	σ (mS/cm)	WU %	UTS (MPa)	*E* (MPa)
SPSp	1.48	56.9	33.34	6.65	2.78
QPSp	1.61	47.5	39.26	6.63	3.04
PVA	–	28.3	63.11	14.93	1.01
PVA_V_2O_5-ns	–	35.6	76.41	15.47	1.26
BPM_1	–	24.7	47.23	7.67	1.77
BPM_PVA	–	31.3	71.54	11.15	1.18
BPM_VO-ns (PVA)	**–**	**37.6**	**82.05**	**12.43**	**1.47**

7.4.7. Optimization of Bipolar Membrane for Water Dissociation

The main objective of fabricating the BPMs is to dissociate water into the constituent ions, H^+ and OH^-. To analyse the WD property of the fabricated BPMs, they were subjected to potentiodynamic analysis in a 4-probe cell (as shown in **Figure 2.3**). The thickness of the AEL and CEL was optimized by varying the thickness of the SPSp and QPSp membranes. **Figure 7.4.10a** depicts the CVC of BPM_1 of different thickness and it was observed that with ~100 (± 10) μm thick AEL and CEL the WD performance was better which may be due to the adequate water incorporation and lower co-ion transportation at higher current density. The thickness of PVA layer in the IL region is crucial for the performance of the BPM_PVA. A thicker layer will result in increase of electrical resistance between the layer and a thinner will have less capacity to hold water for its dissociation leading to drying up of the interfacial region.[2,12,30,35] **Figure 7.4.10b** shows optimization of the thickness of PVA layer and was found that a layer more than 15 μm resulted in decrease of the water dissociation reaction at the IL region. Thus, ~6 (± 2) μm PVA layer was chosen as optimum thickness for the IL layer to bind the AEL and CEL together. Finally, optimum amount of WDC is also critical for the high performance of a bipolar membrane towards water dissociation. **Figure 7.4.10c** represents the optimization of the amount of V_2O_5-ns in the IL region blended with PVA molecule. The amount of V_2O_5-ns was varied from 2-8 mg/mL while keeping the thickness of the WDC layer as ~6 (± 2) μm. It was found that 6 mg/mL V_2O_5-ns solution blended with PVA gave the best WD performance for BPM_VO-ns. Excess catalyst in the IL hinders the adsorption of water molecules onto its surfaces thereby reducing the WD performance.[2,12,35]

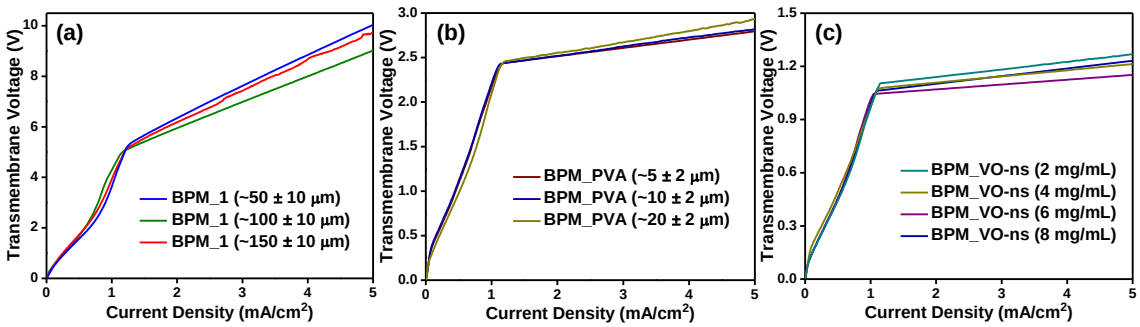

Figure 7.4.10: Current-voltage curve for the optimization of (a) thickness of the ion-exchange membrane layers, (b) thickness of the PVA layer at the IL region, and (c) concentration of the V_2O_5-ns blended with PVA at IL region for WDC

7.4.8. Water Dissociation Performance of the Optimized Bipolar Membrane

Figure 7.4.11a shows the current-voltage curve (CVC) for all the fabricated BPMs. As can be seen, the composite BPM, BPM_VO-ns, is catalytically active at high current density of 100 mA/cm^2 with transmembrane voltage (V_{trans}) of 3.6 V while that for BPM_PVA is 13.6 V. Thus, the incorporation of V_2O_5-ns into PVA enhanced the catalytic property of the BPM resulting in higher water dissociation at the IL region.

To better understand the effect of PVA and V_2O_5-ns in the enhancement of the performance of the BPM, **Figure 7.4.11b** is represented with the zoomed in X-axis of the **Figure 7.4.11a**. The CVC can be divided into different regions to determine the overall catalytic performance of the bipolar membranes.[2,10,36] The first region is the ohmic resistance (R_{ohm}) of the membrane system, followed by the second region is the pseudo-limiting current ($I_{p\text{-}lim}$) characterizing the current density due to transportation of co-ions across the membranes. The continuous flux of co-ions through the respective IEMs causes depletion of salt ions at the IL region resulting in the formation of large resistance thereby increasing the potential across the BPM with small increase in current density. The inflection point at the pseudo-limiting region corresponds to the transmembrane voltage (V_{diss}), i.e., the minimum voltage required between the layers for the initiation of water dissociation. The third region is the water dissociation resistance (R_{diss}), i.e., the BPM's ability to intensify the water dissociation. Here the membrane voltage exceeds WD potential (V_{diss}), thus significant WD occurs in the BPM IL with protons and hydroxide ions being the contributors to the total current. As can be seen from **Figure 7.4.11a**, the voltage required to achieve the WD process (V_{diss}) is much lowered with the incorporation of PVA (2.68 V) and PVA_V_2O_5-ns (1.11 V) in the IL region. The large transmembrane voltage for the BPM_1 (5.38 V) is due to the combined effect of weak contact

between AEL and CEL (as seen in FESEM image) and absence of any WD catalyst, which increases the electrical resistance (R_{ohm} = 2.92 Ω.cm^2) at the intermediate layer.[2,17]

For BPM_PVA, the PVA molecule results in strong contact between the two layers, minimizing the inter-layer resistance (R_{ohm} = 1.64 Ω.cm^2). In addition, it also acts as catalyst towards the WD due to the presence of –OH groups which forms strong interactions with H_2O through H-bonding and polarity. The hydrophilicity improves the interaction between H_2O and membrane layer and weakens the bonding force of water at the intermediate layer, thereby promoting water molecules to be split into H^+ and OH^- (V_{diss} = 2.68 V).[15,17,35]

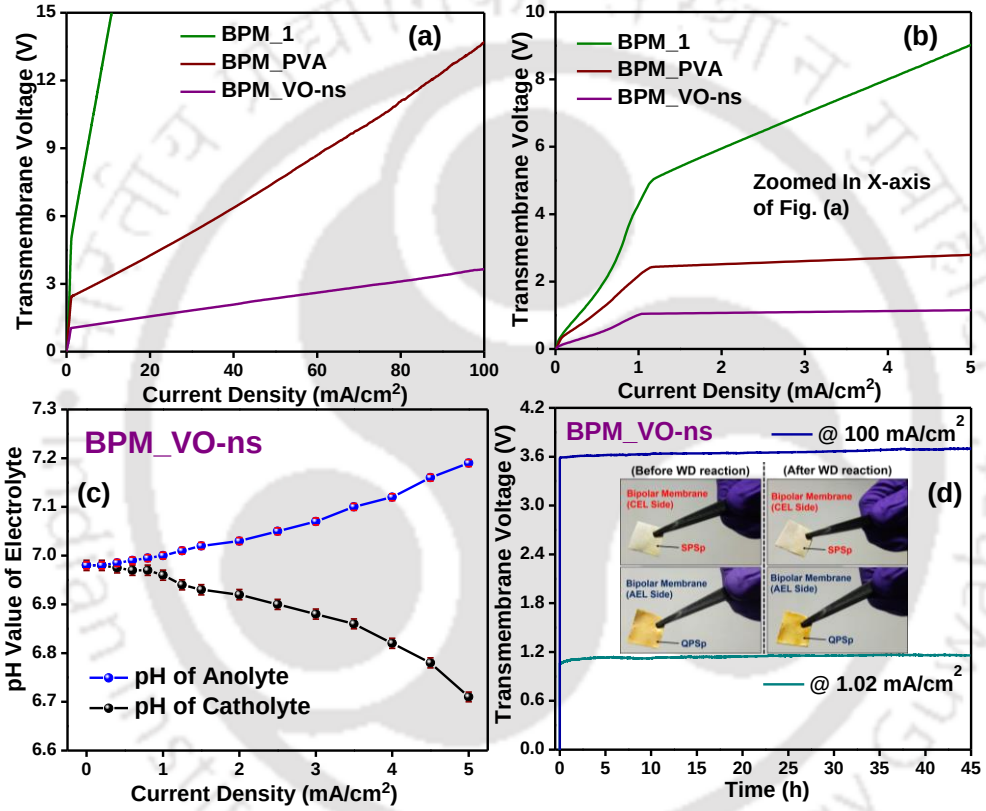

Figure 7.4.11: (a) Current-voltage curves (CVC) of BPM_1, BPM_PVA and BPM_VO-ns, (b) CVC of the BPMs with zoomed in X-axis of Figure a, (c) chronopotentiometry curve of BPM_VO-ns showing its stability for 45 hours operating at lower (1.02 mA/cm^2) and higher (100 mA/cm^2) current densities, with digital images of BPM_VO-ns before (left-side images) and after (right-side images) water dissociation reaction, and (d) Plot of pH change of anolyte and catholyte vs. current density during the water dissociation reaction for BPM_VO-ns

In case of BPM_VO-ns, the 2D V_2O_5-ns further enhances the water dissociation activity by increasing the overall conductivity (R_{ohm} = 0.79 Ω.cm^2) of the IL and its hydrophilic property. The V_2O_5-ns also has higher surface area and active sites for water adsorption thus further improving the interaction between the water molecules and membrane layer.[20–22,28] The water molecules on interaction with the surface of 2D nanosheets of V_2O_5 forms H-bonds

leading to reduction of activation energy for water dissociation process.[2,18–20,24] Thus, the overall WD process at the IL region is enhanced as confirmed by the reduced water dissociation voltage (V_{diss} = 1.11 V). The enhanced WD performance of the composite BPM was also proven by high pseudo-limiting current value at lower reverse bias voltage. At 1 V (V_{trans}), the $I_{p\text{-}lim}$ value for BPM_VO-ns was obtained to be 0.98 mA/cm^2 as compared to that of BPM_PVA (0.45 mA/cm^2) and BPM_1 (0.27 mA/cm^2). The higher current value suggests that along with the co-ions crossover there is occurrence of WD due to the formation of protons and hydroxides at activities less than unity.[36]

To better understand the co-ions crossover at pseudo-limiting region and the WD process, the change in pH of the electrolyte solution (1M NaCl) at both the cathodic (catholyte) and anodic (anolyte) chambers was measured as a function of current density for BPM_VO-ns, as shown in **Figure 7.4.11c**. At the initial (zero current), the pH value of catholyte and anolyte was found to be same (6.98). With increase in the current density there was constancy in the pH value at both chambers till 0.2 mA/cm^2 suggesting that the obtained current is due to the in-flux of co-ions across the layers of the BPM. Past 0.2 mA/cm^2 there was small noticeable change in pH value of both catholyte and anolyte suggesting the occurrence of WD producing H^+ and OH^- ions (at activities less than unity) along with the transportation of co-ions. At 1 mA/cm^2, there was significant change in the pH values of both catholyte and anolyte indicative of the initiation of WD at faster rate. Past 1 mA/cm^2, the pH values changed widely with increase in the current density value suggesting an enhanced water dissociation reaction producing H^+ and OH^- ions extensively. This region in the CVC is reflected by the low R_{diss} value (0.027 Ω.cm^2).

In addition to the high performance of a BPM towards water dissociation, its stability for long duration is also an important parameter. Chronopotentiometry analysis was utilized at both lower, 1.02 mA/cm^2 (current density corresponding to the V_{diss}) and higher, 100 mA/cm^2, current densities to test the durability of BPM_VO-ns. From **Figure 7.4.11d** it can be seen that after 45 hours of test run, there is negligible decrease in the water dissociation performance of BPM_VO-ns depicting the high stability of the fabricated bipolar membrane. The digital images of the BPM_VO-ns captured before and after the WD reaction process has been shown in **Figure 7.4.11d** inset to demonstrate the stability of the bipolar membrane confirming the strong adhesion between the two layers of the BPM.

The observed results of water dissociation reaction for all the fabricated BPMs have been tabulated in **Table 7.2** for better understanding.

Table 7.2: R_{ohm}, $I_{p\text{-}lim}$, V_{diss}, R_{diss} and V_{trans} values of all the fabricated bipolar membranes

Bipolar Membrane	R_{ohm} ($\Omega.cm^2$)	$I_{p\text{-}lim}$ @ 1 V_{trans} ($mA\ cm^{-2}$)	V_{diss} (V)	R_{diss} ($\Omega.cm^2$)	V_{trans} (@ 100 $mA\ cm^{-2}$)
BPM_1	2.92	0.27	5.38	1.03	–
BPM_PVA	1.64	0.45	2.68	0.093	13.6 V
BPM_VO-ns	**0.79**	**0.98**	**1.11**	**0.027**	**3.6 V**

The water dissociation mechanism has been schematically demonstrated in **Figure 7.4.12** displaying the function of PVA and V_2O_5-ns towards the enhancement in WD performance for the composite bipolar membrane, BPM_VO-ns. The PVA polymers binds together the two IELs, SPSp and QPSp, while the dangling O atoms of V_2O_5-ns forms H-bond with the water molecules. The combined effect of the generated potential gradient across the membrane layers and the weakening of the H–OH bond of water due the H-bond formation, results in the dissociation of water producing protons and hydroxyl ions at the interfacial region.

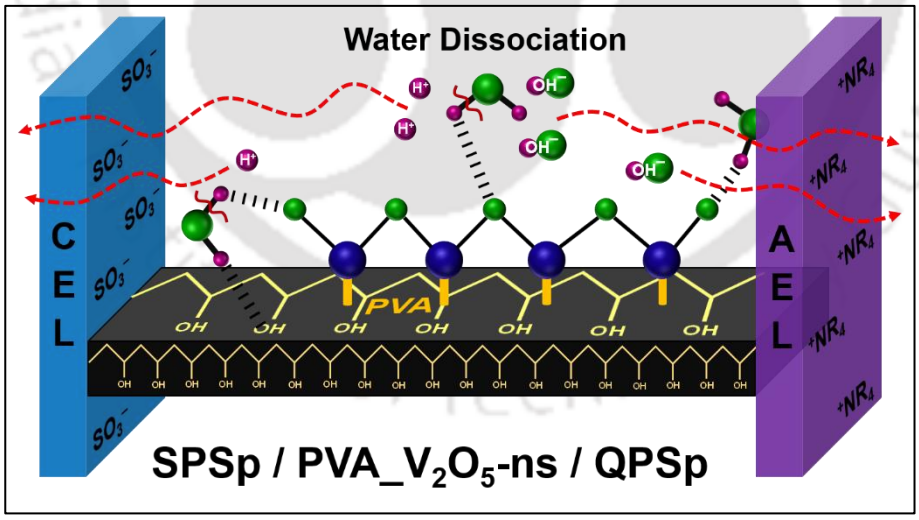

Figure 7.4.12: Schematic diagram of the plausible mechanism for water dissociation in **BPM_VO-ns** (SPSp/PVA_V_2O_5-ns/QPSp) where the V_2O_5-ns acts as the water adsorption sites and aids water cleavage process generating H^+ and OH^- ions

The durability of the fabricated BPM_VO-ns was also proven by the post-stability analyses to determine the structural and mechanical strength integrity. Prior to the analyses, the BPM_VO-ns was dried under vacuum to remove all the absorbed water molecules. **Figure**

7.4.13a confirms the crystal structure (orthorhombic phase) integrity of the 2D V_2O_5-ns catalyst and the cross-sectional FESEM (**Figure 7.4.13b**) image confirms the strong adhesion of AEL and CEL even after the WDR. The mechanical properties after the water dissociation reaction (WDR) were analysed from the stress vs strain plot (**Figure 7.4.13c**) of the composite BPM_VO-ns, and **Figure 7.4.13d** shows the retention of mechanical strength (within experimental error range) even after 45 hours of WDR confirming its high durability.

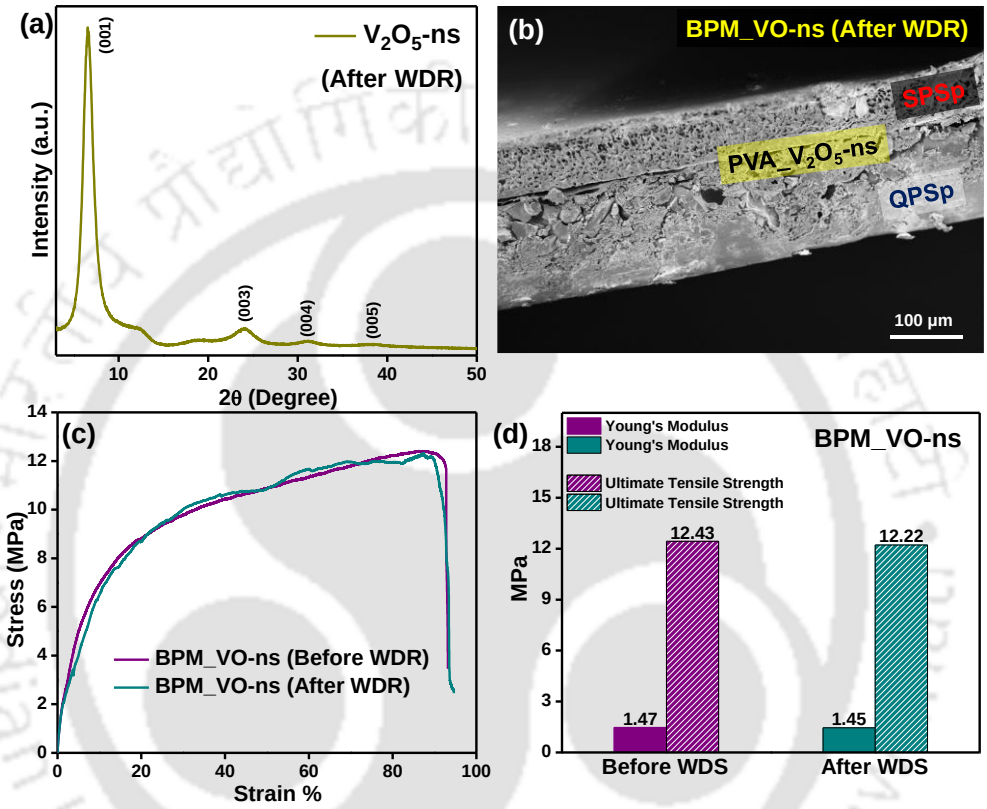

Figure 7.4.13: (a) PXRD spectra of the V_2O_5-ns catalyst extracted out from the BPM_VO-ns after the WD reaction, (b) cross-sectional of BPM_VO-ns after the WD, (c) stress vs strain plot of BPM_VO-ns before and after WD, and (d) Young's modulus and ultimate tensile strength values evaluated from the stress vs strain plots of BPM_VO-ns before and after the WD

7.5. Conclusions

In summary, a high performing bipolar membrane was fabricated using functionalized polysulphones as the ion-exchange layer (IEL) and 2D V_2O_5-nanosheets blended with polyvinyl alcohol (PVA) as the water dissociation catalyst at the interfacial layer. The functionalization of the polysulphone with $-SO_3^-$ and R_4N^+ groups successfully resulted in the increase of hydrophilicity of the polymer molecule as confirmed by the contact angle measurements thereby increasing the water uptake capacity of the membranes. The incorporation of PVA molecules resulted in good contact between the AEL and CEL, increasing the overall conductivity of the BPM as confirmed by decreased R_{ohm} value. The

incorporation of PVA molecule at the IL also enhanced the efficiency towards WD reaction as the water dissociation voltage (V_{diss}) reduced from 5.38 V to 2.68 V for BPM_PVA compared to BPM_1. The blending of V_2O_5-nanosheets with PVA proved to be an effective WDC as confirmed by the increased conductivity (decreased R_{ohm} value compared to BPM_PVA) and efficiency of WD reaction. The BPM_VO-ns displayed water dissociation voltage (V_{diss}) of 1.11 V, much lower than that of BPM_PVA and BPM_1. The high performance of the composite BPM was also demonstrated at higher current density of 100 mA/cm^2 where the transmembrane voltage (V_{trans}) of 3.6 V was obtained with water dissociation resistance (R_{diss}) of 27 mΩ.cm^2. The BPM_VO-ns on subjecting to test run of 45 hours at the low current density of 1.02 mA/cm^2 and high current density of 100 mA/cm^2 displayed negligible change in the transmembrane voltage confirming its high stability.

7.6. References

[1] M. Nazemi, J. Padgett and M. C. Hatzell, *Energy Technol.*, 2017, **5**, 1191.

[2] R. Pärnamäe, S. Mareev, V. Nikonenko, S. Melnikov, N. Sheldeshov, V. Zabolotskii, H. V. M. Hamelers and M. Tedesco, *J. Memb. Sci.*, 2021, **617**, 118538.

[3] F. Hanada, K. Hirayama, N. Ohmura and S. Tanaka, *U.S. Pat. 5*.

[4] J. Balster, R. Sumbharaju, S. Srikantharajah, I. Pünt, D. F. Stamatialis, V. Jordan and M. Wessling, *J. Memb. Sci.*, 2007, **287**, 246.

[5] M. B. McDonald, S. Ardo, N. S. Lewis and M. S. Freund, *ChemSusChem*, 2014, **7**, 3021.

[6] Y. Liu and J. Wang, *J. Memb. Sci.*, 2020, **596**, 117591.

[7] N. M. Jalal, A. R. Jabur, M. S. Hamza and S. Allami, *Energy Procedia*, 2019, **157**, 1494.

[8] P. T. Nonjola, M. K. Mathe and R. M. Modibedi, *Int. J. Hydrogen Energy*, 2013, **38**, 5115.

[9] K. Venugopal and S. Dharmalingam, *Desalination*, 2012, **296**, 37.

[10] A. M. Rajesh, M. Kumar and V. K. Shahi, *J. Memb. Sci.*, 2011, **372**, 249.

[11] J. F. Blanco, Q. T. Nguyen and P. Schaetzel, *J. Appl. Polym. Sci.*, 2002, **84**, 2461.

[12] S. Z. Oener, M. J. Foster and S. W. Boettcher, *Science*, 2020, **369**, 1099.

[13] Z. Ge, M. A. Shehzad, L. Ge, Y. Zhu, H. Wang, G. Li, J. Zhang, X. Ge, L. Wu and T. Xu, *ACS Appl. Energy Mater.*, 2020, **3**, 5765.

[14] M. Manohar and D. Kim, *ACS Sustain. Chem. Eng.*, 2019, **7**, 16493.

[15] S. Abdu, K. Sricharoen, J. E. Wong, E. S. Muljadi, T. Melin and M. Wessling, *ACS*

Appl. Mater. Interfaces, 2013, **5**, 10445.

[16] P. Kulasekaran, B. Maria Mahimai and P. Deivanayagam, *RSC Adv.*, 2020, **10**, 26521.

[17] Y. Liu and J. Wang, *J. Memb. Sci.*, 2020, **606**, 118151.

[18] G. Tocci and A. Michaelides, *J. Phys. Chem. Lett.*, 2014, **5**, 474.

[19] K. C. Hass, W. F. Schneider, A. Curioni and W. Andreoni, *Science*, 1998, **282**, 265.

[20] X. Yin, A. Fahmi, H. Han, A. Endou, S. S. C. Ammal, M. Kubo, K. Teraishi and A. Miyamoto, *J. Phys. Chem. B*, 1999, **103**, 3218.

[21] P. Hejduk, M. Szaleniec and M. Witko, *J. Mol. Catal. A Chem.*, 2010, **325**, 98.

[22] Q. Yang, X. Liu, W. Peng, Y. Zhao, Z. Liu, M. Peng, Y.-R. Lu, T.-S. Chan, X. Xu and Y. Tan, *J. Mater. Chem. A*, 2021, **9**, 3044.

[23] X. Zheng, M. Qin, S. Ma, Y. Chen, H. Ning, R. Yang, S. Mao and Y. Wang, *Adv. Sci.*, 2022, **9**, 2104636.

[24] D. Goodacre, M. Blum, C. Buechner, H. Hoek, S. M. Gericke, V. Jovic, J. B. Franklin, S. Kittiwatanakul, T. Söhnel, H. Bluhm and K. E. Smith, *J. Chem. Phys.*, 2020, **152**, 044715.

[25] K. Jug, B. Heidberg and T. Bredow, *J. Phys. Chem. C*, 2007, **111**, 6846.

[26] K. K. Ghuman, S. Yadav and C. V. Singh, *J. Phys. Chem. C*, 2015, **119**, 6518.

[27] T.-R. Ko, C.-Y. Lin and Y.-H. Lai, *Chem. Eng. J.*, 2022, **433**, 133607.

[28] C. Wang, Y. Yi, H. Li, P. Wu, M. Li, W. Jiang, Z. Chen, H. Li, W. Zhu and S. Dai, *Nano Energy*, 2020, **67**, 104253.

[29] L. Unnikrishnan, S. Mohanty, S. K. Nayak and N. P. Jayan, *Int. J. Plast. Technol.*, 2011, **15**, 1.

[30] M. Kumar, D. McGlade, M. Ulbricht and J. Lawler, *RSC Adv.*, 2015, **5**, 51208.

[31] G. Das, C. Kim, D. Kang, B. Kim and H. Yoon, *Polymers (Basel).*, 2019, **11**, 512.

[32] L. Miao, X. Wang, Y. Fu, B. Hu, Y. Bai and C. Lü, *Solid State Ionics*, 2017, **309**, 170.

[33] D. H. Nagaraju, Q. Wang, P. Beaujuge and H. N. Alshareef, *J. Mater. Chem. A*, 2014, **2**, 17146.

[34] R. K. Gogoi, A. B. Neog, T. J. Konch, N. Sarmah and K. Raidongia, *J. Mater. Chem. A*, 2019, **7**, 10552.

[35] M. B. McDonald and M. S. Freund, *ACS Appl. Mater. Interfaces*, 2014, **6**, 13790.

[36] P. K. Giesbrecht and M. S. Freund, *Chem. Mater.*, 2020, **32**, 8060.

CHAPTER 8

Thesis overview and future perspectives

This chapter, in brief, outlines the outcomes and overview of the current thesis. Herein, it also discusses the possible modification in the near future that can be done with the metal oxides to enhance overall water splitting performance.

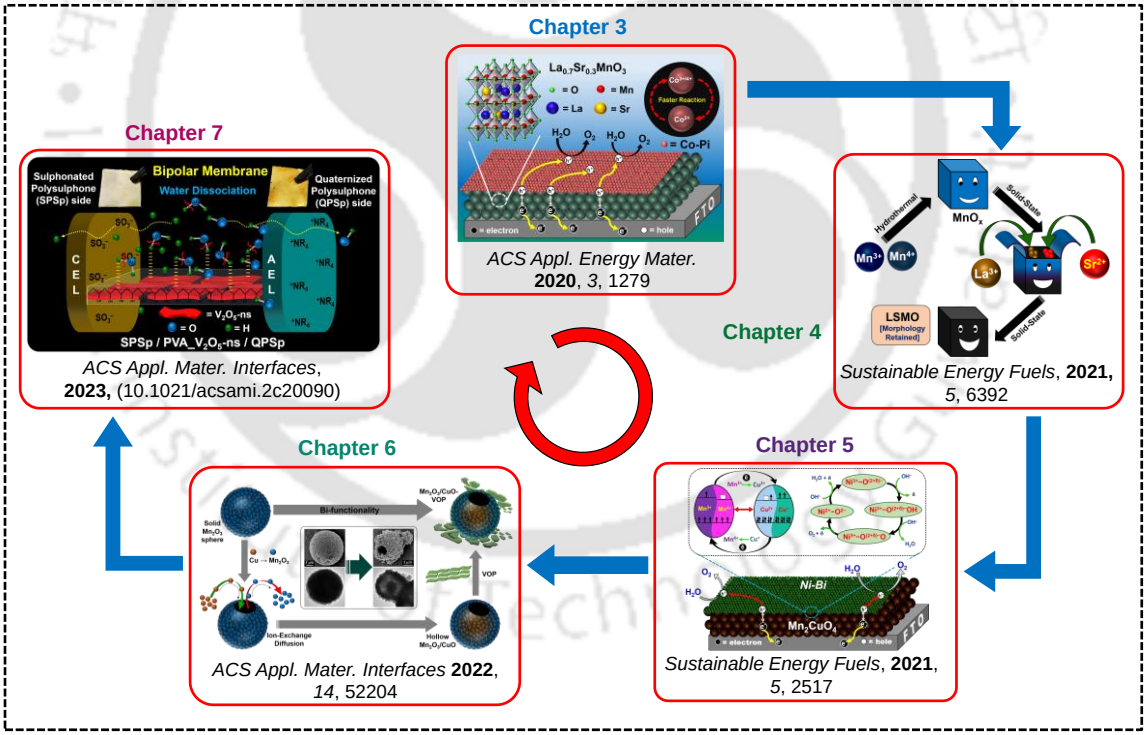

8.1. Thesis Overview

The thesis mainly focused on the diverse strategies to be utilized for the betterment of electrochemical oxygen evolution reaction (OER) and hydrogen evolution reaction (HER), i.e., the overall water splitting by different metal oxides. The electrochemical efficiency of the metal oxides was modified utilizing different methods like elemental doping, morphological tuning, surface overlayer and heterojunction formation. During the synthesis of the electrocatalysts (metal oxides), the hydrothermal and solid-state routes were mainly considered owing to their non-complicacy, cost-effectiveness and environment-friendly nature. For the fabrication of the working electrodes over FTO substrate, general Doctor-blade method as utilized due to its simplicity and cost-effectiveness. The thesis priorities the different strategies utilized for the development of metal oxides and tuning the electronic and/or structural features based on their intrinsic properties. This thesis also discusses about the development and modification of bipolar membranes (BPM) required to separate the anodic and cathodic chambers for practicality of the electrolytic process. The summary and conclusions for each chapter (valuable outcomes obtained from the work done during my Ph.D. tenure) are summarized as follows:

- ✓ **Chapter 1:** Here the global energy consumption and environmental challenges have been introduced along with the need for a sustainable energy source to produce zero-emission H_2/O_2 gas. The basic principle of electrochemical water splitting (producing O_2 and H_2 gases), water dissociation (generation H^+ and OH^- ions) and different strategies to enhance the overall efficiency of the semiconductor and electrocatalysts are discussed. A brief literature survey on the current state-of-the-art as well as challenges related to the modification of metal oxides, fabrication of the electrodes and bipolar membranes are also discussed. At last, this chapter is concluded with the objectives of the present thesis.
- ✓ **Chapter 2:** The different instrumental techniques, performance parameters, and different experimental setups, which were adopted for the characterization of the as-synthesized electrocatalysts and determination of water splitting performance of the fabricated electrodes are discussed in detail. Also, the fabrication technique of the bipolar membrane is also included in this chapter.
- ✓ **Chapter 3:** In this chapter, we have utilized the doping strategy to enhance the electrochemical performance by virtue of its increased bulk conductance. $LaMnO_3$, a 3D perovskite was chosen due to its high flexibility of elemental composition, tunable electronic/defect structure and high stability. Here, Sr^{2+} was doped into the La^{3+} (A-site)

resulting in conversion of some Mn^{3+} to Mn^{4+} state which tends the Mn–O–Mn bond to ~180°, thereby enhancing the conductivity due to facile charge mobility within the bulk. $La_{0.7}Sr_{0.3}MnO_3$ was found to be best performing electrocatalyst and in turn was further modified with an overlayer of cobalt phosphate (Co-Pi). The faster reaction kinetics of cobalt phosphate ($Co^{2+} \leftrightarrow Co^{3+} \leftrightarrow Co^{4+}$) at the electrolyte interface led to ~4-fold enhanced turnover frequency of the composite due to the ~12-fold reduced charge transfer resistance (R_{ct}) value. A remarkable low overpotential of 220mV @ 10 mA cm^{-2} with a significantly small Tafel slope of 62 mV per decade is attained for $La_{0.7}Sr_{0.3}MnO_3$/Co-Pi which is comparable to the benchmark RuO_2 water oxidation catalysts (performed under similar experimental conditions). Systematic study on the effect of strontium doping at different concentrations and the deposition of Co-Pi overlayer at different time have also been studied. Further, the ~98% Faradaic yield and 16 hours long-run stability proved the high efficiency of the composite electrocatalyst.

- ✓ **Chapter 4:** In this chapter, we have utilized the morphological strategy to increase the electroactive sites and the charge conductivity of 3D perovskites thereby enhancing their electrochemical performance. The traditional high temperature synthetic procedure leaves little scope for morphological tuning using structure-directing and/or high temperature unstable reagents. To obtain desired morphologies of complex metal oxide, an alternate methodology has been adopted where rationally designed hard-template precursors with desired morphology are utilized for transcription of the corresponding morphologies to its higher analogues. In present work, we chose strontium doped lanthanum manganite (LSMO) as model system to demonstrate our transcription methodology. A library of unique morphologies of LSMO is achieved by tuning rational morphologies of manganese oxide (Mn_xO_y) and utilizing it as template during the high temperature calcination process. Diffusion controlled solid-state route enables transcription of the pre-defined morphologies of Mn_xO_y into the corresponding LSMO. A step-by-step formation mechanism of the synthesized Mn_xO_y and LSMO are well demonstrated graphically. Rietveld analysis was executed to determine the presence of dual phase, orthorhombic and rhombohedral, of the synthesized morphological LSMO where the dominant phase is governed by the phase of its analogous Mn_xO_y. The synthesized LSMO were then utilized as electrocatalyst for the oxygen evolution reaction (OER) to establish the morphology–property correlations. A ~4-fold enhanced electrocatalytic performance of the champion morphological (wire shaped) LSMO compared to its solid-state synthesized counterpart was obtained supporting the

motivation of the morphology modification via transcription methodology. Also, comparing electrocatalytic performance of all the morphological LSMO, the 1D structures (wires, rods, fused-rods) showed better efficiency than the 3D structures (spheres, cuboids, flakes, nano-blocks, fused-cubes) owing to their higher electroactive sites and charge transfer mobility as confirmed by the ECSA (C_{dl}) and R_{ct} values. Thus, the overall OER efficiency of the synthesized LSMO can be summarized as wires > rods > fused-rods > spheres > cuboids > nano-blocks > flakes > fused-cubes based on the obtained overpotential, Tafel slope and turnover frequencies of the respective LSMO.

- ✓ **Chapter 5:** In this chapter, we have synthesized a bi-metal oxide, di-manganese copper oxide, having high stability and electrochemical activity by virtue of the mixed valence states of Mn (III/IV) and Cu (II/I). The 2D flake-like structures of as-synthesized Mn_2CuO_4 provided better exposed surface for the incoming electrolyte molecules to interact with the electroactive sites and the redox couple ($Mn^{3+} + Cu^{2+} \leftrightarrow Mn^{4+} + Cu^{+}$) within the bulk stabilized the molecule during the OER, thus the high electrochemical performance. The OER kinetics was further boosted by depositing nickel borate (Ni-B_i) over its surface via electrodeposition. The redox cycle of Ni atom ($Ni^{2+} \leftrightarrow Ni^{3+}$) facilitated the charge transfer process at the electrolyte interface thereby accelerating the overall water oxidation process. A low overpotential of 230 mV @ 10 mA cm^{-2} with a small Tafel slope of 56 mV per decade was attained for Mn_2CuO_4/Ni-B_i which is comparable to the benchmark RuO_2 water oxidation catalysts (performed under similar experimental conditions). Systematic study of the individual metals in the complex oxide and the deposition of Ni-B_i overlayer at different time have been studied. The Mn_2CuO_4/Ni-B_i also showed an impressive turnover frequency (TOF) of 0.05 s^{-1} and excellent stability of 20 hours under alkaline conditions. The electrochemical active surface area (ECSA) of the Mn_2CuO_4 was also enhanced by Ni-B_i deposition resulting in an enhanced double layer capacitance (C_{dl}) value of 55 mF/cm^2. Probable mechanistic pathway involved an efficient extraction of carriers by the overlying Ni ions supported by the redox cycle of Mn and Cu within the bulk. The impedance spectroscopy depicted a decreased charge transfer resistance (R_{ct}) value for Mn_2CuO_4/Ni-B_i of 13.15 Ω suggesting facile movement of the carriers at interface thereby enhancing the reaction kinetics resulting in an exceptional electrocatalytic activity. A Faradaic yield close to unity (~98 %) for the OER suggested the oxygen evolved during the reaction was solely from the water oxidation.

- ✓ **Chapter 6:** In this chapter, we have inherited effective bi-functional (HER-OER) property by coupling Mn_2O_3 (promising OER catalyst) with CuO (promising HER catalyst) using solvothermal method. The synthesized Mn_2O_3/CuO also formed *n-p* type heterojunction (confirmed using Mott-Schottky technique) leading to better charge separation and accumulation at the semiconductor interface. Also, the difference in rate of diffusion coefficients of the respective metal ions ($D_{Mn} > D_{Cu}$) led to transformation of Mn_2O_3 solid spheres into hollow spherical structures of Mn_2O_3/CuO due to the ion-exchange Kirkendall effect. The hollow spheres led to the increase in number of electroactive sites owing to more exposed surface area. Thus, Mn_2O_3/CuO showed advancement in bi-functional electrocatalytic behavior with overpotential (η_{10}) of 280mV for OER and 310 mV for HER corresponding to Tafel slopes of 124 mV/decade and 160 mV/decade, respectively. The increased electrochemical active surface area (ECSA, i.e., C_{dl} = 34 mF/cm^2) and reduced charge transfer resistance (R_{ct} = 17.8 **Ω**) also resulted the formed Mn_2O_3/CuO hollow spheres to achieve ~3-fold enhanced turnover frequency (TOF) compared to bare Mn_2O_3. The electrocatalytic efficiency of Mn_2O_3/CuO was further enhanced by virtue of the faster charge transfer coefficient of two-dimensional (2D) vanadyl phosphate hexahydrate (VOP) sheets deposited over its surface. This boosted the overall water splitting with attained overpotential (η_{10}) values of 190 mV and 220 mV with Tafel slopes of 60 mV/decade and 105 mV/decade for OER and HER, respectively. The high charge transfer coefficient value of VOP aided the ease transfer of charge carriers from the semiconductor to the electrolyte interface thus increasing the overall reaction kinetics. This is well supported by the ~3-fold enhanced TOF in OER and ~2-fold enhanced TOF in HER for the composite, Mn_2O_3/CuO-VOP, compared to Mn_2O_3/CuO. The durability of the composite electrocatalyst was also examined with 36 hours of long-run stability test for both OER and HER while its electrochemical activity towards water splitting was confirmed from the obtained average Faradaic yield of ~98%. Thus, the triple modified semiconductor resulted in an overall ~10-fold boosted bi-functional (HER-OER) performance towards overall water splitting.
- ✓ **Chapter 7:** In this chapter a different experimental route has been taken to enhance the electrolysis of water. Here we have utilized a bipolar membrane (BPM) in between the cathodic and anodic chambers and modified the water dissociation process occurring at the interfacial layer (IL) generating H^+ and OH^- ions which are then converted to H_2 and O_2 at cathode and anode, respectively. Herein, a high performing bipolar membrane (BPM) was fabricated using functionalized polysulphones as the ion-exchange layer

(IEL) and 2D V_2O_5-nanosheets blended with polyvinyl alcohol (PVA) as the water dissociation catalyst (WDC) at the interfacial layer. The composite BPM showed a low ohmic resistance of 0.79 $\Omega.cm^2$ confirming the good contact between IEL and WDC much needed for the electrical conductivity. It also demonstrated high water dissociation performance with pseudo-limiting current density of 0.98 mA/cm^2 at transmembrane voltage of 1 V in the presence of 1M NaCl electrolytic solution. The water dissociation voltage was found to be 1.11 V for the composite BPM. The functionalization of the polysulphone with $–SO_3^-$ and R_4N^+ groups successfully resulted in enhanced hydrophilicity of the polymer thereby increasing the water uptake capacity of the membranes. The blending of 2D V_2O_5-nanosheets with PVA proved to be an effective WDC as confirmed by the increased conductivity and efficiency of WD reaction. The 2D V_2O_5-ns have great potential towards water adsorption onto its surface thereby interacting with the water molecules weakening the bonding force of water, dissociating it into H^+ and OH^-. The high performance of the composite bipolar membrane (BPM_VO-ns) was demonstrated at higher current density of 100 mA/cm^2 with water dissociation resistance of 0.027 $\Omega.cm^2$ while the durability was confirmed by subjecting it to test run of 45 hours at the lower (1.02 mA/cm^2) and higher (100 mA/cm^2) current densities displaying negligible change in the interlayer voltage. Thus, the fabricated composite bipolar membranes pave its way to be utilized for efficient and durable water dissociation reaction at the neutral electrolytic conditions.

8.2. Future Perspectives

The presented thesis outlined the several aspects and new findings in designing and development of metal oxide-based electrochemical water splitting and water dissociation during the research tenure. A detailed study on the electrocatalysts was carried out to resolve issues related to adsorption of reactant species onto surface, interfacial charge transfer resistance, ohmic contact at the interface, electrochemical active surface sites, and reaction kinetics. Although, several strategies have been adopted here making substantial advancements in the field of electrochemical water splitting, numerous scopes are still available to further improve the overall efficiency towards commercialization. The plausible scopes for the advancement of electrochemical water splitting towards practicality are as follows:

- ✓ Usage of double dopants for both A-site and B-site in ABO_3 type perovskite will further enhance the bulk conductivity and charge transfer kinetics towards OER.
- ✓ Utilization of double perovskites with multi-valent ions can increase the stability and activity towards both OER and HER owing to the presence of multiple redox centers. Also, double perovskite provides larger scope for tuning of their electronic and structural features thereby upgrading the intrinsic properties towards catalysis.
- ✓ The transcription methodology and Kirkendall effect can also be utilized for the synthesis of different complex metal oxides ascribed with desired morphologies thus increasing the exposed surface area of the catalyst.
- ✓ Synthesis of two-dimensional compounds with multi-valent metal ions having higher oxidation states for the reduction of water adsorption energy and also simultaneous redox reaction thereby enhancing both active sites and reaction kinetics.
- ✓ Formation of heterojunction between champion HER and OER electrocatalysts to induce bi-functional behavior in the semiconductor with high efficiency.
- ✓ Development of ion-exchange membranes with functional groups having conjugation and capable of forming inter-molecular interactions thus increasing the conductivity and forming strong adhesion among the CEL and AEL thereby enhancing the water dissociation reaction at IL region.
- ✓ Incorporation of metal-organic framework (MOF) as water dissociation catalysts between the AEL and CEL for boosted dissociation of water reaction owing to the presence of two different catalytic sites – the inorganic catalytic groups (metal groups) in the centre and organic catalytic groups in the ligands.

LIST OF PUBLICATIONS AND CONFERENCES / WORKSHOPS ATTENDED

Journal Articles:

✓ ***Scientific Contributions (Included in Thesis):***

1. **S. Bhowmick**, et. al. Vanadium oxide nanosheets infused functionalized polysulphone bipolar membrane for efficient water dissociation reaction. *ACS Applied Materials & Interfaces*, **2023**, DOI: 10.1021/acsami.2c20090.
2. **S. Bhowmick**, et. al. Diffusion mediated morphological transformation in bifunctional Mn_2O_3/CuO-$(VO)_3(PO_4)_2.6H_2O$ for enhanced electrochemical water splitting. *ACS Applied Materials & Interfaces*, **2022**, *14*, 52204–52215.
3. **S. Bhowmick**, et. al. Transcription methodology for rationally designed morphological complex metal oxides: a versatile strategy for improved electrocatalysis. *Sustainable Energy & Fuels*, **2021**, *5*, 6392-6405.
4. **S. Bhowmick**, et. al. Bimetallic cyclic redox couple in dimanganese copper oxide supported by nickel borate for boosted alkaline electrocatalytic oxygen evolution reaction. *Sustainable Energy & Fuels*, **2021**, *5*, 2517-2527.
5. **S. Bhowmick**, et. al. Low Overpotential and Stable Electrocatalytic Oxygen Evolution Reaction Utilizing Doped Perovskite Oxide, $La_{0.7}Sr_{0.3}MnO_3$, Modified by Cobalt Phosphate. *ACS Applied Energy Materials*, **2020**, *3*, 1279-1285.

✓ ***Scientific Contributions (Off the Thesis):***

1. A. Katare, S. Sharma, H. Horo, **S. Bhowmick**, et. al. An investigation on the effects of both amine grafting and blending with biodegradable chitosan membrane for the CO_2 capture from flue gases. *Chemical Engineering Journal*, **2023** (revision submitted).
2. A. Sahu, P. Pandey, **S. Bhowmick**, et. al. Spectator metal ion guided cobalt oxy hydroxide as a redox dominant electrode for a high-performance supercapacitor. *Chemical Communications*, **2023**, DOI: 10.1039/D2CC06162G.
3. P. Pandey, **S. Bhowmick**, et. al. Aluminium triggered lattice transition in urchin shaped Ni-Co-Cu carbonate hydroxide for high performance pseudocapacitor. *Sustainable Energy & Fuels*, **2022** (in peer review).
4. N. Kalita, **S. Bhowmick**, et. al. Synchronized redox pairs in metal oxide/hydroxide chemical analogues for efficient oxygen evolution reaction. *Chemical Communications*, **2022**, 58, 13747-13750.

5. M. K. Mohanta, T. K. Sahu, **S. Bhowmick**, et. al. Synchronized carrier extraction and injection through boron nitride nanoplatelets in hierarchical $BiVO_4$/CoCr-layered double hydroxides for efficient water oxidation. *Electrochimica Acta*, **2022**, 415, 140269.
6. **S. Bhowmick**, et. al. Spontaneous Fenton-like dye degradation in clustered-petal di-manganese copper oxide by virtue of self-cyclic redox couple. *Journal of Environmental Chemical Engineering*, **2021**, *9*, 106094.
7. C. T. Moi, **S. Bhowmick**, et. al. Hierarchical FeO(OH)–CoCeV(Oxy)hydroxide as a Water Cleavage Promoter. *ACS Applied Materials & Interfaces*, **2021**, *13*, 51151-51160.
8. A. K. Shah, **S. Bhowmick**, et. al. Hollow cuboidal $MnCo_2O_4$ coupled with nickel phosphate: a promising oxygen evolution reaction electrocatalyst. *Chemical Communications*, **2021**, *57*, 8027-8030.
9. C. T. Moi, **S. Bhowmick**, et. al. Electrocatalytic oxygen evolution surpassing benchmark RuO_2 using stable, noble metal free vanadium doped hematite co-modified by NiFe Layered Double Hydroxide. *Electrochimica Acta*, **2021**, *370*, 137726.
10. T. K. Sahu, S. Alam, **S. Bhowmick**, et. al. Phosphorus nitride nano-dots as a versatile and metal-free support for efficient photoelectrochemical water oxidation. *Chemical Communications*, **2021**, *57*, 6157-6160.
11. K. K. Sarmah, T. Rajbongshi, **S. Bhowmick**, et. al. First-line antituberculosis drug, pyrazinamide, its pharmaceutically relevant cocrystals and a salt. *Acta. Crystallogr. B. Struct. Sci. Cryst. Eng. Mater.* **2017**, *73*, 1007-1016.

Conferences/Workshops:

1. Oral Presentation in the 58th Annual Convention of Chemists, 2021 & International Conference on "*Recent Trends in Chemical Sciences (**RTCS-2021**)*" organized by the Indian Chemical Society, Kolkata, India.
2. Flash Talk Presentation in the 7th "*International Conference on Advanced Nanomaterials and Nanotechnology (**ICANN 2021**)*", organized by the Centre for Nanotechnology, IIT Guwahati, Assam, India.

3. Oral Presentation at "*Recent Advances and Innovations in Solar Energy (**RAiSE 2021**)*" organized by DST-IITM Solar Energy Harnessing Centre, Indian Institute of Technology Madras, India.
4. Oral Presentation in the International Conference on "*Progress and Challenges in Modern Day Science (**PCMDS-2021**)*" organized by Department of Chemistry, B. Borooah College in association with Assam Science Society, India.
5. Poster Presentation in "*Frontiers in Chemical Sciences (**FICS 2018**)*" organized by Department of Chemistry, Indian Institute of Technology, Guwahati, India.
6. Participation in online workshop on **Powder X-Ray Diffraction Techniques and its Applications, 2021**, North East Centre for Biological Sciences and Healthcare Engineering (NECBH), Indian Institute of Technology Guwahati, India.
7. Attended **RSC-IISER Desktop Seminar with ChemComm** organized by RSC (Royal Society of Chemistry) Publishing Webinars in August, 2021.